Experimental Determination of U and Th Partitioning Between Clinopyroxene, Garnet, Olivine, and Natural and Synthetic Silicate Melt

Thesis by

Tom LaTourrette

In Partial Fulfillment of the Requirements

for the Degree of

Doctor of Philosophy

California Institute of Technology

Pasadena, California

1993

(Submitted September 10, 1992)

Acknowledgements

I would like to thank Don Burnett for his guidance and support. I have benefited from his high standards and penchant for pursuing subtle complexities. Ed Stolper has been very supportive, opened his laboratory facilities to me, and introduced me to the benefit and joy of creative thinking. George Rossman has guided me in understanding crystal structure, trace element substitution, and the U valence state distribution in silicate melts. Discussions, advice, and encouragement from Leon Silver, Charles Bacon, Dorothy Woolum, Arden Albee, and Ian Carmichael are genuinely appreciated. I thoroughly enjoyed participating in the NASA Graduate Student Researchers Program, which provided me with three years of financial support.

Much of what I know about experimental petrology has been gleaned from numerous helpful confabulations with John Beckett, Mike Baker, Glen Mattioli, and Mary Johnson. Mike Baker graciously spent many hours teaching me how to use the piston-cylinder press. Paul Carpenter's assistance was invaluable during my many hours of electron microscope and electron microprobe time. Tom Crofoot and Pat Rogers of U. C. Irvine ran the neutron irradiations and Allen Kennedy kindly conducted the SIMS analyses. Vic Nenow's expertise kept all of the laboratory equipment in good repair. Thanks to Jim O'Donnell and Pat Kelly for maintaining such a well organized and pleasant library.

Special thanks go all of my fellow graduate students, especially my classmates D. J. Wood, Jen Blank, Linda Rowan, Andrea Donnellan and Lori Chamberlin for stimulating discussions, encouragement, and friendship during my graduate work. I am also indebted to Stew McKean, Jey Giuliano, Paul Kirk, and all of the other musicians that I've played with for the joy that music brings me. Finally, I thank Andrea Ghez for everything. This thesis is dedicated to Todd Sutherland.

I counted over 192,000 fission and alpha tracks in the course of this study.

Abstract

The distribution of U and Th between crystals and quenched silicate melt has been measured in experimentally crystallized natural and synthetic starting compositions. Clinopyroxene was crystallized from two natural basalts and a synthetic composition on the diopside-anorthite join, olivine from one of the natural basalts, and garnet from a synthetic andesite. Clinopyroxene and olivine were crystallized at atmospheric pressure under controlled oxygen fugacity and U and Th distributions were determined by particle track radiography. Garnet crystals were grown at 27 Kbars and actinide distributions were determined by secondary ion mass spectrometry. Crystals were grown by slow cooling in an effort to maintain chemical equilibrium at the crystal-melt interface.

Clinopyroxene- and olivine-melt partition coefficients ($D_i^{xtl/liq} = C_i^{xtl}/C_i^{liq}$) were calculated from track distributions by correcting for chemical zoning in the crystals (a result of fractional crystallization) and particle range differences between the crystals and glass. Over the range of fO_2s and compositions studied, $D_U^{cpx/liq} = 0.0021 - 0.0093$, $D_{Th}^{cpx/liq} = 0.0047 - 0.021$, and $D_{U;Th}^{ol/liq} < 0.00005$. Garnet-melt partition coefficients are $D_U^{gt/liq} = 0.0013$ and $D_{Th}^{gt/liq} = 0.0122$. In order to study the effect of the U valence state distribution on U-Th fractionation, clinopyroxene crystallization experiments were run at oxygen fugacities corresponding to the Ni-NiO (NNO), Fa-Mt-Qz (FMQ) and 1 log unit more oxidizing than Fe-FeO (IW+1) oxygen buffers. All compositions show an increase in $D_U^{cpx/liq}$ with decreasing fO_2, presumably from the increasing proportion of U^{4+} in the melt. $D_{Th}^{cpx/liq}$ displays little variation with fO_2, consistent with the fact that Th is solely tetravalent. $D_{Th}^{cpx/liq}$ does show an apparent small decrease with decreasing fO_2 in one composition, and this is interpreted to be due to compositional changes stemming from variable amounts Na-loss with fO_2. A limited compositional analysis indicates that actinides may be incorporated into clinopyroxene by means of a $(U,Th)^{4+} + 2Na^{+} \Leftrightarrow$

$3Ca^{2+}$ coupled substitution in the M2 site. This mechanism predicts a positive dependence of the actinide partition coefficients on $(D_{Ca}^{cpx/liq})^3/(D_{Na}^{cpx/liq})^2$.

While there is evidence for deviations from interfacial equilibrium during crystal growth, $D_{Th}^{xtl/liq}$ and $D_{U}^{xtl/liq}$ are affected similarly. This results in $D_{Th}^{xtl/liq}/D_{U}^{xtl/liq}$, which gives a measure of the degree of U-Th fractionation possible by crystal-melt partitioning, being insensitive to these deviations. $D_{Th}^{cpx/liq}/D_{U}^{cpx/liq}$ is well behaved, approximately independent of composition, and decreases by a factor of 2 - 3 as the fO_2 decreases from NNO to IW+1. This indicates that U-Th fractionation by crystal-melt partitioning is fO_2 dependent.

These results indicate that U-Th fractionation by clinopyroxene-melt partitioning during partial melting will result in a melt with Th/U less than the clinopyroxene, U-Th fractionation by olivine will be insignificant for physically realistic melt fractions, and U-Th fractionation by garnet will result in a melt with Th/U greater than the garnet. The observed pattern of ^{238}U-^{230}Th disequilibrium in oceanic basalts (MORB and OIB) requires a net U-Th fractionation that is large, ubiquitous, and results in $(^{238}U/^{230}Th) < 1$. With these constraints, fractionation by partial melting of spinel lherzolite is ruled out. The sense of U-Th fractionation by garnet is consistent with oceanic basalts, but the magnitude of fractionation is much smaller than the entire range in observed fractionations. Since partial melts of neither spinel nor garnet lherzolite can match the sense and magnitude of ^{238}U-^{230}Th disequilibrium in MORB and OIB, partial melting is considered unimportant in generating ^{238}U-^{230}Th disequilibrium in oceanic basalts. ^{238}U-^{230}Th disequilibrium in MORB and OIB must therefore result from some process other than partial melting, and possible alternative mechanisms are presented.

Contents

List of Figures

List of Tables

Chapter One

Introduction

Measurements of U and Th in igneous rocks indicate that U and Th exhibit fairly similar geochemical behavior and are highly incompatible in the major rock forming minerals. Thus, little U-Th fractionation is expected in planetary igneous processes. In accordance with this expectation, there is a relatively strong coherence for U and Th in lunar rocks and meteorites (e.g., Taylor 1982), and during planetary differentiation actinide elements become highly concentrated in the crust. However, despite their geochemical similarity and highly magmaphile nature, significant fractionation of U and Th can occur. There are well documented deviations from the solar system Th/U value of $\approx 3.5 - 4$ in virtually all types of terrestrial volcanic rocks, chondrites, CAIs, and Apollo 17 mare basalts (Gill et al. 1992; Hagee et al. 1990; Murrell and Burnett 1987; Laul and Fruchter 1976). Our present understanding of the geochemical behavior of U and Th during igneous processes is derived mainly from measurements in natural rocks, where the temperature, pressure, phases involved, compositions, oxidation state, etc. of the system are often not well constrained. Consequently the origins of these fractionations are poorly understood. I undertook this study to provide the beginnings of an experimental framework with which to interpret U-Th fractionations in nature.

1.1 Background: Th/U and U-Th Fractionation

1.1.1 U-Th Fractionation in Terrestrial Volcanism as Revealed by ^{238}U-^{230}Th Disequilibrium

Th/U in terrestrial rocks varies considerably in both space and time (Gill et al. 1992; Tatsumoto 1978). One of the best illustrations of this variation is the existence of ^{238}U-^{230}Th disequilibrium in young volcanic rocks. Because of the relatively short half-life of ^{230}Th (75.4 Ka), this disequilibrium requires that fractionations of U and Th be recent, and

thus gives a measure of the present rate of Th/U evolution in the mantle. Secular disequilibrium between ^{238}U and its radiogenic daughter, ^{230}Th, results when either U or Th is preferentially extracted from or added to a system. Subsequent to this change, radioactive decay brings the system back into secular equilibrium in 3 - 5 half-lives, or 225 - 375 Ka. The existence of ^{238}U-^{230}Th disequilibrium in volcanic rocks therefore provides unequivocal evidence for U-Th fractionation within the last $\approx$ 0.3 Ma. Because the half-life of ^{230}Th is relatively short, ^{238}U and ^{230}Th in the source regions for volcanic rocks are often assumed to be in secular equilibrium, and thus their activities equal. This means that the initial conditions are much better constrained than for other radioactive decay systems. Thus, this system has the unique advantage that the degree of ^{238}U-^{230}Th disequilibrium provides a quantitative measure of the amount of U-Th fractionation. Immediately following a fractionation event the degree of radioactive disequilibrium is equal to the degree of U-Th fractionation produced during the event (i.e., $(^{238}U/^{230}Th)_{melt} = [U/Th]_{melt}/[U/Th]_{source}$, where parentheses indicate activity ratios and brackets indicate elemental ratios). Therefore we know that a young volcanic rock with $(^{238}U/^{230}Th) =$ 0.85, for example, has U/Th 15% lower than that of its source.

^{238}U-^{230}Th disequilibrium and Th isotope measurements are extremely powerful tools for understanding a variety of petrologic problems. In many cases, however, the interpretation of these measurements is limited by a lack of accurate knowledge of U-Th fractionation mechanisms. These limitations can be illustrated in four important applications of U-series disequilibrium: 1) Determining the degree of partial melting in the source (McKenzie 1985; Williams and Gill 1989). Perhaps the most profound aspect of ^{238}U-^{230}Th disequilibrium is that the degree of disequilibrium can potentially provide a quantitative measure of the degree of melting. This application depends on the assumption that the disequilibrium arises from partial melting and requires detailed knowledge of the crystal-melt partitioning behavior of U and Th. 2) Discerning Th/U variations in a magmatic source region (e.g., Ben Othman and Allègre 1990). The Th/U of a magmatic

source can be inferred from ($^{230}Th/^{232}Th$) of erupted lavas, provided that the fractionation event was more or less instantaneous and little time has passed since segregation from the source. For regions undergoing roughly continuous volcanism, such as mid-ocean ridges, melting is probably more of a continuous process and any disequilibrium in the erupted lavas will reflect time-integrated fractionations. Only with adequate knowledge of the extent and variation of U-Th fractionation with melting, transport, and crystallization can meaningful $[Th/U]_{source}$ values be extracted from ($^{230}Th/^{232}Th$). 3) Providing constraints on magmatic evolution (Condomines et al. 1982). Variations in ($^{230}Th/^{232}Th$) through the eruptive history of a single volcano can be used to distinguish open or closed system magmatic evolution and identify episodes of magmatic reinjection or contamination. A quantitative understanding of U-Th fractionation would help determine origin and amounts of such added components. 4) Dating young volcanic rocks. ^{238}U-^{230}Th disequilibrium can be used to date a U-Th fractionation event in one of two ways. An internal isochron can be constructed with measurements of individual phases separated from a sample; this method presumably dates U-Th fractionation accompanying crystallization (e.g., Condomines et al. 1982). In general, the details of U-Th fractionation are unimportant for interpreting ages determined with this method. As long as the isochron is defined by at least three phases, the individual mineral fractionations are constrained to be coeval and must have occurred after melting and before eruption. Whole rock ^{238}U-^{230}Th disequilibrium ages, however, are subject to more uncertainty (e.g., Goldstein et al. 1992). The U-Th fractionation being exploited with this technique is that of the erupted lava relative to the source and it is not constrained to have occurred in the magma chamber. While whole rock ^{238}U-^{230}Th disequilibrium is thought to occur during partial melting, there is often no way to rule out fractionation of the source prior to melting, or fractionation after eruption by alteration. This represents a significant temporal uncertainty. It may be possible to distinguish these alternative fractionations with detailed knowledge of the partitioning behavior of U and Th.

As has been seen for various other isotopic and trace element systems, it is quite likely that the applications and our interpretations of ^{238}U-^{230}Th disequilibrium will evolve with our understanding of the geochemistry of U and Th.

1.1.2 Long Term Evolution of Terrestrial Th/U From Pb Isotopes

In contrast to ^{238}U-^{230}Th disequilibrium, Pb isotopes are sensitive to long term variations in Th/U, and, combined with recent Th/U measurements, indicate that Th/U has varied on a billion year time scale (e.g., Tatsumoto 1978). A time-integrated Th/U for the upper mantle, <Th/U>, can be estimated from Pb isotopes in MORB by measuring ^{208}Pb and ^{206}Pb, which are the stable radiogenic daughters of ^{232}Th and ^{238}U, respectively. <Th/U> is calculated from [$^{208}Pb/^{206}Pb$] after correcting for the primordial [$^{208}Pb/^{206}Pb$] (estimated from meteorites) and the decay of ^{232}Th and ^{238}U over the age of the Earth. From measurements of young MORB, <Th/U> $\approx$ 3.75. This calculated value for <Th/U> integrates changes over the history of the Earth and represents an average value. The present Th/U of the upper mantle can be estimated from ($^{230}Th/^{232}Th$) of MORB lavas. Assuming that the source region is in secular equilibrium and the time between partial melting and eruption is short, $(^{230}Th)_{sample} = (^{230}Th)_{source} = (^{238}U)_{source}$. $[Th/U]_{source}$ and $(^{230}Th/^{232}Th)_{sample}$ are then inversely related by the decay constants of ^{232}Th and ^{238}U. This type of estimate for the present Th/U gives 2 - 2.5, significantly lower than <Th/U> (Galer and O'Nions 1985). This discrepancy is enigmatic, as the modern Th/U is too low to support the long term radiogenic growth of ^{208}Pb, but is broadly consistent with $(^{238}U/^{230}Th) < 1$ in MORB lavas, which indicates that repeated extraction of MORB will progressively decrease Th/U of the source (Oversby and Gast 1968). An understanding of U-Th fractionation mechanisms can add constraints to Pb isotope evolution models.

1.1.3 Th/U in Meteorites and Lunar Samples

As previously mentioned, Th/U in meteorites and lunar rocks shows much less variation than in terrestrial samples. Most lunar mare basalts have Th/U between 3.4 and

4.2 (Taylor 1982) and most chondrites do not vary significantly from a range of Th/U = 3.5 - 4.0 (Hagee et al. 1990; Chen et al. 1992a,b). There are, however, marked exceptions to these values. Most notably, the Apollo 17 mare basalts have very low Th/U = 2 - 3.5 (Laul and Fruchter 1976), and the Harleton and Glatten L6 chondrites have very high Th/U > 6 (Unruh 1982; Chen et al. 1992a). While not as common, U-Th fractionations in lunar and meteoritic samples are important to understand because they arise under very different petrogenetic conditions (e.g., very reducing, absence of appreciable water) from terrestrial fractionations. In addition to helping illuminate petrogenetic processes, understanding U-Th partitioning is necessary for determining whole planet U and Th abundances. These values are required for accurate cosmochemical and heat flow modelling, and often must be calculated from measurements of only a small portion (i.e., the crust) of a planet due to sampling limitations.

1.2 Thesis Approach and Scope

This thesis was motivated by the problem of understanding U-Th fractionations in igneous processes. Trace elements can be fractionated during virtually every step of the geochemical cycle. Some common processes known to fractionate trace elements are partial melting, separation of immiscible liquids, crystallization, assimilation of xenolithic material, degassing, oxidation, hydrothermal alteration, and weathering. Each trace element conforms to a specific set of rules, and thus responds uniquely to a given process. Consequently, one of the most useful features of trace element fractionations is their ability to betray the petrologic history of a sample. However, in order to properly interpret the trace element signature of a sample, the rules for a given element must be known. One way to determine these rules is by experimentally measuring behavior of trace elements in response to known parameters. Results from such experimental studies, when used with appropriate caution, can be extremely useful in interpreting data collected from the Earth.

In this study I specifically addressed the extent to which crystal-melt partitioning can fractionate U and Th. Of the several igneous processes mentioned above that may fractionate trace elements, partial melting, buoyant rise of magma, and subsequent crystallization are thought to be the primary differentiation processes in the terrestrial planets, and therefore have been regarded as the most fundamental trace element fractionation mechanisms. As yet, there is a dearth of such basic crystal-melt partitioning data for the actinides. This is perhaps surprising considering the fairly large amount of data for some other trace elements, for example the rare earths. Two possible reasons for this deficiency are that (1) U and Th are extremely magmaphile, and thus their crystal-melt partition coefficients are very difficult to measure and (2) the potential implications of ^{238}U-^{230}Th disequilibrium are only recently being recognized and utilized (e.g., McKenzie 1985).

High temperature crystal growth experiments were run with natural and synthetic silicate starting compositions. The U and Th distribution between the resulting crystal and glass (quenched melt) run products were then used to determine the equilibrium crystal-melt partition coefficients. While the data were acquired from crystallization experiments, their main applicability is in partial melting. Actual partial melting experiments (e.g., Harrison 1981) were not performed because the successful execution and interpretation of such experiments is much more difficult than crystallization experiments. The phase equilibria is much more complicated (4-6 solid phases + melt as compared to 1 solid phase + melt in crystallization experiments), making it very difficult to assign crystal-melt partition coefficients to individual phases. In addition, complete trace and major element equilibration between a partial melt and coexisting solid phases is a very slow process, limited by solid-state diffusion. Finally, large (> 100 μm) crystals are needed to measure the very low actinide partition coefficients with particle track radiography, the technique used in this study.

Of the major mineral phases thought to comprise upper mantle, clinopyroxene, with its large, 8-fold, M2 site, is typically regarded as the primary host for large ion lithophile elements such as U and Th. Evidence for this assumption is discussed in chapter 3. Accordingly, most of my work was on clinopyroxene-melt partitioning experiments. While the trace element content of olivine is typically quite small, its large modal abundance enhances the significance of olivine in terms of bulk partition coefficients, so I have determined limits on olivine-melt partition coefficients. Garnet is an important residual phase in the petrogenesis of ocean island alkali basalts (e.g., Frey et al. 1991), and possibly some MORBs (Salters and Hart 1989; Johnson et al. 1990; Bender et al. 1984), so garnet-melt partition coefficients were determined.

The basalt compositions I studied are representative of two of the more common basalt types on Earth, a MORB and an alkali basalt, and between them span a moderate range in composition. In addition to the data being applicable to basalts with similar compositions, the data put some constraints on the compositional dependence of U-Th partitioning.

Some earlier measurements of the U and minor element distribution between Fe-Ti oxides, zircon, and glass in partially melted granodiorites from Crater Lake, Oregon are included as Appendix I (LaTourrette et al. 1991). This work was done in collaboration with Charles Bacon of the U. S. Geological Survey in Menlo Park, California and it was initiated while he was a visiting professor at Caltech. The measurements were prompted by the frequent use of "magnetic mineral separates" to define internal isochrons in ^{238}U-^{230}Th disequilibrium dating studies (e.g., Condomines et al. 1982). These measurements are not discussed in the body of the thesis, and the important conclusions of that study were: Fe-Ti oxide crystallization cannot significantly fractionate U from Th in the residual melt (nor can retention of Fe-Ti oxides in the source during partial melting) under the shallow crustal conditions studied, and the ^{238}U-^{230}Th disequilibrium measured in magnetic mineral separates is probably due to contaminants such as apatite; due to their slow dissolution

rates and isolation in large plagioclase crystals, accessory phases such as zircon and apatite may be retained in the source region during crustal fusion well beyond the point that they should be consumed according to equilibrium considerations; the granodiorite blocks, interpreted to be fragments of the walls of the Crater Lake magma chamber (Bacon 1992), may have been partially molten for 800-8000 years. Partitioning measurements on natural samples are important for determining the extent of possible non-equilibrium partitioning in nature and the effects of conditions impossible to reproduce in the laboratory (e.g., very long time scales, equilibration in silica-rich systems, both of which apply to this study).

CHAPTER TWO

Experimental and Analytical Techniques

2.1 Overall Experimental Plan

2.1.1 Bulk Compositions

I used five bulk starting compositions in this study (Table 2.1): two modified natural basalts and one synthetic composition for the clinopyroxene experiments, the unmodified form of one of the basalts for the olivine experiments, and a second synthetic composition for the garnet experiments.

Of the three clinopyroxene-bearing compositions, the first is an aphyric basalt from the extreme southern end of the Juan de Fuca ridge (TT152-37). This sample was recovered from a dredge haul on cruise 152 of the R/V *T. Thompson* (University of Washington) and was provided by D. Stakes. It is an Fe- and Ti-rich MORB and is briefly described in Eaby et al. (1984) and Liias (1986). The second composition is an alkali basalt from Takashima, Japan (Kuno 1965) provided by H. Nagasawa. I chose this sample for compositional variation and because Nagasawa and Wakita (1968) measured U and Th partition coefficients between large augite crystals and groundmass in the original rock. The analytical work of Nagasawa and Wakita appeared to be carefully done, thus this sample offered an interesting opportunity to compare experimental and phenocryst-matrix partition coefficients. The third is a synthetic Diopside + Anorthite glass ($Di_{71}An_{29}$ by mole), which I included to a) serve as a chemically simple and stable composition (I expected some alkali- and Fe-loss from the basalts), b) increase the compositional variation among the samples and c) to compare to the results for $Di_{50}An_{25}Ab_{25}$ of Benjamin et al. (1980). The major compositional differences among the three are the FeO and alkali contents.

Because clinopyroxene experiments were run at atmospheric pressure, I added 10 wt% $CaSiO_3$ to the two basalts in order to saturate them with clinopyroxene at 1 atm (the Takashima and Juan de Fuca basalts have olivine and plagioclase, respectively, as liquidus phases at 1 atm). For the Takashima basalt, I found that adding wollastonite was the quickest route to clinopyroxene saturation, and 10 wt% is the minimum amount necessary. For simplicity, I did the same thing with the Juan de Fuca basalt and was successful. Additional wollastonite raises the CaO content, but the SiO_2 content is virtually unchanged, as wollastonite has about the same amount of SiO_2 as the basalts. Olivine crystals were grown from the unmodified Takashima basalt

The synthetic garnet-bearing composition is andesitic ("Andesite" from Green and Ringwood 1968). I chose it because it has garnet as the sole solid phase on the liquidus. This insured that I would encounter no complications from actinide partitioning into multiple crystallizing phases. A potential drawback is that the data may not be directly applicable to mantle melting.

2.1.2 Run Conditions

I ran most experiments (clinopyroxene and olivine runs) at 1 atm total pressure in order to utilize the advantages of fO_2 control by gas mixing. Th is solely tetravalent, while U has multiple valence states and has been shown to be multivalent in systems of similar composition and fO_2 (Calas 1979; Schreiber 1983). It is therefore likely that U partitioning is sensitive to fO_2. To investigate this, I crystallized each composition at oxygen fugacities corresponding to 3 different oxygen buffers: Ni-NiO (NNO), Fa-Mt-Qz (FMQ) and 1 log unit more oxidizing than Fe-FeO (IW+1). In addition to affecting the valence state distribution of U, changing the fO_2 can alter the phase compositions and possibly the crystal and melt structures in Fe-bearing systems, and in doing so may have additional effects on trace element partitioning.

Because garnet is not stable at 1 atm, the garnet crystallization experiments were run at high pressure in a piston-cylinder press. The fO_2 in these experiments is fixed near Ni-NiO by the capsule assembly (Taylor and Green 1986) and was not varied in these runs.

I grew crystals by slowly cooling the sample from the liquidus. I used this method, as opposed to isothermal runs, for two reasons. First, I was not convinced that the crystals could equilibrate with the melt isothermally in any practical time period. When an experimental charge is brought directly to a sub-liquidus temperature the crystals grow extremely rapidly and are often radically out of chemical equilibrium with the melt because movement of components is limited by diffusion. Subsequent re-equilibration of crystal and melt is limited by diffusion in the crystal, which is extremely slow for trace elements (Seitz 1973a; Sneeringer et al. 1984), or by crystal dissolution and reprecipitation, which can only equilibrate the crystal rims. Second, I need large ($\approx$ 100 μm), inclusion free crystals for particle track analysis. Isothermally grown crystals are typically skeletal or acicular.

The cooling rate appears to have been slow enough to allow diffusive homogeneity of major and trace elements in the melt during crystal growth (see section *3.1.4*), but diffusion in the crystals is too slow to allow continual re-equilibration with the melt. Crystal growth by slow cooling should therefore approach fractional crystallization with equilibrium maintained at the crystal-melt interface. It is important to note that in this type of experiment the bulk crystal is not in equilibrium with the final melt composition, but with the assumption that local equilibrium was maintained at the crystal-melt interface during growth, crystal liquid partition coefficients can be calculated with a fractional crystallization (zoning) correction.

2.1.3 Trace Element Spikes

2.1.3.1 Clinopyroxene and Olivine Experiments

^{235}U and ^{230}Th were added to the starting compositions for particle track analysis. In addition, I added higher concentrations of ^{238}U and ^{232}Th for ion probe analysis. In an effort to study potential sources of Ra-Th fractionation, I also added Ba as a chemical homolog of Ra in some of the mixtures. Lastly, I added Sm to the starting compositions. The partitioning behavior of Sm in clinopyroxene is well documented and Sm is compatible enough to be measured with an electron microprobe, allowing me to monitor trace element distribution with higher spatial resolution than is possible with particle tracks.

2.1.3.2 Garnet Experiments

Because of the low modal abundance of garnet observed in mantle xenoliths, garnet must significantly fractionate U and Th to significantly affect U/Th of a partial melt. For 8% modal garnet and 5% melting, a garnet-melt partition coefficient below about 0.05 will have little effect. Consequently, to simplify the analyses, I designed the garnet crystallization experiments with spike levels such that U or Th concentrations in garnet corresponding to $D^{gt/liq} \geq 0.05$ could be determined from electron microprobe analyses. This minimum partition coefficient value, coupled with an electron microprobe detection limit of $\approx$ 500 ppm, required ^{238}U and ^{232}Th spike levels of 1 wt%. In addition to U and Th, I added 3000 ppm Sm. As for clinopyroxene, $D^{gt/liq}_{Sm}$ was also determined with the electron microprobe in order to compare to previous experimental studies.

As it turned out, electron microprobe analyses of the garnet crystallization experiments indicated that U and Th concentrations in the garnets were below the limits for quantitative analysis, but it appeared that $D^{gt/liq}_{U} > D^{gt/liq}_{Th}$. The magnitudes of the partition coefficients are small, but because D_{Th}/D_{U} appeared to be the opposite sense of that found for clinopyroxene, I obtained secondary ion mass spectrometry (SIMS) analyses of these experiments.

2.2 Preparation of Starting Materials

2.2.1 Clinopyroxene and Olivine Experiments

Preparation of the starting materials is presented in flow chart form in Fig 2.1. I sawed a single ≈ 100 g chunk of the Takashima basalt into ≈ 1 x 2 x 5 cm pieces with a diamond saw, ground the saw marks off with SiC, and boiled the pieces in distilled water. I then broke these pieces into cm^3-sized pieces in plastic bags with a steel hammer, crushed them to fine gravel size in a mini jaw crusher and ground them to powder in a tungsten-carbide shatter box. The Juan de Fuca ridge basalt was received in sub-cm^3-sized pieces, 100 g of which I washed in distilled water and ground in a tungsten-carbide shatter box.

To make the wollastonite component, I mixed SiO_2 and $CaCO_3$ (Johnson-Matthey Puratronic) together and decarbonated it in an alumina crucible by slowly heating to 900°C in air and holding for 10 hours, and then grinding the mixture in an alumina mortar and pestle for 20 minutes. In this and all following steps, I did all grinding under ethanol, and all decarbonations and fusions in the Deltech furnace in 214 N. Mudd.

For each basalt composition I made a 5 g mixture of basalt + 10 wt% wollastonite (4.5 g basalt + 0.5 g wo) and ground it in an automatic agate mortar and pestle for 4 - 5 hours. I then fused this mixture at 1300°C at FMQ for 2 hours in an open, Fe-presaturated Pt crucible (see Appendix 2.1). An aliquot of wo-free Takashima basalt was also fused for the olivine crystallization experiments. I found that the easiest way to extract the glass from the crucible that also minimized crucible wear and tear was to gently squeeze the crucible in a teflon-jawed vice until the glass cracked. I then placed a short teflon cylinder with a diameter smaller than the crucible vertically in a large tray, and holding the crucible upside-down, banged the glass onto the cylinder. After removal from the crucible I re-ground the

Figure 2.1 Flow chart describing the preparation of the starting materials. Natural basalts (Juan de Fuca and Takashima basalts) went through steps 1b - 12. $Di_{71}An_{29}$ composition went through steps 1s - 12, and G14 went through 1s - 3s, 7 - 9, and then was reground/mixed. Grind/mix steps were done in an automatic agate mortar and pestle under ethanol.

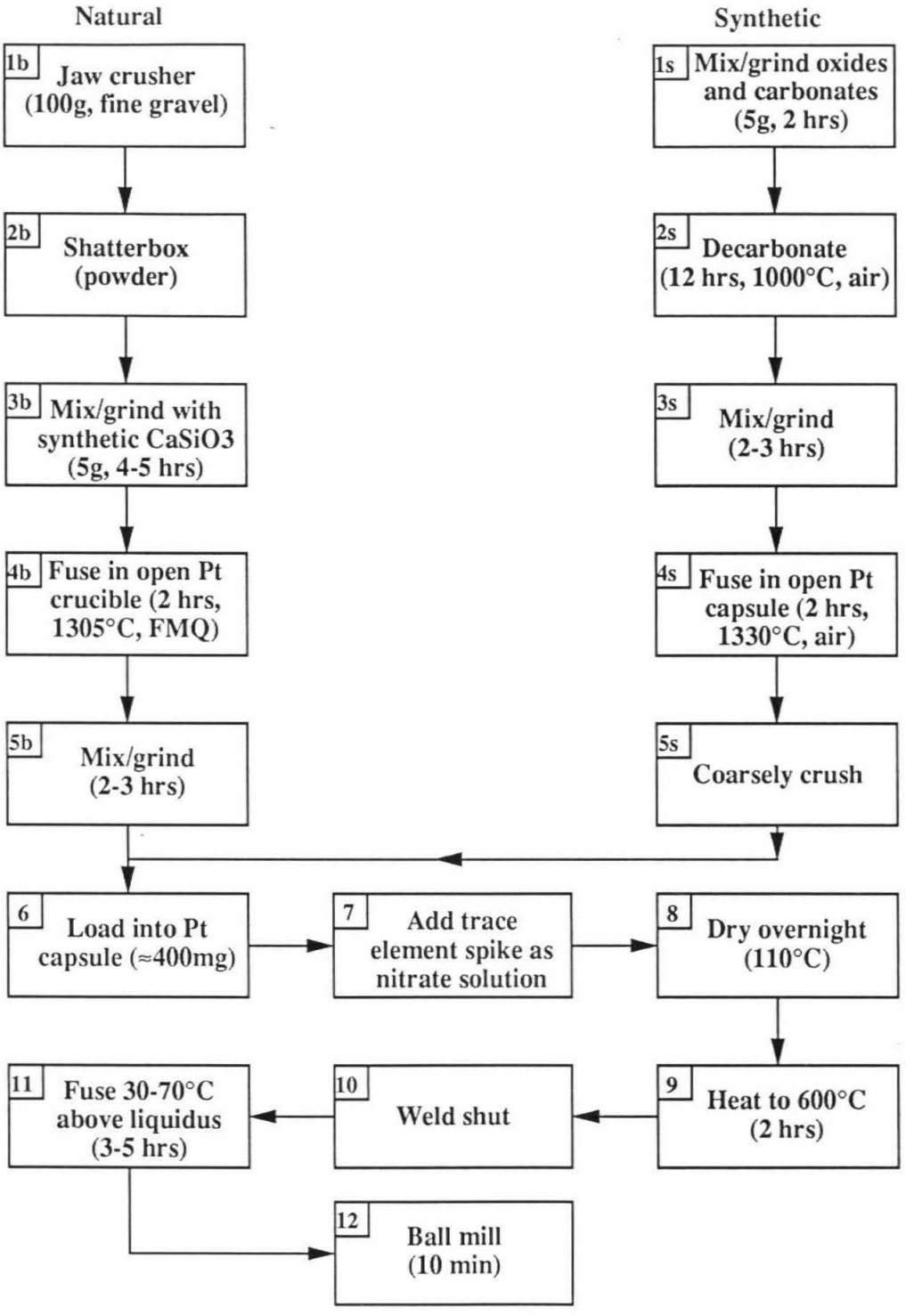
Natural
Synthetic
1b Jaw crusher (100g, fine gravel)
1s Mix/grind oxides and carbonates (5g, 2 hrs)
2b Shatterbox (powder)
2s Decarbonate (12 hrs, 1000°C, air)
3b Mix/grind with synthetic CaSiO3 (5g, 4-5 hrs)
3s Mix/grind (2-3 hrs)
4b Fuse in open Pt crucible (2 hrs, 1305°C, FMQ)
4s Fuse in open Pt capsule (2 hrs, 1330°C, air)
5b Mix/grind (2-3 hrs)
5s Coarsely crush
6 Load into Pt capsule (≈400mg)
7 Add trace element spike as nitrate solution
8 Dry overnight (110°C)
9 Heat to 600°C (2 hrs)
10 Weld shut
11 Fuse 30-70°C above liquidus (3-5 hrs)
12 Ball mill (10 min)

Figure 2.1

glass in agate for 2 - 3 hours and dried at 110°C overnight. These glasses are labelled "T" (Takashima + wollastonite), "J" (Juan de Fuca + wollastonite), and "TO" (Takashima).

I prepared 4.2 g of the Diopside-Anorthite ($Di_{71}An_{29}$ by mole) composition by mixing Johnson-Matthey Puratronic SiO_2, MgO, Al_2O_3, and $CaCO_3$ together in an agate mortar and pestle for 1.5 hours, decarbonating in air in an alumina crucible overnight at 980°C, and then re-grinding in agate for 3 hours. I then fused 1 g of this mixture in air in an open 0.25" i.d. Pt tube at 1330°C for 2 hours and then coarsely crushed the resulting glass in agate. This glass is labelled D2.

Trace element spikes were added as acid solutions to the starting glass powders. I used Johnson-Matthey Specpure ICP/DCP standard solutions for ^{232}Th, Ba, and Sm (10,000 μg/ml as nitrates in 5% HNO_3 solution), and made a similar 10,000 μg/ml ^{238}U solution by dissolving UO_2 in 5% HNO_3. I used pre-existing ^{235}U (376 μg/ml in HCl) and ^{230}Th (74.3 μg/ml in HNO_3) solutions for the radioisotope spikes. Procedures that involved radioactive materials were performed in a lexan glove box whenever possible, and I wore a respirator whenever material was removed from the box.

I weighed out approximately 400 mg of starting glass and then quantitatively pipetted the spike solutions into a single teflon beaker in the amounts to result in concentrations of 3000 ppm each of Ba and Sm + 1000 ppm each of U and Th + 50 ppm each of ^{235}U and ^{230}Th. I then dried this down to about 100 μl and pipetted in one or two drops into a capsule made from 0.25" i.d. Pt tubing. Note that this procedure insures U and Th isotopic equilibration and guarantees constant relative amounts of trace elements within a single starting composition. All Pt tubing was annealed at ≈ 1000°C and boiled in 6N HCl prior to welding and loading, and Pt tubing used for the basalts was Fe-presaturated (Appendix 2.1). In some cases I loaded the glass into the Pt capsule first, and added the spike solution directly onto the glass. In other cases spikes were added to empty Pt capsules and dried before the glass was loaded. Both techniques appear to result in complete homogenization after fusing and ball milling.

The Pt capsule containing the glass + spike was dried at 110°C overnight, then crimped and slowly heated under N_2 to 600°C (the trace element nitrates from the spikes all break down to oxides at or below 500°C) for 2 - 3 hours. I then removed the capsules from the furnace and quickly welded them shut. I fused the spiked glasses for 3 - 5 hours 70 – 100°C above their liquidi to homogenize and drop quenched them in water. After removal from the Pt capsule the glass was ball-milled in agate for ≈ 10 minutes. The spiked glasses are labelled according to their bulk composition and spike (Th + U + Ba + Sm = TUBAS): T-TUBAS, TO-TUBAS, J-TUBAS, D2-TUBAS. Bulk compositions were determined from microprobe analyses of 2 hour super-liquidus runs at FMQ (Table 2.1).

Experimental charges for TUBAS runs were made 2 to 4 at a time by mixing the spiked glass with polyvinyl alcohol and drying on Fe-unsaturated Pt wire loops (Fig. 2.2). I made all charges from the same initial batch of starting material. I used 0.004" Pt wire for the basalts to minimize Fe-loss during the runs, however Fe-loss was significant in some runs. Ir wire, which results in less Fe-loss, was not used because it is incompatible with neutron irradiations. For the $Di_{71}An_{29}$ runs I used 0.01" Pt wire.

2.2.2 Garnet Experiments

I prepared the garnet-bearing andesitic composition by mixing Johnson-Matthey Puratronic SiO_2, Al_2O_3, $CaCO_3$, MgO, Fe_2O_3, Na_2CO_3, K_2CO_3, and TiO_2 together in an agate mortar and pestle, decarbonating in air in an alumina crucible overnight at 1000°C, and then re-grinding in agate for 2 hours. This composition is labelled G14. I added 1 wt% ^{238}U and ^{232}Th and 3000 ppm Sm as nitrate solutions to ≈ 600 mg of G14 + ethanol in an Al_2O_3 mortar and pestle and then ground the mixture for one hour. After drying overnight at room temperature the mixture was heated to 500°C in air for 3 hours to decompose the nitrates. The spiked composition is labelled G14-SMUT (Sm + U + Th =

TABLE 2.1

Starting compositions[a]

Name Label Liquidus phase	Takashima[b] T-TUBAS cpx	Juan de Fuca[b] J-TUBAS cpx	$Di_{71}An_{29}$ D2-TUBAS cpx	Andesite G14-SMUT garnet	Takashima[c] TO-TUBAS olivine
SiO_2 (wt%)	49.9±.8[d]	51.2±.2	50.2±.7	60.7±.5	49.6±.4
TiO_2	1.64±.03	1.71±.01		1.05±.03	1.78±.12
Al_2O_3	14.09±.09	12.43±.04	12.25±.01	16.8±.2	16.1±.4
FeO*[e]	8.3±.2	10.49±.16		5.82±.09	9.7±.9
MnO	.151±.003	.197±.004			nd[f]
MgO	7.21±.11	6.19±.06	11.83±.04	2.39±.01	8.3±.4
CaO	12.58±.18	14.68±.06	24.2±.06	4.95±.08	8.5±.3
Na_2O	2.41±.05	1.88±.03		3.16±.08	4.3±.4
K_2O	1.41±.05	.087±.011		2.00±.04	1.86±.16
U (ppm)	1020±320	730±90	1000±150	7900±510	(1000)[g]
Th	790±250	700±100	780±180	8200±410	(1000)
Sm	3260±190	2910±200	2930±140	3260±360	(3000)
Ba	3230±30	2850±100	2610±130		(3000)
Total	98.6	99.7	99.3	99.0	100.1

(a) Analyses of super-liquidus quench glasses (average of 3-4 points in a single sample)
(b) With 10 wt% wollastonite added
(c) No wollastonite added, EDS analysis
(d) One counting statistics standard deviation
(e) FeO* = total Fe as FeO
(f) nd = not determined
(g) Values in parnethesis are nominal pipetted-in concentrations and were not determined

Figure 2.2 (a) 1 atm furnace head assembly showing sample holder, thermocouple, and oxygen sensor. A: Pt-$Pt_{90}Rh_{10}$ thermocouple, supported by bored Al_2O_3 rod. B: Al_2O_3 sample holder rod with Pt sample hanging wires. C: fO_2 sensor assembly: 0.01" Pt wires connect to reference and sample sides of doped zirconia electrolyte, D, welded to the end of an Al_2O_3 support tube. $fO_2 = 1$ on reference side by means of a continuous flow of O_2 through inlet E in inner, bored Al_2O_3 rod. fO_2 on sample side is maintained by continuous flow of $CO + CO_2$ through inlet F. G: O-ring gas seals. H: Brass furnace head. I: Al_2O_3 muffle tube. (b) Sample assembly. Powdered glass sample, A, bound with polyvinyl alcohol on thin (0.004" - 0.01") Pt wire loop, B, hangs from 4-bore Al_2O_3 disk, C. Sample is drop quenched by applying 15v across heavy gauge (0.02") Pt hanging wires, D, fusing thin (0.004") Pt suspension wire, E.

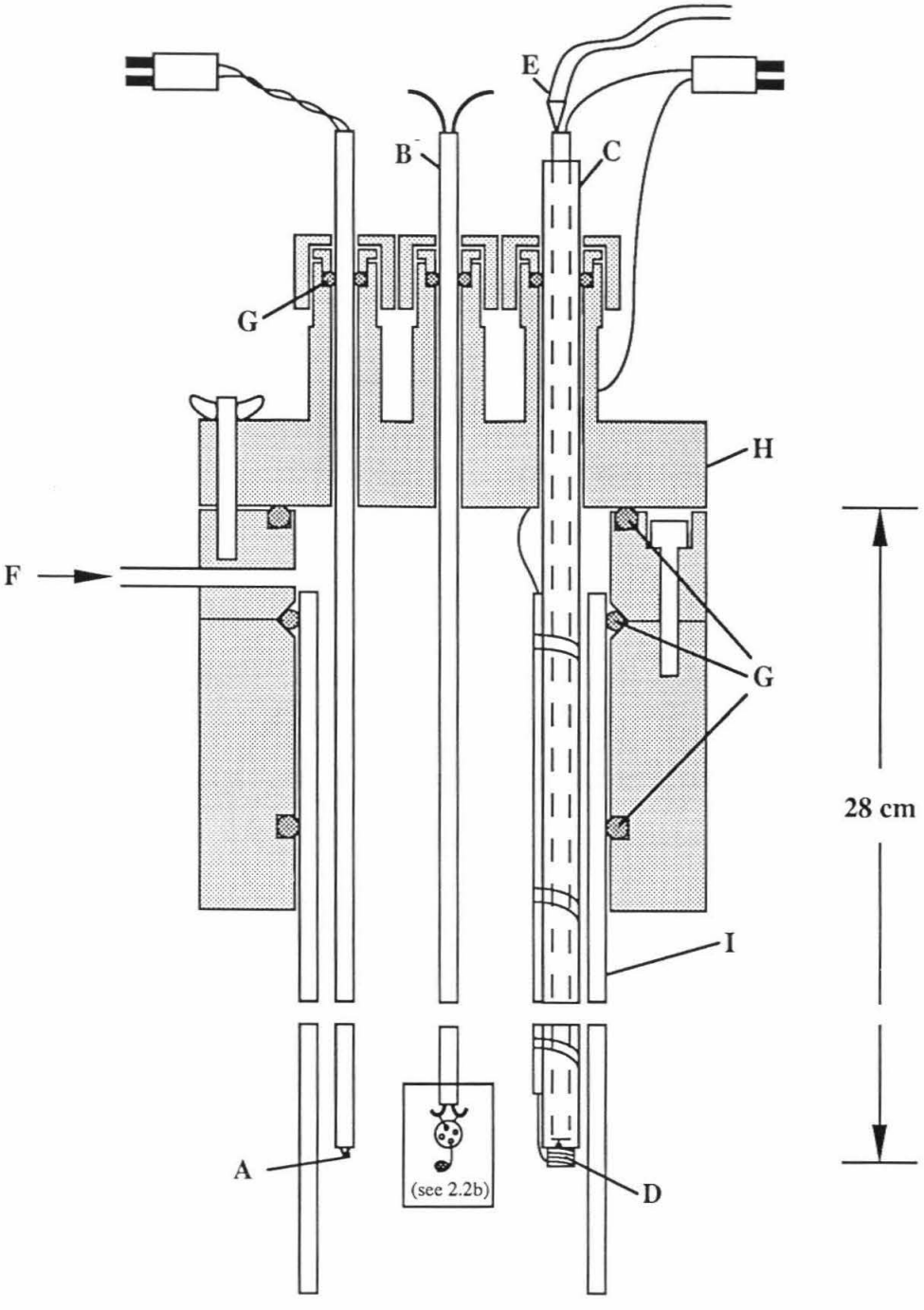

Figure 2.2a

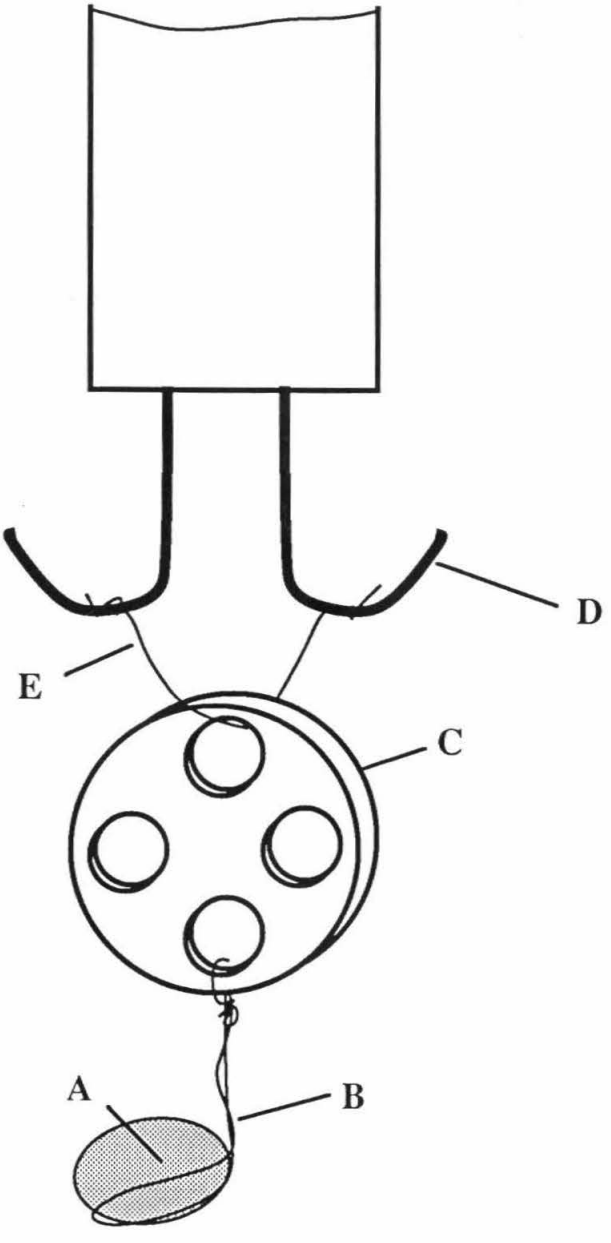

Figure 2.2b

SMUT). The bulk composition was determined from electron microprobe analyses of a super-liquidus run (Table 2.1).

2.3 Crystallization Runs

2.3.1 Clinopyroxene and Olivine Experiments

I ran experiments at 1 atm pressure in a vertical quench furnace (Deltech; Fig. 2.2). The fO_2 in the TUBAS runs was controlled with CO-CO_2 gas mixtures and monitored with a yttria-doped zirconia electrolyte calibrated to the Fe-FeO transition (Huebner 1987). The precision and accuracy of the fO_2 are believed to be ±0.07 and ±0.12 log units, respectively. Temperature was measured with a Pt-$Pt_{90}Rh_{10}$ thermocouple calibrated to the melting points of gold and palladium. The precision and accuracy of the temperature are believed to be ±2 and ±5°C, respectively. I calibrated the thermocouple and O_2 sensors about every four runs.

I grew crystals by slowly cooling the sample according to the following recipe: melt at 6 - 16°C above the liquidus (T_i) for 1 - 2 hours (t_i), drop to 0 - 2°C below the liquidus (T_l) and hold for 24 hours (t_l), slowly cool, typically at 1.7°C/hr, to 20 - 35°C below the liquidus (T_f), and hold for 1 - 24 hours at this temperature (t_f). A schematic time-temperature diagram is shown in Fig. 2.3. The general shape of this cooling path is derived from past lore in this laboratory, as well as my own investigations. For this technique to work well the liquidus temperature must be known precisely. Consequently, I made several preliminary runs with the unspiked and spiked glasses to determine the liquidus and plagioclase-in temperatures (Appendix 2.2). In theory, the initial period at T_i melts most of the charge, leaving only a few nuclei. The period at T_l is needed to allow a few small seed crystals to nucleate and to allow the U valence state distribution to equilibrate with the fO_2 (Schreiber 1980).

Runs were initiated by putting the complete furnace head assembly, which includes the sample, thermocouple, and O_2 sensor (Fig. 2.2), directly into the hot spot of the

Figure 2.3 Schematic time-temperature path of 1 atm crystallization experiments. Initial, liquidus, and final times and temperatures are indicated.

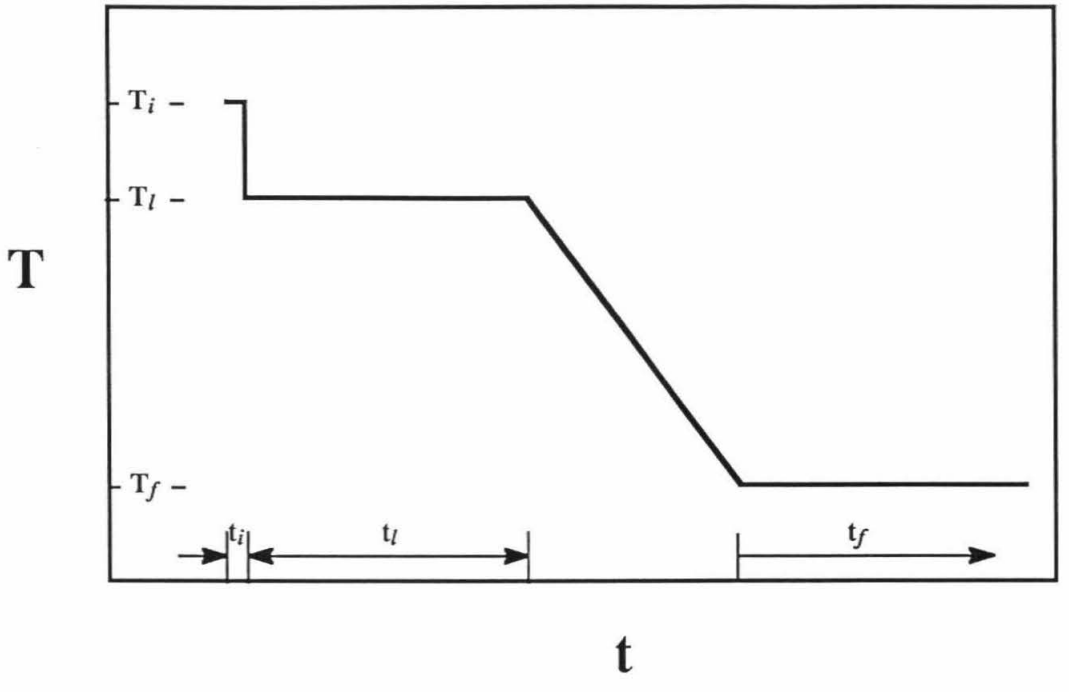

Figure 2.3

furnace, previously stabilized at T_i, under N_2 flow. I then sealed the furnace shut, shut off the N_2, and admitted a preset mixture of CO-CO_2 gas flow to the furnace before the sample reached 800°C. The sample reached T_i after about 10 minutes. I ended all 1 atm runs by drop quenching the charge in distilled water. Time-temperature histories are listed in Table 2.2. This technique successfully generated a few (1 - 5) large euhedral crystals and occasional smaller crystals in each experiment. Individual runs are given an alphabetical index (e.g., J-TUBAS-**E**) and individual crystals are given a numerical index (e.g., J-TUBAS-E**2**).

2.3.2 Garnet Experiments

Garnet crystallization were run in a piston-cylinder press and temperature was monitored with a $W_{95}Re_5$-$W_{74}Re_{26}$ thermocouple. I used the piston-in method and applied a 3.7% (1 Kbar) pressure correction. I ran all experiments at 27 Kbar and made no correction for the effect of pressure on the thermocouple emf. A schematic diagram of a run assembly is shown in Fig 2.4. The sample is loaded into a graphite capsule, which is then sealed in platinum. Under conditions of fluid saturation, the fO_2 of this capsule assembly will be buffered by the C-CO-CO_2 oxygen buffer. Under fluid-absent conditions (the likely case in these experiments), however, this capsule assembly can reduce the oxidation state of the charge, but not oxidize it. In this case the C-CO-CO_2 oxygen buffer will be an upper limit for the fO_2 of the experiment. Determining the exact fO_2 requires knowledge of the Fe valence state distribution and CO_2 concentration in the melt (Holloway et al. 1992). I do not have this information, and thus can only be sure that the the fO_2 of these experiments was below C-CO-CO_2 buffer. I added Fe as Fe_2O_3 and performed decarbonations and denitrations in air, however, so the initial starting material was very oxidized. The fO_2 of these experiments may thus be near the C-CO-CO_2 buffer. The fO_2 of the C-CO-CO_2 buffer is pressure and temperature dependent and for these conditions $\log fO_2 = -6.66$ (Taylor and Green 1986), which is just below the NNO oxygen buffer.

Figure 2.4 Schematic cross section of piston-cylinder sample assembly used for garnet crystallization experiments. Assembly is cylindrical.

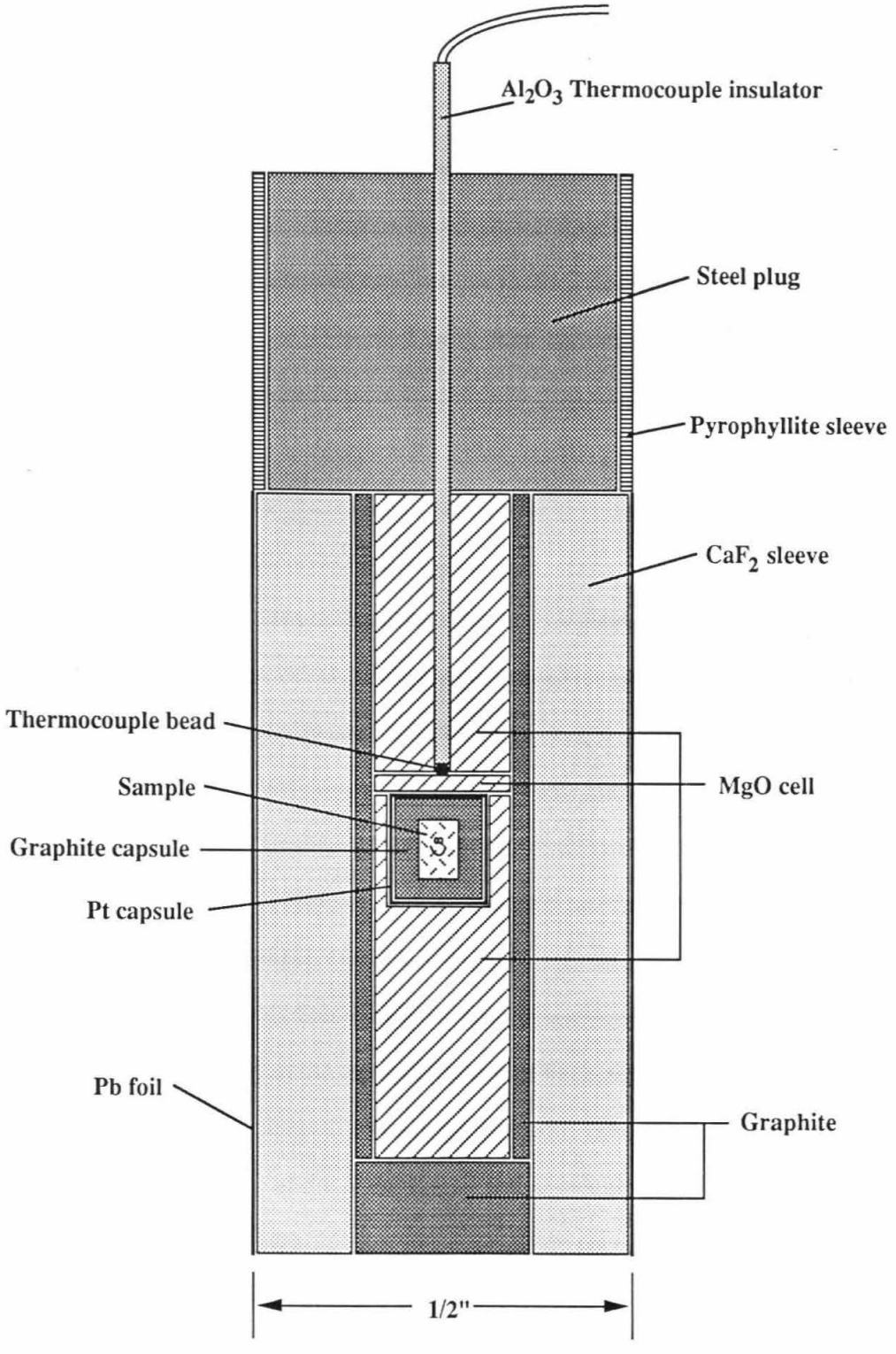
Al_2O_3 Thermocouple insulator
Steel plug
Pyrophyllite sleeve
CaF_2 sleeve
Thermocouple bead
Sample
Graphite capsule
Pt capsule
MgO cell
Pb foil
Graphite
1/2"

Figure 2.4

Thus, the fO_2 of the garnet experiments is at least as low as the most oxidizing 1 bar clinopyroxene runs.

Crystals were grown by slow cooling from the liquidus. After pressurizing, the sample was brought to the run temperature in about 5 minutes, held for a half hour, and cooled 42 - 48°C at 4 - 6°C/hr. Samples were quenched by shutting off the power to the furnace. Time-temperature histories are listed in Table 2.2. Individual runs are given an numerical index (e.g., G14-SMUT-**6**) and individual crystals are given a numerical index preceded by an x (e.g., G14-SMUT-6x**1**)

2.4 Analytical Techniques

2.4.1 Fission Track Measurements

U microdistributions were determined from a ^{235}U fission particle track map in a muscovite detector (Benjamin et al. 1980; Burnett and Woolum 1983). I potted the samples, either whole or partially crushed, in Epoxylite epoxy (R-86 resin + C-304 hardener) and ground them until one or more suitable (> 100 μm) crystals were exposed. After polishing to 0.25 μm, freshly cleaved muscovite detectors (Hughes Liberty) were then tightly clamped onto the samples, and the assemblies irradiated with thermal neutrons for 25 minutes for a total fluence of 1.8×10^{15} n/cm^2. I also included a U standard glass (National Bureau of Standards Standard Reference Material 961; contains 461 ppm depleted U, 1.10 ppm ^{235}U) in the top and bottom of each sample tube. Although not strictly necessary for partition coefficient measurements, I included these standards to monitor the vertical gradient of the neutron flux and to calculate absolute U concentrations. The details of the physical assembly are similar to those used by Benjamin (1980). Irradiations were performed in the lazy susan of the TRIGA reactor at U. C. Irvine, Irvine, CA. Four irradiations were done throughout the course of the study; the irradiation number for each sample is listed in Table 3.2.

TABLE 2.2

Experimental Run Conditions

Experiment	P	fO_2	T_i (°C)	t_i (hr)	T_l	t_l	Ramp (°C/hr)	T_f	t_f
D2-TUBAS-G	1 bar	NNO	1312	1.5	1306	24	1.7	1273	17.5
D2-TUBAS-E	1 bar	FMQ	1312	1.5	1306	12	1.7	1274	3
D2-TUBAS-F	1 bar	FMQ	1312	1.5	1306	24	1.7	1273	27
D2-TUBAS-N	1 bar	FMQ	1313	1.5	1306	24	0.1	1279	1.7
D2-TUBAS-H	1 bar	IW+1	1312	2.2	1306	24	1.7	1273	26
D2-TUBAS-L	1 bar	IW+1	1313	1.5	1307	24	1.7	1275	24
J-TUBAS-G	1 bar	NNO	1209	1.5	1200	27	1.7	1179	27
J-TUBAS-E	1 bar	FMQ	1210	1.5	1200	24	1.7	1178	12.5
J-TUBAS-F	1 bar	FMQ	1210	1.5	1200	24	1.7	1179	17
J-TUBAS-H	1 bar	IW+1	1210	1.5	1200	24.5	1.7	1182	14
J-TUBAS-L	1 bar	IW+1	1214	1.5	1201	24	1.7	1185	21.5
T-TUBAS-C	1 bar	NNO	1210	1.5	1192	24	1.7	1159	4
T-TUBAS-I	1 bar	NNO	1210	1.5	1195	24	1.7	1163	0
T-TUBAS-B	1 bar	FMQ	1210	1.5	1195	24	1.7	1159	1
T-TUBAS-D	1 bar	IW+1	1209	1.5	1193	24	1.7	1163	3.4
T-TUBAS-H	1 bar	IW+1	1214	2	1194	24	1.7	1164	24
TO-TUBAS-D	1 bar	FMQ	1236	1.8	1227	24	1.7	1186	25.5
G14-SMUT-6	27Kb	FMQ+0.3			1355	0.5	6	1313	2.5
G14-SMUT-8	27Kb	FMQ+0.3			1355	0.5	4.2	1307	0

I etched the detectors in 50% HF in two steps. After an initial 3 minute etch, I gold coated the mica and measured the high track density in the glass ($\approx 10^8$ trx/cm^2) at 17-18K power magnification with a scanning electron microscope (Camscan; backscattered electron image; resolution = 5; working distance = 31 mm). The magnification is checked twice yearly with a calibrated grid. Etching for longer times at these densities causes the tracks to overlap, complicating counting. I then removed the gold coat (Appendix 2.3) and re-etched the detectors for 3 minutes and counted the track densities in the crystals at 1000 power magnification with an optical microscope. The additional etching minimized losses of tracks at the lower magnification. Tests indicate that SEM counts are 10% higher than optical (Appendix 2.4), and I therefore included a 10% increase in all my crystal densities to compare with SEM data on the glass. I determined the track density in the glass by counting $\approx$ 400 tracks from photographs at each of three or four points in the sample. Each "point" was composed of 8 adjacent photographs of 30 μm^2 fields of view, an area equivalent to an 18 μm diameter circle, and each photograph typically contained 40 - 60 clearly resolved and easily countable tracks (Fig 2.5). I measured the track densities in the crystals by counting tracks under transmitted light with a calibrated reticle grid. A single fission fragment has a 10 μm average range in these samples, so the outer 20 μm of the crystals adjacent to the glass were not counted to avoid any tracks contributed by the glass.

2.4.2 Alpha Track Measurements

Th was measured in a manner analogous to U. A map of ^{230}Th alpha particle tracks was made by exposing the sample to a cellulose nitrate (Kodak-Pathé CN 85) detector (Benjamin et al. 1980). However, because the plastic detectors have a much wider range in track widths and lengths than the micas, large errors can result in comparing counts in plastics with highly differing track densities (Benjamin et al. 1980). Thus, I made two exposures for each sample: one for the glass (1 - 2 days) and one for the crystals (30 days). The exposure times were such that the densities for the glass and crystals were

Figure 2.5 Scanning electron micrographs of ^{235}U fission track map in muscovite mica detector after irradiating with 1.8×10^{15} n/cm^2 and etching in 50% HF for 3 minutes. (a) Secondary electron micrograph of entire sample. Bright area results from high fission track density in region corresponding to glass, which has high ^{235}U concentration. Areas corresponding to crystal and Pt wire have much lower ^{235}U concentration, and thus lower fission track densities, and appear dark. (b) Close-up of crystal from (a). (c) Typical high power backscattered electron micrograph of glass region used for fission track counting. Note distinctive diamond shape.

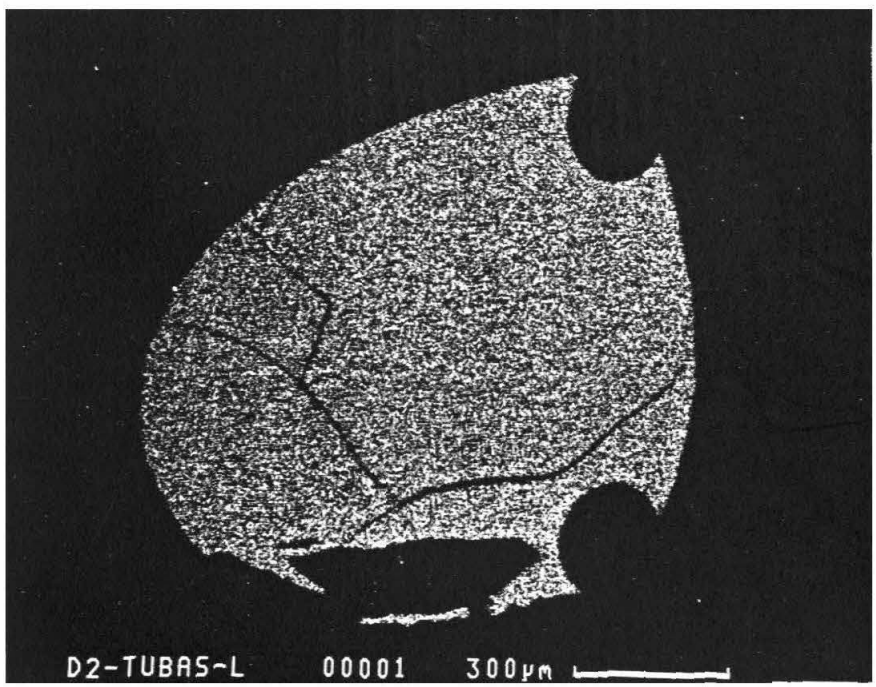
D2-TUBAS-L 00001 300µm

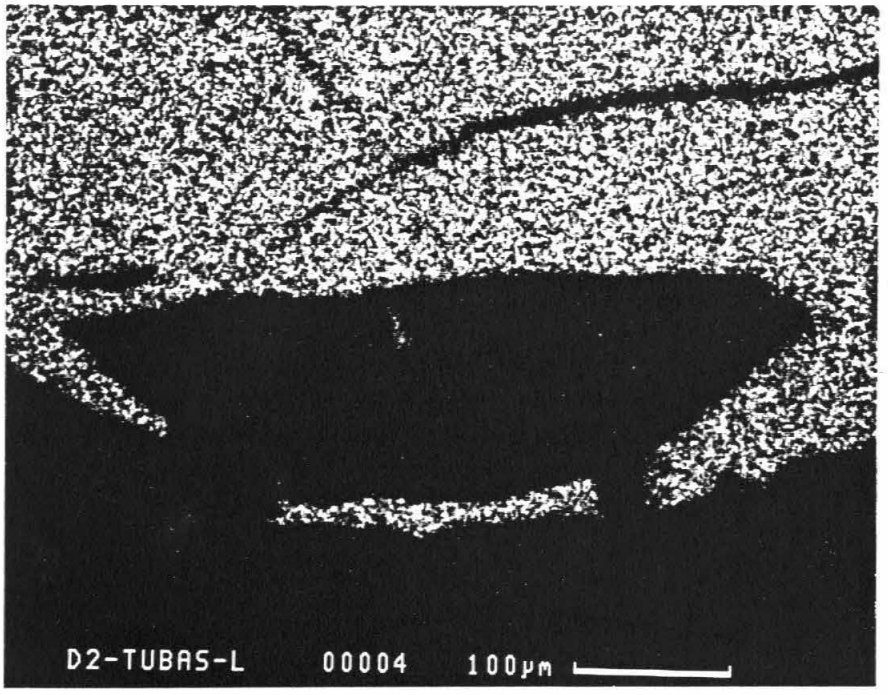
D2-TUBAS-L
00004
100µm

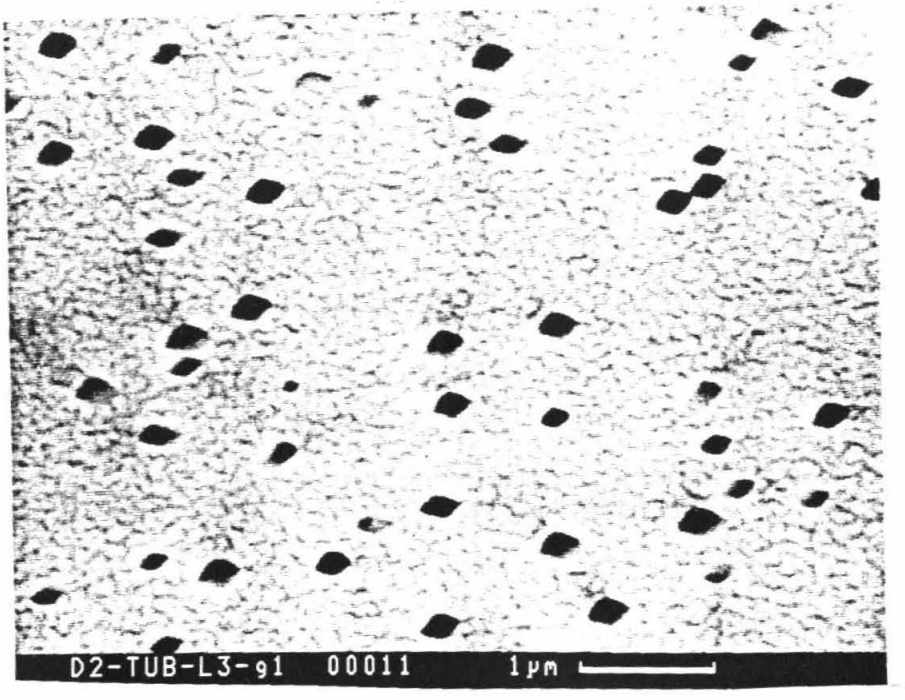
D2-TUB-L3-91 00011 1μm

similar. To avoid any etching variations, I etched both detectors simultaneously. This way, all alpha tracks were counted at about the same density, so any errors in the glass and crystal counts tended to cancel in the ratio of the crystal and glass track densities. A check showed no evidence for track fading during the month long exposure (Appendix 2.5). Detectors were etched in 6 N NaOH for 50 - 60 minutes at 40°C (Benjamin et al. 1980) and all tracks were counted at 1000 power magnification with an optical microscope using transmitted light. As with the fission tracks, the outer 20 μm of the crystal was not counted, as ^{230}Th alpha particles have fixed 15 μm range in these samples.

For both U and Th, I did all the counting under nearly the same conditions. Counts on a selected sample were closely reproduced by another person (DSB), indicating little counter bias occurs. Occasional checks of older samples suggested a small drift in optical counting efficiency with time. This will affect only the U partition coefficients, as they are determined from an optical count and an SEM count. The Th partition coefficients are insensitive to drift because they are determined from optical counts made within a week of each other (Appendix 2.6). These reproducibility errors are usually significantly less than the counting statistics errors for the crystal densities (6 - 27%, averaging about 11%), and, while they are included, do not contribute significantly to the reported partition coefficient errors.

2.4.3 Microprobe Measurements

Crystals and glasses from the experiments were analyzed with the JEOL 733 electron microprobe at Caltech and raw data were reduced with the CITZAF correction procedure (Armstrong 1988). Analyses of clinopyroxene and olivine experiments were made at 50 nA with a 10 μm diameter beam. Na was always measured first, but some alkali -loss from the glass probably occurred during analysis, as evidenced by the low totals for the glasses relative to the crystals and the lower totals for the more alkali-rich Takashima basalt. Glass compositions were measured at 3 or 4 points in the sample, and crystals were

measured at a point approximately half-way between the center and the edge. Standard minerals were used as standards for the major elements. UO_2 and ThO_2 were used for the U and Th standards, benitoite for Ba, and the Drake and Weill glass REE2 was used for Sm (Drake and Weill 1972).

For the garnet experiments, the beam current and diameter were 35 nA and 10 μm for the glass and 100 nA and 1 μm for the crystals. Special care was taken in setting the background position for the U measurements: since the background rises abruptly on the low wavelength side of the U peak, the background was measured only on the high wavelength side. Because of the curvature of the background, this technique has the potential to record U when there is none, but checks on garnets from unspiked experiments show no U when measured with this arrangement. As previously mentioned, U and Th concentrations in the garnet crystals are too low to obtain reliable analyses, but the presence of U was suggested by a convex upward zoning profile across a crystal. Th was completely below background levels.

2.4.4 Secondary Ion Mass Spectrometry Measurements

Garnet crystallization experiments were analyzed for U, Th, and Sm with PANURGE, a modified Cameca ims-3f secondary ion mass spectrometer (SIMS or ion probe) at Caltech. Analyses were conducted by Allen Kennedy. A primary beam of O^- ions was accelerated from the source at 12.5 KeV, and the primary beam current was 1 nA, giving a beam spot size of approximately 10 μm. This beam bombarded the sample, sputtering off secondary ions. The positively-charged secondary ions were then accelerated at 4.5 KeV into a mass spectrometer. Secondary ion intensities were measured with an electron multiplier, and all count rates were normalized to ^{30}Si. Undesirable molecular ion interferences were eliminated by energy filtering (Zinner and Crozaz 1986). An offset voltage applied to the the secondary ion beam suppresses molecular ions due to their lower average kinetic energy relative to atomic ions. An offset voltage of -45 V was

used in this study. Ion intensities were not systematically measured as a function of offset voltage, but for the heavy elements measured, molecular interferences are expected to be small. No correction was made for dead time.

^{26}Mg, ^{30}Si, ^{149}Sm, ^{232}ThO (mass = 248), and ^{238}UO (mass = 254), intensities were measured and normalized to the intensity of ^{30}Si. The magnetic field is adjusted to change masses, and each analysis cycle consisted a scan of masses 25.9, 26.0, 30.0, 148.9, 149.0, 247.9, 248, 253.9, and 254.0. The time required for the magnetic field to stabilize after each step increases with the size of the step, so the magnetic field was briefly set one-tenth of a mass unit below each mass of interest in order to minimize magnetic field instabilities. At each whole number mass the magnetic field was stepped from the low energy side of the peak, to the centroid, and high energy side of the peak. The centroid counting times for masses 149.0, 248.0, and 254.0 were 10 seconds, and all other centroids and peak side counting times were 1 second. The peak positions for 149.0, 248.0, and 254.0 were determined on glass spots with no offset voltage at the beginning of an analysis session, and these positions were used throughout the course of the session. A complete analysis consisted of 5 blocks of 6 cycles, and took about 35 minutes to complete. Because of the relatively high spike levels, ion count rates were quite high (lowest value was > 2500 counts for Th in garnet). The resulting counting statistics errors are less than the standard deviation of the ^{30}Si normalized intensities of the 30 cycles, so I used the latter as a measure of the analytical error. Variation in ion intensity from cycle to cycle results from variable transmission rates, which in turn result from sample charging. After the primary beam has initially burned through the gold coat and allowed to stabilize on the sample, this variation is not systematic.

A proper standard for U and Th in garnet was not available, so partition coefficients were calculated directly from the ^{30}Si normalized ion intensities, after correcting for the difference in Si concentration between garnet and glass.

Appendix 2.1: Fe-Presaturation of Pt Containers

Fe alloys with Pt, especially at low fO_2. In order to minimize loss of Fe from my samples to the Pt containers, I presaturated the Pt crucible and Pt tubing used to melt the basalts with Fe. The method I chose was to fill the container with the appropriate basalt powder and melt it, letting the Fe soak into the Pt. In principal the Pt becomes saturated with Fe for the specific composition, temperature, and fO_2 of the actual sample fusion. I then discard the glass used to saturate the container and load the sample that will be used for the experiments.

In the case of the 10 ml Pt crucible used for the initial fusions I repeated the saturation step a second time with fresh glass before fusing the sample. Each saturation was for 2 hours at 1300°C at FMQ and following the second time I removed the glass mechanically and washed the crucible in 50% HF. I saturated the Pt tubing used to glass the spiked basalts by welding one end, packing it with basalt and melting it at 1300°C at FMQ overnight. I removed the basalt mechanically and by soaking the capsule in 50% HF. The Fe-Pt alloy is quite brittle and care must be taken not to crack or tear it during handling. It is also much more difficult to weld than pure Pt.

It is unclear how well this technique works, but it is not that crucial for this study because the Fe-presaturation was done only to prevent progressive Fe-loss during the repeated glassings required to prepare the starting materials. To hold the sample during crystallization I used Pt wire loops that were not Fe-saturated but were made from very thin wire (0.004") in order to minimize Fe-loss. In retrospect, I probably should have presaturated these with Fe as well, as there was 10 - 15% Fe-loss in most runs and more in some reducing runs (Table 3.1).

Appendix 2.2: Preliminary Runs Used to Determine Phase Equilibria and Crystal Growth Recipes[a]

Run[b]	Temp (°C)	time (hrs)	phases present[c]
TB-9	1194	2.5	L + ol
TB-11	1207	19	L + ol
TB-12	1230	12	L + ol
TB-13	1258	4.8	L
TB-14	1245	3.3	L
TB-16	1248	8.5	
	1248→1179	5.6°C/hr	
	1179	3.5	L + ol
TB-17	1247	1.5	
	1241	23	
	1241→1160	2.8°C/hr	L + ol
TB-22	1247	2	
	1245	8	
	1245→1122	2.8°C/hr	
	1122	19.6	L + ol + plag
TB-24	1238	14.2	L
TB-25	1240	2	
	1230	20	
	1230→1175	1.7°C/hr	
	1175	2	L + ol
TO-TUBAS-A	1235	24	L
TO-TUBAS-B	1231	4	L
TO-TUBAS-C	1223	5	L + ol
TB10di-1	1220	6.5	L + ol
TB20di-1	1220	5.3	L + ol
TB20di-2	1242	3	
	1220	15	L + ol
TB16wo-1	1240	1.3	
	1190	3	L + cpx
TB16wo-2	1240	2	
	1166	9.5	L + cpx
TB5wo-1	1240	1	
	1190	2.5	L
TB5wo-2	1200	1.5	
	1125	3.6	L + ol
TB5wo-3	1200	5	
	1128	7	L + ol
TB10wo-4	1200	2	
	1096	4	L + cpx + ol
TB10wo-5	1200	1.5	
	1117	2.7	L + cpx + ol?
TB10wo-6	1200	1.5	
	1125	3.6	L + cpx + ol?
TB10wo-7	1200	5	
	1128	7	L + cpx
TB10wo-9	1200	3	
	1160	6.5	L + cpx
TB10wo-10	1200	12	L + cpx (tr)
TB10wo-11	1241	16.5	L
TB10wo-12	1222	3	L

TB10wo-13	1212	3	L
TB10wo-14	1205	11	L + cpx
TB10wo-15	1206	12	
	1206→1170	1.7°C/hr	
	1170	3	L + cpx
TB10wo-16	1242	2.5	
	1201	10	
	1160	58	L + cpx
TB10wo-17	1204	21	L + cpx (tr)
TB10wo-18	1199	10	L + cpx
TB10wo-19	1201	12	
	1201→1169	1.7°C/hr	
	1169	1	L + cpx
TB10wo-20'	1210	1	
	1199	24	
	1199→1165	1.7°C/hr	L + cpx
TB10wo-22	1194	20	L + cpx
TT-1	1249	1	
	1219	2.3	L
TT-2	1258	1	
	1180	17	L
TT-4	1240	1	
	1132	3	L + plag
TT10wo-1	1295	9	L
TT10wo-3	1240	1	
	1077	2.5	L + cpx + plag
TT10wo-4	1240	0.5	
	1130	1.5	L + cpx +plag
TT10wo-6	1240	0.5	
	1185	2.8	L
TT10wo-7	1240	0.5	
	1177	2	L + cpx
TT10wo-8	1240	0.5	
	1181	6.3	L + cpx
J-TUBAS-A	1197	1.5	
	1182	24	
	1182→1146	1.7°C/hr	
	1146	16	L + cpx + plag
J-TUBAS-B	1194	1.5	
	1182	24	
	1182→1146	1.7°C/hr	
	1146	3	L + cpx + plag
TT10wo-9	1192	1.5	
	1160	17	L + cpx + plag
J-TUBAS-C	1198	1.5	
	1184	24	
	1182→1166	1.7°C/hr	L + cpx + plag
J-TUBAS-D	1196	1.5	
	1176	7.5	L + cpx
TT10wo-10	1196	1.5	
	1166	4.5	L + cpx + plag (tr)
TT10wo-11	1196	1.5	
	1184	2.1	L + cpx
TT10wo-12	1204	1.5	
	1188	15	L + cpx
TT10wo-13	1204	1.5	
	1189	0.3	

	1194	3.5	L + cpx (tr)
TT10wo-14	1194	9.3	L + cpx
TT10wo-15	1205	2.2	L
TT10wo-16	1200	3	L + cpx (tr)
TT10wo-17	1210	1.5	
	1200	24	
	1200→1180	1.7°C/hr	
	1180	16	L + cpx
D2-1	1301	17.5	L
D2-2	1301	0.8	
	1293	2	L + cpx (tr)
D2-TUBAS-A	1301	1.8	
	1293	24	
	1293→1260	1.7°C/hr	
	1260	22	L + cpx
D2-TUBAS-B	1301	1.5	
	1292	22	L + cpx
D2-TUBAS-C	1301	1.5	L + cpx (tr)
D2-TUBAS-D	1312	4	L

(a) All runs made at FMQ

(b) TB = unspiked Takashima basalt
TO-TUBAS = spiked Takashima basalt + 10 wt% wo
##di = ## wt% diopside added
##wo = ## wt% wollastonite added
TT = unspiked Juan de Fuca basalt (TT-152-37)
J-TUBAS = spiked Juan de Fuca basalt + 10 wt% wo
D2 = unspiked $Di_{71}An_{29}$
D2-TUBAS = spiked $Di_{71}An_{29}$

(c) L = liquid, cpx = clinopyroxene, plag = plagioclase, ol = olivine, (tr) = trace

Appendix 2.3: Removal of Gold Coats From Micas

In order to re-etch the mica fission track detectors after SEM counting, the gold coats must be removed. This can be easily done by swirling the mica in a slightly acidic bromine water solution. The recipe, developed by G. Rossman, is: 10 ml H_2O + 2 g NaBr + 2 ml fresh liquid bleach + 2 - 3 drops dilute HCl. After about a minute most of the gold will flake off, but small ($\approx$ 1 μm) specs may remain for a bit longer. All of the gold is usually removed in 5 minutes, with no damage to the mica. This must be done in a fume hood.

Appendix 2.4: SEM/Optical Correction Factor for Fission Track Counts

Because of the very different fission track densities in the crystals and glass, the crystals were counted with an optical microscope and the glass counted with the SEM. It is therefore important to calibrate the SEM measurements to the optical measurements, as different types of images and magnifications are used. The NBS standard glasses, which were included in the irradiations to determine U concentrations, were used for the calibration because they have a track density which can be counted on both instruments, and are homogeneous, minimizing complications from track densities that vary with location (such as a zoned crystal). To best simulate an actual sample measurement, I counted the mica detector on the SEM, then re-etched it and counted the same point optically. This calibration thus preserved the order: etch → SEM → etch → optical that was used for partition coefficient measurements. The results, shown in Table A2.4.1, indicate that the SEM counts are 10% higher than the optical counts, though there is some spread. Because of this uncertainty, some error is introduced in making this correction, and the correct representation is the standard error of the mean ($\sigma/\sqrt{n}$). Thus, the SEM/optical correction factor I use is $1.10 \pm .04$.

Table A2.4.1

Sample	$N_{SEM}/10^{6(a)}$	$N_{optical}/10^6$	$N_{SEM}/N_{optical}$
961-B1	2.64 ± .12	2.42 ± .08	1.09
961-D1	2.82 ± .12	2.77 ± .10	1.02
961-A2	3.09 ± .15	2.92 ± .11	1.06
961-C2	3.13 ± .16	2.58 ± .12	1.21
Average			1.10 ± .04

(a) N = track density (tracks/cm^2)

Appendix 2.5: Test for Alpha Track Fading

During the month long exposure necessary to record ^{230}Th alpha tracks from the crystals, it is important to be sure that tracks in the cellulose nitrate detector do not anneal. As a check for this, a sample was exposed for 24 hours, the detector removed and stored next to the sample for a month, and then the sample re-exposed for 24 hours with a new detector. The two detectors were then etched simultaneously and counted. The results, listed in Table A2.5.1, show that the track densities in the two detectors cannot be distinguished and that there is no evidence for fading.

Table A2.5.1

Exposure	$N/10^{6(a)}$
1	3.31 ± .16
2	3.45 ± .16

(a) N = track density (tracks/cm^2)

Appendix 2.6: Track Counting Reproducibility

Track counting requires practice and can vary with time, especially after periodic hiatuses. For Th, all tracks were counted optically and I measured crystal and glass densities within one week of each other. Thus, Th partition coefficients are insensitive to systematic drifts in counting efficiency. For U, the glass and crystal track densities were counted with separate techniques, and thus a drift in partition coefficients with time is possible. I checked long term track counting reproducibility by periodically recounting sample detectors over the course of the study. Because of the high resolution of the SEM photographs, there is essentially no difference in repeat counts of U glass densities.

Variations in the repeat measurements of the glass densities result from uncertainty as to what is or isn't a track, and are subject to counting statistics errors because exact relocation is impossible. In the case of crystal densities, variations in repeat measurements can result from both ambiguous tracks and crystal zoning. As track densities increase towards the crystal rim, the measured density will depend on the choice of the outer limit of the crystal section to count. Variations in the repeat measurements of the crystal densities should not, in principal, be subject to counting statistics errors because essentially the same tracks are counted each time. As shown in Table A2.6.1, there do appear to be small differences in repeat track density measurements. Given the limited amount of data I am uncertain whether these variations are systematic or random, but the data appear to suggest that density measurements systematically decrease with time. The U crystal data give an average decrease of 5%, and a ±5% reproducibility standard deviation is included in all U crystal track densities. As previously mentioned, $D_{Th}^{xtl/liq}$ is insensitive to a purely systematic drift, and no reproducibility error is be assigned for Th.

A second possible source of reproducibility error is short term random variations in track counting consistency, which would apply to both U and Th. The absence of significant random counting fluctuations is supported by the fact that glass track densities

between different spots in a given sample (all counted within 1 - 2 days) statistically agree (Table 3.2).

I did all of the track counting for this study, so personal counting bias should not affect the results. As a matter of course, one Th detector was also counted by DSB to determine the effect of personal bias. As shown in Table A2.6.1, there is no significant difference for different counters.

Table A2.6.1

Element	Sample	Counter	Date	# tracks	$N/10^{6(a)}$
Th	D2-TUBAS-E1	TLaT	5-24-91	298	0.77
"	"	"	12-19-91	253	0.73
"	"	DSB	7-1-91		0.74
"	J-TUBAS-E-g1	TLaT	3-12-91	623	4.9±0.2
"	"	"	4-18-91	626	4.9±0.2
"	"	"	12-19-91	587	4.6±0.2
U	D2-TUBAS-L1	"	6-19-91	355	1.53
"	"	"	12-19-91	429	1.51
"	T-TUBAS-A1	"	12-7-90	60	0.91
"	"	"	3-6-91	49	0.82

(a) N = track density (tracks/cm^2)

CHAPTER 3

Experimental Results

3.1 Clinopyroxene

3.1.1 General Description

The run products from the clinopyroxene crystallization experiments consist of large, euhedral, inclusion free diopsidic clinopyroxene and quenched melt. One run, J-TUBAS-E, also crystallized ≈ 1% plagioclase. No quench crystals are visible in any of the runs. All runs yielded at least one, though typically 2 - 4, large (> 75 μm in shortest dimension) crystals. Several of the runs with the natural basalts also produced a few small crystals, which may have either nucleated late in the experiment or nucleated along with the rest and grew at a much slower rate. Most crystals appear to have nucleated on the surface of the charge or the Pt hanging wire. The size of the crystals increased and the number of crystals per run decreased in the order Takashima basalt, Juan de Fuca basalt, $Di_{71}An_{29}$. This is the general order in which the experiments were run, and the improvement probably reflects a combination of my improved crystal growing skill and increased diffusion rates and lower viscosity (Bottinga and Weill 1976) for bulk compositions with lower alkali contents. A representative photomicrograph of a run product is shown in Fig. 3.1. Samples underwent 5 - 25% crystallization in the different compositions (Table 3.1; the method for calculating of the amount of crystallization is given in section *3.1.2.2*). The lowest degree of crystallization is in the Juan de Fuca basalt and is limited by the onset of plagioclase crystallization.

A few runs have bubbles in the glass. When present, there are usually very few (1 - 5) relatively large (20 - 400 μm) bubbles, that are typically adhering to the platinum wire or a crystal. In at least one case it appears that a crystal nucleated on a bubble, indicating that the bubbles were present throughout the experiment rather than being formed by exsolution

Figure 3.1 Backscattered electron micrograph of sectioned charge from a clinopyroxene crystallization experiment. The very bright regions (upper left and along top) are the Pt wire loop. The glass is intermediate brightness, and the crystals are darker, due to their lower atomic number.

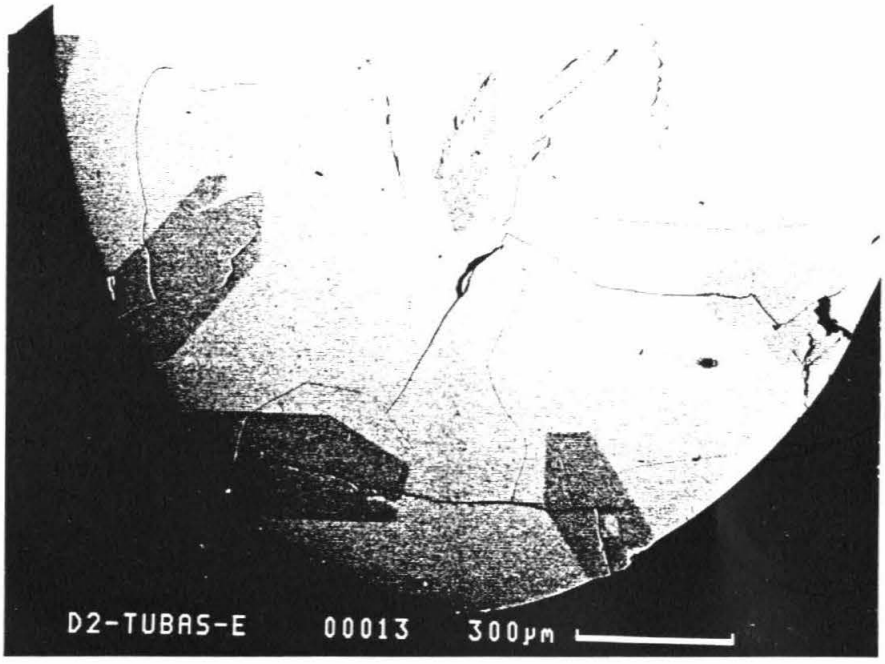
D2-TUBAS-E
00013
300µm

TABLE 3.1

Major Element Compositions of Crystals and Quenched Liquid From Clinopyroxene and Olivine Crystallization Experiments[a]

Experiment	SiO_2	TiO_2	Al_2O_3	Cr_2O_3	FeO	MnO	MgO	CaO	Na_2O	K_2O	Total	n[b]	F_{xtl}[c]
Clinopyroxene:													
D2-TUBAS-G	54.5		3.46				17.89	25.4			101.3	2	.25
D2-TUBAS-E	52.6		3.00				18.16	25.3			99.2	3	.22
D2-TUBAS-F	54.0		3.37				17.95	25.3			100.7	2	.23
D2-TUBAS-N	54.77		2.74				18.09	24.85			100.49	2	.22
D2-TUBAS-H	54.4		3.38				18.09	25.2			101.2	3	.25
D2-TUBAS-L	53.9		3.55				18.13	24.8			98.8	1	.07
J-TUBAS-G	51.9	1.01	3.86	nd[d]	5.80	.131	15.01	22.7	.181		100.7	3	.09
J-TUBAS-E	52.3	.933	3.57	.204	5.44	.148	15.33	22.8	.151		100.9	4	.08
J-TUBAS-F	52.4	.929	3.54	.157	5.65	.145	15.36	22.6	.160		101.0	3	.08
J-TUBAS-H	51.6	.998	3.31	.160	5.15	.148	15.71	22.5	.119		99.6	2	.04
J-TUBAS-L	52.2	.869	3.03	nd	4.49	.163	16.12	22.7			99.8	3	.04
T-TUBAS-C	51.6	1.00	4.41	.709	4.42	.118	15.76	22.0	.238		99.8	2	.14
T-TUBAS-I	51.5	1.02	4.45	.387	4.36	.099	16.20	22.3	.253		100.7	1	.13
T-TUBAS-B	50.2	1.24	4.59	.304	4.35	.111	15.54	22.0	.203		98.5	5	.11
T-TUBAS-D	50.8	1.38	4.75	nd	3.89	.123	16.12	21.7	.157		99.2	3	.10
T-TUBAS-H	52.1	1.17	4.43	.746	3.42	.134	16.85	21.8	.141		100.3	5	.12
Olivine:													
TO-TUBAS-D	40.3	.01	.063	.059	14.82	.241	45.55	.262			101.3	1	.06

Experiment	SiO_2	TiO_2	Al_2O_3	Cr_2O_3	FeO	MnO	MgO	CaO	Na_2O	K_2O	Total	Na_2O/Na_2O_i[e]	FeO/FeO_i[e]
Glass:													
D2-TUBAS-G	48.0		15.07				9.88	24.0			98.0		
D2-TUBAS-E	49.6		14.82				10.03	24.1			99.6		
D2-TUBAS-F	50.4		15.01				9.83	24.0			100.2		
D2-TUBAS-N	49.97		15.15				9.90	23.55			98.9		
D2-TUBAS-H	49.2		15.13				9.67	23.9			98.9		
D2-TUBAS-L	50.9		12.96				11.43	23.4			100.5		
J-TUBAS-G	51.0	1.81	13.39		9.96	.205	5.45	14.00	1.87	.103	98.6	.92	.92
J-TUBAS-E	52.4	1.81	13.41		9.53	.202	5.52	14.19	1.67	.091	99.7	.81	.86
J-TUBAS-F	51.7	1.79	13.38		9.91	.216	5.46	14.13	1.71	.086	99.2	.84	.90
J-TUBAS-H	50.4	1.78	13.30		9.12	.200	5.91	14.68	1.23	.068	97.6	.63	.86
J-TUBAS-L	53.0	1.76	13.35		7.43	.203	6.03	14.93	.716	.025	98.5	.36	.67
T-TUBAS-C	51.7	1.71	15.63		7.63	.153	5.77	10.95	2.58	1.57	98.7	.90	.84
T-TUBAS-I	51.3	1.70	15.57		7.60	.157	6.07	11.10	3.17	1.61	98.7	.99	.81
T-TUBAS-B	50.2	1.68	15.03		8.08	.151	6.08	11.25	2.61	1.58	97.5	.97	.92
T-TUBAS-D	50.9	1.68	15.39		7.06	.149	6.29	11.78	1.86	1.41	97.4	.68	.80
T-TUBAS-H	54.0	1.80	16.34		5.87	.152	6.18	12.00	1.36	1.06	99.7	.46	.62
TO-TUBAS-D	51.5	1.84	16.55		8.11	.167	6.42	8.84	3.08	1.665	98.5		

(a) Averages of 3-4 points per sample for glass, 1-2 points from each crystal
(b) n = number of crystals analyzed
(c) F_{xtl} determined from major element mass balance (see section *1.5.2*)
(d) nd = not determined
(e) Na_2O and FeO loss during run: sum of concentration in crystals and glass divided by concentration in staring material

of volatiles during the quench. The presence of these bubbles, which probably contain predominantly nitrogen, is not significant for this study, as the particle track maps show that no measurable amounts of U or Th partitioned into them. Even if U and Th did partition into this vapor, it would probably equilibrate with the melt very rapidly, and as long as the bubbles were present throughout the run, partitioning into the vapor will not affect the crystal-melt partitioning.

In terms of major element compositions, the pyroxenes are quite homogeneous, with the enstatite and ferrosilite contents changing less than 1% from core to rim. The crystal compositions are plotted on the standard pyroxene quadrilateral in Fig. 3.2 (calculation of end-member mole fractions follows the procedure of Lindsley and Andersen 1983; see Appendix 3.3 for details), and average compositions are listed in Table 3.1. There is a small change in pyroxene composition with fO_2 in the natural basalts, with the more reducing runs having slightly less ferrosilite component. This change is most likely due to greater amounts of Fe-loss to the Pt hanging wire at low fO_2. In addition to the quadrilateral components, all pyroxenes contain significant amounts of Al_2O_3, and pyroxenes from the natural basalts also contain measurable quantities of TiO_2, Cr_2O_3, MnO, and Na_2O.

3.1.2 Calculation of Partition Coefficients From Particle Track Maps

3.1.2.1 Range Correction

Fission track densities are related to ^{235}U concentration by the equation:

$$N_{FT} = (^{235}\sigma\Phi^{235}U^{235}r\rho^{235}\eta)/2,$$

where N_{FT} = fission track density (tracks/cm^2), $^{235}\sigma$ = thermal neutron fission cross section for ^{235}U (cm^2), Φ = total thermal neutron fluence during irradiation (neutrons/cm^2), ^{235}U = concentration of ^{235}U (atoms/g), ^{235}r = average range of a single ^{235}U fission fragment (cm), ρ = density of matrix (g/cm^2), $^{235}\eta$ = etching efficiency (the fraction of tracks entering the detector that are revealed by etching), and the factor 1/2 is

Figure 3.2 Major element compositions of experimentally grown clinopyroxene crystals plotted on diopside ($CaMgSi_2O_6$)-hedenburgite ($CaFeSi_2O_6$)-enstatite (Mg_2SiO_6)-ferrosilite (Fe_2SiO_6) pyroxene quadrilateral. Concentrations are in atomic proportions and were calculated by the scheme of Lindsley and Andersen (1983; see Appendix 3.3). The positions of the clinopyroxenes from the basalts are typical for mafic igneous rocks. All crystals contain Al_2O_3, and the basaltic clinopyroxenes also contain measurable quantities of TiO_2, Cr_2O_3, MnO, and Na_2O.

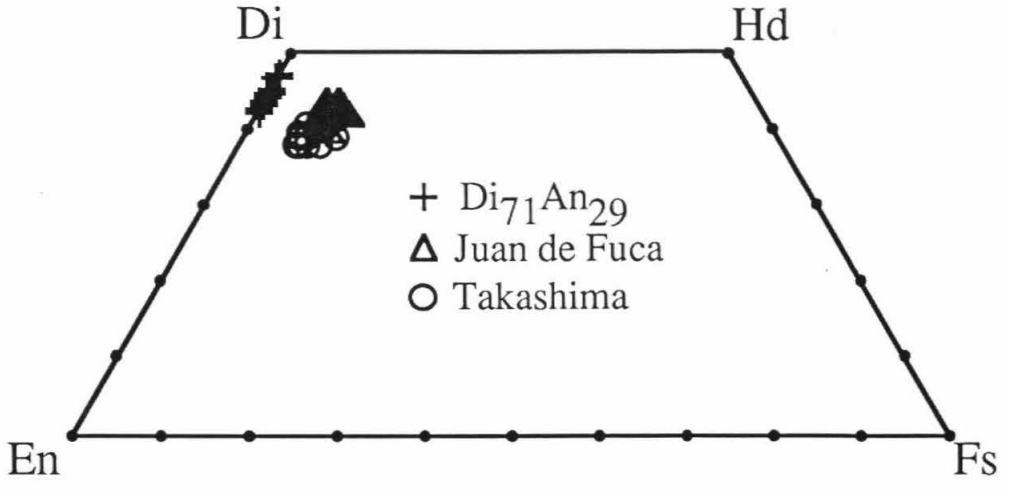

Figure 3.2

needed because only half of the fission fragments are registered in the external mica detector (Fleischer et al. 1975). The atomic ratio of ^{235}U between the clinopyroxene and glass is then:

$$\frac{^{235}U_{cpx}}{^{235}U_{gl}} = \left(\frac{N_{cpx}}{N_{gl}}\right)_{FT}\left(\frac{r_{gl}}{r_{cpx}}\right)_{FT}\left(\frac{\rho_{gl}}{\rho_{cpx}}\right),$$

where $^{235}\sigma$, Φ, and $^{235}\eta$ for the clinopyroxene and glass are equal and cancel. Upon converting the concentrations to mass fractions and the fission fragment ranges to g/cm^2 (R), this reduces to:

$$\frac{[^{235}U]_{cpx}}{[^{235}U]_{gl}} = \left(\frac{N_{cpx}}{N_{gl}}\right)_{FT}\left(\frac{R_{gl}}{R_{cpx}}\right)_{FT},$$

which is the crystal-melt partition coefficient. Thus, the fission track ratio is related to the partition coefficient by the inverse of the fission fragment range ratio.

A similar relationship between N and ^{230}Th concentration holds for alpha particle tracks:

$$N_{AT} = (t^{230}\lambda^{230}Th^{230}r\rho^{230}\eta)/4,$$

where N_{AT} = alpha track density ($tracks/cm^2$), t = exposure time, $^{230}\lambda$ = alpha decay constant for ^{230}Th, and the other terms are analogous to the terms in the expression for ^{235}U. The corresponding ^{230}Th partition coefficient is thus:

$$\frac{[^{230}Th]_{cpx}}{[^{230}Th]_{gl}} = \left(\frac{N_{cpx}}{N_{gl}}\right)_{AT}\left(\frac{R_{gl}}{R_{cpx}}\right)_{AT}\left(\frac{t_{gl}}{t_{cpx}}\right)_{AT}.$$

Since two separate exposures are made for each sample (see section *2.4.2*), the alpha track ratios require both a range and an exposure time correction.

Particle ranges are a function of the atomic number of the matrix; equations are given in Benjamin (1980). In these samples, the fission fragment and ^{230}Th alpha particle ranges are about 10 μm and 16 μm, respectively, which sets a lower limit on the spatial resolution of particle track mapping. The atomic numbers of the clinopyroxene and glass in my experiments are very similar, and so the range corrections required are small (1 - 4%). A

fission fragment and alpha particle range correction was calculated for each experiment, and is listed in Appendix 3.1.

3.1.2.2 Zoning Correction

The clinopyroxene crystals in these experiments were grown by slowly cooling the sample from the liquidus. Because diffusion in clinopyroxene is extremely slow, crystal-melt partitioning should be governed by Rayleigh fractionation. The concentration of elements rejected by the clinopyroxene will increase in the melt as the crystal fraction increases, so that the crystals will develop a zoning profile for incompatible elements that increases from core to rim. Such zoning is observed for the minor elements, as seen with the electron microprobe traverses (see section *3.1.5*). The crystal track density is too low to see track density gradients in the crystals, but the existence of minor element zoning indicates that U and Th are similarly zoned. It is necessary to correct for this zoning when determining partition coefficients from the track densities, because only the rim of the crystal is in equilibrium with the final quenched melt, while the crystal track density must be determined from the crystal interior. Since the actinide concentrations increase from core to rim, the zoning correction will always increase the apparent partition coefficient determined from the ratio of crystal and glass track densities.

In calculating the zoning correction, I assume that the crystals grew from the melt by perfect fractional crystallization. Clinopyroxene and melt are the only phases present in all but one experiment (a minor amount of plagioclase crystallized in J-TUBAS-E, but its effect is negligible), so I assume that the zoning profiles are not modified by the onset of crystallization of an additional phase and that $D_i^{cpx/liq} = D_i^{bulk/liq}$. For the purposes of this correction, I also assume that the partition coefficients are constant over the temperature and compositional range of crystallization. Ideally, the track density I measure in a crystal would reflect the actinide concentration in the melt integrated over the entire range of crystallization, but in practice my measurements are biased towards the core of the crystal because I cannot count the outer 20 μm of the crystal. Therefore, the correction must

account for the zoning present only in fraction of crystallization represented by the area fraction of the crystal I analyze. The correction then takes the form (see Appendix 3.2):

$$D_z = D_m \frac{vF}{(F - 1)\ln(1 - vF)},$$

where D_z is the zoning corrected partition coefficient, D_m is the measured partition coefficient (the ratio of crystal and glass track densities), F is the total fraction of crystallization in the experiment, and v is the fraction of total crystallization measured for U and Th. F is determined from the composition of the starting material and crystals and glass from the experiment using a least squares mass balancing routine (M. B. Baker, priv. comm.). Oxides present in concentrations of < 1% in either phase and FeO, Na_2O, and K_2O, which are subject to loss during the experiments, are excluded from the mass balance. The remaining oxides used are CaO, MgO, Al_2O_3, SiO_2, and TiO_2. When using MgO alone, I obtain nearly identical F values. v is defined as $(A_m/A_t)^{1.5}$, where A_m = the area of the crystal section counted and A_t is the total area of the crystal section, measured from a SEM photograph. The exponent of 1.5 is needed to convert the area ratio to a volume ratio. Inherent in this correction factor is the additional assumption that the fraction of crystallization analyzed goes from zero to vF; in other words, that the crystal nucleated on the liquidus and that the analyzed crystal section includes the crystal nucleus. In reality, this assumption does not always hold. However, as long as the analyzed section is near center of the crystal, failure of this assumption will result in only a slight over correction because compositions vary little near the crystal cores. In any case, it is important to note that the magnitude of the zoning correction is controlled by the fraction of crystallization, which is relatively small (Table 2.2); in no case can the correction be greater than 1/(1 - F), or 8 - 32% for the three compositions. Since the 20 μm unanalyzed rim is a constant, the volume fraction analyzed increases, and hence the magnitude of the correction decreases, with increasing crystal size.

3.1.2.3 Partition Coefficients and Errors

The U and Th partition coefficients for clinopyroxene and olivine are calculated from the track densities by means of a particle range, exposure time, and zoning correction. The complete expression is then:

$$D = \left(\frac{N_{cpx}}{N_{gl}}\right)\left(\frac{R_{gl}}{R_{cpx}}\right)\left(\frac{t_{gl}}{t_{cpx}}\right)\left(\frac{vF}{(F - 1)\ln(1 - vF)}\right),$$

where $t_{gl} = t_{cpx}$ for the fission tracks. This equation is used to calculate all the partition coefficients presented below.

The quoted errors in Tables 3.3 - 3.5 include contributions from counting statistics for the crystal and glass track densities, and errors for the SEM/optical correction (Appendix 2.3) and reproducibility (Appendix 2.5) for the U crystal track densities. I calculated an additional error to account for the variation in the required zoning correction. In making this correction I assume that the crystal nucleated at the liquidus and grew uniformly throughout the cooling interval. In fact, it is possible that different crystals may nucleate at different times during the slow cooling, resulting in variably higher core concentrations. It is also likely that some of the analyzed crystal sections do not contain the cores of crystals, again resulting in variably higher measured concentrations. Since the actual correction required can vary from the calculated correction (crystal nucleated on liquidus and section through core) down to 1.0 (no correction; section through rim) the maximum error possible is $(D_z/D_m - 1)$. I assigned this range an error of 2σ, and included the 1σ error of $(D_z/D_m - 1)/2$ in all zoning corrections. The magnitude of this error depends on F, and is approximately 11%, 5%, and 7% for the $Di_{71}An_{29}$, Juan de Fuca, and Takashima compositions, respectively. The cumulative errors for individual crystals range from 9% to 29%, average about 14%, and are dominated by the counting statistics errors.

3.1.3 Approach to Interfacial Equilibrium

For reasons discussed in the previous chapter, the crystals in these experiments were grown by slowly cooling the charge from the liquidus temperature. Diffusion rates of large ion lithophile cations in clinopyroxene are extremely slow (Seitz 1973a; Sneeringer 1984) and can be considered insignificant on the time scale of my experiments (3 - 4 days). Hence, the trace element concentration of the crystal interior will not re-equilibrate with the increasing melt concentration as crystallization proceeds. The time-temperature path of the experiments (Table 2.2, Fig. 2.3) was chosen to optimize the possibility of maintaining equilibrium at the crystal-melt interface during crystal growth (interfacial equilibrium), and thus incorporation of trace elements should be governed by Rayleigh fractionation. However, as reversal of this type of experiment is impossible, it is difficult to definitively establish that interfacial equilibrium was maintained. In addition to defect partitioning, sector zoning, and any other surface disequilibrium processes, I consider boundary layer formation (the melt compositional near the crystal-melt interface differing from the bulk melt composition) a non-equilibrium partitioning effect.

Based on the results of Lindstrom (1983), large deviations from interfacial equilibrium should not be expected during crystal growth because of a compensating effect: as a boundary layer of excess of incompatible elements builds up around a growing crystal, so will a deficiency of compatible major elements. This deficiency causes crystal growth to slow down, allowing the boundary layer to diffuse away. I have addressed the question of interfacial equilibrium by (1) using theoretical considerations to check the possibility of maintaining diffusional homogeneity in the melt during crystal growth, (2) evaluating the homogeneity of the melt from the chemical analyses of the glass, (3) comparing measured crystal zoning profiles to those predicted for ideal Rayleigh fractionation, (4) evaluating the reproducibility of the results, and (5) running a test experiment at an order of magnitude lower cooling rate. These topics are addressed in turn in the following sections. Lastly,

based on their geochemical similarity and general coupled behavior in many geologic processes, U and Th should be similarly affected during non-equilibrium partitioning, making $D_{Th}^{cpx/liq}/D_{U}^{cpx/liq}$ less sensitive to deviations from interfacial equilibrium than $D_{U}^{cpx/liq}$ or $D_{Th}^{cpx/liq}$ alone. This expectation is born out in my experiments, proving that deviations from interfacial equilibrium are filtered out in the ratio $D_{Th}^{cpx/liq}/D_{U}^{cpx/liq}$, as discussed below in section *3.1.6.1*.

3.1.4 Glass Homogeneity

For interfacial equilibrium to be maintained, the melt must remain homogeneous during crystallization. As crystallization proceeds, elements that are concentrated in the melt relative to the crystal (low crystal-melt partition coefficient) are rejected by the growing crystal and must move away from the interface by diffusion. Conversely, elements enriched in the crystal must move towards the interface. Thus, to maintain interfacial equilibrium, the melt must undergo continual mixing. This is presumably accomplished predominantly by diffusion, with possible contributions from mechanical mixing resulting from crystal sinking and convection.

One way to evaluate whether the melt was homogeneous during crystallization is to compare the crystal growth rate with the characteristic diffusional velocity of the trace elements of interest in the melt. The characteristic diffusional velocity can be estimated two ways; both give similar results. The first is to use the crystallization time to calculate the characteristic length for diffusion in a semi-infinite medium from $l \approx 2\sqrt{Dt}$ (Crank 1975), where t is duration of the slow cooling interval of the experiment and D is the diffusion coefficient. The velocity is then the ratio of length and time, or $2\sqrt{D/t}$. The second method is to calculate the characteristic time scale for diffusion in a semi-infinite medium from $t \approx l^2/4D$, where l is approximated from the distance between crystals, which is on the order of 0.05 cm. In this case the velocity that emerges is 4D/l. U and Th diffusion in basaltic melts have never been measured, so I have made an approximation based on data for U^{6+}

in a super-cooled borosilicate melt (60% SiO_2) at 560 - 800°C (Dunn 1987). Extrapolation of this data up to 1200°C gives $D = 6.9 \times 10^{-9}$, which gives diffusional velocities from 5 - 8 x 10^{-7} cm/sec for the two methods. The average crystal growth rate can be calculated from the crystal size and cooling duration (Table 2.2) and is approximately 1.5 x 10^{-7} cm/sec. Thus, it appears that the characteristic diffusional velocity is the same order of magnitude as the crystal growth rate. Therefore, on the basis of diffusion, it appears that it is possible for equilibrium to be maintained at the crystal-melt interface under these experimental conditions. It is important to note, however, that allowing for local super-cooling and variations in the actual crystal growth rate, some chemical boundary layers may still exist.

The homogeneity of the melt during crystallization can also be estimated from the homogeneity of the glass (quenched melt) from the crystallization experiments. The glasses were analyzed for major and minor elements by electron microprobe and for U and Th by particle track radiography. The analytical techniques are discussed in chapter 2. The results are listed in Tables 3.1 and 3.2. Microprobe and particle track analyses were made on approximately the same points in most cases, and I typically made 3 - 4 measurements per run. As discussed below, the electron microprobe and fission track measurements of the glasses show that any concentration gradients present during crystal growth were not measurable in most samples, further supporting a satisfactory approach to interfacial equilibrium.

The major element concentrations in the $Di_{71}An_{29}$ and Juan de Fuca basalt compositions are homogeneous to within 3%. The degree of homogeneity appears to be independent of the duration that the charge was held at the final temperature (Table 2.2). The Takashima basalt shows slightly more variability: the major element concentrations are homogeneous to within 4% in all but one run. In run T-TUBAS-D, K_2O, Na_2O, and MgO vary by 6 - 7%. To illustrate the degree of major element homogeneity, I have plotted MgO vs. Al_2O_3 for all of the glass analyses in Fig. 3.3. The starting compositions plot to the

TABLE 3.2

Raw Fission and Alpha Track Data

Sample	Irrad.	# Fission trx (U)	$\rho_U/10^6$ (trx/cm^2)	# Alpha trx (Th)	$\rho_{Th}/10^6$ (trx/cm^2)	t_{Alpha} (hr)	$\nu^{(a)}$
D2-TUBAS-G-glass	3	1195	169.5	1302	3.399	31.2	
D2-TUBAS-G1[(b)]	3	399	0.4713	654	0.8003	715	.67
D2-TUBAS-G2	3	292	0.4173	396	0.6801	715	.52
D2-TUBAS-E-glass	3	1377	195.3	1280	3.341	31.2	
D2-TUBAS-E1	3	258	0.7268	298	0.7728	715	.57
D2-TUBAS-E2	3	287	0.7542	299	0.7410	715	.37
D2-TUBAS-E3	3	329	0.7299	306	0.6566	715	.48
D2-TUBAS-F-glass	3	1313	186.2	1280	3.341	31.2	
D2-TUBAS-F1	3	241	0.9297	159	0.7325	715	.17
D2-TUBAS-F2	3	255	0.8053	331	0.9291	715	.60
D2-TUBAS-H-glass	3	1307	185.4	1294	3.378	31.2	
D2-TUBAS-H1	3	488	1.225	312	0.7831	715	.36
D2-TUBAS-H2	3	356	1.102	148	0.5766	715	.62
D2-TUBAS-H3	3	1071	1.279	565	0.9123	715	.35
D2-TUBAS-L-glass	3	1277	181.1	1058	2.762	31.8	
D2-TUBAS-L1	3	355	1.528	156	0.6713	743.5	.37
D2-TUBAS-N-glass	4	1439	182.0	522	4.088	43.5	
D2-TUBAS-N1	4	368	.4626	280	.3874	795.7	.82
D2-TUBAS-N2	4	163	.4327	179	.4784	795.7	.67
D2-TUBAS-N3	4	324	.4444				.68
J-TUBAS-G-glass	2	1330	168.2	1888	4.929	48.5	
J-TUBAS-G1	2	134	0.6031	179	0.7831	746	.30
J-TUBAS-G2	2	38	0.4960	68	1.044	746	.05
J-TUBAS-G3	2	32	0.5967	43	1.086	746	.18
J-TUBAS-E-glass	2	1835	195.2	1924	5.023	48.5	
J-TUBAS-E1	2	123	0.7896	260	1.249	746	.18
J-TUBAS-E2	2			46	1.001	746	.26
J-TUBAS-E4	2	27	0.7552	39	0.8038	746	.08
J-TUBAS-E5	2	81	0.6821	82	0.7298	746	.23
J-TUBAS-F-glass	2	1838	177.4	1879	4.905	48.5	
J-TUBAS-F1	2	97	0.6783	113	0.8762	746	.37
J-TUBAS-F3	2	42	0.8656	34	0.9510	746	.27
J-TUBAS-F4	2	24	0.6713	19	0.6764	746	.14

Sample	Irrad.	# Fission trx (U)	$\rho_U/10^6$ (trx/cm^2)	# Alpha trx (Th)	$\rho_{Th}/10^6$ (trx/cm^2)	t_{Alpha} (hr)	v
J-TUBAS-H-glass	2	1761	184.4	1864	4.866	47.5	
J-TUBAS-H1	2	153	0.9821	96	0.6112	648	.14
J-TUBAS-H2	2	114	1.145	129	0.8862	648	.13
J-TUBAS-L-glass	4	1424	180.1	1227	3.203	31.8	
J-TUBAS-L1	4	62	0.8230	14	0.3537	743.5	.14
J-TUBAS-L2	4	181	1.074	100	0.6637	743.5	.44
T-TUBAS-C-glass	2	1449	175.0	2061	5.416	47.5	
T-TUBAS-C1	2	53	1.092	44	1.723	648	.21
T-TUBAS-C2	2	14	1.566				.06
T-TUBAS-I-glass				543	4.252	43.5	
T-TUBAS-I1				78	1.175	795.5	.34
T-TUBAS-I4				94	1.067	795.5	.14
T-TUBAS-B-glass	1	1151	143.2	1768	4.615	48.5	
T-TUBAS-B1	1	54	1.458				.13
T-TUBAS-B2	1	36	1.512	55	1.873	746	.18
T-TUBAS-B3	1	58	1.253	169	2.816	746	.18
T-TUBAS-B4	1	36	1.237	34	2.421	746	.18
T-TUBAS-B5	1			150	3.091	746	.10
T-TUBAS-D-glass	2	1259	159.3	1793	4.681	47.5	
T-TUBAS-D1	2			367	1.661	648	.15
T-TUBAS-D2	2	202	2.985				.17
T-TUBAS-D3	2	109	3.557	83	2.955	648	.08
T-TUBAS-H-glass	3	1412	200.3	1300	3.394	31.8	
T-TUBAS-H1	3	114	2.626	45	1.175	743.5	.17
T-TUBAS-H2	3	274	2.283	135	1.244	743.5	.31
T-TUBAS-H3	3	180	2.043	89	0.9419	743.5	.21
T-TUBAS-H4	3	259	3.121	76	1.653	743.5	.22
T-TUBAS-H5	3	116	2.163				.26
TO-TUBAS-D-glass	4	471	178.7	301	2.357	29.6	
TO-TUBAS-D4	4	1	.0052	1	.0052	1576	.35

(a) v = fraction of crystal section analyzed for U and Th
(b) Each run has an alphabetical index, each crystal has a numerical index

Figure 3.3 MgO vs. Al_2O_3 (wt%) for glasses from clinopyroxene crystallization experiments and super-liquidus quench runs. Quench glasses plot to the upper left and are circled for clarity. Clinopyroxene crystallization moves melt compositions downward and to the right. Glasses from $Di_{71}An_{29}$ and Juan de Fuca basalt crystallization experiments plot in relatively tight clusters, indicating uniform compositions. Glasses from Takashima basalt crystallization experiments show more spread, but thin lines connecting analyses from individual experiments show that most of the scatter is from run to run variations. T-TUBAS-D (TTD on figure) shows more scatter, which is consistent with the greater heterogeneity found for all elements in this run.

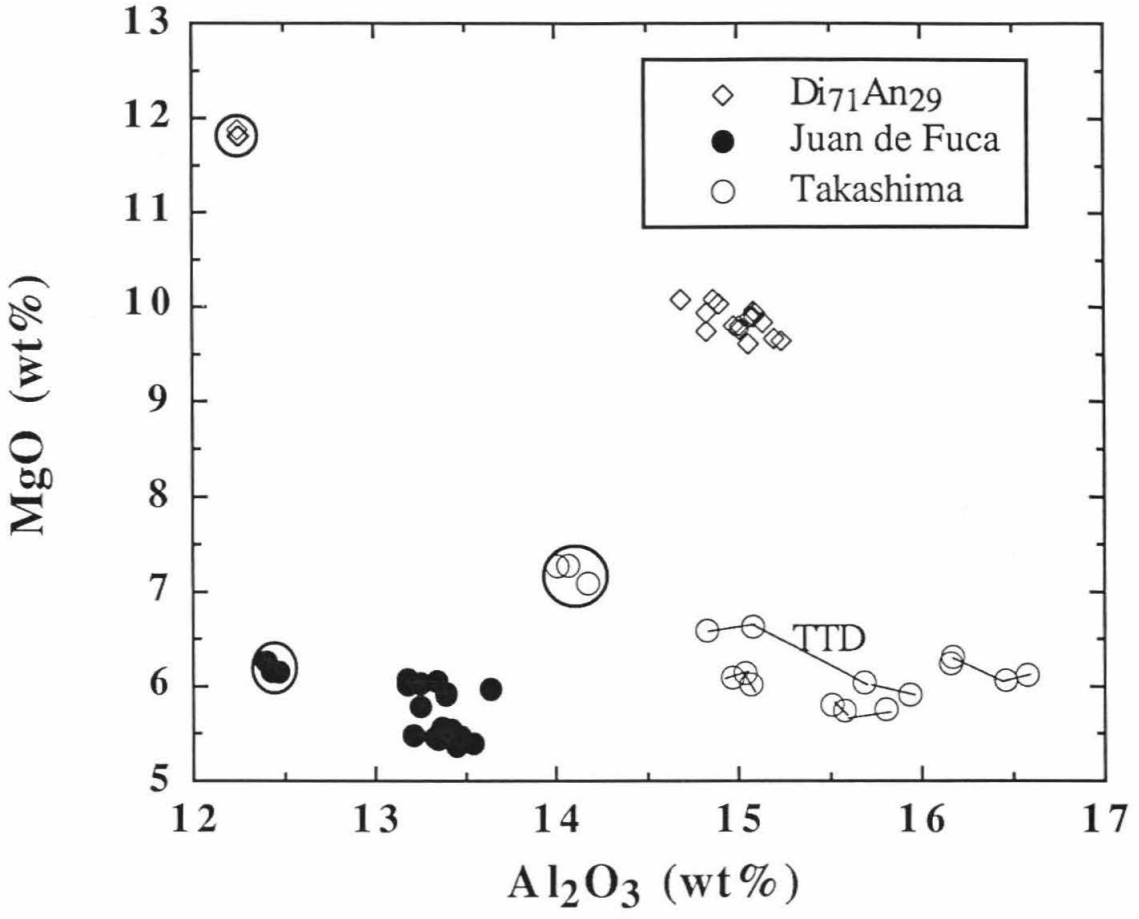
Di71An29
Juan de Fuca
Takashima
TTD
MgO (wt%)
Al2O3 (wt%)
13
12
11
10
9
8
7
6
5
12
13
14
15
16
17

Figure 3.3

upper left on this graph, and crystallization moves the melt composition towards the lower right. The $Di_{71}An_{29}$ and Juan de Fuca compositions plot as tight clusters, while the Takashima data is more spread out along the crystallization trend. As can be seen by the grouping of separate experiments, most of this spread can be attributed to run to run variation. This suggests that the individual runs were homogeneous, with the variation resulting from minor heterogeneities in the starting material. However, different points from T-TUBAS-D, the run noted above to be more heterogeneous, show a large spread. This may be important, as a crystal from this run has anomalously high partition coefficients.

Although small in absolute terms, most of these spatial chemical variations are greater than expected from counting statistics and thus may reflect incomplete homogenization of the melt. I checked this by a making line profile in the glass moving away from crystals in one sample of each composition. In the basalt samples there are no discernable concentration gradients, but there are small ($\approx$ 1.2% per 100 μm) MgO and Al_2O_3 gradients in D2-TUBAS-L. While the U and Th partition coefficients for this sample are not atypical, this sample underwent an anomalously low degree of crystallization (Table 3.1), which, combined with the observed concentration gradients, suggests some super-cooling in this sample. In itself this is not a serious problem because the effect that the observed degree of heterogeneity can have on the measured U and Th partition coefficients is negligible, but it does suggest the formation of boundary layers.

The counting statistics errors on the particle track analyses for glass points are 4 - 5%, which sets a lower limit on the degree of heterogeneity I can document. Within this error, U and Th are homogeneous in the glass. The standard deviation among the track densities at the different points in the glass divided by the average counting statistics error is less than 1.7 for all samples, and measurements made near the crystals are indistinguishable from those far from crystals. In a further attempt to observe U or Th concentration gradients, I made a linear track density measurement profile in

D2-TUBAS-L, the sample that showed mild major element gradients. I detected no gradient for either U or Th. The observation that U and Th are homogeneous supports the assumption of interfacial equilibrium. The glass track densities listed in Table 3.2 are calculated using the sum of all tracks counted in the sample.

All charges for each composition were made from the same 400 - 600 mg batch of starting material that had been through at least two cycles of glassing and grinding in order to minimize compositional variation from run to run. The calculated degree of crystallization (see section *3.1.2.2*) varies somewhat from run to run, which may indicate inhomogeneities in the starting material, or that some samples were super-cooled. Using the calculated degree of crystallization and the BaO content of the glass, I have determined the total BaO content in each charge, assuming that Ba is totally incompatible in clinopyroxene (Shimizu 1974). Within the ≈ 5% counting statistics error the BaO contents are the same in all experiments of a single composition, indicating that the starting material is relatively homogeneous.

3.1.5 Crystal Compositions

For crystals grown by perfect fractional crystallization, incorporation of trace elements should be governed by Rayleigh fractionation. Gradual enrichment or depletion of trace elements in the residual melt as crystallization proceeds should generate crystals that are chemically zoned from core to rim. Zoning profiles of Al_2O_3, Cr_2O_3, and TiO_2 concentrations were taken across several crystals and analyses from one crystal are shown in Fig. 3.4. Also shown are calculated profiles for ideal Rayleigh fractionation (see caption for calculation details). The measured profiles for Al_2O_3 and Cr_2O_3 roughly coincide with the ideal Rayleigh fractionation trends, although from 45 - 80 μm the correlations degrade. The agreement for TiO_2 is poor for all but the central region of the crystal.

Deviations from the predicted profiles could result from non-uniform crystal growth, heterogeneities in the melt, or crystal-melt partition coefficients varying during growth.

Figure 3.4 Measured minor element zoning profiles in experimentally grown clinopyroxene crystal (T-TUBAS-C1) compared to profiles calculated for ideal Rayleigh fractionation. Graphs show oxide concentrations in wt% as a function of distance across crystal for Al_2O_3 (a), Cr_2O_3 (b), and TiO_2 (c). The Rayleigh fractionation profile was calculated assuming continuous homogenization of melt during crystal growth, negligibly slow diffusion in clinopyroxene, and that the crystal nucleated on the liquidus and grew uniformly throughout the cooling interval. The Rayleigh profiles were calculated from the expression: $C_i^{xtl} = C_{i_0}^{liq} D[1 - F_t(r/R)^3]^{D-1}$, where F_t is the total amount of crystallization in the run, r is the distance from the crystal center to the point measured, and R is the total distance from the center to the edge of the crystal along the measured profile. $C_{i_0}^{liq}$ is taken from concentration in the starting material, and D is a constant crystal-liquid partition coefficient defined as the concentration of the crystal core divided by $C_{i_0}^{liq}$. Al_2O_3 is rejected by the growing crystal ($D_{Al_2O_3}^{cpx/liq} = 0.28$) and hence its concentration increases in the melt as crystal growth proceeds, generating a concave up zoning profile (a). Cr_2O_3 is enriched in the crystal relative to the melt ($D_{Cr_2O_3}^{cpx/liq} = 12$) and depletes the melt, generating a concave down profile (b).

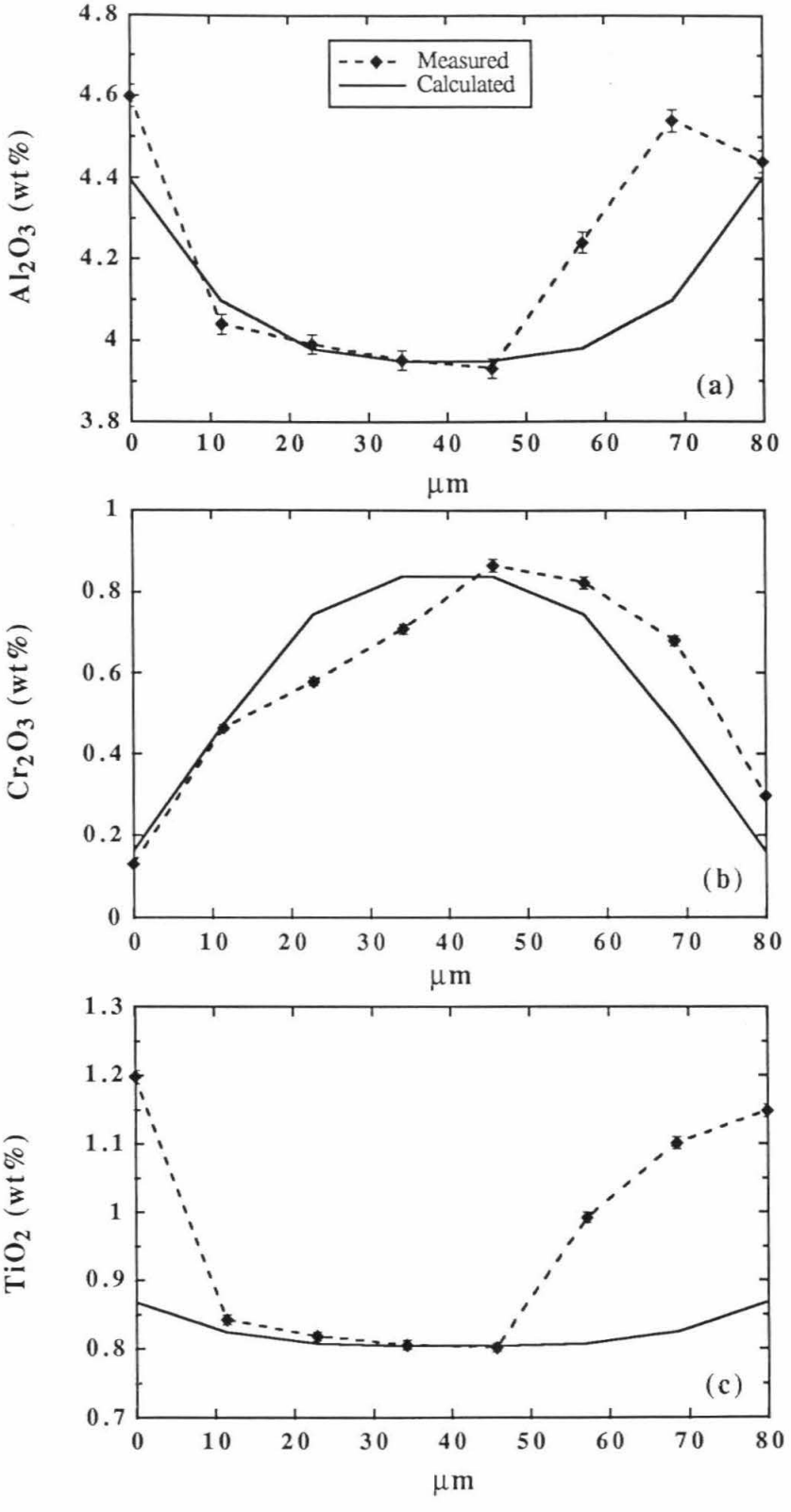

Figure 3.4

The relatively small change in temperature and major element composition from core to rim argue against large changes in partition coefficients and the glass analyses (see previous section) give no evidence for melt heterogeneities of the degree required to explain the deviations in Fig. 3.4. There could have been local super-cooling or boundary layers that were not detected in the glass analyses, however, and the crystal zoning aberrations thus suggest that crystal growth was not entirely uniform. Considering all of the crystals analyzed, the shapes of the measured and predicted zoning profiles qualitatively agree, and the degree of core to rim zoning is seldom very different from what is expected. However, the anomalous behavior of the zoning profiles indicate that the zoning profiles are not a strong argument either for or against interfacial equilibrium.

3.1.6 U and Th Partitioning

3.1.6.1 TUBAS Runs

Range and zoning corrected clinopyroxene-melt partition coefficients are listed in Tables 3.3 - 3.6 and shown in Figs. 3.5, 3.7, and 3.9. These results show that $D_U^{cpx/liq}$ and $D_{Th}^{cpx/liq}$ are both quite small, illustrating the extremely incompatible nature of the actinides in clinopyroxene. A great advantage of in-situ analysis is that crystal-melt partition coefficients for U and Th can be determined on individual crystals, allowing important checks for internal consistency and interfacial equilibrium. Several of the experiments were repeated, and in most cases the inter-crystal and inter-run results agree within statistical precision. There are some exceptions, however, primarily for the Takashima basalt, and the possible reasons for these are discussed in detail below. The 1.7°C/hr experiments behave in an internally consistent manner, and thus the $Di_{71}An_{29}$ run cooled at 0.1°C/hr is discussed separately. Further, if interfacial equilibrium is not maintained during growth, incompatible elements will be incorporated into crystals in excess of their equilibrium amounts and the partition coefficients I report will be too high. The 0.1°C/hr experiments demonstrate this to some extent.

TABLE 3.3

Clinopyroxene-Melt Partition Coefficients for U and Th: $Di_{71}An_{29}$

Sample	fO_2	$D_U^{cpx/liq}$	±	$D_{Th}^{cpx/liq}$	±
D2-TUBAS-G1[a]	NNO	0.0039	0.0005[b]	0.0130	0.0015[b]
D2-TUBAS-G2	NNO	0.0035	0.0005	0.0112	0.0014
D2-TUBAS-E1	FMQ	0.0049	0.0006	0.0122	0.0013
D2-TUBAS-E2	FMQ	0.0052	0.0007	0.0120	0.0014
D2-TUBAS-E3	FMQ	0.0050	0.0006	0.0104	0.0012
D2-TUBAS-F1	FMQ	0.0072	0.0011	0.0126	0.0018
D2-TUBAS-F2	FMQ	0.0059	0.0008	0.0151	0.0017
D2-TUBAS-H1	IW+1	0.0096	0.0014	0.0133	0.0018
D2-TUBAS-H2	IW+1	0.0083	0.0011	0.0094	0.0013
D2-TUBAS-H3	IW+1	0.0100	0.0014	0.016	0.002
D2-TUBAS-L1	IW+1	0.0101	0.0013	0.0113	0.0011
D2-TUBAS-N1[c]	FMQ	0.0033	0.0003	0.0061	0.0006
D2-TUBAS-N2[c]	FMQ	0.0032	0.0003	0.0077	0.0009
D2-TUBAS-N3[c]	FMQ	0.0033	0.0003		

(a) Each run has an alphabetical index, each crystal has a numerical index
(b) Errors are 1σ and are predominantly from counting statistics (see section *1.5.3*)
(c) 0.1°C/hr experiment

TABLE 3.4

Clinopyroxene-Melt Partition Coefficients for U and Th: **Juan de Fuca**

Sample	fO_2	$D_U^{cpx/liq}$	±	$D_{Th}^{cpx/liq}$	±
J-TUBAS-G1[(a)]	NNO	0.0044	0.0005	0.0115	0.0011
J-TUBAS-G2	NNO	0.0036	0.0007	0.015	0.002
J-TUBAS-G3	NNO	0.0044	0.0008	0.016	0.003
J-TUBAS-E1	FMQ	0.0050	0.0006	0.0182	0.0016
J-TUBAS-E2	FMQ			0.014	0.002
J-TUBAS-E4	FMQ	0.0048	0.0010	0.012	0.002
J-TUBAS-E5	FMQ	0.0043	0.0006	0.0106	0.0013
J-TUBAS-F1	FMQ	0.0047	0.0006	0.0128	0.0014
J-TUBAS-F3	FMQ	0.0061	0.0010	0.014	0.003
J-TUBAS-F4	FMQ	0.0047	0.0010	0.010	0.002
J-TUBAS-H1	IW+1	0.0062	0.0007	0.0098	0.0011
J-TUBAS-H2	IW+1	0.0073	0.0009	0.0142	0.0014
J-TUBAS-L1	IW+1	0.0055	0.0008	0.0052	0.0014
J-TUBAS-L2	IW+1	0.0071	0.0008	0.0096	0.0011

(a) Each run has an alphabetical index, each crystal has a numerical index
(b) Errors are 1σ and are predominantly from counting statistics (see section *1.5.3*)

TABLE 3.5

Clinopyroxene- and Olivine-Melt Partition Coefficients for U and Th: **Takashima**

Sample	fO_2	$D_U^{cpx/liq}$	±	$D_{Th}^{cpx/liq}$	±
Clinopyroxene:					
T-TUBAS-C1[(a)]	NNO	0.0083	0.0015	0.028	0.005
T-TUBAS-C2	NNO	0.012	0.003		
T-TUBAS-I1	NNO			0.017	0.002
T-TUBAS-I4	NNO			0.016	0.002
T-TUBAS-B1	FMQ	0.013	0.002		
T-TUBAS-B2	FMQ	0.013	0.002	0.030	0.004
T-TUBAS-B3	FMQ	0.0109	0.0017	0.045	0.004
T-TUBAS-B4	FMQ	0.011	0.002	0.039	0.007
T-TUBAS-B5	FMQ			0.050	0.005
T-TUBAS-D1	IW+1			0.030	0.003
T-TUBAS-D2	IW+1	0.024	0.003		
T-TUBAS-D3	IW+1	0.028	0.004	0.054	0.007
T-TUBAS-H1	IW+1	0.018	0.003	0.018	0.003
T-TUBAS-H2	IW+1	0.0152	0.0019	0.019	0.002
T-TUBAS-H3	IW+1	0.0137	0.0019	0.015	0.002
T-TUBAS-H4	IW+1	0.021	0.003	0.025	0.004
T-TUBAS-H5	IW+1	0.014	0.002		
Olivine:					
TO-TUBAS-D4	FMQ	< 0.00004		< 0.00005	

(a) Each run has an alphabetical index, each crystal has a numerical index
(b) Errors are 1σ and are predominantly from counting statistics (see section *1.5.3*)

Thorium

Individual clinopyroxene-melt partition coefficients for Th are plotted against -logfO_2 in Fig. 3.5. The $Di_{71}An_{29}$ composition displays the most consistent partitioning for Th (Fig. 3.5a). While $D^{cpx/liq}_{Th}$ is not expected to vary, I have treated both U and Th data at different fO_2s independently. $D^{cpx/liq}_{Th}$ for all crystals in this composition lie within 2 standard deviations of the weighted mean and thus are statistically equivalent, apparently showing no change with fO_2. By the same criterion, $D^{cpx/liq}_{Th}$ for the Juan de Fuca basalt (Fig. 3.5b) could also be constant for all but two crystals, although there is significant dispersion and an apparent decrease at IW+1. When looking at each fO_2 separately, these same two crystals are still significantly different. $D^{cpx/liq}_{Th}$ for the Takashima basalt (Fig. 3.5c) is larger but also more variable than in the other two compositions. At the time Appendix II was published, $D^{cpx/liq}_{Th}$ appeared to decrease at IW+1 for the Takashima basalt. Additional data, however, has failed to confirm the decrease, suggesting that there is no systematic change in $D^{cpx/liq}_{Th}$ with fO_2 for this composition. All data are plotted in Fig. 3.5c. In general, all three compositions appear to display greater variability at IW+1.

As Th is solely tetravalent, any change in $D^{cpx/liq}_{Th}$ cannot be due to valence state changes and thus the cause for variations in the Th partition coefficients must be related to some other effects. It is possible that the low fO_2 Juan de Fuca experiments coincidentally achieved a closer approach to equilibrium. Alternatively, the apparent decrease in Th partition coefficient for the Juan de Fuca composition at IW+1 indicates that, while not due to valence state changes, there still may be some dependence of $D^{cpx/liq}_{Th}$ upon fO_2. One possibility is that Th partitioning may be sensitive to changes in composition that arise from changes in fO_2. Several studies have shown that trace element partition coefficients can depend on crystal and melt composition (e.g., Watson 1977; Mysen and Virgo 1980; Lesher 1986; Beckett et al. 1990). There was a significant amount of Na- and Fe-loss during these experiments (Table 3.1). The amount of loss of these components varied from run to run, and while there appears to be some correlation with fO_2, other factors

Figure 3.5 Individual crystal clinopyroxene-melt partition coefficients for Th as a function of oxygen fugacity for TUBAS runs. (a) $Di_{71}An_{29}$, (b) Juan de Fuca basalt, (c) Takashima basalt. Experiments were run at the Ni-NiO, Fa-Mt-Qz, and 1 log unit more oxidizing than the Fe-FeO oxygen buffers. Offsets in $-\log fO_2$ between compositions for a given buffer are the result of temperature differences. Separate experiments at a single buffer are distinguished by small offsets in $-\log fO_2$ for clarity. Error bars represent 1σ errors as defined in section *3.1.2.3*.

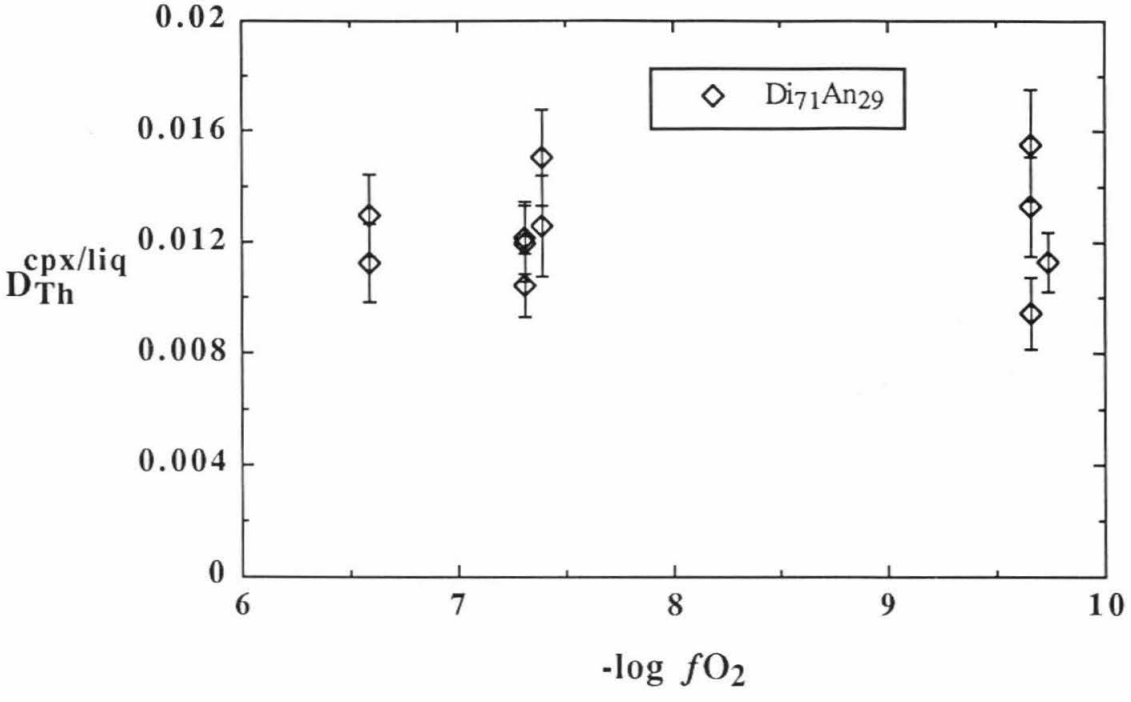

Figure 3.5a

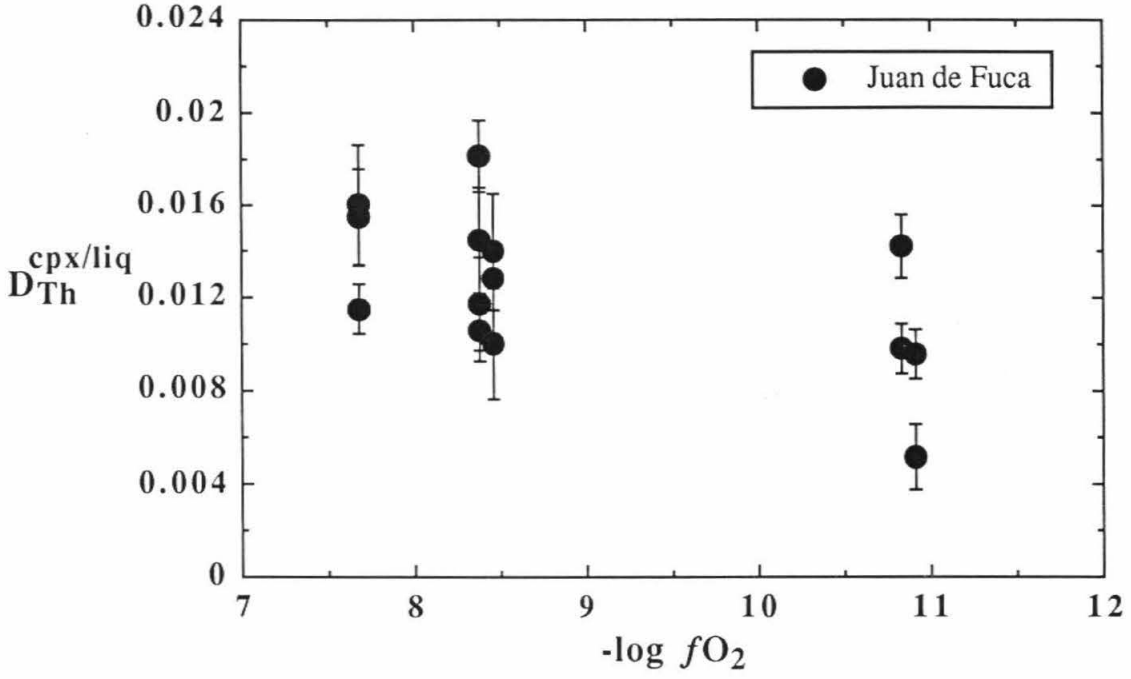
0.024
0.02
0.016
0.012
0.008
0.004
0
cpx/liq
D Th
Juan de Fuca
7
8
9
10
11
12
-log fO2

Figure 3.5b

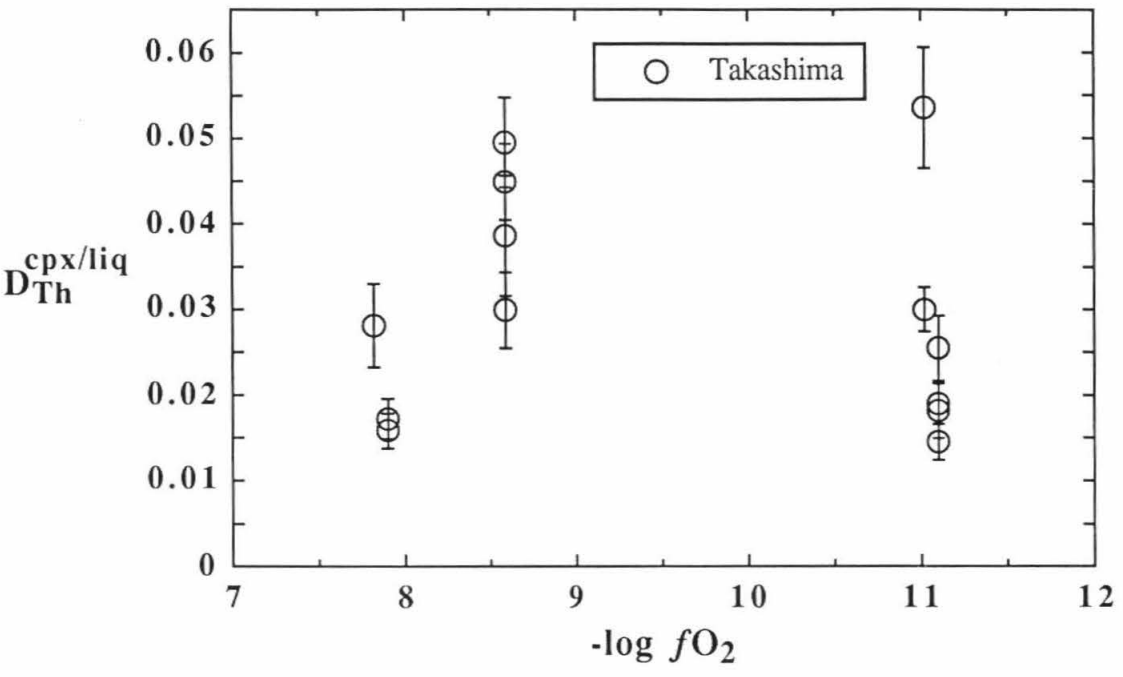
Takashima
0.06
0.05
0.04
0.03
0.02
0.01
0
7
8
9
10
11
12
$D_{Th}^{cpx/liq}$
-log fO_2

Figure 3.5c

such as the mass of the charge must have played a role as well. Some Fe- and Na-loss was expected as an inevitable consequence of running experiments on Pt wires in the presence of a flowing, reduced gas, but it turns out that the Na-loss may shed some light on the compositional dependence of actinide partitioning. There is a rough positive correlation between $D_{Th}^{cpx/liq}$ and $[Na]_{cpx}$ (Fig. 3.6), which suggests that the presence of Na may somehow enhance the incorporation of actinides into the clinopyroxene. This interpretation is supported by several other observations: (1) The magnitudes of the U and Th partition coefficients increase from the Na-free $Di_{71}An_{29}$ composition to the Na-rich Takashima basalt; (2) The Na-free $Di_{71}An_{29}$ composition shows less variability than the basalts. The amount of Na-loss from the basalts was variable and may contribute to the scatter in these data; (3) The apparent decrease in $D_{Th}^{cpx/liq}$ for the Juan de Fuca composition at IW+1 is consistent with the greater amount of Na-loss at low fO_2; (4) The relatively minor increase in $D_U^{cpx/liq}$ with decreasing fO_2 for the Juan de Fuca basalt (Fig. 3.7b and discussed below) may be due to increasing Na-loss approximately cancelling the increase in $D_U^{cpx/liq}$ that would result from reducing the U valence state in the system; (5) A compositional analysis based on a $3Ca^{2+} \Leftrightarrow (U,Th)^{4+} + 2Na^{+}$ coupled substitution in the clinopyroxene M2 site appears to account for the variation in my experimental data (see section *3.2.1*).

Uranium

Individual clinopyroxene-melt partition coefficients for U are plotted against $-\log fO_2$ in Fig. 3.7. The $Di_{71}An_{29}$ composition again displays very consistent partitioning for U (Fig. 3.7a). Individual crystal values for $D_U^{cpx/liq}$ at each fO_2 agree to within 1.2 σ of the weighted mean for that fO_2. $D_U^{cpx/liq}$ also increases with decreasing fO_2. $D_U^{cpx/liq}$ for the Juan de Fuca basalt is similarly well behaved (Fig. 3.7b), with all crystals at a given fO_2 statistically agreeing to within 1.1 σ. The data are consistent with being constant as a function of fO_2 within 1 σ of the weighted mean for all crystals, although there appears to be a slight increase with decreasing fO_2. In terms of the standard error of the weighted

Figure 3.6 Clinopyroxene-melt partition coefficients for Th plotted against $[Na]_{crystal}$ for TUBAS runs. Note rough positive correlation, suggesting that the presence of Na may somehow enhance the incorporation of actinides into the clinopyroxene.

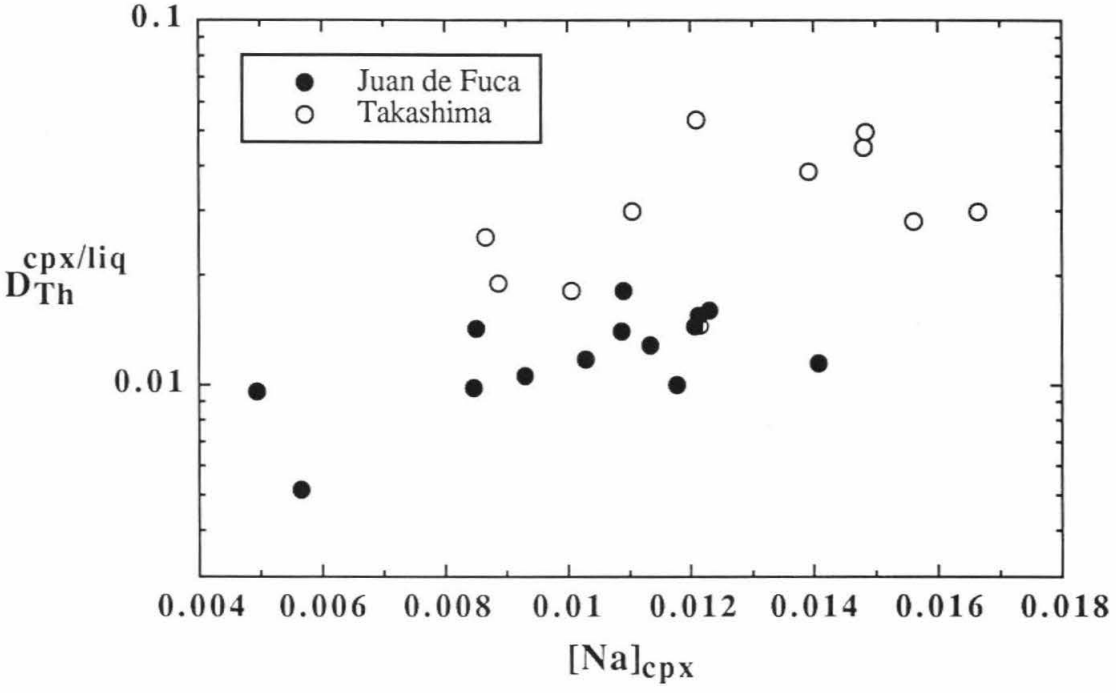
0.1
0.01
Juan de Fuca
Takashima
$D_{Th}^{cpx/liq}$
0.004
0.006
0.008
0.01
0.012
0.014
0.016
0.018
$[Na]_{cpx}$

Figure 3.6

Figure 3.7 Individual crystal clinopyroxene-melt partition coefficients for U as a function of oxygen fugacity for TUBAS runs. (a) $Di_{71}An_{29}$, (b) Juan de Fuca basalt, (c) Takashima basalt. In most cases the same crystals were analyzed for U and Th. Offsets in $-\log fO_2$ are as in Fig. 3.5. The low values illustrate the very incompatible nature of U in clinopyroxene. All compositions show an apparent increase in $D_U^{cpx/liq}$ with decreasing fO_2, which I interpret as resulting from an increase in the proportion of U^{4+} in the melt. Note: The low fO_2 runs for the Juan de Fuca basalt have been reanalyzed since publication of Appendix II, resulting in a slight modification of this figure relative to Fig. 1 of that paper.

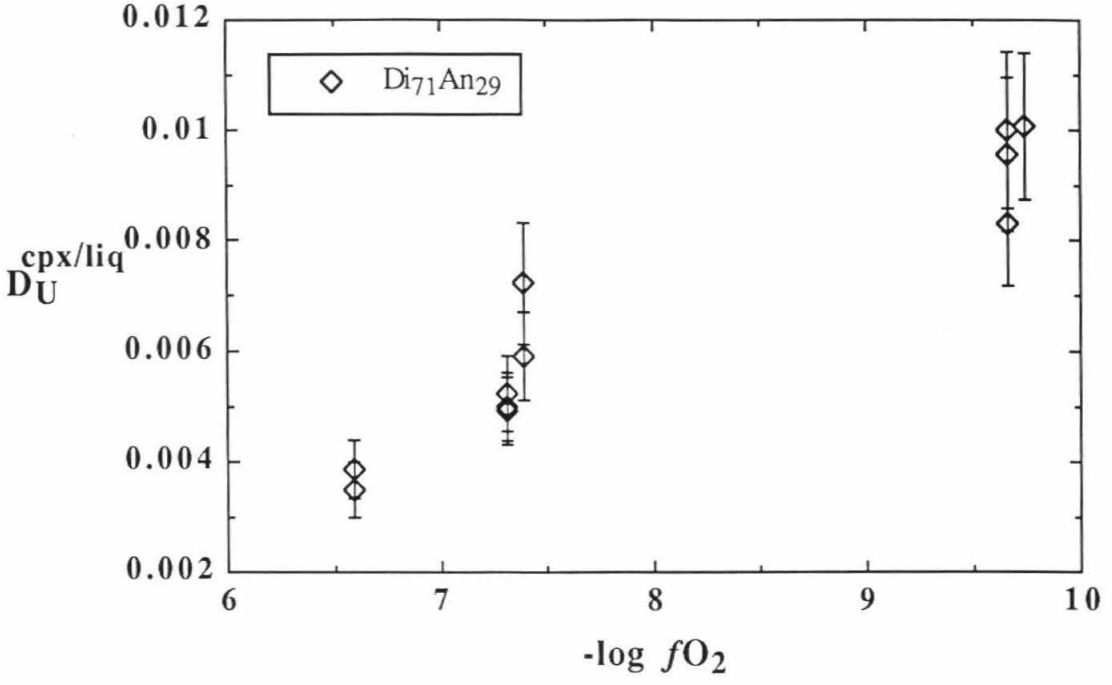
0.012
0.01
0.008
0.006
0.004
0.002
$D_U^{cpx/liq}$
$Di_{71}An_{29}$
6
7
8
9
10
-log fO_2

Figure 3.7a

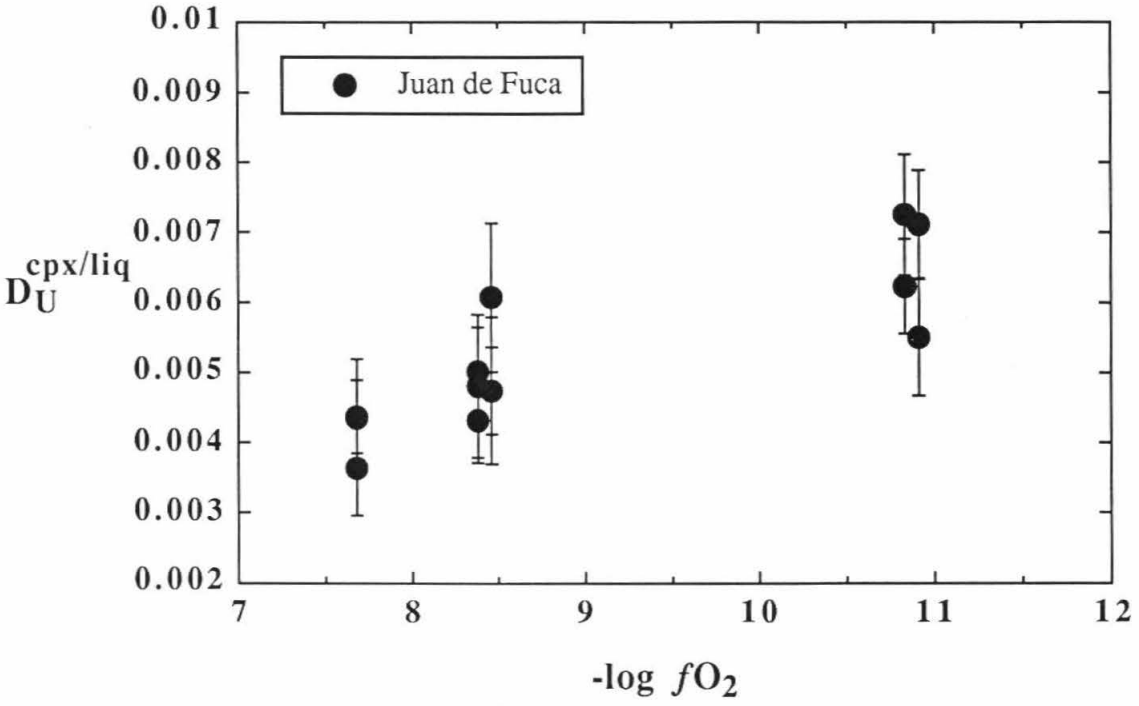
0.01
0.009
0.008
0.007
0.006
0.005
0.004
0.003
0.002
Juan de Fuca
$D_U^{cpx/liq}$
7
8
9
10
11
12
-log fO_2

Figure 3.7b

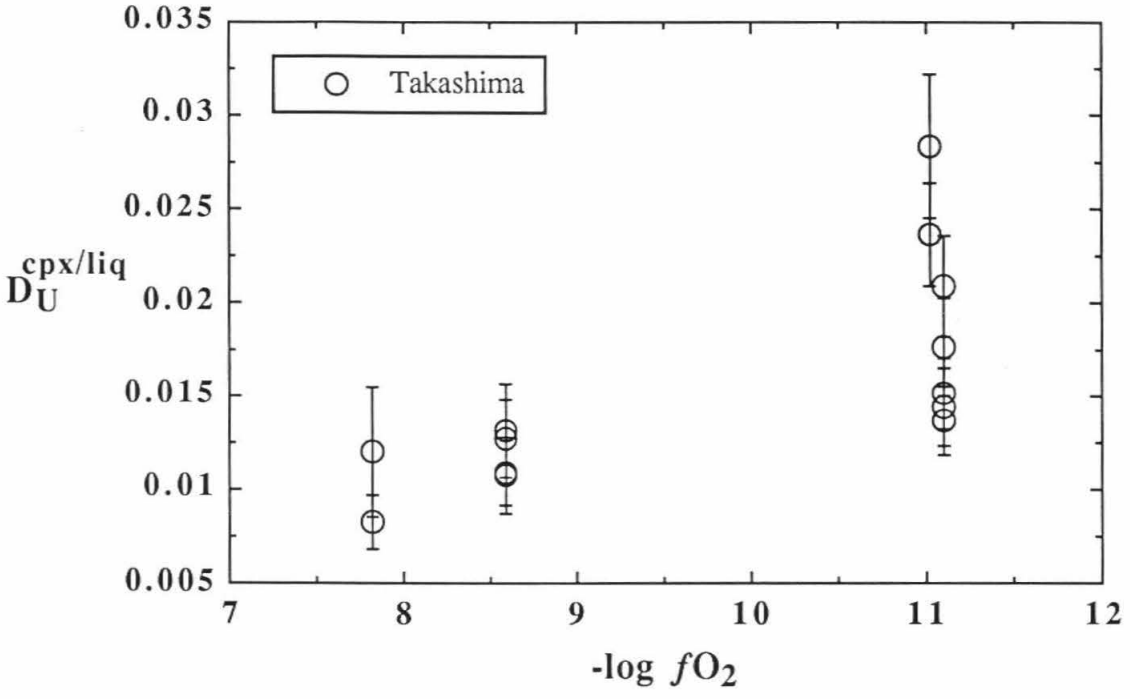
Takashima
0.035
0.03
0.025
0.02
0.015
0.01
0.005
$D_U^{cpx/liq}$
7
8
9
10
11
12
-log fO_2

Figure 3.7c

means, the IW+1 data is 3.5 σ higher than the NNO data. As with Th, $D_U^{cpx/liq}$ for the Takashima basalt (Fig. 3.7c) is consistently larger but also more variable than in the other two compositions, with the variability increasing at IW+1. Even with the scatter, however, $D_U^{cpx/liq}$ appears to increase with decreasing fO_2.

The results for U for all three compositions are consistent with an increase in $D_U^{cpx/liq}$ with decreasing fO_2. I interpret this behavior as a consequence of the fact that clinopyroxene preferentially incorporates U^{4+} over the higher valence states of U. An increase in the relative proportion of U^{4+} with decreasing fO_2 will then lead to an increase in $D_U^{cpx/liq}$. A preference for U^{4+} in clinopyroxene can be understood in terms of established partition coefficient-ionic radius and partition coefficient-charge systematics (e.g., Onuma et al. 1968). These systematics show that trace cations prefer to substitute into crystallographic sites of similar ionic radius and charge as the major cation (e.g., Sr for Ca in plagioclase). Although it has a higher than optimal charge, U in the tetravalent state is closest to Ca^{2+} relative to U^{5+} and U^{6+}. For a given ionic radius, the magnitudes of crystal-melt partition coefficients drop off precipitously as the charge difference between the trace (U) and major (Ca) cation increases. Thus in clinopyroxene, where $D_{Tb^{3+}}^{cpx/liq} \gg D_{Th^{4+}}^{cpx/liq}$, it is inevitable that $D_{U^{4+}}^{cpx/liq} \gg D_{U^{5-6+}}^{cpx/liq}$. The relative proportion of U^{4+} in silicate melts has been shown to increase with decreasing fO_2 (Schreiber 1983; Calas 1979). Therefore, while I have not measured the U valence state distribution in any of my experiments, the observed decrease in $D_U^{cpx/liq}$ with decreasing fO_2 is readily understandable in terms of a change in the U valence state distribution with fO_2, and I am confident that it is real.

In an attempt to estimate the change in $D_U^{cpx/liq}$ as a function of the change in the U redox state, I have estimated U^{4+}/U^{5+} in my experiments using published measurements of the U valence state distribution in similar compositions. By combining expressions for U^{4+}/U^{5+} and $D_U^{cpx/liq}$ as functions of oxygen fugacity, I can estimate the change in $D_U^{cpx/liq}$ with U^{4+}/U^{5+}. Schreiber (1983) has determined U^{4+}/U^{5+} as a function of oxygen fugacity

for quenched melts in the Di-Ab-An system at 1250°C. While I have not made any suitable partition coefficient measurements in this system, I will compare these results to my partitioning experiments in the $Di_{71}An_{29}$ composition. Schreiber's data can be represented by the expression:

$$-\log fO_2 = 12.8 + 5.21(\log R), \quad [1]$$

where $R = U^{4+}/U^{5+}$. A linear fit to the $Di_{71}An_{29}$ data in Fig. 3.7a gives the relation:

$$-\log fO_2 = 4.28 + 565(D_U^{cpx/liq}). \quad [2]$$

Setting these two equations equal to each other and solving for logR results in:

$$\log R = 108(D_U^{cpx/liq}) - 1.64, \quad [3]$$

which can be used to estimate U^{4+}/U^{5+} for any given value of $D_U^{cpx/liq}$. This expression is based only on the measured variations of U^{4+}/U^{5+} and $D_U^{cpx/liq}$ with fO_2 and involves no assumptions other than the two data sets being compatible. $D_U^{cpx/liq}$ is plotted against R in Fig. 3.8. As expected, the U partition coefficient increases with increasing proportion of U^{4+}. If the clinopyroxene accepts only U^{4+}, then $D_U^{cpx/liq}$ should go to zero as the proportion of U^{4+} goes to zero, and the curve in Fig. 3.8 should pass through the origin. This appears to be approximately true, indicating that the change in $D_U^{cpx/liq}$ with fO_2 is largely controlled by the change in the relative proportion of U^{4+}. The fact that U^{4+}/U^{5+} at $D_U^{cpx/liq} = 0$ is slightly greater than zero may arise from the failure of the assumptions that Schreiber's data apply here or that the variation of $D_U^{cpx/liq}$ with $-\log fO_2$ is linear. Also, the increasing presence of hexavalent U under oxidizing conditions (U^{6+} may be more abundant than U^{5+} at $\log fO_2 = -2$) makes the actual proportion of U^{4+} ($U^{4+}/\Sigma U$) much smaller than U^{4+}/U^{5+}.

Note that Schreiber's (1983) data predicts that less than 10% of the U is tetravalent at FMQ (Fig. 3.8). With the assumption that clinopyroxene accepts only U^{4+}, the U partition coefficient can also be expressed as $D_U^{cpx/liq} = (U^{4+}/U^{5+})D_{U^{4+}}^{cpx/liq}$ and the relationship shown in Fig. 3.8 indicates that $D_{U^{4+}}^{cpx/liq} = 0.07$ at FMQ. This value is high compared to $D_{Th}^{cpx/liq}$, which may mean that U^{4+}/U^{5+} is systematically higher in the $Di_{71}An_{29}$

Figure 3.8 Calculated change in $D_U^{cpx/liq}$ with U^{4+}/U^{5+} for crystallization experiments in the $Di_{71}An_{29}$ system. Expressions for $D_U^{cpx/liq}$ as a function of fO_2 (from Fig. 3.7a) and U^{4+}/U^{5+} as a function of fO_2 (from Schreiber 1983) were combined to give: $\log(U^{4+}/U^{5+}) = 108(D_U^{cpx/liq}) - 1.64$. Positive correlation shows that $D_U^{cpx/liq}$ increases with increasing proportion of U^{4+}, supporting the interpretation that clinopyroxene preferentially incorporates U^{4+} over higher valence states of U. Arrow labelled "FMQ" identifies $D_U^{cpx/liq}$ from runs at Fa-Mt-Qz oxygen buffer, and corresponds to $U^{4+}/U^{5+} < 0.1$. Due to the increasing proportion of U^{6+} under oxidizing conditions, the proportion of U^{4+} at the point that the curve passes through $D_U^{cpx/liq} = 0$ is actually much smaller than indicated by U^{4+}/U^{5+}.

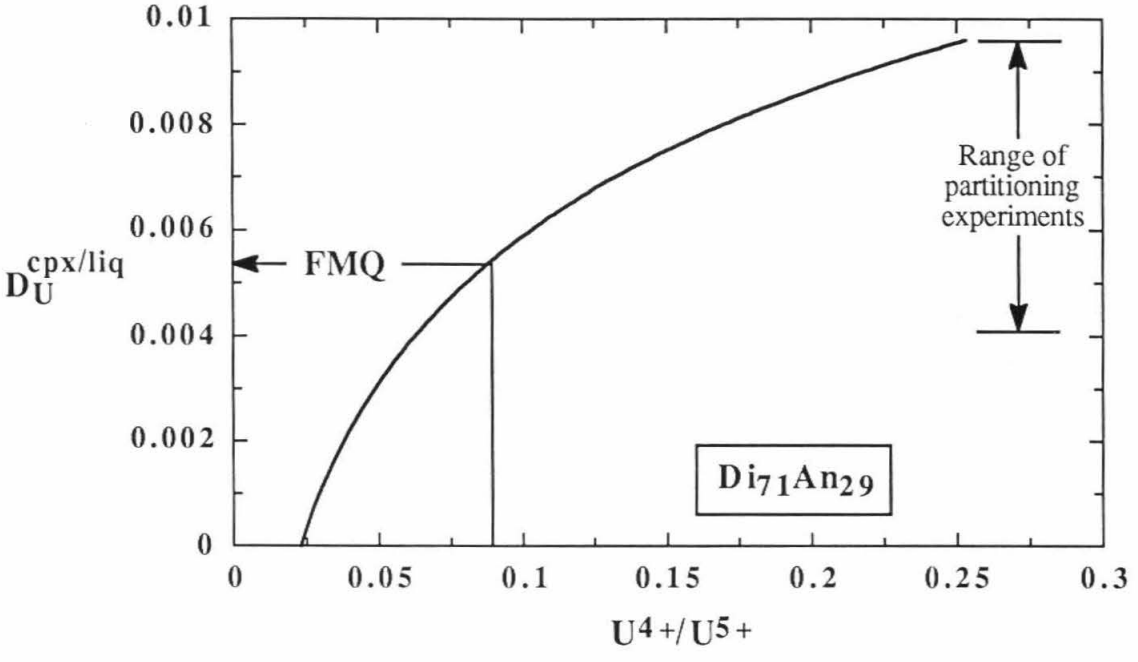
0.01
0.008
0.006
0.004
0.002
0
$D_U^{cpx/liq}$
FMQ
Range of partitioning experiments
$Di_{71}An_{29}$
0
0.05
0.1
0.15
0.2
0.25
0.3
U^{4+}/U^{5+}

Figure 3.8

composition than that of Schreiber (1983). Nonetheless, the relatively large change in $D_U^{cpx/liq}$ with fO_2 indicates that a significant amount of U^{5+} is likely to be present under terrestrial magmatic conditions.

The partition coefficient trends for the Juan de Fuca and Takashima compositions in Fig. 3.7 differ from that for $Di_{71}An_{29}$. This difference should primarily reflect a sensitivity of the U valence state distribution to compositional differences. Calas (1979) has demonstrated that in addition to oxygen fugacity, the U valence state distribution in silicate melts depends strongly on composition. Subsequent studies have shown a specific dependence on the concentrations of other multivalent elements (Schreiber et al. 1987) and a negative correlation of U^{4+}/U^{5+} with (Na + K)/Al in granitic melts (Yudintsev et al. 1990). The latter dependence predicts that $D_U^{cpx/liq}$ should be lowest in the more alkali-rich Takashima basalt, although this is opposite to what I observe. In addition to affecting the valence state distribution of U, compositional variation could affect $D_U^{cpx/liq}$ in other ways as well. For example, the relatively small increase in $D_U^{cpx/liq}$ observed for the Juan de Fuca basalt could also be influenced by the same compositional effect that apparently suppresses $D_{Th}^{cpx/liq}$ in this composition at low fO_2. Such an effect must compete with the increasing proportion of U^{4+} with decreasing fO_2, which should increase the partition coefficient. These competing forces would tend to pull the U partition coefficient in opposite directions, resulting in a relatively small net change in $D_U^{cpx/liq}$ in the different experiments.

Slow Cooling Rate Run

One $Di_{71}An_{29}$ run (D2-TUBAS-N) was cooled at 0.1°C/hr, more than an order of magnitude more slowly than the rest. No published crystallization experiments have been run at this low a cooling rate. The U and Th partition coefficients measured in this run are systematically lower than the runs of the same composition and fO_2 cooled at 1.7°C/hr, indicating that there may be some dependence of partition coefficients on cooling rate

(Table 3.3). The individual crystal values are self-consistent within 1 σ, and the difference between this and the higher cooling rate runs appears to be real. The crystals from this run are no different in appearance from the others, and aside from having slightly less Al_2O_3, have the same major element composition. Thus, the difference in partition coefficients most likely results from a closer approach to interfacial equilibrium in the slower cooling rate run. This is especially likely given that the fractional decreases are nearly identical for both U and Th, resulting in $D_{Th}^{cpx/liq}/D_{U}^{cpx/liq}$ that is indistinguishable from the 1.7°C/hr experiments at the same fO_2. This indicates that, despite evidence for melt homogeneity and major element equilibration in the 1.7°C/hr runs, there were still deviations from equilibrium for U and Th. A likely cause for such deviations is that U and Th were enriched in the melt adjacent to the crystal-melt interface as a result of crystal growth outpacing diffusion of these elements in the melt. An alternative explaination is that U and Th remained homogeneous in all runs, but their partition coefficients increase with the Al_2O_3 content of the crystal. The higher actinide partition coefficients in the 1.7°C/hr runs would thus result from Al_2O_3-rich boundary layers leading to increased Al_2O_3 contents. In either case, there appears to be no practical alternative to circumvent this problem: because of the extremely slow diffusion of trace elements in clinopyroxene, isothermal experiments would require about 9 months to equilibrate a 20 μm crystal, the smallest practical size for SIMS analysis.

The relatively well behaved partitioning behavior of U and Th in the 1.7°C/hr experiments indicates that, despite deviations from interfacial equilibrium, a pseudo-steady state existed and that the response of the partition coefficients to factors such as fO_2 and composition can be understood in terms of valence state distributions, substitution mechanisms, and other equilibrium effects.

Adopted Partition Coefficient Values

As noted above, in some cases is there is variability in the U and Th partition coefficients, even within a single run, that is beyond the designated errors. It is possible that some of the observed partition coefficient variability is due to changes in the partition coefficients with temperature during crystallization. In principle all crystals nucleate at the liquidus and grow over the same temperature range, so such an effect would affect all crystals equally. In reality, although the majority of crystals are of similar size, crystal size does vary, and it is possible that crystals nucleate over a range in temperature. However, the temperature range over which crystals were grown is quite small (Table 2.2), and in addition, my particle track measurements are only made on the central regions of the larger crystals, further filtering any temperature effects. Another possible effect of temperature is to change the U valence state distribution in the melt as crystallization proceeds. This could conceivably be a fairly large effect (the data of Schreiber (1983) indicate that U^{4+}/U^{5+} could decrease by 40% over the temperature range of my experiments), but while it may affect the U data, there is no equivalent mechanism for the Th variations. Thus, temperature variations can only play a minor role in accounting for the partition coefficient variations.

None of the crystals synthesized in this study are morphologically anomalous, and I made a conscious effort to only analyze the largest, most euhedral crystals. However, in light of the systematically lower partition coefficients from the slow cooling rate run, much of the partition coefficient variation in the 1.7°C/hr runs is likely due to variations in the approach to interfacial equilibrium, e.g., fluctuations of boundary layers from steady-state during crystal growth. As previously noted, deviations from interfacial equilibrium will make the measured U and Th partition coefficients high, and in such a case the lower values would best approximate the equilibrium values. Thus it is possible that the lower values of $D_{Th}^{cpx/liq}$ in the Juan de Fuca basalt at IW+1 reflect a closer approach to

equilibrium, with the higher values at the higher fO_2s being caused by relatively greater non-equilibrium effects. This implies that the low fO_2 somehow induces a closer approach to equilibrium, or that a closer approach to equilibrium in the lower fO_2 Juan de Fuca runs was simply fortuitous. While these possibilities cannot be ruled out, I know of no plausible reason why low fO_2 should be special in this regard. Thus, to allow for an fO_2 dependent compositional control on $D_{Th}^{cpx/liq}$, I treat $D_{Th}^{cpx/liq}$ at each fO_2 separately.

The results of the 0.1°C/hr experiment represent the closest approach to equilibrium. Nonetheless, as discussed above, it is very likely that the systematic partition coefficient variations with composition and especially with fO_2 in the 1.7°C/hr experiments are real. In order to examine the extent of these variations, I must adopt a single value for each composition and fO_2 from the 1.7°C/hr data. The simplest option is to take the average. However, if there is a very large spread in the data for a given composition and fO_2, an average may not be appropriate because boundary layer fluctuations will increase the measured partition coefficient. In order to weight the lower end of the distributions, I took the averages of all crystals of a given composition and fO_2 that plot within 2 σ of the crystal with the lowest value. These are listed in Table 3.6. Only in the case of the Takashima basalt at IW+1 are these values significantly different from the straight averages. Assuming that the average degree of disequilibrium in the 1.7°C/hr experiments is the same for all three compositions, the differences between these values illustrate compositional effects. To estimate the equilibrium value for each composition and fO_2, I have systematically multiplied the values in Table 3.6 by 0.57, the ratio of the partition coefficients from the 0.1 and 1.7°C/hr experiments (same for both U and Th). These values are listed in Table 3.7. They are my best estimates of the equilibrium U and Th clinopyroxene-melt partition coefficients, and retain all of the compositional and fO_2 variation observed in the 1.7°C/hr experiments.

TABLE 3.6

Summary of Clinopyroxene-Melt U and Th Partition Coefficients From 1.7°C/hr Experiments

Composition	fO_2	$D_U^{cpx/liq}$	±	$D_{Th}^{cpx/liq}$	±	$D_{Th}^{cpx/liq}/D_U^{cpx/liq}$	±
$Di_{71}An_{29}$							
	NNO	0.00368	0.00019[a]	0.0121	0.0009	3.3	0.3[b]
	FMQ	0.0057	0.0010	0.0124	0.0017	2.2	0.5
	IW+1	0.0095	0.0008	0.012	0.003	1.3	0.3
Juan de Fuca							
	NNO	0.0041	0.0003	0.014	0.002	3.4	0.5
	FMQ	0.0050	0.0006	0.0123	0.0018	2.5	0.5
	IW+1	0.0065	0.0008	0.008	0.003	1.2	0.5
Takashima							
	NNO	0.0101	0.0019	0.020	0.007	2.0	0.8
	FMQ	0.0119	0.0011	0.037	0.006	3.1	0.6
	IW+1	0.016	0.003	0.019	0.004	1.2	0.3

(a) Error is the sample standard deviation
(b) Error of ratio is the propagated error of D_U and D_{Th} from first two columns

TABLE 3.7

Adopted Clinopyroxene-Melt Partition Coefficients for U and Th[a]

Composition	fO_2	$D_U^{cpx/liq}$	±	$D_{Th}^{cpx/liq}$	±	$D_{Th}^{cpx/liq}/D_U^{cpx/liq}$	±
$Di_{71}An_{29}$							
	NNO	0.00210	0.00011[b]	0.0069	0.0005	3.3	0.3[c]
	FMQ	0.0032	0.0006	0.0071	0.0010	2.2	0.5
	IW+1	0.0054	0.0005	0.0068	0.0017	1.3	0.3
Juan de Fuca							
	NNO	0.00234	0.00017	0.0080	0.0011	3.4	0.5
	FMQ	0.0029	0.0003	0.0070	0.0010	2.4	0.4
	IW+1	0.0037	0.0005	0.0046	0.0017	1.2	0.5
Takashima							
	NNO	0.0058	0.0011	0.011	0.004	2.1	0.8
	FMQ	0.0068	0.0006	0.021	0.003	3.1	0.6
	IW+1	0.0091	0.0017	0.011	0.002	1.2	0.3

(a) Values are derived from Table 3.6 by scaling for results of 0.1°C/hr experiment (see text)
(b) Error is the sample standard deviation
(c) Error of ratio is the propagated error of D_{Th} and D_U from first two columns

$D_{Th}^{cpx/liq}/D_{U}^{cpx/liq}$

One very important aspect of these partition coefficient measurements is that both the inter-crystal and inter-run variations in $D_{Th}^{cpx/liq}$ and $D_{U}^{cpx/liq}$ are correlated (i.e., the crystals with lower $D_{Th}^{cpx/liq}$ also have lower $D_{U}^{cpx/liq}$). Such a correlation would be expected for any of the variability mechanisms discussed above, and the result is that much of the variation in the 1.7°C/hr partition coefficients cancels in their ratio, most noticeably at low fO_2 (Fig. 3.9). This correlation is even more strongly confirmed by the results of the 0.1°C/hr experiment, which give $D_{Th}^{cpx/liq}/D_{U}^{cpx/liq}$ equal to those for the 1.7°C/hr runs, despite a decrease in both partition coefficients (Fig. 3.9a). This correlation is evidence that $D_{Th}^{cpx/liq}/D_{U}^{cpx/liq}$, which gives a measure of the degree of U-Th fractionation possible by clinopyroxene-melt partitioning, is more reliably determined than either partition coefficient separately. While there is still some residual scatter in the data, the spread is less than for the individual partition coefficients. All values for $D_{Th}^{cpx/liq}/D_{U}^{cpx/liq}$ for a given composition and fO_2 agree to within 2 σ of the weighted mean for that fO_2, and for the $Di_{71}An_{29}$ composition the values agree to within 1 σ.

Several other observations in Fig. 3.9 deserve noting. First, over the range of fO_2s studied, $D_{Th}^{cpx/liq} > D_{U}^{cpx/liq}$. This establishes that Th is more compatible than U in clinopyroxene for the compositions studied, and thus that a coexisting melt must be enriched in U relative to Th. The second important observation is that as fO_2 decreases, $D_{Th}^{cpx/liq}/D_{U}^{cpx/liq}$ decreases by up to a factor of three. This decrease results primarily from the increase in $D_{U}^{cpx/liq}$, and demonstrates that the degree of U-Th fractionation generated by crystal-melt partitioning is fO_2 dependent. $D_{Th}^{cpx/liq}/D_{U}^{cpx/liq}$ is also approximately independent of composition (Fig. 3 in Appendix II). These observations suggest that U^{4+} and Th^{4+} may be almost indistinguishable in silicate melt-crystal systems, and that the main reason $D_{Th}^{cpx/liq} > D_{U}^{cpx/liq}$ is that U exists in three valence states, only one of which enters the clinopyroxene, while all Th is tetravalent. I cannot make any quantitative arguments

Figure 3.9 $D_{Th}^{cpx/liq}/D_{U}^{cpx/liq}$ plotted against oxygen fugacity for crystals shown in Figs. 3.5 and 3.7. (a) $Di_{71}An_{29}$, (b) Juan de Fuca basalt, (c) Takashima basalt. Offsets in -logfO_2 are as in Fig. 3.5. The error bars represent the formally propagated 1σ errors of the individual Th and U partition coefficients. Much of the variation in Figs 3.5 and 3.7, especially in the low fO_2 runs, is gone because $D_{Th}^{cpx/liq}$ and $D_{U}^{cpx/liq}$ are correlated. The decrease with increasing fO_2 is due primarily to the increase in $D_{U}^{cpx/liq}$. Note that $D_{Th}^{cpx}/D_{U}^{cpx} > 1$ in all cases, showing that U-Th fractionation by clinopyroxene-liquid partitioning during partial melting will result in a liquid has Th/U less than the clinopyroxene in its source.

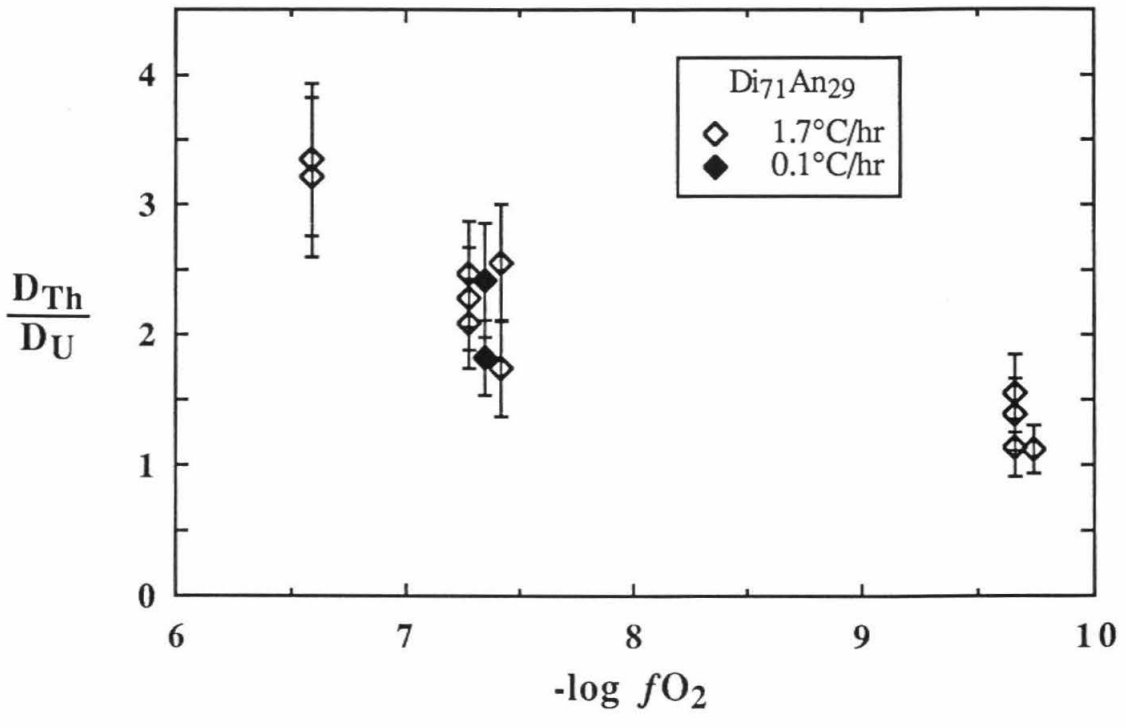

Figure 3.9a

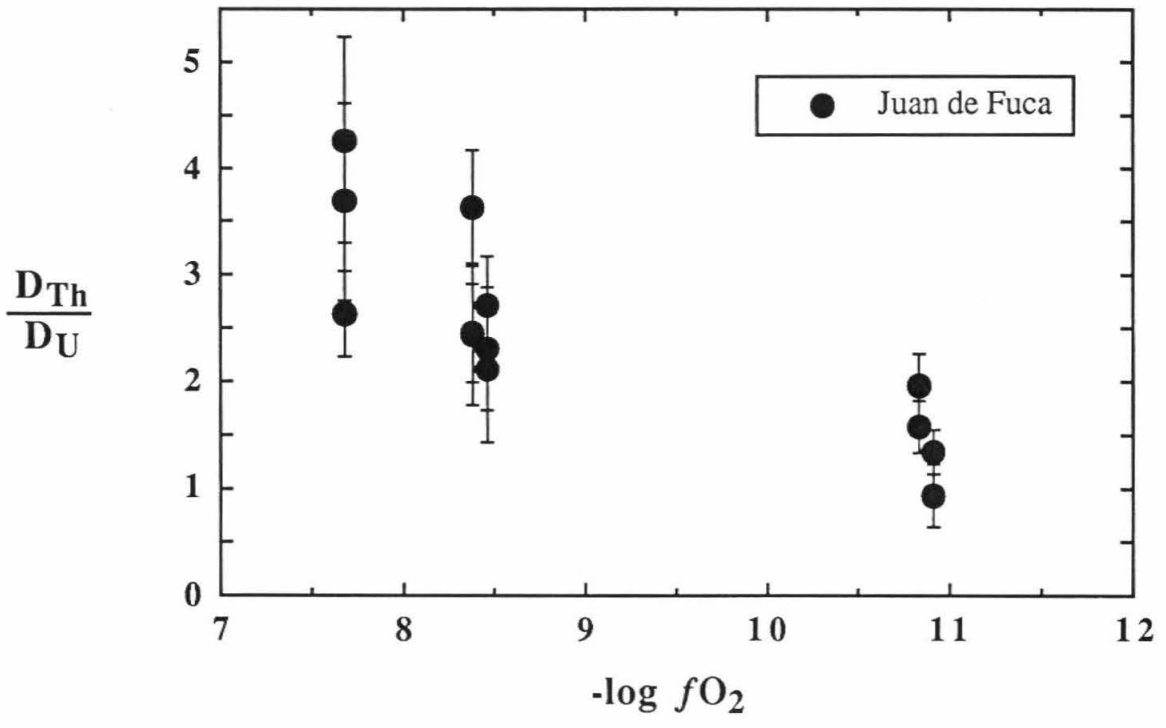

Figure 3.9b

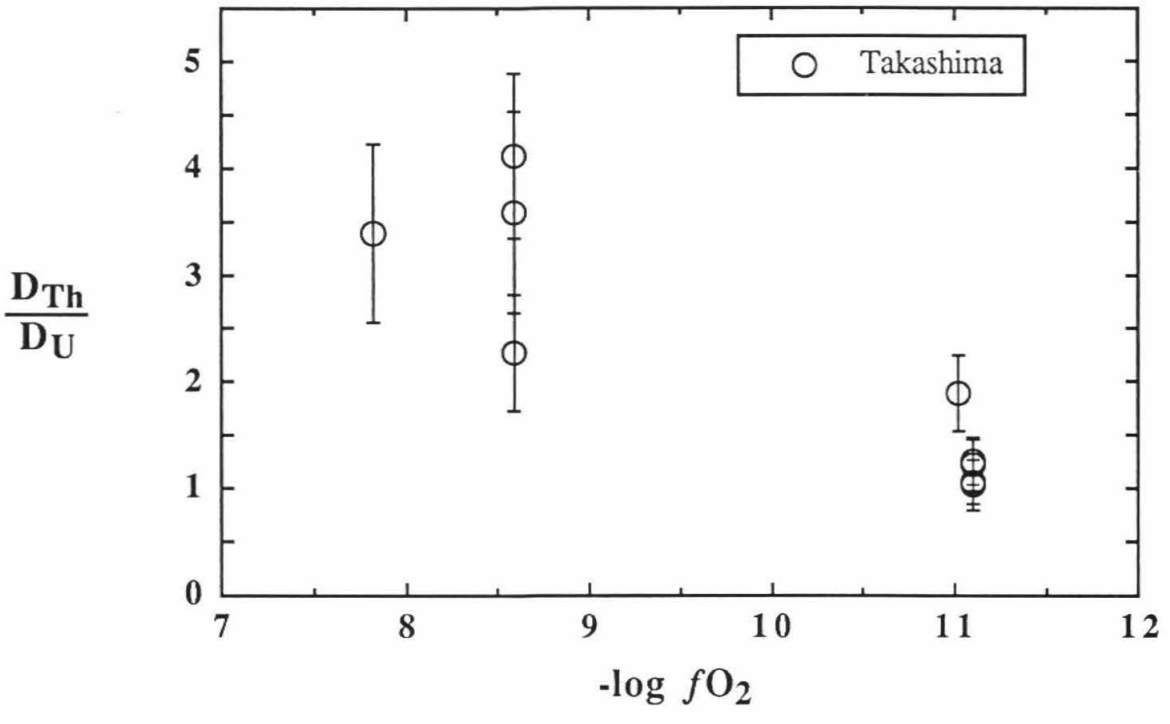

Figure 3.9c

without actually measuring the U valence state distribution in the experiments, but it remains as an interesting possibility.

3.1.6.2 YULO Runs

Prior to the TUBAS experiments, a preliminary set of clinopyroxene crystallization experiments, initiated by Mary Johnson, were run in order to test the hypothesis that $D_U^{cpx/liq}$ should be sensitive to fO_2 within the range of fO_2s relevant to solar system magmatic processes. The starting composition, YULO (yellow uranium-low), was a synthetic $Ab_{25}An_{25}Di_{50}$ glass spiked with 50 ppm ^{235}U and no Th. The procedure used to prepare this composition, the crystallization method, and the microprobe and U fission track analyses were the same as for the D2 composition (T_i = 1278°C, T_l = 1265°C, T_f = 1200°C, cooling rate = 1.7°C/hr). The fO_2 in most runs was controlled by CO-CO_2 mixtures; the lowest fO_2 runs were made in graphite capsules in a pure CO atmosphere. All runs consist of clinopyroxene and quenched melt, and some runs produced anorthitic plagioclase crystals as well. While all runs extended into the plagioclase stability field, plagioclase crystallization is normally not observed for $Ab_{25}An_{25}Di_{50}$. However, all runs show major Na-loss, which may facilitate plagioclase crystallization.

Clinopyroxene-melt partition coefficients for U from the YULO experiments are plotted against -logfO_2 in Fig. 3.10. While the quality of this data is lower than that of the more comprehensive TUBAS experiments, it is sufficient to study the behavior of U partitioning over a wide range in fO_2. The data display an apparent increase in $D_U^{cpx/liq}$ with decreasing fO_2, although the scatter precludes a firm conclusion about whether $D_U^{cpx/liq}$ continues to increase below logfO_2 = -12. The most obvious interpretation of this increase is that it results from an increase in the proportion of U^{4+} in the system with decreasing fO_2.

The fO_2s of these experiments span from those of terrestrial basalts down to solar nebula conditions. By analogy with La (same charge and similar ionic radius; see section *4.3*), a partition coefficient of ≈ 0.07 is expected for purely trivalent U. This is such a

Figure 3.10 Individual crystal clinopyroxene-melt partition coefficients for U from YULO experiments plotted against oxygen fugacity. fO_2s extend to more reducing conditions than TUBAS runs. Results show an apparent increase in $D_U^{cpx/liq}$ with decreasing fO_2.

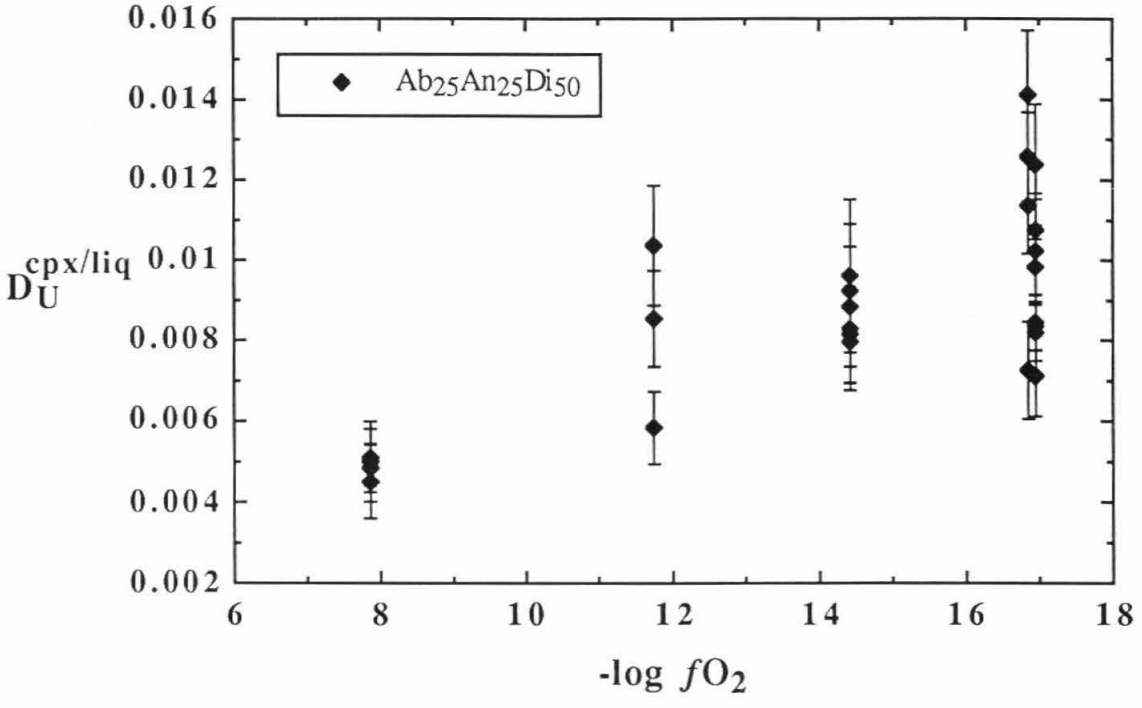
0.016
0.014
0.012
0.01
0.008
0.006
0.004
0.002
$D_U^{cpx/liq}$
$Ab_{25}An_{25}Di_{50}$
6
8
10
12
14
16
18
-log fO_2

Figure 3.10

large increase that even a small amount of trivalent U should cause a significant change in $D_U^{cpx/liq}$. The absence of a large increase in the reducing runs argues that most of the U was tetravalent, but 10% U^{3+} at the lowest fO_2 cannot be ruled out.

To be sure that the apparent increase in $D_U^{cpx/liq}$ with decreasing fO_2 is due to the change in the U valence state distribution, the experiments should ideally be identical in all other ways. However, the Al_2O_3 content of the crystals in these runs appears to increase with decreasing fO_2 as well, resulting in a new variable (Fig. 3.11). In the initial phases of this study this was a concern, as Al_2O_3 nominally should not change with fO_2 in this system. The observation that it does change suggests that factors other than changes in the valence state distribution may contribute to changes in the U partition coefficient with fO_2.

The reason for the increase in Al_2O_3 with decreasing fO_2 is unknown; it does not occur in the TUBAS experiments. One possibility is that the Al partition coefficient increases with decreasing temperature, and that at low fO_2 there was some super-cooling of the melt and the crystals nucleated and grew during a lower temperature portion of the cooling range. Alternatively, an increasing proportion of oxygen vacancies with decreasing fO_2 could affect the crystal stoichiometry. Increasing oxygen vacancies would lead to a positive charge excess and thus may favor substitution of Al^{3+} for Si^{4+} in the tetrahedral site. This latter effect can be quite important in perovskites (Smyth 1989), with large deviations from stoichiometry resulting in separate, oxygen-deficient layers in the crystal structure. Whatever the reason, it is possible that the change in $D_U^{cpx/liq}$ with fO_2 is also due to these effects, in which case the valence state distribution may not be the primary control on U partitioning. However, the relatively small change in Al_2O_3 and temperature compared to the factor of three increase in $D_U^{cpx/liq}$ argues that the U redox state is the dominant control. Thus, while U partitioning may be very sensitive to compositional effects, changes in $D_U^{cpx/liq}$ with fO_2 for a given composition are predominantly controlled by changes in the valence state distribution of U. This conclusion is supported by the results of the TUBAS runs.

Figure 3.11 Variation of Al_2O_3 with oxygen fugacity for clinopyroxene crystals from YULO experiments. Each point represents the mean value of the crystals from a single run, and the error bar represents the total range of Al_2O_3 concentrations. There appears to be a slight positive trend, indicating that the Al_2O_3 concentration may depend on fO_2.

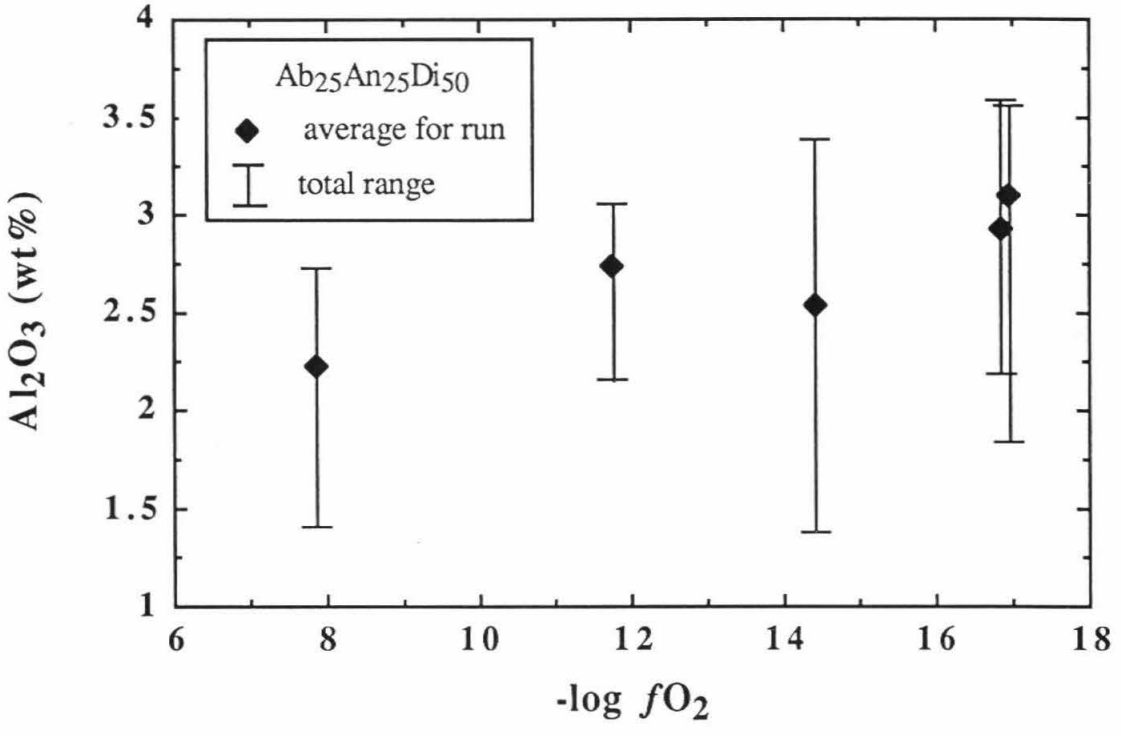
Ab25An25Di50
average for run
total range
Al2O3 (wt%)
-log fO2
4
3.5
3
2.5
2
1.5
1
6
8
10
12
14
16
18

Figure 3.11

$D_U^{cpx/liq}$ for the Na-bearing YULO composition appears to be slightly lower than for the Na-free $Di_{71}An_{29}$ at the same fO_2 (see Fig. 3.7a). This indicates that, despite evidence for actinide partition coefficients being influenced by the Na content (e.g., the correlation shown in Fig. 3.6 and the discussion in the following section), other compositional factors must also play a role.

3.2 Compositional Dependence of Actinide Partitioning in Clinopyroxene

3.2.1 Clinopyroxene Substitution Mechanisms for the Actinides

Although I did not set out to rigorously determine the compositional dependence of crystal-melt actinide partitioning, the compositional variation among the three different starting materials for the clinopyroxene crystallization experiments allows me to make an approximate compositional analysis. Several important details such as the location of the actinide ions in the clinopyroxene, the valence state distribution of U in the melt and clinopyroxene, and the effect of the change in temperature during crystallization have not been determined and are bound to affect the results. For example, as the actinides are highly incompatible, changes in the density of lattice defects or vacancies may contribute to the observed variation in actinide partition coefficients. Also, the compositional range of my samples is quite small compared to the range in magma and clinopyroxene compositions found in nature, so the resolution is limited. Given these considerations, the results should not be considered definitive and can be taken as aids in determining a more rigorous compositional dependence.

I have chosen to model the incorporation of actinides into clinopyroxene with a cationic substitution reaction. There are no independent data to confirm that this is correct, but the results of the model are consistent with such a mechanism. Electron paramagnetic resonance measurements suggest that Gd^{3+} resides in the M2 (Ca) site in diopside (Morris 1975). The ionic radii of eight-fold coordinated U^{4+}, or U_{VIII}^{4+}, and Th_{VIII}^{4+} (1.00 and 1.05 Å, respectively; Shannon 1976), are comparable to that of Gd_{VIII}^{3+} (1.053 Å), suggesting

that the actinides may also substitute into the M2 site. U^{5+}_{VII} and U^{6+}_{VIII} (0.84 and 0.86 Å) are much smaller than Ca^{2+}_{VIII} (1.12 Å) and thus are unlikely substitutes. The radii of U^{5+}_{VI} and U^{6+}_{VI} (0.76 Å and 0.73 Å) are comparable to that of Mg^{2+}_{VI} (0.72 Å), but their higher charges would require increasingly complicated coupled substitutions. Thus, in accordance with the partition coefficient-ionic radius and partition coefficient-charge systematics of Onuma et al. (1968), U^{4+} is likely to be the only important valence state of U incorporated into clinopyroxene. The observed increase in $D_U^{cpx/liq}$ with decreasing fO_2 (Fig. 3.7) also suggests that clinopyroxene prefers lower valence states of U over higher ones. With these constraints, I considered coupled substitutions of the form:

$$3Ca^{M2} \Leftrightarrow (U,Th)^{M2} + 2Na^{M2}$$

$$Ca^{M2} + Al^{M1} + Si^{T} \Leftrightarrow (U,Th)^{M2} + (Mg,Fe)^{M1} + Al^{T}$$

$$Ca^{M2} + 2Si^{T} \Leftrightarrow (U,Th)^{M2} + 2Al^{T}$$

$$Ca^{M2} + Ti^{M1} \Leftrightarrow (U,Th)^{M2} + (Mg,Fe)^{M1}$$

and the exchange reactions I considered are:

(1) $Ca_3(Mg,Fe)_3Si_6O_{18}^{pyx} + (U,Th)O_2^{liq} + 2NaO_{1/2}^{liq} \Leftrightarrow$

$$(U,Th)Na_2(Mg,Fe)_3Si_6O_{18}^{pyx} + 3CaO^{liq}$$

(2) $CaAlAlSiO_6^{pyx} + (U,Th)O_2^{liq} + (Mg,Fe)O^{liq} \Leftrightarrow$

$$(U,Th)(Mg,Fe)Al_2O_6^{pyx} + CaO^{liq} + SiO_2^{liq}$$

(3) $Ca(Mg,Fe)Si_2O_6^{pyx} + (U,Th)O_2^{liq} + 2AlO_{3/2}^{liq} \Leftrightarrow$

$$(U,Th)(Mg,Fe)Al_2O_6^{pyx} + CaO^{liq} + 2SiO_2^{liq}$$

(4) $CaTiAl_2O_6^{pyx} + (U,Th)O_2^{liq} + (Mg,Fe)O^{liq} \Leftrightarrow$

$$(U,Th)(Mg,Fe)Al_2O_6^{pyx} + CaO^{liq} + TiO_2^{liq}$$

All of these reactions are possible for the basalts, while only (2) and (3) are available options for the synthetic $Di_{71}An_{29}$ composition. This may be part of the reason for the smaller partition coefficients in this composition.

To get a better understanding of the compositional dependence of actinide partitioning, it is useful to determine an equilibrium constant for the exchange reaction. For

reaction (1) this can be expressed as: $K_1 = \frac{(a^{liq}_{CaO})^3(a^{pyx}_{U;Thp})}{(a^{liq}_{NaO_{1/2}})^2(a^{pyx}_{Di})(a^{liq}_{U;ThO_2})}$, where $a^{pyx}_{U;Thp}$ is the activity of the actinide-bearing pyroxene component in the clinopyroxene. Given activity-composition relationships for the melt and clinopyroxene components, the equilibrium constant can be evaluated. I have assumed ideal mixing in the melt ($a^{liq}_i = X^{liq}_i$, where X_i = mole fraction); application of the two lattice melt structure model of Nielsen (1985) does not improve the internal consistency of my data. In deriving activity-composition relationships in the clinopyroxenes I have assumed ideal random mixing of cations separately on the M2, M1, and T lattice sites. This assumption has been shown to be a good approximation for aluminous clinopyroxenes (Cohen 1986). The derivation is given in Appendix 3.4 and follows the treatment in Beckett et al. (1990).

Equations [A12], [A14], and [A8] from Appendix 3.4 can be combined to calculate ideal activities of the end-member pyroxene components and the equilibrium constants for the exchange reactions can be evaluated. For reaction (1) I get:

$$a_{Di} = \frac{1}{64}(X_{Di} + X_{CaTs} + X_{Hd} + X_{TiA})^3(X_{Di} + X_{En} + X_{U,Thp})^3(2 - 2X_{TiA} - X_{CaTs})^6$$

$$a_{U,Thp} = \frac{1}{1728}X_{U,Thp}(3X_{Jd} + 2X_{U,Thp})^2(X_{Di} + X_{En} + X_{U,Thp})^3(2 - 2X_{TiA} - X_{CaTs})^6.$$

Noting that $X_{U,Thp}$ is much smaller than any other mole fraction, the equilibrium constant is:

$$K_1 = \frac{(X^{liq}_{CaO})^3}{(X^{liq}_{NaO_{1/2}})^2}\,\frac{X_{U;Thp}}{X^{liq}_{U;ThO_2}}\,\frac{(X_{Jd})^2}{3(X_{Di} + X_{CaTs} + X_{Hd} + X_{TiA})^3}. \qquad [16]$$

To make equation [16] more useful, the mole fraction of actinides in the crystal and melt can be written in terms of the crystal-melt partition coefficient. At this point, however, the valence state distribution in the melt must be addressed. For Th, which is all tetravalent, we have simply

$$\frac{X_{Thp}}{X^{liq}_{ThO_2}} = \emptyset_{Th} D^{cpx/liq}_{Th}. \qquad [17]$$

where $\emptyset_{Th}$ is the conversion from a mole fraction ratio to a concentration ratio for Th, i.e.,

$\frac{X_{Thp}}{X^{liq}_{ThO_2}} = \emptyset_{Th}\frac{C^{cpx}_{Th}}{C^{liq}_{Th}}$, where C is the concentration in weight fraction. For the very small U and Th partition coefficients, Ø can be considered constant and is essentially compositionally independent. For U, the partition coefficient is the ratio of the concentration of U in the crystal, which is assumed to be all tetravalent, to the U concentration in the melt, which includes varying amounts of U^{5+} and U^{6+}, neither of which are included in the exchange reactions. Thus, in order to include $D_U^{cpx/liq}$ in equation [16], I need an expression for the fraction of U^{4+} in the melt (F_{U4+}). F_{U4+} could be estimated from the U valence state distribution data of Schreiber (1983), but, as was shown in section *3.1.6.1*, the compositional differences between the two data sets cast doubt on their compatibility. An alternative is to assume that only U^{4+} is partitioned into the clinopyroxene and that the change in $D_U^{cpx/liq}$ with fO_2 is proportional the change in F_{U4+}. This can be expressed as:

$$D_U^{cpx/liq} = CF_{U4+}, \qquad [18]$$

where $C = D_{U^{4+}}^{cpx/liq}$ (i.e., $\frac{[U^{4+}]^{cpx}}{[U^{4+}]^{liq}}$) and is assumed to be independent of fO_2 and constant for a given composition. Note that equations [3] and [18] relate $D_U^{cpx/liq}$ to the proportion of U^{4+} in the melt in different forms. The difference stems from the assumptions used. In deriving equation [3] I assumed that Schreiber's (1983) and the $Di_{71}An_{29}$ partitioning data were compatible but I assumed nothing about the variation of $D_U^{cpx/liq}$ with fO_2. Equation [18] is for $D_{U^{5-6+}}^{cpx/liq} = 0$. As long as $D_{U^{4+}}^{cpx/liq}$ is independent of fO_2 and constant for a given composition equation [18] is appropriate here because I never have to actually calculate $D_{U^{4+}}^{cpx/liq}$. This avoids any problems with comparing incompatible data sets. It is possible that $D_{U^{4+}}^{cpx/liq}$ varies slightly with fO_2 as a result of variable Na- or Fe-loss, in which case equation [18] would not be completely accurate. However, based on the previous comparison with Schreiber's (1983) U valence state data, the observed change in $D_U^{cpx/liq}$ with fO_2 is comparable to what would be expected as a result of the change in F_{U4+}, indicating that to a first approximation this change can be used to calculate F_{U4+}. A linear

fit through the data in Fig. 3.7 gives $D_U^{cpx/liq}$ as a function of fO_2 for each composition, and can be expressed as:

$$D_U^{cpx/liq} = -(\log fO_2)/A - B, \qquad [19]$$

where A and B are constants. A and B for each composition are listed below.

Takashima: $A_T = 190$, $B_T = 0.0323$

Juan de Fuca: $A_J = 1406$, $B_J = 0.00116$

$Di_{71}An_{29}$: $A_{D2} = 565$, $B_{D2} = 0.00758$

Equations [18] and [19] can then be combined to give $F_{U^{4+}}$ as a function of fO_2:

$$F_{U^{4+}} = [-(\log fO_2)/A - B]/C. \qquad [20]$$

With equation [20], $D_U^{cpx/liq}$ can be inserted into the expression for the equilibrium constant by means of the relation:

$$\frac{X_{Up}}{X_{UO_2}^{liq}} = \frac{\emptyset_U D_U^{cpx/liq}}{F_{U^{4+}}}$$

$$= \frac{C\emptyset_U D_U^{cpx/liq}}{-(\log fO_2)/A - B}. \qquad [21]$$

Thus, substituting [17] into [16] for Th and [21] into [16] for U gives:

$$K_{1_{Th}} = \emptyset_{Th} D_{Th}^{cpx/liq} \frac{(X_{CaO}^{liq})^3}{(X_{NaO_{1/2}}^{liq})^2} \frac{(X_{Jd})^2}{3(X_{Di} + X_{CaTs} + X_{Hd} + X_{TiA})^3}; \qquad [22a]$$

$$K_{1_U} = \frac{C\emptyset_U D_U^{cpx/liq}}{-(\log fO_2)/A - B} \frac{(X_{CaO}^{liq})^3}{(X_{Na_2O}^{liq})} \frac{(X_{Jd})^2}{3(X_{Di} + X_{CaTs} + X_{Hd} + X_{TiA})^3}. \qquad [22b]$$

Finally, solving for D gives:

$$D_{Th}^{cpx/liq} = \frac{3K_{1_{Th}}}{\emptyset_{Th}} \frac{(X_{NaO_{1/2}}^{liq})^2}{(X_{CaO}^{liq})^3} \frac{(X_{Di} + X_{CaTs} + X_{Hd} + X_{TiA})^3}{(X_{Jd})^2}; \qquad [23a]$$

$$D_U^{cpx/liq} = \frac{3K_{1_U}[-(\log fO_2)/A - B]}{C\emptyset_U} \frac{(X_{NaO_{1/2}}^{liq})^2}{(X_{CaO}^{liq})^3} \frac{(X_{Di} + X_{CaTs} + X_{Hd} + X_{TiA})^3}{(X_{Jd})^2}. \qquad [23b]$$

At a fixed temperature and pressure, equations [23a-b] describe the compositional

dependence of clinopyroxene-melt actinide partitioning according to reaction (1) for the compositions I studied. I cannot determine the dependence of the equilibrium constant, K_1, on temperature or pressure with my data, so this expression does not take into account the "thermodynamic" effect of temperature and pressure (i.e., that contribution that is not manifest as compositional changes).

Figure 3.12 shows the correlation between D and the right-hand side of equations [23a-b] (excluding the constant terms 3, K, Ø, and C) for the two basalt compositions. There is a positive correlation for both U and Th, indicating that reaction (1) is a viable substitution reaction for the basalts. Because the constant terms are neglected, different compositions may have different slopes. The fit is not exceptional, and there are several possible reasons for the scatter: (1) The partition coefficients are measured from a track map of the entire crystal while the microprobe analyses are from one spot. Since the crystals are zoned, variations in the location of the probe analysis with respect to the zoning profile will introduce scatter; (2) Na-loss from the charges could introduce scatter if occurred variably before, during, and after crystallization; (3) Variable deviations from interfacial equilibrium may introduce actinide partition coefficient variations not reflected in other components. Most notably, the anomalously high Takashima point in Fig. 3.12a is from T-TUBAS-D, the run with the most heterogeneous glass (see Fig. 3.3); (4) The activity-composition relationships I've used may be incorrect. Non-ideal mixing in the clinopyroxene or melt may introduce error in the analysis; (5) The equilibrium constant is temperature dependent and the crystals were grown over a range in temperature. While ΔT is small, this may account for some scatter; (6) The electron microprobe analyses for Na in the glasses may be affected by variable degrees of Na migration during electron microprobe analysis; (7) For U, there may be an error in the fO_2 correction, as it is impossible to completely separate the influence of composition and fO_2 on $D_U^{cpx/liq}$; (8) Other substitution reactions may be variably important in some cases. Given these complications, the correlations in Fig. 3.12 are about as good as can be expected.

Figure 3.12 Experimentally determined clinopyroxene-melt U and Th partition coefficients for individual crystals plotted against the expressions derived from the substitution reaction $3Ca^{M2} \Leftrightarrow (U,Th)^{M2} + 2Na^{M2}$ (see text).

(a) $D_{Th}^{cpx/liq}$ vs. $\dfrac{(X_{NaO_{1/2}}^{liq})^2}{(X_{CaO}^{liq})^3} \dfrac{(X_{Di} + X_{CaTs} + X_{Hd} + X_{TiA})^3}{(X_{Jd})^2}$

(b) $D_{U}^{cpx/liq}$ vs. $[-(\log fO_2)/A - B] \dfrac{(X_{NaO_{1/2}}^{liq})^2}{(X_{CaO}^{liq})^3} \dfrac{(X_{Di} + X_{CaTs} + X_{Hd} + X_{TiA})^3}{(X_{Jd})^2}$

The positive trend in both diagrams supports the proposed actinide + Na coupled substitution.

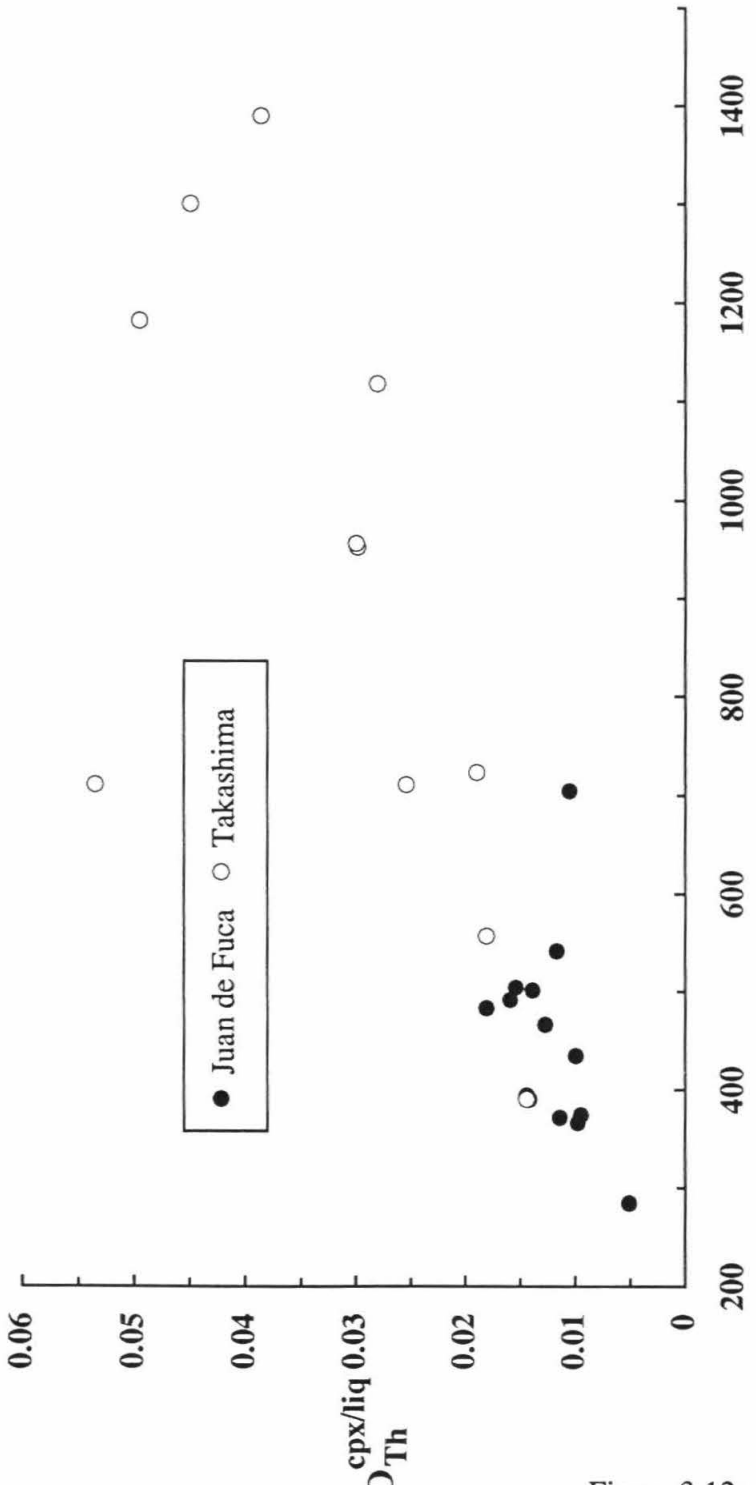
0.06
0.05
0.04
0.03
0.02
0.01
0
$D^{cpx/liq}_{Th}$
200
400
600
800
1000
1200
1400
equation [23a]
● Juan de Fuca ○ Takashima

Figure 3.12a

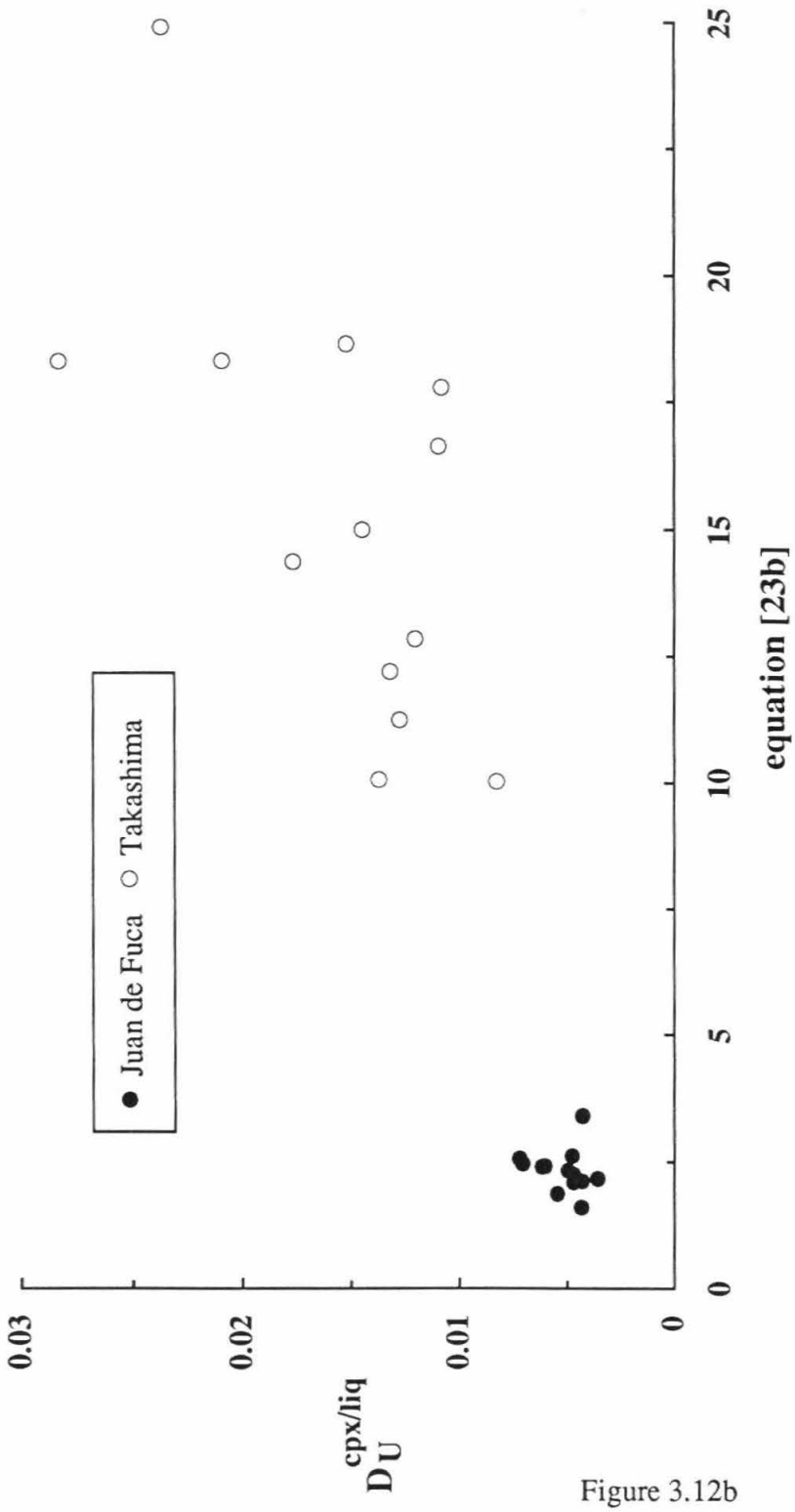
0.03
0.02
0.01
0
$D_U^{cpx/liq}$
0
5
10
15
20
25
equation [23b]
● Juan de Fuca ○ Takashima

Figure 3.12b

In addition to the above limitations, the preceding analysis addresses only the crystal chemical control on actinide partitioning in clinopyroxene. An example of the additional importance of melt chemistry was discovered by Benjamin et al. (1980) and Jones and Burnett (1987). For the base composition $Di_{50}Ab_{25}An_{25}$ they found that diopside-melt partition coefficients for U, Th, and Pu decreased by factors of 2 - 9 when 2 - 8% P_2O_5 was added to the system. They concluded that P_2O_5 stabilizes the actinides in the melt by forming complexes, resulting in a dramatic drop in partition coefficients. This interpretation is consistent with the results of Ryerson and Hess (1980), who concluded that REE also form phosphate complexes in silicate melts. While it cannot be isolated, this effect is not apparent in my results: partition coefficients for the natural, P_2O_5-bearing basalts are not low relative to the P_2O_5-free $Di_{71}An_{29}$ composition. However, the P_2O_5 contents in the basalts are probably at least an order of magnitude lower than the quantities added by Benjamin et al. (1980) and Jones and Burnett (1987), making a comparison difficult. The likely presence of melt composition effects on actinide partitioning hinder extrapolation of equations [23a-b] to vastly differing bulk compositions.

Equations [23a-b] hold for substitution reaction (1) and can only pertain to the basaltic compositions; the $Di_{71}An_{29}$ composition is restricted to reactions (2) and (3). Expressions analogous to [23a-b] can be written for these reactions by redefining the actinide-bearing pyroxene component accordingly. Upon doing so, only reaction (2) appears to be potentially viable. The resulting equations for this reaction are:

$$D_{Th}^{cpx/liq} = \frac{4K_{2_{Th}}}{\emptyset_{Th}} \frac{(X_{MgO}^{liq})}{(X_{SiO_2}^{liq})(X_{CaO}^{liq})} \times$$

$$\frac{(X_{Di} + X_{CaTs} + X_{Hd} + X_{TiA})(2 - 2X_{TiA} - X_{CaTs})(X_{CaTs} + X_{Jd})}{(X_{CaTs} + 2X_{TiA})(X_{Di} + X_{En})};$$

[24a]

$$D_U^{cpx/liq} = \frac{4K_{2U}[-(\log fO_2)/A - B]}{C\emptyset_U} \frac{(X_{MgO}^{liq})}{(X_{SiO_2}^{liq})(X_{CaO}^{liq})} \times$$

$$\frac{(X_{Di} + X_{CaTs} + X_{Hd} + X_{TiA})(2 - 2X_{TiA} - X_{CaTs})(X_{CaTs} + X_{Jd})}{(X_{CaTs} + 2X_{TiA})(X_{Di} + X_{En})} .$$

[24b]

Plots of D vs. the right-hand side of equations [24a-b] for all three compositions are shown in Fig. 3.13. These results indicate that reaction (2) may be significant in some cases. For the $Di_{71}An_{29}$ composition there is a fairly good correlation for U; there is little variation in partition coefficient or equation [24a] for Th. The correlation for the Juan de Fuca basalt is good for both Th and U, indicating that reaction (2) may also be a substitution mechanism for this composition. Both correlations are poor for the Takashima basalt. Based on the quality of the correlations, the most likely substitution mechanisms appear to be reaction (1) for the Takashima basalt, reactions (1) and (2) for the Juan de Fuca basalt, and perhaps reaction (2) for $Di_{71}An_{29}$.

3.2.2 Relationships Between Actinide Partitioning and Major Element Composition

Based on the above analysis, the $3Ca^{M2} \Leftrightarrow (U,Th)^{M2} + 2Na^{M2}$ coupled substitution (reaction (1)) appears to be the predominate actinide substitution mechanism for the clinopyroxenes in the two natural basaltic systems I studied. Reaction (2) also appears to be important for the Juan de Fuca composition. If substitution reaction (1) is important for basaltic rocks in general, it may be possible to qualitatively predict actinide partitioning behavior based on composition. The compositional term on the right side of equations [23a-b] is fairly complicated, and its relationship to more conventional compositional classifications (e.g., peralkaline vs. peraluminous) is not obvious. However, certain inferences can be made. For example, the expression $(X_{Di} + X_{CaTs} + X_{Hd} + X_{TiA})$ will typically be dominated by X_{Di}, suggesting that actinide partition coefficients may be sensitive to the diopside content of pyroxenes. McKay et al. (1986) have observed a

Figure 3.13 Individual crystal clinopyroxene-melt U and Th partition coefficients plotted against expressions derived for substitution reaction of the form $Ca^{M2} + Al^{M1} + Si^{T} = (U,Th)^{M2} + (Mg,Fe)^{M1} + Al^{T}$:

(a) $D_{Th}^{cpx/liq}$ vs. $\dfrac{(X_{MgO}^{liq})}{(X_{SiO_2}^{liq})(X_{CaO}^{liq})} \times$

$$\frac{(X_{Di} + X_{CaTs} + X_{Hd} + X_{TiA})(2 - 2X_{TiA} - X_{CaTs})(X_{CaTs} + X_{Jd})}{(X_{CaTs} + 2X_{TiA})(X_{Di} + X_{En})}$$

(b) $D_{U}^{cpx/liq}$ vs. $[-(\log fO_2)/A - B] \dfrac{(X_{MgO}^{liq})}{(X_{SiO_2}^{liq})(X_{CaO}^{liq})} \times$

$$\frac{(X_{Di} + X_{CaTs} + X_{Hd} + X_{TiA})(2 - 2X_{TiA} - X_{CaTs})(X_{CaTs} + X_{Jd})}{(X_{CaTs} + 2X_{TiA})(X_{Di} + X_{En})}$$

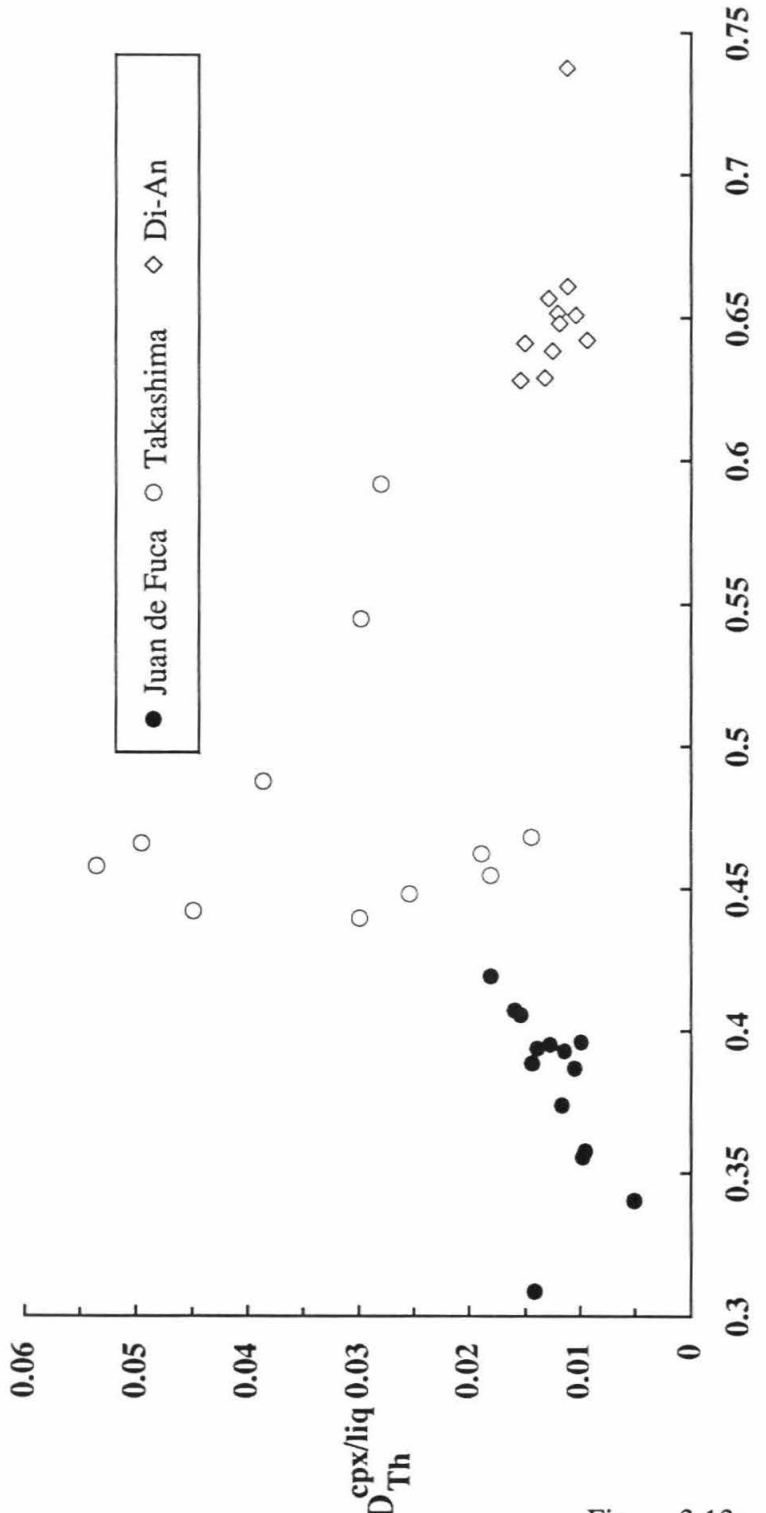
● Juan de Fuca ○ Takashima ◇ Di-An
$D^{cpx/liq}_{Th}$
0.06
0.05
0.04
0.03
0.02
0.01
0
0.3
0.35
0.4
0.45
0.5
0.55
0.6
0.65
0.7
0.75
equation [24a]

Figure 3.13a

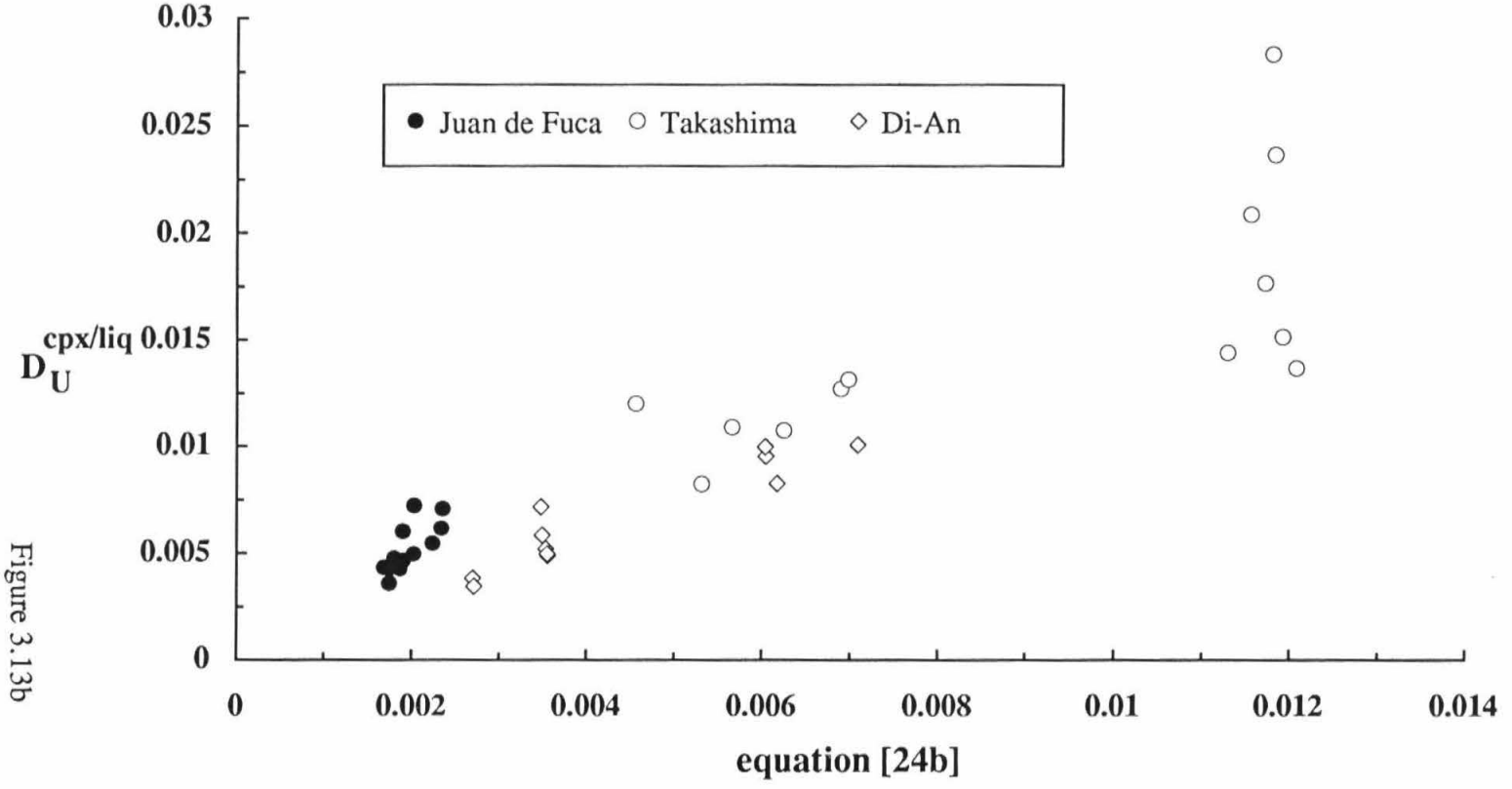
0.03
0.025
0.02
0.015
0.01
0.005
0
$D_U^{cpx/liq}$
Juan de Fuca
Takashima
Di-An
0
0.002
0.004
0.006
0.008
0.01
0.012
0.014
equation [24b]

Figure 3.13b

broadly analogous correlation between $D_{REE}^{px/liq}$ and the pyroxene wollastonite content in a synthetic shergottite composition. Also, the equal weight of the diopside and hedenbergite components indicates that actinide partition coefficients should be independent of the Fe/Mg ratio of the clinopyroxenes. The above examples illustrate some potential compositional dependencies of clinopyroxene-melt partitioning for the actinides. However, as all compositional changes are interrelated, identifying a causal relationship between only a part of equations [23a-b] and partition coefficients may be misleading. Another approach is to make some approximations in order to simplify equations [23a-b] down to a petrologically more intuitive expression. I have approximated equation [23a] in the following expression:

$$D_{Th}^{cpx/liq} \approx \frac{(X_{NaO_{1/2}}^{liq})^2}{(X_{CaO}^{liq})^3} \frac{(X_{CaO}^{cpx})^3}{(X_{NaO_{1/2}}^{cpx})^2}$$

$$\approx \frac{(D_{Ca}^{cpx/liq})^3}{(D_{Na}^{cpx/liq})^2}, \qquad [25]$$

where the constant terms have been dropped. As before, dropping K may limit its applicability to samples that span very large ranges temperature or pressure. Otherwise, this expression is a fairly good approximation of equation [23a], as confirmed with the Juan de Fuca and Takashima data. The main deficiencies are that the Al and Ti contents of the pyroxenes are not represented. The Ti content of most terrestrial pyroxenes is fairly low, and to a first approximation the presence of the CaTs and Jd components in the numerator and denominator, respectively, will tend to cancel the effect of Al to some extent. The effect of fO_2 will vary in different systems, but could be approximately accounted for by including a generic correction analogous to that in equation [23b].

Equation [25], which is based on substitution reaction (1), should approximately describe the crystal-chemical contribution to the compositional dependence of clinopyroxene-melt partitioning of U and Th for natural systems. Unfortunately, the existing data set of clinopyroxene-matrix partition coefficients for U and Th is considered

unreliable, mainly due to the likelihood of accessory phase contamination (see section *4.2*). Therefore, a test of this expression must wait until more reliable in situ U and Th partition coefficient measurements are available.

3.3 Olivine

The 1 atm liquidus phase for the "unfortified" Takashima basalt (without the 10 wt% $CaSiO_3$) is olivine, and a batch of this composition was spiked in order to measure olivine-melt partition coefficients for U and Th. A single run was performed at FMQ (see chapter 2 and Table 2.2 for experimental details), which produced large (≈ 100 x 150 μm) subhedral to skeletal olivine crystals. The compositions of the olivine and coexisting quenched melt are listed in Table 3.1. A zoning profile shows that the major and minor elements vary smoothly, with the major elements zoned from Fo_{86} at the core to Fo_{84} at the rim. As expected, the U and Th partition coefficients for olivine are very low. Using the same analytical procedures as for the clinopyroxene experiments, both $D_U^{ol/liq}$ and $D_{Th}^{ol/liq}$ are below the detection limits (no tracks from the olivine crystals were recorded). In an effort to further limit the Th partition coefficient, the ^{230}Th alpha particle exposure was repeated, this time for over two months (1576 hours) and still no alpha tracks from the olivine were recorded.

From these null results, I can assign upper limits for olivine-melt partition coefficients. Since there are no tracks from the crystals, I used an upper limit of one track per crystal to calculate a partition coefficient. These values, which have been range and zoning corrected, are listed in Table 3.5. To illustrate how low these partition coefficients are, they are plotted along with the total range of experimentally measured values for clinopyroxene in Fig. 3.14. The reason that these partition coefficients are so low is presumably because of the large difference in ionic radius between the actinides and Mg. In the case of clinopyroxene, the M2 site normally occupied by Ca^{2+}_{VIII} (ionic radius = 1.12 Å; Shannon 1976), is large enough to accommodate some U^{4+}_{VIII} and Th^{4+}_{VIII} (1.00 and 1.05

Figure 3.14 Upper limits for olivine-melt partition coefficients for U and Th from the olivine crystallization experiment plotted against oxygen fugacity. Note log scale on Y axis. No tracks were recorded for olivine crystals, and upper limits were determined by assigning one track to a crystal. The downward arrow from data points indicates upper limit. The range of TUBAS clinopyroxene values is plotted for reference, showing that the actinides can be considered almost totally incompatible in olivine.

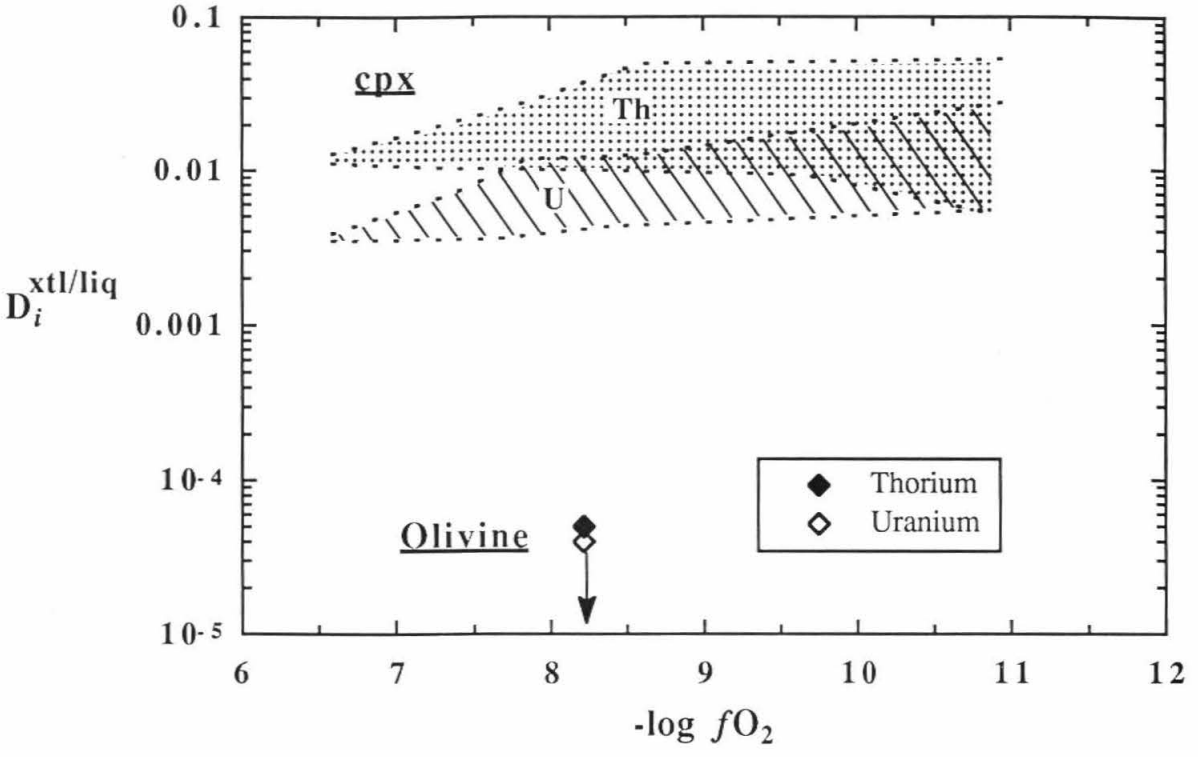
0.1
0.01
0.001
10-4
10-5
$D_i^{xtl/liq}$
cpx
Th
U
Olivine
Thorium
Uranium
6
7
8
9
10
11
12
-log fO_2

Å, respectively), while the much smaller M1 site in olivine, normally occupied largely by Mg^{2+}_{VI} (0.72 Å) is apparently too small to incorporate U^{4+}_{VI} and Th^{4+}_{VI} (0.89 and 0.94 Å). Thus, as with most other large ion lithophile elements, the actinides are strongly excluded from the olivine structure.

These low olivine melt partition coefficients place upper limits on any non-equilibrium partitioning mechanisms or analytical artifacts that are not sensitive to a specific mineral, such as incorporation of melt micro-inclusions or surfacial polishing contamination.

These extremely small olivine-melt partition coefficients, which are effectively zero for most purposes, rule out olivine as playing any role in equilibrium crystal-melt U-Th fractionation.

3.4 Garnet

The garnet crystallization experiments (see chapter 2 and Table 2.2 for experimental details) yielded 1 - 3 medium to large (40 - 100 μm in diameter) euhedral garnet crystals plus numerous smaller (5 - 25 μm) garnet crystals and quenched silicate melt. All of the crystals are concentrated on the margins of the charge, with most located near the bottom. Representative major element compositions of the large garnet crystals and quenched melt are given in Table 3.8. The crystal fractions, also listed in Table 3.8, are 10 - 14%. One of the runs (G14-SMUT-8) contains irregularly shaped SiO_2 inclusions concentrated towards the center of the large crystals. I am uncertain whether they are crystalline or glassy, or how they formed. They resemble melt inclusions, although I find it unlikely that a melt inclusion could subsequently differentiate to garnet + SiO_2. One possible origin of these inclusions is that they are quartz crystals that were either present in the initial starting material or formed during the initial heating of the charge. Before they were able to dissolve they apparently acted as nucleation sites for the garnet and were then isolated from the melt and persisted throughout the subsequent cooling interval. In their phase

TABLE 3.8

Compositions of Crystals and Quenched Melt From Garnet Crystallization Experiments[a]

Experiment	SiO_2	TiO_2	Al_2O_3	FeO	MgO	CaO	Na_2O	K_2O	Sm_2O_3	Total	F_{xtl}
Garnet[b]:											
G14-SMUT-6	40.0	1.126	22.6	19.6	11.7	5.90	.05		0.15	101.1	.10
G14-SMUT-8	38.5	0.66	22.9	19.4	11.9	6.02	.06			99.4	.14
Glass[c]:											
G14-SMUT-6	63.3	1.135	16.5	4.92	1.55	5.03	2.99	2.16	0.33	99.8	
G14-SMUT-8	64.4	1.02	17.5	4.93	1.42	4.92	3.43	2.19		99.8	

(a) G14-SMUT-6 measured with electron microprobe (WDS), G14-SMUT-8 with SEM (EDS)
(b) Mean value; garnets are zoned (see Fig. 3.15)
(c) Average of 4 - 8 points

equilibrium study, Green and Ringwood (1968) found that at 27 Kb, clinopyroxene + quartz + garnet are stable in this composition up to 20°C below the liquidus temperature. Whatever their origin, the inclusions represent less than about 15% of the total crystal area and are only present in the centers of the largest garnet crystals in one run. The outer regions of these garnets are clean, inclusion-free, euhedral crystals.

The garnet crystals are zoned, and the core to rim variation in major element concentrations of the garnets, cast in terms of end-member components, is approximately $Pyrope_{51-39}Almandine_{34-42}Grossular_{14-19}$. The range of compositions is also shown on a pyrope-almandine-grossular ternary plot in Fig. 3.15. These compositions are somewhat more almandine-rich than garnets found in peridotites or that crystallize from basalts. In the glass, concentrations of compatible and incompatible elements decrease and increase, respectively, towards the end of the charge containing the bulk of the crystals. Thus, variability in the ratio of an incompatible to compatible element is the most sensitive index of heterogeneity. The standard deviations of FeO/K_2O are 5.8% and 7.8% in runs G14-SMUT-6 and 8, respectively. Although not especially large, these variations indicate that there are moderate chemical heterogeneities in the glass, apparently indicating that the melt did not remain homogeneous during crystallization. Given the high silica and alkali contents of this composition and the higher cooling rates relative to the clinopyroxene runs, this degree homogeneity is acceptable.

Garnet and quenched melt were analyzed for U, Th and Sm by SIMS measurements on the crystals and glass, and results are listed in Table 3.9. The SIMS glass analyses are homogeneous within measurement error in both samples, and the average value is used for partition coefficients. Because of the large beam diameter (10 μm), difficulties in spot placement, and the relatively small garnet crystal size, SIMS analyses were restricted to crystal cores in all but one crystal, in which a rim analysis was also obtained. No SIMS analyses were made on crystals with visible SiO_2 inclusions. ^{30}Si-normalized ion intensities and partition coefficients are listed in Table 3.9. Partition coefficients were

Figure 3.15 Range of major element compositions of experimentally grown garnet crystals plotted on a pyrope ($Mg_3Al_2Si_3O_{12}$)-almandine ($Fe_3Al_2Si_3O_{12}$)-grossular ($Ca_3Al_2Si_3O_{12}$) garnet ternary. The plotted range is $Py_{51\text{-}39}Al_{34\text{-}42}Gr_{14\text{-}19}$, and represents the amount of compositional zoning from core to rim of single crystals. The compositions are more almandine-rich than basaltic or peridotitic garnets.

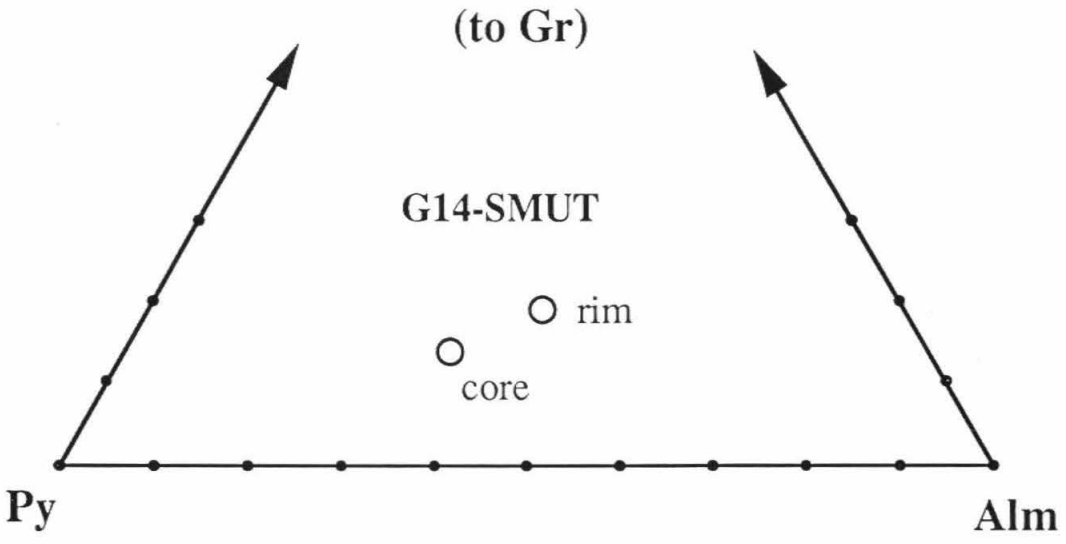

Figure 3.15

TABLE 3.9

SIMS Analyses of Quenched Melt and Crystals From Garnet Crystallization Experiments

Experiment	$\frac{^{149}Sm}{^{30}Si}$	$\frac{^{232}ThO}{^{30}Si}$	$\frac{^{238}UO}{^{30}Si}$	$D_{Sm}^{gt/liq}$[a]	$D_{Th}^{gt/liq}$[a]	$D_{U}^{gt/liq}$[a]	D_{Th}/D_{U}
Glass:							
G14-SMUT-6	.0223±.0005[b]	.187±.013	.147±.011				
G14-SMUT-8	.0229±.0008	.20±.02	.152±.017				
Garnet:							
G14-SMUT-6x1C[c]	.0126±.0003	.000361±.000015	.00265±.00015	.36±.02	.0012±.0001	.0110±.0012	.112±.017
G14-SMUT-6x1R[c]	.0147±.0019	.00048±.00011	.0036±.0006	.43±.06	.0017±.0004	.015±.003	.11±.03
G14-SMUT-6x2	.0157±.0003	.000488±.000014	.00337±.00015	.45±.02	.0017±.0002	.0140±.0015	.119±.017
G14-SMUT-6x3	.0136±.0003	.00040±.00002	.00301±.00014	.39±.02	.00134±.00014	.0122±.0013	.110±.017
G14-SMUT-6x4	.0144±.0004	.000437±.000014	.00305±.00012	.42±.02	.00149±.00014	.0126±.0013	.118±.017
G14-SMUT-8x1	.0168±.0011	.00048±.00008	.0033±.0005	.43±.03	.0014±.0003	.013±.002	.11±.03
G14-SMUT-8x4	.0188±.0007	.00068±.00011	.0042±.0005	.48±.03	.0020±.0004	.016±.003	.12±.03
G14-SMUT-8x5	.0158±.0005	.00042±.00005	.0030±.0003	.43±.02	.0013±.0002	.0114±.0018	.11±.03
G14-SMUT-8x6	.0162±.0009	.00053±.00007	.0033±.0005	.41±.03	.0015±.0003	.013±.002	.12±.03
Preferred[d]				.40±.02	.0013±.0001	.0122±.0013	.107±.014

(a) $D = \left(\frac{R^{xtl}}{R^{gl}}\right)\left(\frac{SiO_2{}^{xtl}}{SiO_2{}^{gl}}\right)$, where R = ^{30}Si normalized intensity ratio. SiO_2 from electron microprobe analyses

(b) Errors represent one standard deviation among the intensities measured in 30 mass scan cycles (see section *2.4.4*)
(c) C = core analysis, R = rim analysis; one analysis per crystal otherwise
(d) Preferred Ds are G14-SMUT-6x1C values corrected for zoning: $D_{pref} = (1.111)D_{G14\text{-}SMUT\text{-}6x1C}$ (see text)

calculated directly from the ion intensity ratios because no standard was available for U and Th in garnet. While this is an oversimplification, I believe that the partition coefficient values determined this way are accurate to within ±30% because (1) the sensitivity factors for geochemically similar elements such as U and Th are likely to be similar. Further, the ratio of the sensitivity factors between glass and garnet for U and Th are likely to be even more similar (A. Kennedy, pers. comm.), so that D_{Th}/D_U is insensitive to sensitivity factors and is more tightly constrained than either partition coefficient separately; (2) CaO concentration is often the most important compositional variable in determining matrix effects (I. Hutcheon, pers. comm.), and the difference in CaO contents between the glass and garnet in my experiments is less than 2 wt% (Table 3.8); (3) the Sm partition coefficients determined from ion intensity ratios agree with partition coefficients determined from electron microprobe analyses (Table 3.10).

SiO_2 inclusions are present in the 3 largest garnet crystals in G14-SMUT-8, but the SIMS analyses were made only on crystals with no visible SiO_2 inclusions. I suspect that some of the analyzed crystals in this sample also have such inclusions, but that the sections of these crystals are above or below the center. While there are some variations in the intensity ratios outside of errors, there is no systematic difference between the two samples. This indicates that, if present in any of the analyzed crystals, SiO_2 inclusions had no detectable effect upon crystal-melt partitioning during subsequent garnet growth.

The crystal core analysis in G14-SMUT-6x1 gives the lowest intensity ratios for either sample. This crystal is nearly twice the diameter of all others analyzed, and the higher values in the smaller crystals probably indicate that they nucleated substantially below the liquidus and hence grew from a more trace element enriched melt. This may be enhanced by local super-cooling, leading to rapid growth and boundary layer enrichments. A less likely possibility is that the smaller crystals were able to re-equilibrate with the melt through solid-state diffusion. The rim analysis from G14-SMUT-6x1 gives higher apparent partition coefficients than the core, consistent with increasing incompatible

TABLE 3.10

Comparison of $D_{Sm}^{gt/liq}$ determined by SIMS and electron microprobe (EMP) analysis

Crystal	$D_{Sm}^{gt/liq}$ SIMS	EMP[a]
G14-SMUT-6x1C	.36±.02[b]	.42±.06
G14-SMUT-6x1R	.43±.06	.51±.07
G14-SMUT-6x2	.45±.02	.48±.07
G14-SMUT-6x3	.39±.02	.45±.06
G14-SMUT-6x4	.42±.02	.49±.07

(a) Determined from an average of 3-7 points near crystal core, except G14-SMUT-6x1R, which was determined from 2 rim analyses.

(b) Errors represent one standard deviation among the intensities measured in 30 mass scan cycles (see section *2.4.4*)

element concentrations from core to rim. For Rayleigh fractionation of highly incompatible elements, the rim and core partition coefficients should be related by the expression:

$$\frac{D_{rim}}{D_{core}} = (1 - F_x)^{D - 1} \approx (1 - F_x)^{-1},$$

and for 10% crystallization (Table 3.8) this equation predicts $\frac{D_{rim}}{D_{core}} = 1.11$. The data in Table 3.9, however, give rim/core partition coefficient ratios higher than predicted. In addition, because of the 10 μm beam diameter and difficulties with spot location, the rim analysis was not actually at the crystal rim, and the true D_{rim} is probably higher than measured.

A potentially straightforward interpretation of this departure from the predicted zoning behavior is that boundary layers developed adjacent to the growing garnet crystals. A second possibility, however, is that $D_{Th}^{gt/liq}$ and $D_{U}^{gt/liq}$ vary during garnet growth in response to major element zoning. Unlike the case for the clinopyroxene crystallization experiments, there is a considerable degree of major element zoning in these garnets (Fig. 3.15). It is quite possible that garnet-melt partition coefficients for trace elements depend on the major element composition of the garnet, and major element variations may result in trace element partition coefficients not being constant throughout the crystallization. Further, the temperature interval in these experiments is relatively large (Table 2.2), which also may affect trace element partition coefficients. Nonetheless, as the contribution of these latter effects cannot be quantified, I have calculated preferred partition coefficient values from the core analysis of G14-SMUT-6x1 using the zoning correction above. These preferred garnet-melt partition coefficients, also listed in Table 3.9, are near the low end of the total spread but conform with the values for several of the smaller crystals. This conformity is consistent with smaller crystals nucleating late during the cooling interval, and thus attaining higher bulk trace element concentrations. If the compositional or temperature variations are important, the rim values may reflect the true equilibrium values and the preferred values will be slightly low.

The low U and Th partition coefficients listed in Table 3.9 indicate that, as with clinopyroxene, U and Th are very incompatible in garnet. G14-SMUT garnet-melt partition coefficients for U and Th are plotted against oxygen fugacity in Fig. 3.16. The range of clinopyroxene values is also shown for reference. A very important observation in Fig. 3.16 is that $D_U^{gt/liq} \gg D_{Th}^{gt/liq}$, opposite to what was found for clinopyroxene. This observation is further illustrated in Fig. 3.17, which shows $D_{Th}^{gt/liq}/D_U^{gt/liq}$ vs. $-\log fO_2$, again with the clinopyroxene data for reference. The fact that $D_{Th}^{gt/liq}/D_U^{gt/liq} < 1$ means that U is more compatible than Th in garnet, and thus that a partial melt will have a greater Th/U than the garnet remaining in the source. While the magnitudes of the partition coefficients are still small, the sense of U-Th fractionation possible by garnet-melt partitioning is opposite to that of clinopyroxene. This may have very important implications for MORB and OIB petrogenesis, as discussed in the next chapter.

Figure 3.16 Garnet-melt partition coefficients for U and Th plotted against oxygen fugacity for high pressure G14-SMUT experiments. Horizontal arrows on points indicate that the fO_2 plotted is for the C-CO-CO_2 buffer and is an upper limit for the actual conditions of the experiments. Range of values from TUBAS clinopyroxene experiments is shown for reference. Partition coefficients are quite small, indicating that U and Th are highly incompatible in garnet. Note however, that $D_U^{gt/liq} > D_{Th}^{gt/liq}$, opposite to what was found for clinopyroxene.

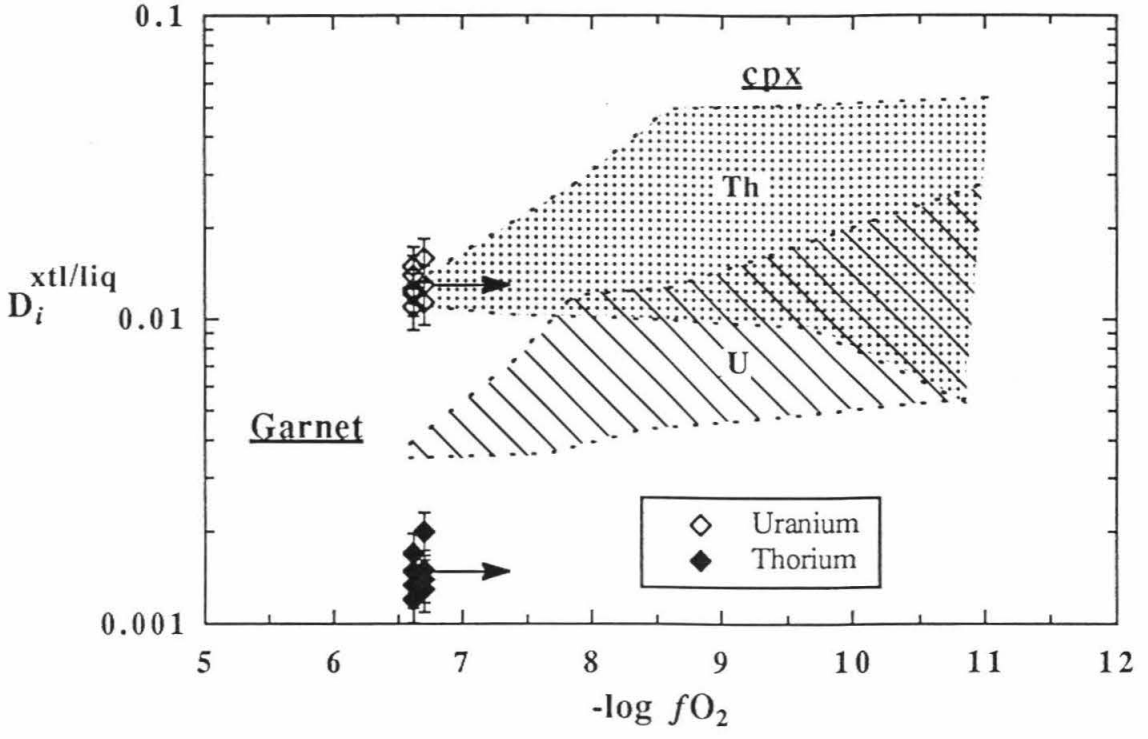
0.1
0.01
0.001
xtl/liq
D_i
cpx
Th
U
Garnet
Uranium
Thorium
5
6
7
8
9
10
11
12
-log fO_2

Figure 3.16

Figure 3.17 $D_{Th}^{gt/liq}/D_{U}^{gt/liq}$ vs. -logfO_2 for the partition coefficients shown in Fig. 3.14, with the TUBAS clinopyroxene data plotted for reference. Horizontal arrow on points indicates that the fO_2 plotted is for the C-CO-CO_2 buffer and is an upper limit for the actual conditions of the experiments. $D_{Th}^{gt/liq}/D_{U}^{gt/liq} < 1$ for garnet, indicating that U is more compatible that Th in garnet and thus that a partial melt will have Th/U greater than its source.

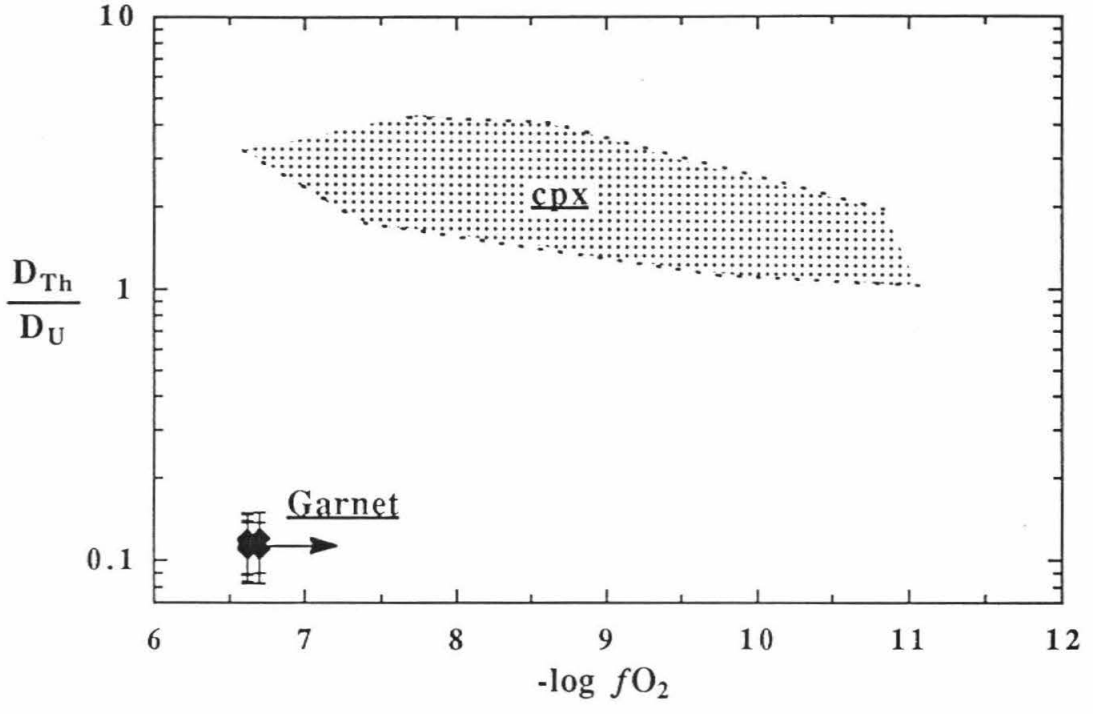

Figure 3.17

Appendix 3.1: Fission and Alpha Particle Range Correction Factors

Fission and alpha particle ranges are expressed in mg/cm^2, and are dependent upon the atomic number of the matrix. Equations for fission fragment ranges are given by Mory et al. (1970), and for alpha particle ranges by Friedlander et al. (1964); these equations are also listed in Benjamin (1980). The correction factors, tabulated as $\frac{R_{gl}}{R_{cpx}}$, are all greater than one. Track density ratios are multiplied by this correction factor and, in the case of ^{230}Th alpha tracks, an exposure time correction, to give the mass concentration ratios:

$$\frac{[^{235}U]_{cpx}}{[^{235}U]_{gl}} = \left(\frac{N_{cpx}}{N_{gl}}\right)_{FT}\left(\frac{R_{gl}}{R_{cpx}}\right)_{FT}, \text{ and}$$

$$\frac{[^{230}Th]_{cpx}}{[^{230}Th]_{gl}} = \left(\frac{N_{cpx}}{N_{gl}}\right)_{AT}\left(\frac{R_{gl}}{R_{cpx}}\right)_{AT}\left(\frac{t_{gl}}{t_{cpx}}\right)_{AT}$$

Sample	R_{gl}/R_{cpx} Fission	Alpha	Sample	R_{gl}/R_{cpx} Fission	Alpha
D2-TUBAS-G	1.045	1.041	J-TUBAS-H	1.028	1.032
D2-TUBAS-E	1.003	1.004	J-TUBAS-L	1.020	1.018
D2-TUBAS-F	1.013	1.013	T-TUBAS-C	1.014	1.013
D2-TUBAS-N	1.015	1.013	T-TUBAS-I	1.002	1.004
D2-TUBAS-H	1.034	1.032	T-TUBAS-B	1.014	1.014
D2-TUBAS-L	1.017	1.018	T-TUBAS-D	1.020	1.022
J-TUBAS-G	1.028	1.032	T-TUBAS-H	1.007	1.009
J-TUBAS-E	1.020	1.018	TO-TUBAS-D	1.037	1.032
J-TUBAS-F	1.024	1.022			

Appendix 3.2: Derivation of Zoning Correction

The crystals in these experiments were grown by fractional crystallization and are therefore chemically zoned. Because fission and alpha particles have a non-zero range, tracks in the crystal near the crystal-glass boundary may be contributed by the glass and cannot be counted. I therefore must correct for zoning only up to the fraction of crystallization analyzed. The measured track density in a crystal corresponds to the average concentration of a trace element, *i*, in the crystal integrated up to the analyzed fraction of the total amount of crystallization. This can be expressed as:

$$\langle C_i^{xtl} \rangle = \frac{\int_0^{vF} C_i^{xtl}\, dF'}{\int_0^{vF} dF'}, \qquad [a]$$

where C is concentration, F is the total crystal fraction, and v is the volume fraction of F analyzed. If the true partition coefficient, D, is defined as C_i^{xtl}/C_i^{liq}, then at any point during fractional crystallization the concentrations in the crystal and liquid are:

$$C_i^{xtl} = C_{i_o}^{liq} D(1 - F)^{D-1}, \qquad [b]$$

and

$$C_i^{liq} = C_{i_o}^{liq}(1 - F)^{D-1}, \qquad [c]$$

where $C_{i_o}^{liq}$ is the initial concentration of *i* in the liquid. Substituting [b] into [a] and performing the integration yields:

$$\langle C_i^{xtl} \rangle = \frac{C_{i_o}^{liq}}{vF}[1 - (1 - vF)^D]. \qquad [d]$$

The measured partition coefficient, D_m, is given by $\langle C_i^{xtl} \rangle / C_i^{liq}$. Substituting [c] and [d] into this expression gives:

$$D_m = \frac{[1 - (1 - vF)^D]}{vF(1 - F)^{D-1}}. \qquad [e]$$

This can be linearized by setting $g(D) = (1 - vF)^D$ and taking a first order Taylor Series expansion about D = 0:

$$g(D) = 1 + D\ln(1 - vF), \qquad [f]$$

and

$$[1 - (1 - vF)^D] = 1 - g(D) = -D\ln(1 - vF). \qquad [g]$$

Similarly, setting $y = D - 1$, $h(y) = (1 - F)^y$, and taking a first order Taylor Series expansion about $y = -1$ we get:

$$h(y) = \frac{[1 + D\ln(1 - F)]}{(1 - F)}, \qquad [h]$$

and

$$vF(1 - F)^{D - 1} = \frac{vF[1 + D\ln(1 - F)]}{(1 - F)}. \qquad [i]$$

Substituting [g] and [i] into the numerator and denominator of [e] and solving for D results in:

$$D = D_m \frac{vF}{(F - 1)\ln(1 - vF) - vFD_m\ln(1 - F)}. \qquad [j]$$

Noting that the right hand term in the denominator is much smaller than the left hand term for the very small partition coefficients I measure, this can be simplified to:

$$D = D_m \frac{vF}{(F - 1)\ln(1 - vF)}, \qquad [k]$$

where D is the zoning corrected partition coefficient.

Appendix 3.3: Calculation of Pyroxene End-Members

The method I used to calculate the proportions of the various pyroxene end-member components is only slightly different from that of Lindsley and Andersen (1983). The pyroxene analyses are first converted cation proportions based on six oxygens. The ferric-ferrous Fe ratio is not determined in electron microprobe analyses, and rather than attempt to calculate it, I have taken all Fe as Fe^{2+}. This eliminates acmite as a possible end-member. Tetrahedral Al is calculated as 2 - Si, and the remaining Al is taken as octahedral (Al_{VI}). Cr and Mn are combined with Al_{VI} and Fe, respectively. Mole fractions of pyroxene end-members are then calculated as follows:

1. Jadeite (Jd; $NaAlSi_2O_6$) = Na
2. Ti-augite (TiA; $CaTiAl_2O_6$) = Ti
3. Ca-Tschermak's (CaTs; $CaAl_2SiO_6$) = Al_{VI} - Na.

For the purposes of plotting pyroxene compositions on a Wo-En-Fs ternary, the main Ca-, Mg-, and Fe-bearing components are calculated in terms of normalized Wo-En-Fs:

4a. Wollastonite (Wo; $Ca_2Si_2O_6$) = [Ca - (TiA + CaTs)]/2

5a. Enstatite (En; $Mg_2Si_2O_6$) = (1 - Wo)*(1 - Fe#)

6a. Ferrosilite (Fs; $Fe_2Si_2O_6$) = (1 - Wo)*Fe#,

where Fe# = Fe/(Fe + Mg).

For calculating mole fractions of end-member clinopyroxene components to be used for modelling activity-composition relationships, the main Ca-, Mg-, and Fe-bearing components are calculated in terms of Di-Hd-En:

4b. Hedenbergite (Hd; $CaFeSi_2O_6$) = Fe

5b. Diopside (Di; $CaMgSi_2O_6$) = Ca - (TiA + CaTs + Hd)

6b. Enstatite (En; $Mg_2Si_2O_6$) = (Mg - Di)/2.

The mole fractions of the end members are listed in Table A3.3.1.

TABLE A3.3.1 Clinopyroxene Atom Proportions and Mole Fractions of End-Member Components

Sample	Si	Al	Fe	Mg	Ca	Mn	Na	Ti	Cr	O	ΣM(a)
D2-TUBAS-G1	1.939	0.145		0.947	0.958					6	1.989
D2-TUBAS-G2	1.930	0.144		0.948	0.973					6	1.996
D2-TUBAS-E1	1.909	0.142		0.982	0.986					6	2.019
D2-TUBAS-E2	1.918	0.120		0.994	0.988					6	2.021
D2-TUBAS-E3	1.921	0.125		0.983	0.986					6	2.015
D2-TUBAS-F1	1.921	0.149		0.961	0.971					6	2.003
D2-TUBAS-F2	1.938	0.135		0.952	0.971					6	1.995
D2-TUBAS-H1	1.932	0.142		0.966	0.955					6	1.996
D2-TUBAS-H2	1.938	0.141		0.942	0.971					6	1.992
D2-TUBAS-H3	1.933	0.143		0.966	0.953					6	1.995
D2-TUBAS-L1-2	1.930	0.144		0.969	0.954					6	1.997
D2-TUBAS-L1-3	1.927	0.155		0.964	0.949					6	1.995
J-TUBAS-G1	1.889	0.175	0.180	0.818	0.889	0.0040	0.0141	0.0295	0.0005	6	2.000
J-TUBAS-G2	1.899	0.168	0.179	0.813	0.890	0.0036	0.0121	0.0283	0.0005	6	1.994
J-TUBAS-G3	1.904	0.158	0.174	0.825	0.892	0.0045	0.0123	0.0258	0.0007	6	1.997
J-TUBAS-E1	1.913	0.143	0.169	0.848	0.887	0.0046	0.0109	0.0205	0.0004	6	1.998
J-TUBAS-E2	1.901	0.165	0.170	0.822	0.887	0.0045	0.0121	0.0288	0.0005	6	1.992
J-TUBAS-E4	1.907	0.154	0.164	0.836	0.888	0.0044	0.0103	0.0275	0.0005	6	1.993
J-TUBAS-E5	1.908	0.152	0.161	0.826	0.906	0.0048	0.0093	0.0255	0.0003	6	1.994
J-TUBAS-F1	1.911	0.150	0.168	0.840	0.884	0.0048	0.0113	0.0249	0.0006	6	1.995
J-TUBAS-F3	1.910	0.151	0.179	0.830	0.881	0.0046	0.0109	0.0255	0.0004	6	1.993
J-TUBAS-F4	1.907	0.156	0.171	0.832	0.886	0.0041	0.0118	0.0260	0.0006	6	1.995

Sample	Si	Al	Fe	Mg	Ca	Mn	Na	Ti	Cr	O	ΣM(a)
J-TUBAS-H1	1.909	0.144	0.162	0.860	0.878	0.0043	0.0085	0.0275	0.0005	6	1.995
J-TUBAS-H2	1.898	0.143	0.156	0.868	0.899	0.0049	0.0085	0.0280	0.0004	6	2.006
J-TUBAS-L1	1.921	0.129	0.139	0.877	0.890	0.0050	0.0057	0.0246	0.0004	6	1.992
J-TUBAS-L2	1.920	0.127	0.140	0.887	0.891	0.0049	0.0049	0.0207	0.0004	6	1.997
J-TUBAS-L3	1.906	0.138	0.134	0.882	0.901	0.0053	0.0054	0.0268	0.0005	6	2.000
T-TUBAS-C1	1.901	0.171	0.130	0.887	0.862	0.0035	0.0156	0.0224	0.0022	6	1.997
T-TUBAS-C2-1	1.883	0.185	0.131	0.870	0.880	0.0034	0.0142	0.0300	0.0021	6	2.000
T-TUBAS-C2-2	1.878	0.196	0.140	0.860	0.870	0.0037	0.0129	0.0323	0.0007	6	1.997
T-TUBAS-C2-3	1.897	0.211	0.142	0.829	0.842	0.0040	0.0249	0.0263	0.0002	6	1.979
T-TUBAS-B1	1.877	0.203	0.133	0.854	0.867	0.0035	0.0171	0.0345	0.0025	6	1.993
T-TUBAS-B2	1.878	0.197	0.130	0.859	0.874	0.0035	0.0167	0.0323	0.0031	6	1.996
T-TUBAS-B3	1.852	0.206	0.134	0.867	0.897	0.0034	0.0148	0.0370	0.0018	6	2.014
T-TUBAS-B4	1.868	0.201	0.141	0.856	0.880	0.0037	0.0139	0.0355	0.0011	6	2.001
T-TUBAS-B5	1.865	0.195	0.138	0.884	0.870	0.0035	0.0148	0.0338	0.0019	6	2.009
T-TUBAS-D1	1.874	0.194	0.112	0.888	0.874	0.0042	0.0111	0.0363	0.0016	6	1.997
T-TUBAS-D2	1.874	0.202	0.123	0.893	0.848	0.0038	0.0105	0.0360	0.0015	6	1.993
T-TUBAS-D3	1.863	0.223	0.125	0.873	0.841	0.0035	0.0121	0.0420	0.0016	6	1.987
T-TUBAS-H1	1.890	0.187	0.104	0.908	0.848	0.0043	0.0101	0.0320	0.0016	6	1.987
T-TUBAS-H2	1.887	0.192	0.105	0.907	0.851	0.0043	0.0089	0.0310	0.0009	6	1.988
T-TUBAS-H3	1.905	0.168	0.100	0.909	0.855	0.0036	0.0122	0.0298	0.0023	6	1.986
T-TUBAS-H4	1.879	0.205	0.105	0.917	0.833	0.0043	0.0087	0.0333	0.0010	6	1.988
T-TUBAS-H5	1.881	0.194	0.105	0.910	0.849	0.0041	0.0099	0.0335	0.0014	6	1.991

(a) ΣM = sum of cations in M1 and M2 positions (Ca + Mg + Fe + Na + Ti + Al(VI) + Cr + Mn)

Sample	Jd	Ti-Aug	CaTs	Fe#	Wo	En	Fs	Hd	Di	En	Σ(b)
D2-TUBAS-G1			0.0832		0.437	0.563			0.874	0.036	0.994
D2-TUBAS-G2			0.0742		0.449	0.551			0.898	0.025	0.997
D2-TUBAS-E1			0.0502		0.468	0.532			0.936	0.023	1.009
D2-TUBAS-E2			0.0380		0.475	0.525			0.950	0.022	1.010
D2-TUBAS-E3			0.0460		0.470	0.530			0.940	0.022	1.007
D2-TUBAS-F1			0.0705		0.450	0.550			0.901	0.030	1.001
D2-TUBAS-F2			0.0720		0.449	0.551			0.899	0.027	0.997
D2-TUBAS-H1			0.0733		0.441	0.559			0.882	0.042	0.997
D2-TUBAS-H2			0.0780		0.447	0.553			0.893	0.024	0.996
D2-TUBAS-H3			0.0755		0.439	0.562			0.877	0.044	0.997
D2-TUBAS-L1-2			0.0738		0.440	0.560			0.881	0.044	0.999
D2-TUBAS-L1-3			0.0815		0.434	0.566			0.868	0.048	0.997
J-TUBAS-G1	0.0141	0.030	0.0500	0.183	0.405	0.486	0.109	0.184	0.625	0.096	0.999
J-TUBAS-G2	0.0121	0.028	0.0554	0.184	0.403	0.487	0.110	0.183	0.624	0.094	0.997
J-TUBAS-G3	0.0123	0.026	0.0496	0.178	0.408	0.487	0.105	0.178	0.638	0.093	0.997
J-TUBAS-E1	0.0109	0.020	0.0455	0.169	0.410	0.490	0.100	0.173	0.648	0.100	0.998
J-TUBAS-E2	0.0121	0.029	0.0544	0.175	0.402	0.493	0.105	0.174	0.630	0.096	0.995
J-TUBAS-E4	0.0103	0.028	0.0512	0.168	0.405	0.495	0.100	0.169	0.640	0.098	0.996
J-TUBAS-E5	0.0093	0.026	0.0510	0.167	0.415	0.488	0.098	0.165	0.664	0.081	0.996
J-TUBAS-F1	0.0113	0.025	0.0492	0.171	0.405	0.494	0.102	0.173	0.637	0.101	0.997
J-TUBAS-F3	0.0109	0.026	0.0500	0.181	0.403	0.489	0.108	0.183	0.622	0.104	0.996
J-TUBAS-F4	0.0118	0.026	0.0508	0.173	0.405	0.492	0.103	0.175	0.635	0.099	0.997

Sample	Jd	Ti-Aug	CaTs	Fe#	Wo	En	Fs	Hd	Di	En	Σ
J-TUBAS-H1	0.0085	0.028	0.0453	0.162	0.402	0.501	0.097	0.166	0.639	0.111	0.997
J-TUBAS-H2	0.0085	0.028	0.0328	0.156	0.419	0.490	0.091	0.161	0.677	0.095	1.003
J-TUBAS-L1	0.0057	0.025	0.0445	0.141	0.410	0.506	0.083	0.144	0.677	0.100	0.995
J-TUBAS-L2	0.0049	0.021	0.0425	0.141	0.414	0.504	0.082	0.145	0.682	0.103	0.998
J-TUBAS-L3	0.0054	0.027	0.0383	0.136	0.418	0.503	0.079	0.139	0.697	0.093	0.999
T-TUBAS-C1	0.0156	0.022	0.0581	0.131	0.391	0.530	0.080	0.133	0.648	0.119	0.997
T-TUBAS-C2-1	0.0142	0.030	0.0557	0.134	0.397	0.522	0.081	0.134	0.659	0.105	0.999
T-TUBAS-C2-2	0.0129	0.032	0.0612	0.143	0.388	0.524	0.087	0.143	0.633	0.113	0.997
T-TUBAS-C2-3	0.0249	0.026	0.0830	0.149	0.366	0.539	0.095	0.146	0.587	0.121	0.988
T-TUBAS-B1	0.0171	0.035	0.0649	0.138	0.384	0.531	0.085	0.137	0.631	0.112	0.995
T-TUBAS-B2	0.0167	0.032	0.0617	0.135	0.390	0.528	0.082	0.134	0.646	0.106	0.996
T-TUBAS-B3	0.0148	0.037	0.0448	0.137	0.407	0.512	0.081	0.137	0.677	0.095	1.006
T-TUBAS-B4	0.0139	0.036	0.0559	0.144	0.394	0.518	0.088	0.144	0.644	0.106	0.999
T-TUBAS-B5	0.0148	0.034	0.0468	0.138	0.395	0.522	0.084	0.142	0.647	0.118	1.003
T-TUBAS-D1	0.0111	0.036	0.0576	0.115	0.390	0.540	0.070	0.116	0.664	0.112	0.997
T-TUBAS-D2	0.0105	0.036	0.0663	0.124	0.373	0.550	0.078	0.126	0.619	0.137	0.995
T-TUBAS-D3	0.0121	0.042	0.0752	0.129	0.362	0.556	0.082	0.129	0.595	0.139	0.992
T-TUBAS-H1	0.0101	0.032	0.0688	0.107	0.374	0.560	0.067	0.108	0.639	0.135	0.993
T-TUBAS-H2	0.0089	0.031	0.0713	0.107	0.374	0.559	0.067	0.109	0.640	0.133	0.993
T-TUBAS-H3	0.0122	0.030	0.0624	0.102	0.381	0.556	0.063	0.103	0.659	0.125	0.992
T-TUBAS-H4	0.0087	0.033	0.0756	0.107	0.362	0.570	0.068	0.109	0.615	0.151	0.993
T-TUBAS-H5	0.0099	0.034	0.0668	0.107	0.374	0.559	0.067	0.109	0.640	0.135	0.994

(b) Σ = sum of end member mole fractions (Di + Hd + En + CaTs + Jd + TiA)

Appendix 3.4: Derivation of Activity-Composition Relationships for Clinopyroxenes

From the definition of activity, the activity of a component, i, in solid solution at constant temperature and pressure is:

$$a_i = \exp\left[\frac{-1}{RT}\left(\frac{\partial \Delta G_{mix}}{\partial n_i}\right)_{n_j}\right], \qquad [A6]$$

where n_i is the number of moles of component i. The free energy of mixing can be expressed as:

$$\Delta G_{mix} = \Delta H_{mix} - T\Delta S_{mix}. \qquad [A7]$$

For ideal mixing I assume that only configurational entropy terms are important, i.e., that $\Delta S_{mix} = \Delta S_{conf}$, and that $\Delta H_{mix} = 0$ (e.g., Nordstrom and Munoz 1986). Making these simplifications to [A7] and substituting into [A6] gives:

$$a_i = \exp\left[\frac{1}{R}\left(\frac{\partial \Delta S_{conf}}{\partial n_i}\right)_{n_j}\right]. \qquad [A8]$$

The molar configurational entropy change of mixing can be can be calculated from the Plank-Boltzman equation, resulting in:

$$\Delta \bar{S}_{conf} = -R\sum_j [m_j \sum_i N_i^j \ln(N_i^j)], \qquad [A9]$$

where m_j is the number of atoms on the j^{th} crystallographic site, and N_i^j is the mole fraction of the i^{th} atom on the j^{th} site.

Table A3.3.1 lists the cation proportions based on 6 oxygens and the calculated mole fractions of end-member compositions for the clinopyroxenes in this study. It should be noted that end-member clinopyroxene mole fractions and the activity-composition relationships for clinopyroxene derived in this appendix are independent of the number of oxygen atoms used to calculate the cation proportions. The procedure I used to calculate the end-member components is slightly modified from the scheme of Lindsley and Andersen (1983; see Appendix 3.3). From the end-member components listed in Table A3.3.1, the structural formula of the general pyroxene solid solution in my experiments is

$$(Ca,Na,Mg,U,Th)^{M2}(Mg,Fe,Al,Ti)^{M1}(Al,Si)_2^TO_6, \qquad [A10]$$

where the superscripts indicate the eight-fold coordinated M2, octahedrally coordinated M1, and tetrahedral sites. In order to evaluate equation [A9], I need to relate cation mole fractions (N_i^j) to the more useful end-member pyroxene mole fractions (X_i). This is done by equating each cation mole fraction on a particular site to the sum of the mole fractions of the end-member components weighted by their mole fraction of that cation on that site. For the set of major components listed in Table A3.3.1 and the actinide-bearing pyroxene defined by reaction (1) this yields:

$$N_{Ca}^{M2} = X_{Di} + X_{CaTs} + X_{Hd} + X_{TiA} \qquad [A11a]$$

$$N_{Na}^{M2} = X_{Jd} + \frac{2}{3}X_{U,Thp} = \frac{3X_{Jd} + 2X_{U;Thp}}{3} \qquad [A11b]$$

$$N_{Mg}^{M2} = X_{En} \qquad [A11c]$$

$$N_{U;Th}^{M2} = \frac{1}{3}X_{U,Thp} \qquad [A11d]$$

$$N_{Mg}^{M1} = X_{Di} + X_{En} + X_{U,Thp} \qquad [A11e]$$

$$N_{Fe}^{M1} = X_{Hd} \qquad [A11f]$$

$$N_{Al}^{M1} = X_{CaTs} + X_{Jd} \qquad [A11g]$$

$$N_{Ti}^{M1} = X_{TiA} \qquad [A11h]$$

$$N_{Al}^{T} = (2X_{TiA} + X_{CaTs})/2 \qquad [A11i]$$

$$N_{Si}^{T} = X_{Di} + X_{Hd} + X_{Jd} + X_{En} + X_{U,Thp} + \frac{X_{CaTs}}{2} = \frac{2 - 2X_{TiA} - X_{CaTs}}{2}. \qquad [A11j]$$

Substitution of [A11a-j] into [A9] gives the molar configurational entropy of the pyroxene solid solution, [A10]:

$$\Delta\bar{S}_{conf} = -R\Big[3(X_{Di} + X_{CaTs} + X_{Hd} + X_{TiA})\ln(X_{Di} + X_{CaTs} + X_{Hd} + X_{TiA}) + (3X_{Jd} + 2X_{U,Thp})\ln\Big(\frac{3X_{Jd} + 2X_{U;Thp}}{3}\Big) + 3X_{En}\ln X_{En} + X_{U,Thp}\ln\Big(\frac{X_{U;Thp}}{3}\Big) + 3(X_{Di} + X_{En} + X_{U,Thp})\ln(X_{Di} + X_{En} + X_{U,Thp}) + 3X_{Hd}\ln X_{Hd} + 3(X_{CaTs} + X_{Jd})\ln(X_{CaTs} + X_{Jd}) + 3X_{TiA}\ln X_{TiA} + 3(2X_{TiA} + X_{CaTs})\ln\Big(\frac{2X_{TiA} + X_{CaTs}}{2}\Big) + 3(2 - 2X_{TiA} - X_{CaTs})\ln\Big(\frac{2 - 2X_{TiA} - X_{CaTs}}{2}\Big)\Big]. \quad [A12]$$

Equation [A12] must be rederived for each substitution reaction that involves a new pyroxene end-member. In order to use this expression for configurational entropy to calculate activities, equation [A8] must also be converted from cation mole fractions to end-member pyroxene mole fractions. This can be done by noting that $n_i = f(n_{tot}, X_1, X_2, ..., X_c)$ and using the chain rule:

$$\frac{\partial\Delta S}{\partial n_i} = \frac{\partial\Delta S}{\partial n_{tot}}\frac{\partial n_{tot}}{\partial n_i} + \frac{\partial\Delta S}{\partial X_1}\frac{\partial X_1}{\partial n_i} + \frac{\partial\Delta S}{\partial X_2}\frac{\partial X_2}{\partial n_i} + ... + \frac{\partial\Delta S}{\partial X_c}\frac{\partial X_c}{\partial n_i}, \quad [A13]$$

where c is the total number of end-member pyroxene components. $\Delta S = n_{tot}\Delta\bar{S}$, so $\frac{\partial\Delta S}{\partial n_{tot}} = \Delta\bar{S}$, and $\frac{\partial n_{tot}}{\partial n_i} = 1$. The derivatives $\frac{\partial X}{\partial n}$ can be written as:

$$\frac{\partial X_k}{\partial n_i} = \frac{\partial}{\partial n_i}\Big(\frac{n_k}{n_{tot}}\Big) = \frac{-n_k}{n_{tot}^2} = \frac{-X_k}{n_{tot}} \quad \text{and}$$

$$\frac{\partial X_i}{\partial n_i} = \frac{\partial}{\partial n_i}\Big(\frac{n_i}{n_{tot}}\Big) = \frac{n_{tot} - n_i}{n_{tot}^2} = \frac{1 - X_i}{n_{tot}},$$

and equation [A13] becomes:

$$\frac{\partial\Delta S}{\partial n_i} = \Delta\bar{S} + \sum_{k;k\neq i}\frac{\partial\Delta S}{\partial X_k}\Big(\frac{-X_k}{n_{tot}}\Big) + \frac{\partial\Delta S}{\partial X_i}\Big(\frac{1 - X_i}{n_{tot}}\Big)$$

$$= \Delta\bar{S} + \frac{1}{n_{tot}}\Big[\frac{\partial\Delta S}{\partial X_i} - \sum_k X_k\frac{\partial\Delta S}{\partial X_k}\Big]$$

$$= \Delta\bar{S} + \frac{\partial\Delta\bar{S}}{\partial X_i} - \sum_k X_k\frac{\partial\Delta\bar{S}}{\partial X_k}. \quad [A14]$$

Substituting equation [A12] into [A14] gives $\frac{\partial\Delta S}{\partial n_i}$ as a function of the mole fractions of the pyroxene end-members, and substitution of that expression into [A8] then gives the activity of end-member i as a function of the mole fractions of the pyroxene end-members.

CHAPTER 4

Discussion and Application of Results

4.1 Summary of Results

The results of clinopyroxene crystallization experiments show that $D_{Th}^{cpx/liq} > D_{U}^{cpx/liq}$ for the compositions and fO_2s studied (Fig. 3.9). The fO_2s studied range from the Ni-NiO to one log unit more oxidizing than Fe-FeO buffer and span the range of most terrestrial magmas. $D_{Th}^{cpx/liq}$ is approximately independent of fO_2 for two out of the three compositions (Fig. 3.5); in the Juan de Fuca basalt, $D_{Th}^{cpx/liq}$ may decrease with decreasing fO_2. This decrease is correlated with a decrease in the Na concentration of the system, which results from increasing Na-loss from the charge with decreasing fO_2. $D_{U}^{cpx/liq}$ increases with decreasing fO_2, which I interpret as resulting from an increase in the proportion of U^{4+} in the system under more reducing conditions (Fig. 3.7). While I have not measured the valence state of U in my experiments, this interpretation is consistent with studies of the U valence state distribution in silicate melts of similar compositions (Fig. 3.8). Based on such measurements, the melts in these partitioning experiments contain a significant proportion of U^{5+}, possibly as much as 90%.

The partition coefficients are sensitive to composition. Both $D_{Th}^{cpx/liq}$ and $D_{U}^{cpx/liq}$ are greater in the Takashima basalt than in the other two compositions. This distinction may be due to the higher Na_2O concentration in the Takashima basalt, although other factors undoubtedly play a role. The partition coefficients for the basalts appear to be consistent with a $3Ca^{2+} \Leftrightarrow (U,Th)^{4+} + 2Na^{+}$ substitution reaction in the M2 site (Fig. 3.12), which predicts a positive dependence of the actinide partition coefficients on $(D_{Ca}^{cpx/liq})^3/(D_{Na}^{cpx/liq})^2$.

Partition coefficients from a 0.1°C/hr cooling rate experiment are systematically lower than those from the 1.7°C/hr runs, indicating that there were deviations from interfacial equilibrium in the 1.7°C/hr runs. While the individual partition coefficients from the slow

cooling rate run are lower, $D_{Th}^{cpx/liq}/D_{U}^{cpx/liq}$ is independent of cooling rate. At the Fa-Mt-Qz oxygen buffer, which is thought to be a fairly typical fO_2 for terrestrial magmas, $D_{Th}^{cpx/liq}/D_{U}^{cpx/liq}$ = 2 - 3 for all three compositions studied (Fig. 3.9). This means that Th is more compatible than U in clinopyroxene under these conditions, and thus that a partial melt will have a lower Th/U than the residual clinopyroxene in the source. $D_{Th}^{cpx/liq}/D_{U}^{cpx/liq}$ decreases under more reducing conditions, primarily from an increase in $D_{U}^{cpx/liq}$.

Olivine crystallization experiments show that $D_{Th}^{ol/liq}$ and $D_{U}^{ol/liq}$ are less than 5 x 10^{-5}, effectively zero for most purposes (Fig. 3.14). Garnet -melt partitioning experiments demonstrate that $D_{Th}^{gt/liq} < D_{U}^{gt/liq}$. This is opposite to clinopyroxene (Fig. 3.17), but the magnitudes are very low, making large U-Th fractionations difficult.

4.2 Comparison With Previously Published Data

There are few experimental data with which I can compare my results. For clinopyroxene, Benjamin et al. (1980) measured $D_{Th}^{cpx/liq}$ = 0.029 and $D_{U}^{cpx/liq}$ = 0.018 for a $Di_{50}Ab_{25}An_{25}$ composition at 20 Kb, 1500°C, and an fO_2 of 0.5 log unit more reducing than the Fa-Mt-Qz buffer. These values are somewhat higher than my values for the $Di_{71}An_{29}$ TUBAS experiments (Table 3.7) or the $Di_{50}Ab_{25}An_{25}$ YULO experiments. The higher values of Benjamin et al. (1980) may be due to the higher pressure and temperature of those experiments. From an experiment with a natural Kilauea tholeiite at 1200°C and 14 Kb, Tatsumoto (1978) measured $D_{Th}^{cpx/liq}$ = 0.021 and $D_{U}^{cpx/liq}$ = 0.014, which are comparable to the values for the Takashima composition (Table 3.6). Watson et al. (1987) measured $D_{U}^{cpx/liq}$ = 0.0003 for Cr-diopside in an Fe-free haplobasalt sealed in air in a platinum capsule, but as they point out, the high valence states of U likely to be present in these runs casts doubt on the significance of their value to natural conditions. Significantly, both studies that report U and Th partition coefficients are consistent with my results in finding $D_{Th}/D_{U} > 1$.

Kato et al. (1988) have published the only experimental garnet-melt partitioning data for the actinides, and they report only that $D_U^{gt/liq}$ and $D_{Th}^{gt/liq}$ are probably smaller than 0.1 for majoritic garnet in ultrabasic and basic compositions at 16 - 20 GPa and 2090 - 2260°C. This is a rather poorly constrained result, but is consistent with my results for pyrope-almandine garnet-andesite partitioning at 27 Kb (2.7 GPa) and 1355 - 1313°C (Table 3.9).

Nagasawa and Wakita (1968) measured U and Th partition coefficients between large augite crystals and groundmass in the Takashima basalt. In contrast to my results, they measured a lower $D_{Th}^{aug/matrix} = 0.0121$ and a higher $D_U^{aug/matrix} = 0.0167$, giving a significantly lower $D_{Th}/D_U = 0.73$. The reason for this discrepancy is not obvious, but I propose that the composition of the groundmass Nagasawa and Wakita (1968) analyzed may not represent the liquid that the augites equilibrated with. Nagasawa's lab has a reputation for doing very careful, thorough mineral separations, and thus contamination of the clinopyroxene separates with glass seems unlikely. However, as they state, there is no definite evidence that the augites are in equilibrium with the groundmass. Based on the high Al_2O_3 content of the augites and bronzites in the Takashima basalt, Kuno (1965) concluded that these phases crystallized at a pressure corresponding to a depth near the base of the crust. Subsequent lower pressure differentiation, partial re-equilibration of high pressure phases, assimilation of the various mafic inclusions present, or any other fractionation mechanism during the (possibly long) time between augite crystallization and eruption may have changed Th/U of the liquid. One such process is the precipitation of small U- and Th-rich accessory phases after the augite. To facilitate locating such phases, I made a fission track map of a section of the Takashima basalt by irradiating it with a neutron fluence of 1.1×10^{18} n/cm^2 at the University of Missouri-Columbia Research Reactor. The map contains pervasive small, U-rich stars throughout the groundmass. SEM study of the section revealed micron size apatite and zircon crystals, which are undoubtedly the source of these stars. These minerals have high solubilities in basalts (Watson 1980; Delong and Chatelain 1990) and thus would not be stable in the Takashima

basalt at high temperature. This implies that they probably crystallized from the melt when the magmatic temperature dropped during eruption. If these apatite and zircon crystals, which preferentially incorporate U over Th, were then separated from the groundmass in the mineral separation process, the reported $D_U^{aug/matrix}$ will be too high and D_{Th}^{aug}/D_U^{aug} will be too low.

Clinopyroxene-matrix partition coefficients from natural rocks for U and Th give D_{Th}^{cpx}/D_U^{cpx} both greater than and less than 1. Partition coefficients collected from the literature (determined from mineral separates) and my experimentally determined values for the three compositions at FMQ are shown in Fig. 4.1. The data are distinguished by whole rock SiO_2 content. Although it is not obvious that SiO_2 is the best discriminant, it is often the only data available. Phenocryst-matrix partition coefficients for incompatible elements are typically larger than those determined experimentally, and in many cases this discrepancy can be attributed to impure mineral separates. This is especially likely for highly incompatible elements such as U and Th, and this problem is almost certainly responsible for much of scatter in Fig. 4.1. While crystal-melt partition coefficients can vary with melt and crystal composition (Watson 1977; Mysen and Virgo 1980; Beckett et al. 1990), the partition coefficients in Fig. 4.1 vary by up to 4 orders of magnitude, even within a single range in SiO_2. This indicates that the existing phenocryst-matrix data set for the actinides basically unreliable. This large scatter has confused U-Th fractionation modelling, permitting U and Th partition coefficients to be treated as essentially free parameters.

To my knowledge, there are no published garnet-matrix partition coefficients for the actinides in natural rocks. Fission track studies of the U distribution in garnet-bearing xenoliths from kimberlites and basalts show that the ratio of U in garnet to that in clinopyroxene is highly variable, both greater than and less than 1 (Kashkarov et al. 1988 and references therein). This variability precludes calculating reliable garnet-melt partition coefficients from these data.

Figure 4.1 Clinopyroxene-matrix partition coefficients for U and Th taken from the literature. Points along the axes are from studies that report only U or Th data. Data are subdivided by SiO_2 content, and my experimentally determined values for the three compositions at FMQ are shown for reference. Note the large amount of scatter even within a single SiO_2 range. Data from: Nagasawa and Wakita (1968), Lemarchand et al. (1987), Dostal and Capedri (1975), Dostal et al. (1976 1983), Larsen (1979), Mahood and Hildreth (1983), Onuma et al. (1981), Villemant et al. (1981), Francalanci et al. (1987), Mahood and Stimac (1990), Nash and Crecraft (1985), Wörner et al. (1983).

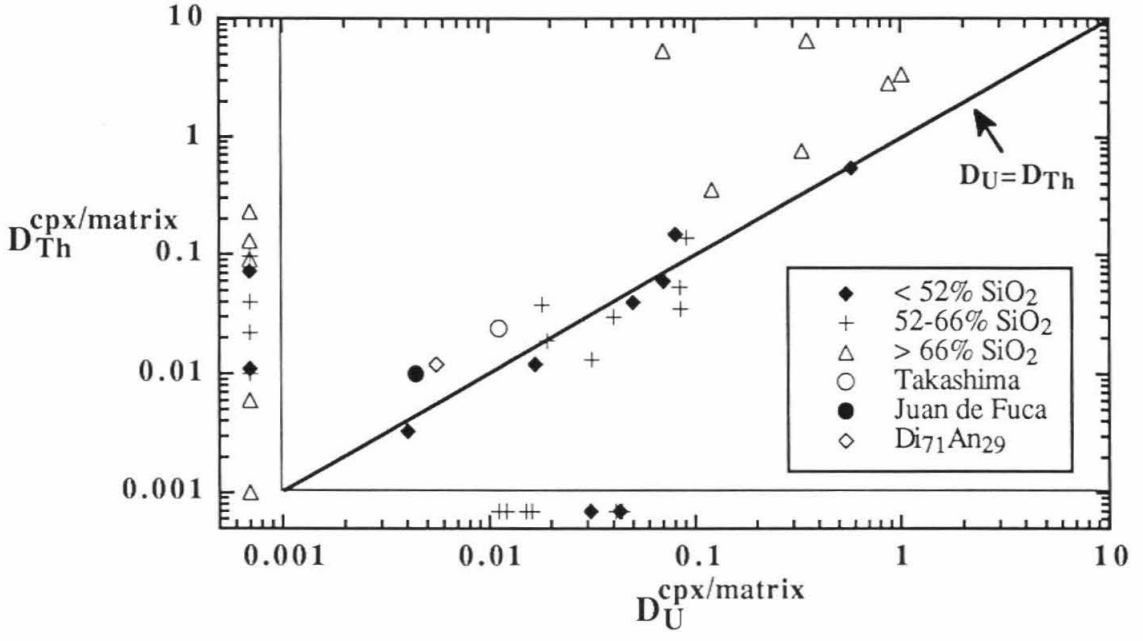
10
1
0.1
0.01
0.001
$D_{Th}^{cpx/matrix}$
0.001
0.01
0.1
1
10
$D_U^{cpx/matrix}$
$D_U = D_{Th}$
< 52% SiO_2
52-66% SiO_2
> 66% SiO_2
Takashima
Juan de Fuca
$Di_{71}An_{29}$

Figure 4.1

In summary, my results for clinopyroxene-melt partitioning are consistent with previous experiments. They constrain clinopyroxene-melt actinide partition coefficients for basaltic systems and show that $D_{Th}^{cpx/liq}$ is greater than $D_{U}^{cpx/liq}$ for fO_2s down to IW+1. There are no quantitative studies of garnet-melt or garnet-matrix partitioning with which to compare my results, though, as discussed in the next section, the relative magnitudes of $D_{U}^{gt/liq}$ and $D_{Th}^{gt/liq}$ are consistent with trends observed for the lanthanides.

4.3 Relative Magnitudes of $D_{Th}^{xtl/liq}$ and $D_{U}^{xtl/liq}$: Clues From the Lanthanides?

In addition to the absolute magnitudes of crystal-melt partition coefficients, a crucial parameter for predicting the extent of trace element fractionation is the relative magnitudes of the partition coefficients. Even if both the U and Th partition coefficients were large, crystal-melt partitioning could not significantly fractionate U from Th unless their individual partition coefficients were substantially different. Thus, the degree of U-Th fractionation produced during melting is very sensitive to the ratio of $D_{Th}^{cpx/liq}$ and $D_{U}^{cpx/liq}$.

Partition coefficient ratios are especially useful considering that compositional, temperature, pressure, and kinetic variations that affect the magnitudes of the individual partition coefficients often tend to cancel out in a ratio. Experimental and phenocryst-matrix partitioning studies have shown that while individual crystal-melt partition coefficients can vary significantly depending on composition, temperature, etc., the ratio of partition coefficients for two elements varies much less (e.g., Ray et al. 1983; Fujimaki et al. 1984). Thus, an estimate of the ratio of two partition coefficients is a convenient tool because it should be fairly insensitive to many petrogenetic variables.

In attempting to predict D_{Th}/D_{U}, it may be possible to draw parallels to the rare earth elements (REEs). Because of the approximately fixed size of crystal lattice sites, trace element partition coefficients for ions of a given charge substituting into a given crystallographic site vary smoothly with ionic radius (e.g., Onuma et al. 1968). For the

REEs, 14 nominally trivalent elements with ionic radii smoothly decreasing from 1.160 Å (La) to 0.977 (Lu) Å (Shannon 1976), crystal-melt partition coefficients often display smooth variations from La to Lu (e.g., see McKay 1989). This regular behavior for the REE element partition coefficients could be used as an aid for predicting actinide element partitioning behavior if the partitioning trends for Th and U, whose ionic radii coincide with those of Tb and Er, respectively (Shannon 1976), match the trends for the REEs. REE- and actinide-matrix partition coefficients for zircon and allanite from the Bishop Tuff and Sierra La Primavera show such a match (Mahood and Hildreth 1983), as do REE and actinide abundances in zircon, allanite, sphene, and apatite from the Penninsular Ranges batholith (Gromet and Silver 1983; L. T. Silver, unpublished data). Thus, it may be possible to infer trends for Th and U partition coefficients for other minerals in other rocks from the trend for REE partition coefficients between Tb and Er. A systematic correlation between actinide and REE partitioning trends would provide one with the advantage of being able to predict actinide partitioning trends from the much larger database of REE partition coefficients.

The Th and U partitioning behavior for the crystalline phases I studied can, to a limited degree, be explained by the slope of the REE partition coefficient trend between Tb and Er. Garnet preferentially incorporates the heavy REE over the lights, and the REE partition coefficient trend for garnet increases quite steeply with decreasing ionic radius. Figure 4.2a shows $D_{REE}^{gt/liq}$ vs. atomic number for a variety of experimental crystal-melt and natural phenocryst-matrix (in-situ analyses only) pairs collected from the literature. The slope is positive and steep, with $D_{REE}^{gt/liq}$ increasing 3 - 5 orders of magnitude from La to Lu. Also shown in Fig. 4.2a are my experimentally determined values for $D_{Th}^{gt/liq}$ and $D_{U}^{gt/liq}$ plotted in the positions of the REE with the same ionic radii (Tb and Er). The trend for Th and U qualitatively matches the trend for the REE. Both have a steep positive slope, demonstrating preferential incorporation of smaller ions. A complication with this comparison is that partition coefficient-ionic radius trends are meaningful only when all

Figure 4.2 Crystal-melt and in situ phenocryst-matrix rare earth element (REE) partition coefficients from the literature for garnet (a), clinopyroxene (b), olivine (c), orthopyroxene (d), and amphibole (e). Data are for a wide range in composition, temperature and pressure. Dashed curves: phenocryst-matrix measurements from natural samples (electron microprobe and SIMS analyses only); solid curves: experimental crystal-melt measurements. Each mineral has a characteristic shape that is largely independent of the particular conditions. Th and U partition coefficients are also plotted in the positions of Tb and Er, the REEs of corresponding ionic radii. Th and U data for garnet and clinopyroxene are from this study, olivine and orthopyroxene are from Kennedy et al. (1992). The steep positive trend for garnet and subtle negative trend for clinopyroxene REE partition coefficients between Tb and Er are qualitatively consistent with the actinide partitioning trends determined in this study. This correspondence does not appear to hold for olivine and orthopyroxene. Partition coefficient-ionic radius trends are only meaningful for ions of the same charge; the presence of U^{5+} causes measured D_U to be lower limit for $D_{U^{4+}}$, complicating the comparison.

Experimental data, garnet: Nicholls and Harris (1980), Shimizu and Kushiro (1975), Ohtani et al. (1989), Yurimoto and Ohtani (1992), Fujimaki et al. (1984); clinopyroxene: Fujimaki et al. (1984), Kuehner et al. (1989), Grutzeck et al. (1974), Nicholls and Harris (1980), Green and Pearson (1983), McKay et al. (1986); olivine: McKay and Weill (1977), Colson et al. (1988); Nielsen et al. (1992), McKay (1986); orthopyroxene: Colson et al. (1988); Nielsen et al. (1992), McKay et al. (1986); amphibole: Nicholls and Harris (1980); Green and Pearson (1985). Natural data, garnet: Sisson and Bacon (1992); clinopyroxene: Sisson (1991), MacRae and Russell (1987); orthopyroxene: Sisson (1991).

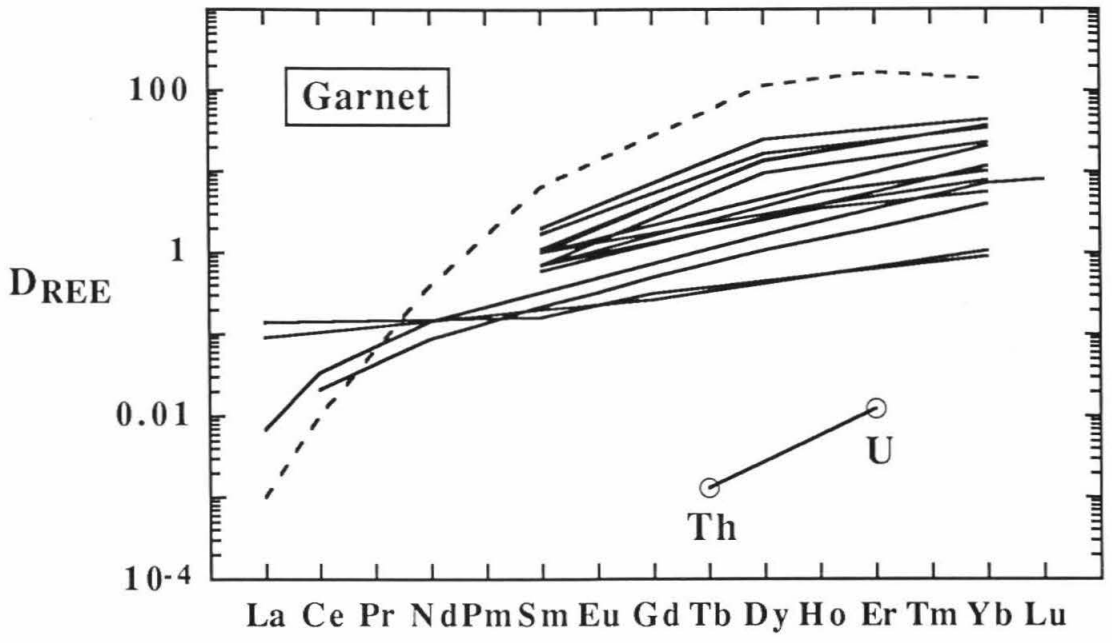
Garnet
100
1
0.01
10-4
DREE
U
Th
La Ce Pr Nd Pm Sm Eu Gd Tb Dy Ho Er Tm Yb Lu

Figure 4.2a

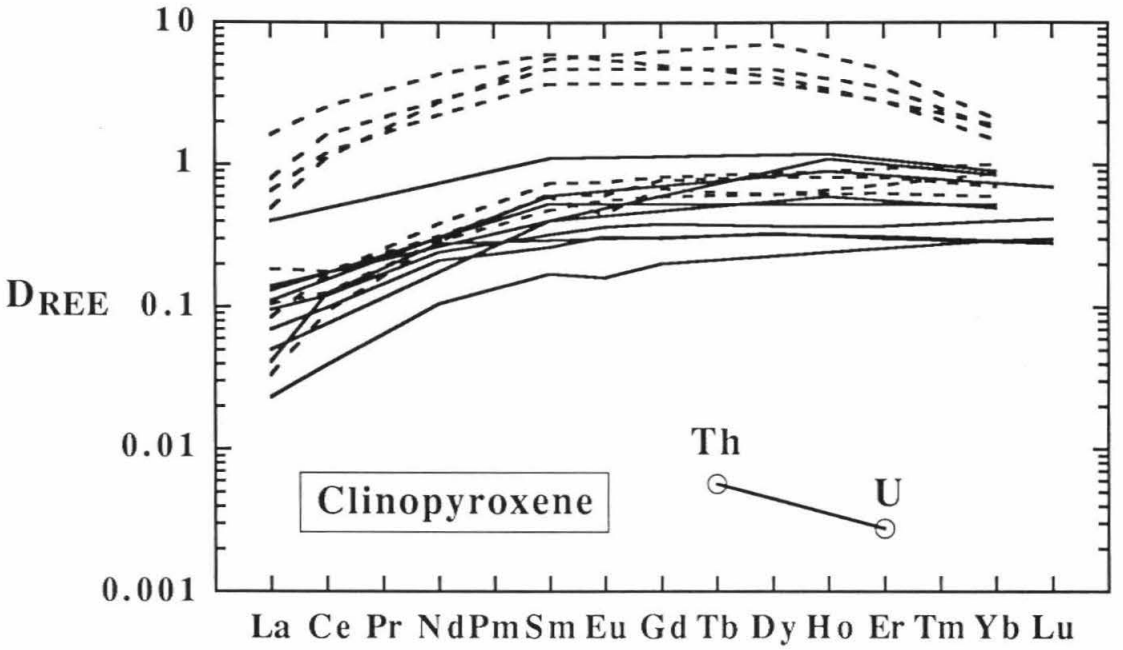
10
1
DREE 0.1
0.01
0.001
Clinopyroxene
Th
U
La Ce Pr NdPmSm Eu Gd Tb Dy Ho Er Tm Yb Lu

Figure 4.2b

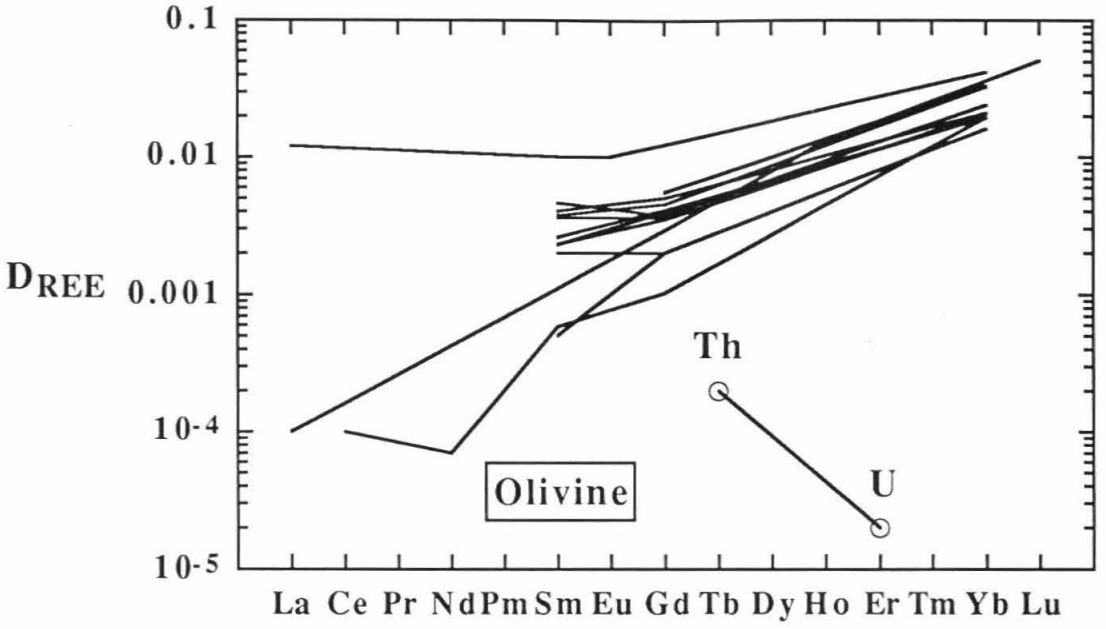
0.1
0.01
DREE 0.001
10-4
10-5
Th
U
Olivine
La Ce Pr Nd Pm Sm Eu Gd Tb Dy Ho Er Tm Yb Lu

Figure 4.2c

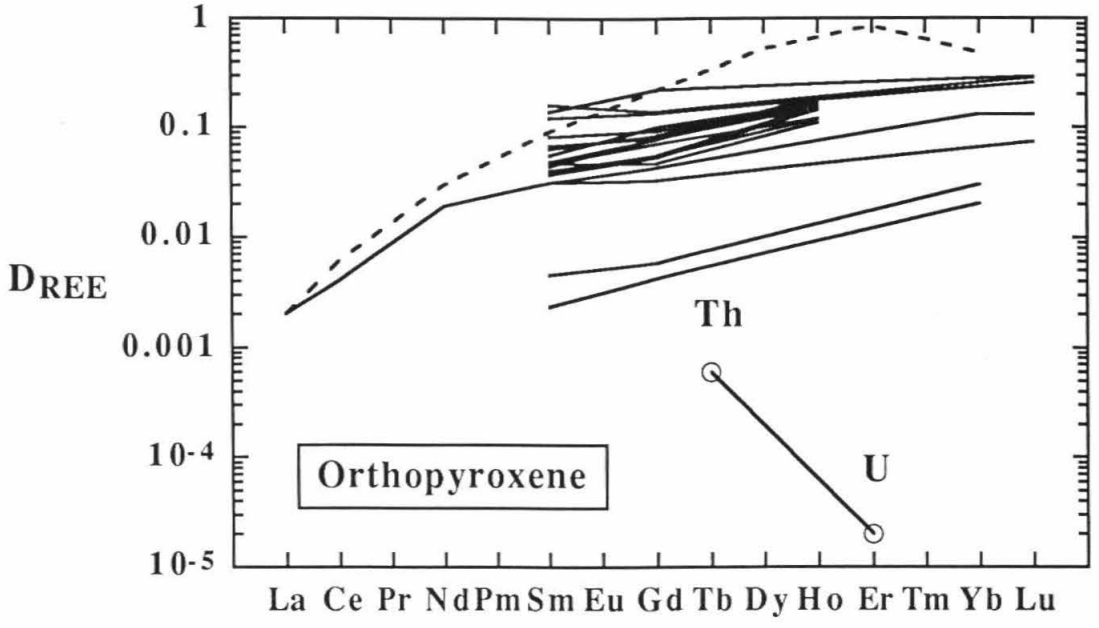
1
0.1
0.01
0.001
10-4
10-5
DREE
Th
U
Orthopyroxene
La Ce Pr Nd Pm Sm Eu Gd Tb Dy Ho Er Tm Yb Lu

Figure 4.2d

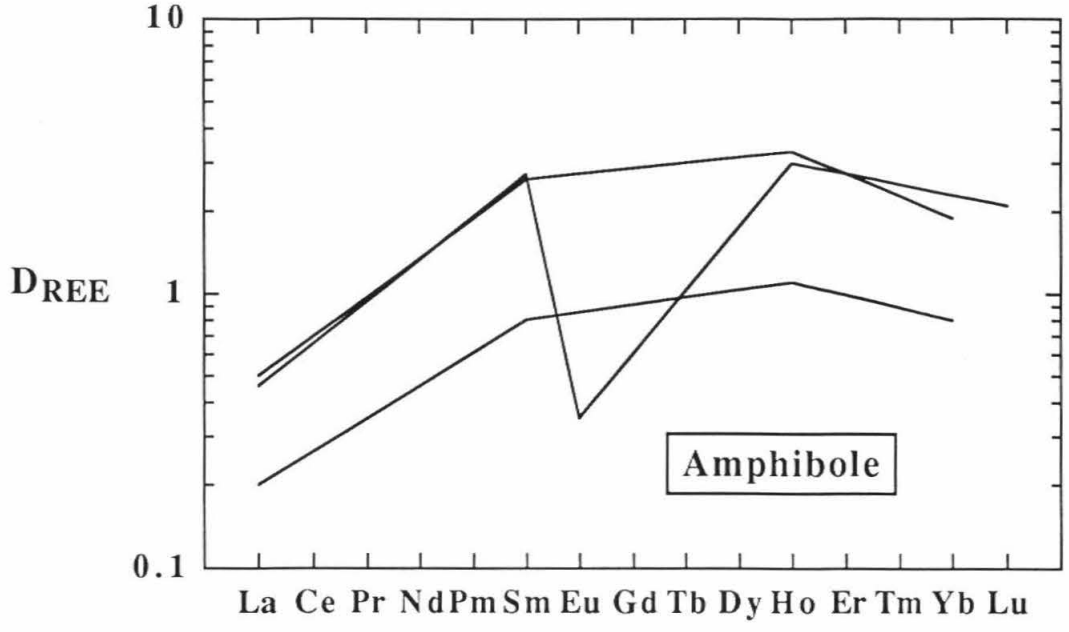

Figure 4.2e

ions in a given trend have the same charge. As discussed in reference to clinopyroxene in section *3.1.6.1*, the likely presence of U^{5+} in my experiments makes $D_U^{gt/liq} < D_{U^{4+}}^{gt/liq}$. Compensating for U^{5+} will steepen the garnet-melt partitioning trend for tetravalent actinides, although increasing $D_U^{cpx/liq}$ by a factor of two would barely be perceptible in Fig. 4.2a.

The REE partitioning pattern for clinopyroxene is less well defined than for garnet. While clinopyroxene partition coefficients are generally lowest for the light REE, the trend towards the heavy REE is fairly flat. This is illustrated in Fig. 4.2b, which shows data for $D_{REE}^{cpx/liq}$ vs. ionic radius collected from the literature. Taken as a whole, the clinopyroxene partition coefficients appear to display essentially no slope through the middle to heavy REEs, although the slope of the high silica rhyolite data of Sisson (1991) is noticeably negative. Compared to the REE trends, my experimentally determined Th and U partition coefficients for the Juan de Fuca basalt have a relatively steep negative slope. However, this difference can be explained entirely by the charge difference between Th and U. Figure 3.9b shows that $D_{Th}^{cpx/liq}/D_U^{cpx/liq} \approx 1$ at IW+1, suggesting that $D_{U^{4+}}^{cpx/liq}$ is at least as large as $D_{Th^{4+}}^{cpx/liq}$. Thus, the tetravalent actinide partition coefficient trend for clinopyroxene will be approximately flat or even have a slightly positive slope, consistent with the HREE trend.

The observation that the actinide and lanthanide partitioning trends may qualitatively mimic each other for different minerals has two important implications. The first is that it suggests that the actinides may substitute into crystal lattice sites as opposed to defects. From an electron paramagnetic resonance study, Morris (1975) concluded that Gd^{3+} and Eu^{2+} reside in the eight-fold coordinated M2 (Ca) site in diopside. In addition, single crystal X-ray structural refinements on clinopyroxenes with known REE contents also support REE substitution into the M2 site (Oberti and Caporuscio 1991). For garnet, Nicholls and Harris (1980) observed a correlation between $D_{Sm}^{gt/liq}$ and the grossular content of the garnet, suggesting that Sm substitutes into the eight-fold cation site normally

occupied by Ca, Mg, and Fe. In light of the existing, albeit limited, evidence that REEs substitute into crystal lattice sites in clinopyroxene and garnet, the qualitative correlation of actinide and REE partitioning trends implies that the actinides may also be incorporated into lattice sites.

The second potential application of an actinide-REE partition coefficient correlation is that it may allow me to qualitatively predict actinide partitioning trends for other minerals for which U and Th partition coefficients are not yet available. Unfortunately this does not appear promising. Olivine and orthopyroxene REE partition coefficients from the literature are shown in Fig. 4.2c and d. Also shown are the recent U and Th partition coefficient measurements of Kennedy et al. (1992) for a synthetic chondrule composition and fO_2 = 0.5 log units below the Fe-FeO buffer. These data are for a 100°C/hr cooling rate experiment and the magnitudes of the individual partition coefficients should perhaps be considered with some caution. However, as was shown in this study, the sense of D_{Th}/D_U is likely to be independent of the cooling rate and thus correct. The positive slope of the D_{REE} trend between Tb and Er for both olivine and orthopyroxene is in stark contrast to the negative actinide trend. Some U^{5+} is likely to still be present at the low fO_2 of these experiments, but, as with garnet, a factor of two increase in $D_U^{ol/liq}$ or $D_U^{opx/liq}$ would not resolve the problem. This contrast therefore appears to be in violation of Onuma systematics.

The trend for D_{REE} in amphibole is similar to that for clinopyroxene (Fig. 4.2e), but with a more pronounced decrease for the REEs heavier than Ho. Neglecting the negative Eu anomaly, the trends are convex upward, with a peak between Gd and Lu. The curvature of the trends suggests that $D_{Tb}^{amph/liq} \geq D_{Er}^{amph/liq}$, and hence that $D_{Th}^{amph/liq} \geq D_{U^{4+}}^{amph/liq}$. The presence of U^{5+} in natural magmas would then require $D_{Th}^{amph/liq} > D_U^{amph/liq}$. This sense is consistent with the amphibole-matrix partition coefficient measurements of Dostal et al. (1983), who found $D_{Th}^{amph/liq}/D_U^{amph/liq} = 5$. The values of D_{REE} for amphibole are greater than those for clinopyroxene, indicating that actinide partition coefficients may also be greater

for amphibole. This may have important consequences for U and Th partitioning during melting of an amphibole-bearing source such as the hydrated mantle wedge above a subducting slab.

The existing data indicate that there is a qualitative correlation between lanthanide and actinide partition coefficient trends as a function of ionic radius for garnet, clinopyroxene, and the accessory phases zircon, allanite, sphene, and apatite. The trends are anti-correlated for olivine and orthopyroxene. All of the correlations are complicated by the presence of U^{5+} in natural and experimental systems, which will make $D_U < D_{U^{4+}}$. The broadly consistent slopes for lanthanides and actinides in several minerals indicates that actinide partitioning is sensitive to ionic radius. Further, the relative magnitudes of lanthanide and actinide partition coefficients are consistent from mineral to mineral, i.e., minerals with large D_{REE} have large $D_{actinide}$. If the anomalous behavior of olivine and orthopyroxene can be explained, the similarities between REE and actinide partitioning trends may be useful for predicting qualitative relationships between REE and U-Th fractionations for different mineral assemblages.

4.4 U-Th Fractionation

4.4.1 ^{238}U-^{230}Th disequilibrium in young MORB and OIB

A unique aspect of U series decay is that a system will always return to secular equilibrium in ≈ 3 - 5 daughter half-lives, providing well constrained initial conditions. In the case of ^{238}U-^{230}Th disequilibrium, this means that, if a system has been undisturbed by any fractionating processes for approximately 300 Ka or more, the activities of ^{238}U and ^{230}Th will be equal. This time scale is short enough that the source regions for volcanic rocks are often considered to be in secular equilibrium. When U and Th are fractionated by a process such as partial melting, secular equilibrium is disturbed, and the system will return to equilibrium through the radioactive decay of ^{238}U and ^{230}Th. Before a significant amount of ^{230}Th has decayed (the first ≈ 10,000 years after fractionation),

however, the degree of ^{238}U-^{230}Th radioactive disequilibrium is equal to the degree of U-Th fractionation produced during the fractionation event (i.e., $(^{238}U/^{230}Th)_{melt} = [U/Th]_{melt}/[U/Th]_{source}$, where parentheses indicate activity ratios and brackets indicate elemental ratios). Therefore, we know that a young volcanic rock with $(^{238}U/^{230}Th) < 1$ has U/Th less than that of its source, and ^{238}U-^{230}Th disequilibrium in young volcanic rocks can be used as a quantitative measure of U-Th fractionation.

^{238}U-^{230}Th disequilibrium measurements have been made on volcanic rocks from a variety of geologic settings; good reviews of the data and the systematics are presented by Condomines et al. (1988) and Gill et al. (1992). Based on such measurements, MORB and OIB are distinguished from other rock types by consistently having $k \leq 1$, where $k \equiv (^{238}U/^{230}Th)$ after Allègre and Condomines (1982). As shown in Fig. 4.3, the maximum degree of disequilibrium observed in young (< 10 Ka) MORB and OIB is about $k = 0.6$, with an average of about $k = 0.87$ for each. This disequilibrium results from a process that fractionates U from Th, the nature of which has been speculated upon, but never determined. Trace element fractionation can result from a variety of geological processes, including partial melting, separation of immiscible liquids, crystallization, assimilation of xenolithic material, degassing, oxidation, hydrothermal alteration, and weathering. It is important to point out, however, that among the different mechanisms thought to exist, U-Th fractionation resulting in ^{238}U-^{230}Th disequilibrium in MORB and OIB is usually ascribed to partial melting (e.g., Condomines et al. 1988; Ben Othman and Allègre 1990; Goldstein et al. 1992; Turekian et al. 1991). In the following paragraphs I use my experimental results to calculate the degree of U-Th fractionation generated by partial melting. With the results of these calculations I then evaluate the hypothesis that ^{238}U-^{230}Th disequilibrium in MORB and OIB originates from partial melting.

The important unknowns in predicting trace element fractionation during partial melting are the composition of the source, the melting process (e.g., equilibrium,

Figure 4.3 ^{238}U-^{230}Th disequilibrium plotted against Th content for young MORB (a) and OIB (b) from the literature. Samples that authors claim have had activities changed by seawater alteration have been excluded. For young rocks (< 10 Ka) the degree of disequilibrium, k, equals U-Th fractionation. Within the indicated typical error, almost all samples have $k \leq 1$. Note that the range in k is nearly identical for both MORB and OIB. There is no correlation between k and Th content, suggesting that the degree of disequilibrium is not related to the degree of melting.

MORB data: FAMOUS and MAPCO: Condomines et al. (1981a); Gorda and Juan de Fuca: Goldstein et al. (1989 1991); RISE: Newman et al. (1983); EPR 13°N: Ben Othman and Allègre (1990); EPR 12°N: Rubin and Macdougall (1988); EPR 11°N: Reinitz and Turekian (1989); Galapagos: Krishnaswami et al. (1984). OIB data: Mauna Loa and Kilauea: Somayajulu et al. (1966), Condomines et al. (1976), Krishnaswami et al. (1984), Newman et al. (1984); Hualalai: Somayajulu et al. (1966), Newman et al. (1984); Loihi: Newman et al. (1984); Iceland: Condomines et al. (1981b), Hemond et al. (1988), Krishnaswami et al. (1984); Tristan de Cunha and Azores: Oversby and Gast (1968); Marion and Samoa: Newman et al. (1984).

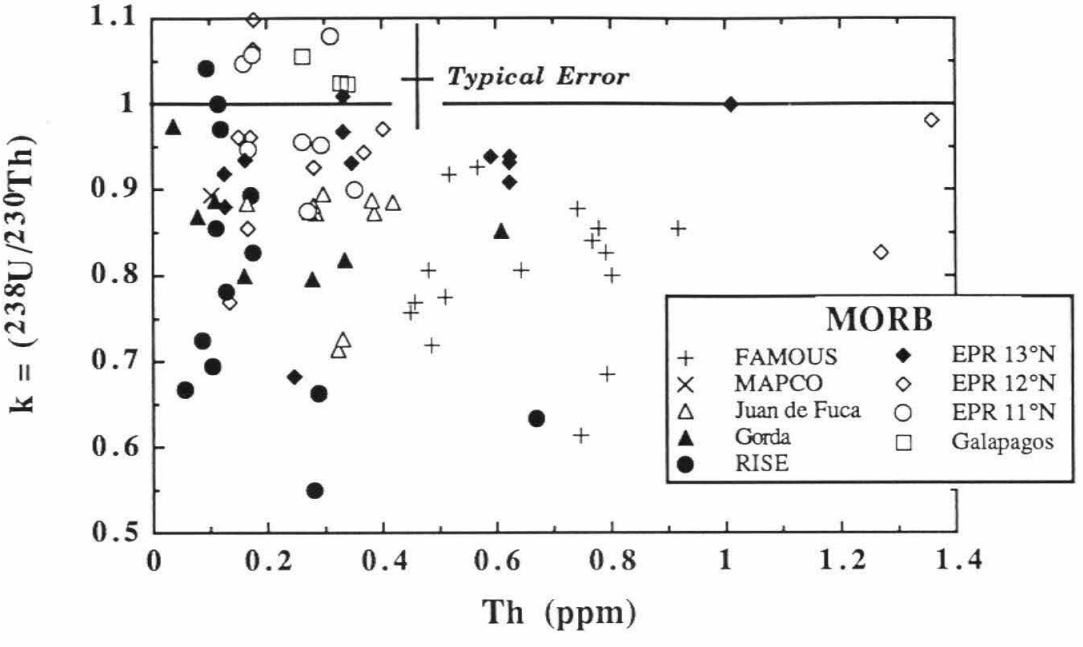
1.1
1
0.9
0.8
0.7
0.6
0.5
k = (238U/230Th)
0
0.2
0.4
0.6
0.8
1
1.2
1.4
Th (ppm)
Typical Error
MORB
FAMOUS
MAPCO
Juan de Fuca
Gorda
RISE
EPR 13°N
EPR 12°N
EPR 11°N
Galapagos

Figure 4.3a

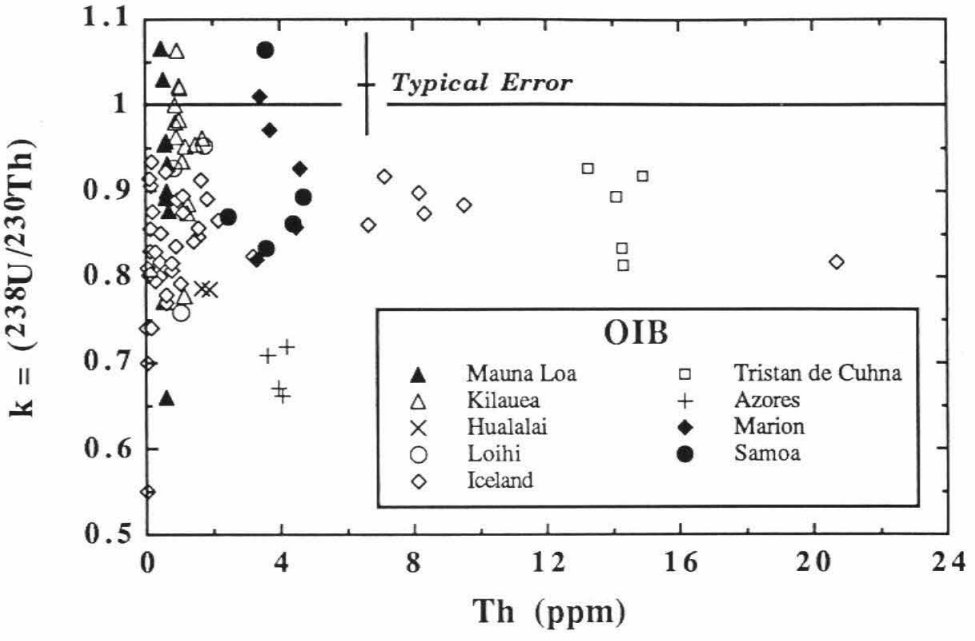
1.1
1
0.9
0.8
0.7
0.6
0.5
k = (238U/230Th)
0
4
8
12
16
20
24
Th (ppm)
Typical Error
OIB
Mauna Loa
Kilauea
Hualalai
Loihi
Iceland
Tristan de Cuhna
Azores
Marion
Samoa

Figure 4.3b

fractional, dynamic), the melting proportions of the various phases in the source, the pressure range and extent of melting, and the crystal-melt partition coefficients of the various solid phases in the source. Results from experimental phase equilibrium studies, analyses of natural MORB glasses and abyssal peridotites, and geophysical and geochemical models, while disagreeing on several details, are generally consistent in finding that MORB is produced by partially melting spinel lherzolite (e.g., Kinzler and Grove 1992a,b; Thompson 1987; Klein and Langmuir 1987; Dick et al. 1984; McKenzie and Bickle 1988). The exact phase proportions in the MORB source are not well constrained. I have used the estimate for primitive upper mantle of $olivine_{57}orthopyroxene_{25.5}clinopyroxene_{15}spinel_{2.5}$ (wt%) from Kostopoulos (1991). I chose this assemblage, which is based on a large number of experimental and analytical studies, because it probably errs on the high side for modal clinopyroxene, which is the most important phase in terms of crystal-melt U and Th partitioning. In general, I have chosen values for uncertain parameters such that the degree of U-Th fractionation generated during melting will be maximized.

The U and Th concentrations in the MORB source are also poorly constrained. While unnecessary for calculating ^{238}U-^{230}Th disequilibrium as a function of degree of melting, some concentration variable is needed to display fractionation trends. For this I have used the Th concentration. Estimates for the composition of the bulk silicate Earth (mantle + crust) based on chondritic abundances, concentrations in mantle lherzolites, and heat flow all give remarkably similar results of about 20 and 75 ppb for U and Th, respectively, giving $Th/U \approx 3.75$ (Taylor 1982; Chen et al. 1992b; Hart and Zindler 1986; Wänke et al. 1984; Anderson 1989; Jagoutz et al. 1979; Ringwood 1977; Taylor 1979). The above models are for a primitive mantle, while the MORB source has been shown to be depleted in most incompatible elements (e.g., Tatsumoto et al. 1965). The extent of this depletion is unknown, but based on Th and U measurements in MORB (e.g., Jochum et al. 1983) I

have estimated values of 5 and 11 ppb to represent the U and Th concentrations in the depleted MORB source.

The calculations were made for two melting models so that the differences can be compared. For any melting model, the contributions of the various phases to the melt, or melting proportions must be constrained. The melting proportions are the constant fractions of each residual phase that are contributed to every increment of melting (Shaw 1970). The data summarized by Kostopoulos (1991) shows that clinopyroxene is by far the major contributor to the melt, with melting proportions ranging from 40 - 73 wt%. The range of melting proportions he determined solely from major element phase equilibria studies is $olivine_{0\text{-}5}orthopyroxene_{5\text{-}15}clinopyroxene_{60\text{-}80}spinel_{10\text{-}20}$ and is in good agreement with the melting proportions inferred from analyses of natural MORBs and peridotites (e.g., Klein and Langmuir 1987). I have used intermediate values of $olivine_5orthopyroxene_{14}clinopyroxene_{66}spinel_{15}$ in my calculations. For reasonable melt fractions (> 5%), modal and non-modal melting produce indistinguishable fractionations for very incompatible elements such as U and Th.

The final parameters required are the crystal-melt partition coefficients. The values I have chosen are listed in Table 4.1. The clinopyroxene partition coefficients are from this study. Analyses of Fe^{3+}/Fe^{2+} in MORB glasses indicate that melting in the MORB source region occurs at an fO_2 about 2 log units more reducing than NNO (Christie et al. 1986; Carmichael 1991). I derived the values in Table 4.1 by interpolating the data for the Juan de Fuca basalt. For olivine, I have used the upper limits of 0.0004 and 0.0005 for $D_U^{ol/liq}$ and $D_{Th}^{ol/liq}$ determined from this study. The orthopyroxene-melt partition coefficients are from Kennedy et al. (1992). The uncertainty on these values is unimportant, as the contribution of olivine and orthopyroxene to U-Th fractionation is negligible compared clinopyroxene. Finally, spinel-melt partition coefficients for U and Th have been arbitrarily set at 0. Again, the uncertainty on this value is unimportant, as the spinel-melt partition coefficients are likely to be less than those for olivine.

TABLE 4.1

U and Th Partition Coefficients Used for Melting Calculations

Phase	$D_U^{xtl/liq}$	$D_{Th}^{xtl/liq}$	reference[a]
olivine	0.0004	0.0005	1
orthopyroxene	0.00002	0.0006	2
clinopyroxene	0.0031	0.0057	1
spinel	0	0	3
garnet	0.0122	0.0013	1

(a) 1: this study; 2: Kennedy et al. (1992); 3: inferred

Using the above parameters, I have calculated the ^{238}U-^{230}Th disequilibrium generated by various degrees of partial melting of a source in secular equilibrium for two simple melting models. Results are plotted as k vs. Th concentration in the melt in Fig. 4.4. Each curve shows the locus of k values for independent melting calulations at various degrees of melt extraction. The solid curve is for an equilibrium melting case (Shaw 1970), assuming $k = [U/Th]_{melt}/[U/Th]_{source}$, as explained at the beginning of this section. The dashed curve is calculated using a dynamic melting model (Langmuir et al. 1977; McKenzie 1985) adapted to ^{238}U-^{230}Th disequilibrium by Williams and Gill (1989). This model approximates a column of upwelling mantle undergoing pressure-release melting. The melting rate remains constant, and the melt is extracted as soon as it is formed. A fixed melt fraction remains in the matrix at all times– this corresponds to the minimum melt fraction required for melt extraction. A significant aspect of this model, pertinent to radioactive disequilibrium, is that it allows for changes in k during a finite melting time. Specific input parameters for this model are listed in the caption to Fig. 4.4. For a typical mantle upwelling rate of 5 cm/yr (estimated from the half-spreading rate at the ridge), the melting rate is slow enough that the U in the residue can produce ^{230}Th fast sufficiently fast to remain in secular equilibrium. The resulting disequilibrium in the extracted melt then attains a constant value expressed as:

$$k = \frac{D_{Th}^{bulk/liq}\rho_s(1 - \emptyset) + \rho_l\emptyset}{D_U^{bulk/liq}\rho_s(1 - \emptyset) + \rho_l\emptyset},$$

where ρ_s and ρ_l = the solid and liquid densities, respectively, and $\emptyset$ = the melt-filled porosity (assumed to remain constant) in the upwelling mantle (McKenzie 1985). Modal melting, while unrealistic, was used for the dynamic melting calculation because dynamic melting models have not been worked out for non-modal melting. Allowing clinopyroxene to melt in the correct proportion will decrease k, i.e., decrease the degree of disequilibrium (move the dashed curve down). However, as noted previously, the difference between modal and non-modal melting will be imperceptible for $F > 0.05$. Comparing the inset in

Figure 4.4 Calculated ^{238}U-^{230}Th disequilibrium generated for partial melting of a model spinel lherzolite plotted as a function of melt Th concentration for equilibrium and dynamic (Williams and Gill 1989) melting. Phase proportions in source = $ol_{57}opx_{25.5}cpx_{15}sp_{2.5}$ and melting proportions (for equilibrium melting only) = $ol_{50}opx_{14}cpx_{66}sp_{15}$. Dynamic melting calculation is modal because non-modal dynamic melting models are not available, though for melt fractions > 5% modal and non-modal melting are indistinguishable. Partition coefficients are listed in Table 4.1. Tick marks along curves give the melt fraction extracted. For dynamic melting, upwelling rate (≈ half spreading rate at ridge) = 5 cm/yr, thickness of melting region = 40 Km (McKenzie and Bickle 1988), ρ_{solid} = 2.8, ρ_{melt} = 2.6, and initial batch melt = porosity throughout melting = 1%. Parameters were chosen such that the magnitude of the calculated disequilibrium is maximized. Melting rate is slow enough that k from dynamic melting attains a constant value (see text). Inset shows same figure with Y axis at the same scale as Fig. 4.3 to emphasize lack of overlap with oceanic basalt data. Note that k is always > 1, opposite of oceanic basalt data (Fig. 4.3a).

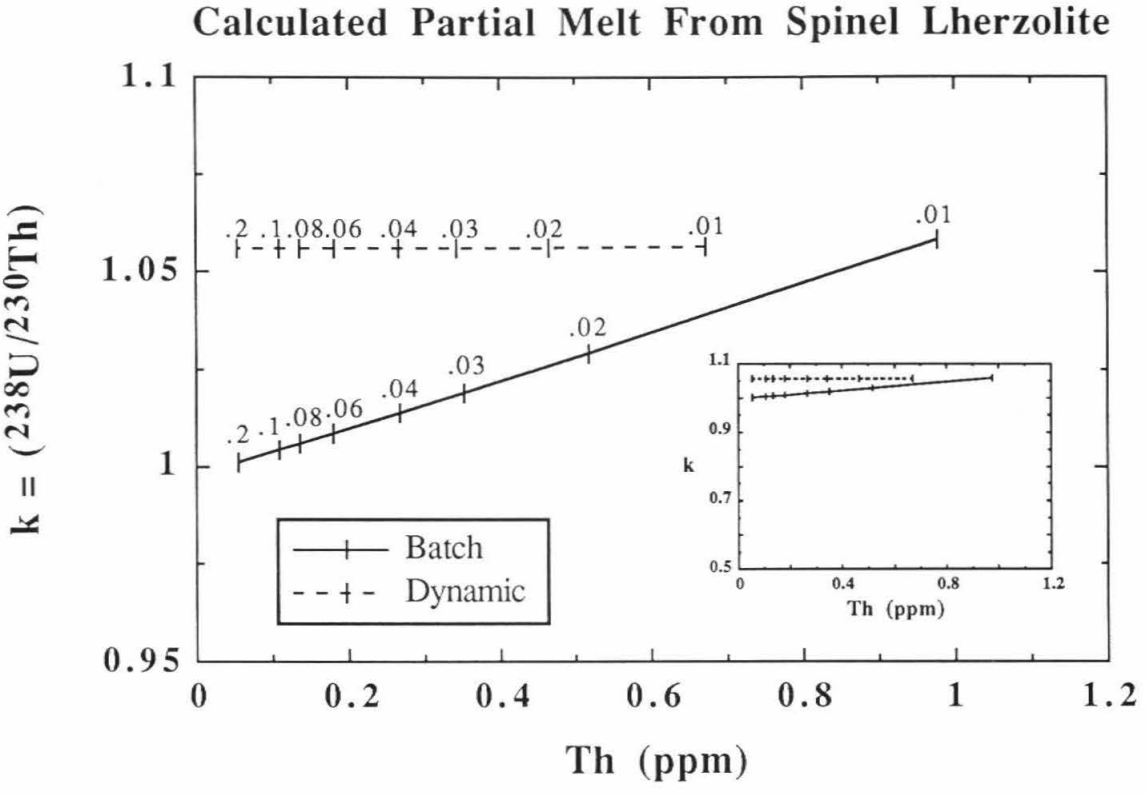
Calculated Partial Melt From Spinel Lherzolite
k = (238U/230Th)
Th (ppm)
Batch
Dynamic
.2
.1
.08
.06
.04
.03
.02
.01
k
Th (ppm)

Figure 4.4

Fig. 4.4 with the field of MORB analyses from Fig. 4.3a, there is essentially no overlap with the calculated trends for either batch or dynamic melting.

The most important result of this calculation is that the ^{238}U-^{230}Th disequilibrium observed in MORB cannot be produced during partial melting of a spinel lherzolite. From Fig. 4.4 it is evident that it is impossible for the melt to have $k < 1$, as this would require bulk $D_U > D_{Th}$. Clinopyroxene exerts the dominant control on the bulk partition coefficients, and the fact that my results show $D_{Th}^{cpx/liq} > D_U^{cpx/liq}$, opposite to what is required by the disequilibrium data, proves that partial melting dominated by clinopyroxene will always generate melts that are ^{230}Th depleted. This sense of fractionation follows from the measured partition coefficients and is independent of any specific model parameters. Looking at the magnitude of fractionation only, batch melting produces less than 2% disequilibrium at 5% melting, far less than the average observed value of 13%. Much larger degrees of melting are indicated for MORB (e.g., McKenzie and Bickle 1988) resulting in even less fractionation. Dynamic melting, on the other hand, is capable of generating somewhat larger degrees of disequilibrium, even at large melt fractions. This suggests that melting a different phase assemblage with $D_U > D_{Th}$ may be able to produce the observed disequilibrium.

A possible alternative to spinel lherzolite is garnet lherzolite. The results of this study indicate that U is more compatible than Th in garnet, opposite to what was found for clinopyroxene. While most phase equilibrium studies indicate that MORB is generated by partial melting of spinel lherzolite, some of these studies call for melting to begin at 25 Kbar (e.g., Elthon and Scarfe 1984), verging on the region of garnet stability (Nickel 1986). In addition, interpretations of trace element signatures from several MORB and abyssal peridotite suites have invoked a garnet-bearing residuum (Johnson et al. 1990; Langmuir et al. 1977; Bender et al. 1984; Salters and Hart 1989), and recent rare earth element modelling calls for MORB melting to begin at about 80 Km depth (McKenzie and O'Nions 1991). I have therefore made a similar calculation for partially melting a garnet

lherzolite. The modal mineral proportions I used are olivine$_{57}$orthopyroxene$_{18}$clinopyroxene$_{10}$garnet$_{15}$ (wt%) from McDonough (1990). As for the spinel lherzolite, I chose these values because they have the highest modal garnet. Melting proportions for this assemblage are not well constrained, as there is only a small experimental data set that includes garnet. The best approximation appears to be the proportions inferred from trace element analyses of diopsides in residual abyssal peridotites (Johnson et al. 1990): olivine$_3$orthopyroxene$_3$clinopyroxene$_{44}$garnet$_{50}$ (wt%). These are in fairly good agreement with the proportions used to model Lu-Hf fractionations in MORB (Salters and Hart 1989), and result in essentially the same melt composition as the melting proportions used for the spinel lherzolite. However, as the melting proportions are not important for the dynamic melting calculation, the uncertainty is not a serious problem. The garnet-melt partition coefficients for U and Th (Table 4.1) are the preferred values from this study. These values were determined for an andesitic composition, and thus are not directly applicable to basalt genesis. Partition coefficients generally increase with increasing silica content (e.g., Watson 1977), and thus the values for basalts may be lower than those used here. This again will make the calculation an upper limit on the effect of garnet in contributing to ^{238}U-^{230}Th disequilibrium.

The results of this calculation (Fig. 4.5) show that melting of a garnet lherzolite produces only a moderate ^{230}Th enrichment. While $D_U^{gt/liq} \gg D_{Th}^{gt/liq}$, its effect is offset by the effect of clinopyroxene, resulting in a bulk $D_U/D_{Th} \approx 2$. The resulting disequilibrium (10%) is somewhat less than the average value for MORB (13%), and is far less than the extreme value of 50% (Fig. 4.3a). As a test, I increased the modal proportion of garnet in the source at the expense of clinopyroxene to increase the degree of disequilibrium. The average of the observed disequilibrium values in MORB, k = 0.87, is attained when the modal proportions of clinopyroxene and garnet are 7% and 18%, respectively. When clinopyroxene is completely replaced by garnet (mode = olivine$_{57}$orthopyroxene$_{18}$clinopyroxene$_0$garnet$_{25}$), k reaches 0.81. While this

Figure 4.5 Calculated ^{238}U-^{230}Th disequilibrium generated for partial melting of a model garnet lherzolite for equilibrium and dynamic melting. Phase proportions in source = $ol_{57}opx_{18}cpx_{10}gt_{15}$ and melting proportions (for equilibrium melting only, see caption to Fig. 4.4) = $ol_{30}opx_{3}cpx_{44}gt_{50}$. Parameters for dynamic melting are as in Fig. 4.4 except thickness of melting region = 100 Km. Inset shows same figure with Y axis at the same scale as Fig. 4.3 to compare with MORB and OIB data. In contrast to melt from spinel lherzolite, k is < 1, consistent with oceanic basalt data, although calculated degree of disequilibrium is much less than observed range (Fig. 4.3).

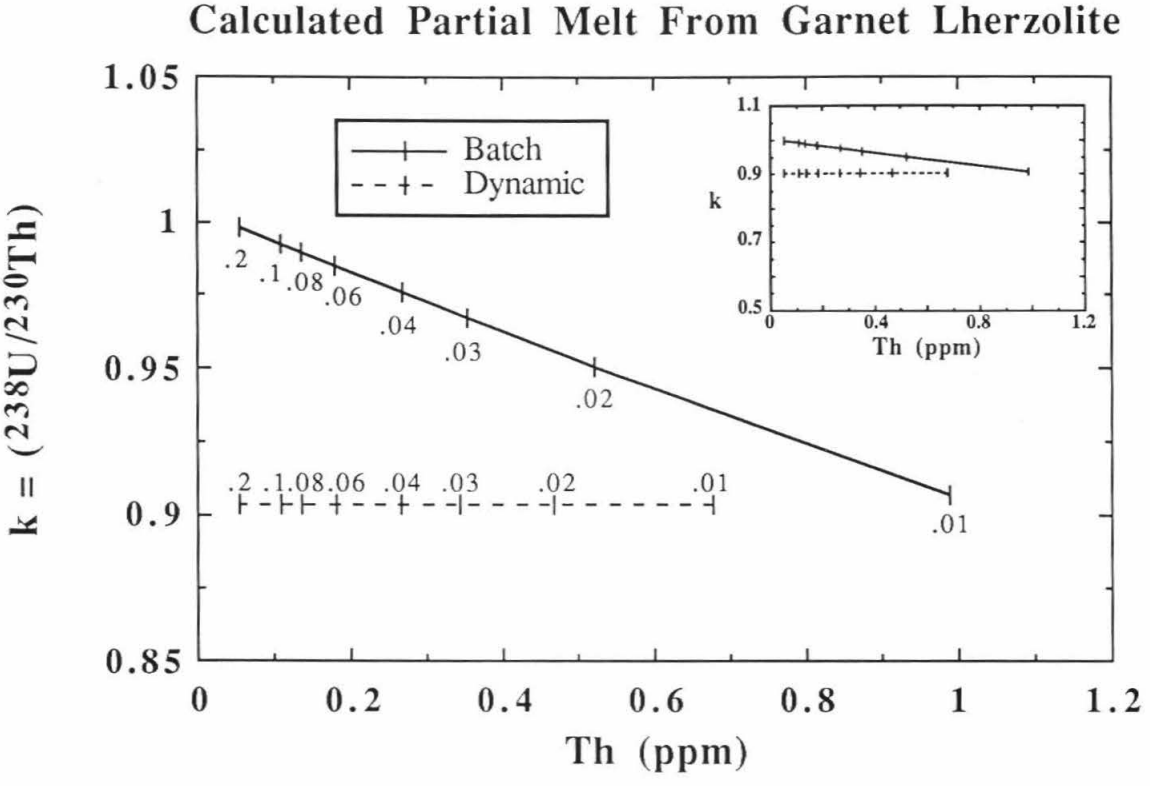
Calculated Partial Melt From Garnet Lherzolite
k = (238U/230Th)
Th (ppm)
Batch
Dynamic
.2
.1
.08
.06
.04
.03
.02
.01
k
Th (ppm)

Figure 4.5

encompasses a moderate fraction of the natural samples (Fig. 4.3a), there are a significant number that have k values well below this. Further, such a clinopyroxene-free mode is not stable in the upper mantle (Nickel 1986).

The result of the above calculation indicates that the range of ^{238}U-^{230}Th disequilibrium measured most MORB cannot be explained by partial melting of a garnet lherzolite. 40% of the samples in Fig. 4.3a, however, have less than 10% disequilibrium ($k > 0.9$) and could be explained by this mechanism, suggesting that it may be viable in some cases. Whether or not garnet-melt partitioning is actually an important U-Th fractionation mechanism in some MORB genesis is difficult to constrain with assurance. There is no geographical or other geochemical distinction between samples with $k > 0.9$ and those with $k < 0.9$. Since there must be some other mechanism causing ^{238}U-^{230}Th disequilibrium in the bulk of the samples, there is no obvious reason to call upon garnet-melt partitioning in a few special cases. Also, the calculations were designed to maximize the disequilibrium. Decreasing the modal garnet and garnet-melt partition coefficients, or increasing the mantle upwelling rate or porosity will result in less disequilibrium. Finally, the melting calculations assume that all of the melt was extracted from a garnet-bearing source. In reality, garnet will be present only in the bottom of the upwelling mantle column (that portion below about 75 Km), further reducing the degree of disequilibrium. Therefore, while it cannot be ruled out for some cases, I suspect that garnet-melt partitioning is generally, if not always, unimportant.

By similar arguments, any ^{238}U-^{230}Th disequilibrium produced by fractional crystallization will mimic the trends for partial melting, and crystallization during transport and in magma chambers is thus not a possible source of the observed disequilibrium. In any case, it should be noted that no significant U-Th fractionation in a melt will result from fractional crystallization of less than about 95%, and no garnet and very little clinopyroxene are thought to crystallize from liquids parental to MORB.

There is ample evidence from REE patterns that OIB genesis requires garnet to remain in the residuum, and thus that OIB is generated by partial melting of garnet lherzolite (Frey et al. 1991; White et al. 1979; Kay and Gast 1973; Sun and Hanson 1975; Clague 1987; Dupuy et al. 1988; Humphris and Thompson 1983). From the above calculations, it is also evident that ^{238}U-^{230}Th disequilibrium in OIB cannot be produced by partial melting of spinel or garnet lherzolite. Aside from the larger Th concentration in OIB, the data sets for OIB and MORB are very similar in terms of the degree of disequilibrium (Fig. 4.3). Thus, the OIB data would plot at the same level on the Y-axis as the MORB fields in Figs. 4.4 and 4.5.

It is possible that U and Th are fractionated by actinide-rich accessory phases in the source region of oceanic basalts. Apatite is a possible accessory phase that preferentially retains U over Th such that a coexisting melt would be Th/U-enriched (Benjamin et al. 1980). The estimated P concentration of the primitive mantle is quite low, however, (Anderson 1989) corresponding to a maximum of 0.03 wt% modal apatite if all P is in apatite. Given partition coefficients of $D_U^{ap/liq} = 1.8$ and $D_{Th}^{ap/liq} = 1.3$ (Benjamin et al. 1980), this amount of apatite will have an insignificant effect on U-Th fractionation. In addition, in order for a phase to impart a trace element fractionation signature to an extracted melt, it must remain in the residuum after the completion of melting. The solubilities of the accessory phases apatite and zircon are quite high in basalts (Watson 1980; Delong and Chatelain 1990), and thus if present, these phases would almost certainly be consumed after a small degree of melting. This interpretation is supported by the extreme rarity of apatite or zircon in mantle xenoliths. Thus, accessory phases are not considered important sources of the ubiquitous U-Th fractionations in oceanic basalts.

The above calculations strongly imply that the ^{238}U-^{230}Th disequilibrium observed in oceanic basalts does not result from partial melting of either a spinel or garnet lherzolite. Since these are thought to be primary phase assemblages in the source regions of these lavas, ^{238}U-^{230}Th disequilibrium in MORB and OIB does not appear to result from partial

melting at all. This conclusion has important significance for our understanding of melting at mid-ocean ridges. Based on ^{238}U-^{230}Th disequilibrium, certain constraints on MORB genesis have been proposed. Assuming that the bulk partition coefficients for U and Th are 0.005 and 0, respectively, McKenzie (1985) argued that the melting region beneath a ridge is over 100 Km wide, the porosity must be less than 2%, and that the melting time must be long compared to the half-life of ^{230}Th. Williams and Gill (1989) propose that MORBs are mixtures of varying proportions of a 1% melt and a 15% melt. Based on lower degrees of inferred initial disequilibrium for off-axis samples compared to axial samples from the Endeavour segment of the Juan de Fuca ridge, Goldstein et al. (1992) suggest that the degree of melting has decreased during the last 10,000 years. While I am not necessarily opposed to these models, my results fail to confirm that ^{238}U-^{230}Th disequilibrium can be used to support such interpretations. On the other hand, to the extent that Th isotope ratios reflect the source region and not U-Th fractionation processes, conclusions regarding mantle heterogeneity or contamination based on variations in ($^{230}Th/^{232}Th$) are unaffected by my results (e.g., Ben Othman and Allègre 1990; Hemond et al. 1988).

The conclusion that ^{238}U-^{230}Th disequilibrium in MORB may not result from crystal-melt partitioning during partial melting is supported by additional observations. Dynamic melting predicts that lavas from slow spreading ridges should have greater disequilibrium than those from faster spreading ridges, but no correlation is observed (Gill et al. 1992). Disequilibrium produced by crystal-melt partitioning should also result in a correlation between k and some indicator of degree of melting, such as the Th content, but it does not (Fig. 4.3a; Gill et al. 1992). Finally, it has been shown that ^{238}U-^{230}Th disequilibrium in arc rocks and some extreme ^{230}Th-^{226}Ra disequilibrium in MORB require models more complex than partial melting (Rubin and Macdougall 1988; Gill and Williams 1990).

Arguing that ^{238}U-^{230}Th disequilibrium in oceanic basalts does not result from partial melting compels me to address some other geochemical data which have been interpreted as indicating that Th is more incompatible than U. Jochum et al. (1983) found a positive

correlation between $^{232}Th/^{238}U$ and ^{232}Th for MORB, although no such correlation exists for the samples plotted in Fig. 4.3a. These authors interpreted this correlation as evidence that Th is preferentially extracted over U with progressive melting. Their interpretation assumes that all of the Th/U variation in MORB reflects Th/U heterogeneity in the source, which in turn results from variable degrees of prior depletion. Also, $(^{230}Th/^{232}Th)$ is negatively correlated with $^{87}Sr/^{86}Sr$ in MORB and OIB (Condomines et al. 1981a), which implies that Th/U and Rb/Sr are positively correlated in the mantle. Based on Rb being more incompatible than Sr, this correlation has also been interpreted as evidence that Th is less compatible than U (Condomines et al. 1988). My results show that these interpretations cannot be the case for a melting of a peridotite source, and suggest that neither U-Th nor Rb-Sr fractionations are crystal-melt controlled.

In order to explain the observed ^{238}U-^{230}Th disequilibrium in oceanic basalts, any U-Th fractionation mechanism must be large, ubiquitous, and result in $k < 1$. Possible alternatives to crystal-melt fractionation during partial melting include: (a) fractionation of the mantle source shortly prior to melting, either by extraction of a minute melt fraction with low Th/U or addition of a high Th/U mobile fluid phase; (b) melt-vapor fractionation during degassing; (c) recent contamination of the magma by hydrothermally altered oceanic crust; (d) reversal of the sense of U-Th fractionation by clinopyroxene at high pressure.

Mechanism (a) is tempting because U and Th are extremely magmaphile and will concentrate in the melt phase after a very small degree of melting. If a recent event, this will leave behind a highly fractionated residual solid (in the correct sense for oceanic basalts, i.e., $k < 1$) that may be still fertile enough to produce basalt. A difficulty with this type of fractionation is separating and hiding the highly fractionated initial melt. Recently, Stolper and Newman (in revision) have successfully modelled variations of 20 trace elements, including U and Th, in a suite of Marianas trough basalts as resulting from the addition of a trace element laden H_2O-rich component to the source. This component is enriched in Th relative to U, and if recent, this addition will decrease k. They assume that

the ultimate origin of this fluid component is the subducting slab; designating the origin of a similar component in the MORB source is somewhat more problematic, but this type of mechanism appears to be viable.

Because of the low volatile content of oceanic basalts, vapor-melt fractionation (b) requires large U and Th enrichments in the vapor phase to be significant. Fission track data from fluid inclusions in ultramafic xenoliths (Polve and Kurz 1984) and rhyolite melt-vapor partitioning experiments (London et al. 1988; Keppler and Wyllie 1990) indicate that very little U or Th partitions into the vapor phase.

Most MORB has undergone extensive hydrothermal alteration (c), as evidenced by ^{18}O exchange (Muehlenbachs 1986). Based on detailed sampling of the Oman ophiolite, Gregory and Taylor (1981) concluded that hydrothermal systems completely surround the magma chamber, and it is likely that stoping and remelting of such hydrothermally altered wall and roof rocks contaminates the magma prior to eruption (H. Taylor priv. comm.). Assimilation of hydrothermally altered crustal rocks is well documented in Iceland (e.g., Sigmarsson et al. 1992). The effect of seawater alteration on U-series disequilibrium in oceanic basalts has been addressed in several previous studies (Newman et al. 1983; Condomines et al. 1981a; Goldstein et al. 1989; Reinitz and Turekian 1989). Because Th is very insoluble, seawater has a very high ($^{230}Th/^{232}Th$) and hence very low ($^{238}U/^{230}Th$); seawater-basalt interaction thus decreases k. A case for contamination of OIB magma by low k crust has been made by Condomines et al. (1976). They attributed $k < 1$ in some Hawaiian lavas to recent assimilation of ^{230}Th-rich altered crust at depth into the primary magma. Alteration by deep hydrothermal circulation thus may affect mid-ocean ridge magma chambers as well. Further, this process may be difficult to detect as the assimilant will typically have the same composition as the magma. It therefore appears that assimilation of hydrothermally altered crust is a possible explanation for the low k of oceanic basalts.

The effect of pressure on actinide fractionation by clinopyroxene (d) is poorly constrained. There is no appreciable difference between the results of Tatsumoto (1978) for a Kilauean basalt at 14 Kb and our results for the Takashima basalt at 1 bar. Compositional differences may compensate for any pressure effect, however. In the $Di_{50}Ab_{25}An_{25}$ system, Seitz (1973b) also saw no change in actinide partition coefficients between 10 and 25 Kb. On the other hand, Benjamin et al. (1980) report $D_U^{cpx/liq} = 0.018$ at 20 Kb and $-\log fO_2 = FMQ - 0.5$, which is significantly greater than the value inferred from the 1 bar YULO results (Fig. 3.10). It is likely that this increase is a consequence of the large temperature difference (200°C) and changes in phase compositions with pressure, but it is also possible that the U valence state distribution is sensitive to pressure, in which case pressure might be an important variable in considering U-Th fractionation. However, as previously noted, Benjamin et al. (1980) report a comparably high value of $D_{Th}^{cpx/liq}$, resulting in $D_{Th}^{cpx/liq}/D_U^{cpx/liq} > 1$, consistent with my 1 bar results. The concurrent increase in both U and Th partition coefficients suggests that the changes are structurally controlled and that any effect of pressure on the U valence state distribution is not important. This is further supported by similar small increases in clinopyroxene-melt partition coefficients with pressure for REE (Green and Pearson 1983). Thus, while it is possible that the absolute values of clinopyroxene-melt actinide partition coefficients change with pressure, the ratio of the partition coefficients will not be significantly different at high pressure.

Of the possibilities listed, I feel that the most plausible U-Th fractionation mechanisms for oceanic basalts are fractionation of the source region by a fluid phase shortly before melting (a) or fractionation of the magma prior to eruption by assimilation of hydrothermally altered crust (c). Confirmation of these possibilities requires further investigation. These mechanisms have the potential to produce variable amounts of disequilibrium under fairly uniform petrogenetic conditions, and based on the results of Stolper and Newman (in revision) and Condomines et al. (1976), they may be able to fractionate U and Th in the correct sense for oceanic basalts.

4.4.2 Evolution of Th/U in the Earth

A fundamental problem in our understanding of U-Th systematics is the apparent discrepancy between the present and time-integrated Th/U of the upper mantle. An estimate of the present Th/U can be made from ($^{230}Th/^{232}Th$) of young MORB lavas if the source region is in secular equilibrium and the transfer time between melting and sampling is less than about 10 Ka. Given these conditions, $(^{230}Th/^{232}Th)_{sample} = (^{230}Th/^{232}Th)_{source} = (^{238}U/^{232}Th)_{source}$, and

$$[Th/U]_{source} = \frac{(\lambda_{238}/\lambda_{232})}{(^{230}Th/^{232}Th)_{sample}} .$$

Based on this equation, the present MORB source, presumably the upper mantle, has Th/U $\leq$ 2.5 (Galer and O'Nions 1985).

On the other hand, the time-integrated Th/U, <Th/U>, which reflects some kind of long term average, can be estimated from Pb isotopes in MORB by measuring ^{208}Pb and ^{206}Pb, which are radiogenic daughters of ^{232}Th and ^{238}U, respectively:

$$<Th/U> = [^{208}Pb^*/^{206}Pb^*]\frac{(e^{\lambda_{238}T} - 1)}{(e^{\lambda_{232}T} - 1)}$$

(Galer and O'Nions 1985), where λ_{238} and λ_{232} = the decay constants for ^{238}U and ^{232}Th, respectively, and T = the age of the Earth (4.55 Ga). $[^{208}Pb^*/^{206}Pb^*]$ is the radiogenic component of $[^{208}Pb/^{206}Pb]$ given by:

$$[^{208}Pb^*/^{206}Pb^*] = \frac{[^{208}Pb/^{204}Pb]_{sample} - [^{208}Pb/^{204}Pb]_{CD}}{[^{206}Pb/^{204}Pb]_{sample}\,[^{206}Pb/^{204}Pb]_{CD}} ,$$

where CD is the Canyon Diablo meteorite (Allègre et al. 1986). <Th/U> calculated this way gives approximately 3.75 (Tatsumoto 1978; Sun 1980; Galer and O'Nions 1985).

This discrepancy presents a problem because on the one hand the modern Th/U is too low to support the long term radiogenic growth of ^{208}Pb, while on the other hand the low Th/U in the upper mantle is presumably an artifact of world-wide depletion, which is thought to have occurred early in the Earth's history (Galer and Goldstein 1991).

Several models have been put forth in an attempt to explain this discrepancy. Armstrong (1968) first proposed that the crust and mantle are in a steady-state in terms Sr and Pb isotopes: the mantle attained its present low Th/U at least 2.5 Ga ago as a result of a worldwide depletion event stemming from extraction of a proto-continental crust. The high $^{208}Pb/^{206}Pb$ in the mantle has been maintained by subduction of ^{208}Pb-rich continental crust. However, isotopic data from crustal sediments and island arc volcanics do not support this model (White 1985; Galer and O'Nions 1985). In contrast, Tatsumoto (1978) suggested that early differentiation increased Th/U in the mantle from the original value of ≈ 3.9 up to $\approx 4.2 - 4.5$. This ratio has then slowly decreased to the present value of ≈ 2 to give $\langle Th/U \rangle = 3.7$. A modified steady-state situation was offered by Galer and O'Nions (1985), who concluded that the source of the high $^{208}Pb/^{206}Pb$ component is the lower mantle. Their central argument is that in order to preserve the high $^{208}Pb/^{204}Pb$ and low Th/U in the upper mantle, the residence times for Th, U, and Pb in the mantle must be short, and the residence times must decrease in the order Pb, U, Th. That the source of this enriched component is the primitive mantle has since been disputed by Ito et al. (1987).

The (^{230}Th)-enrichment observed in young oceanic basalts requires a complementary reservoir, presumably the upper mantle residue, that undergoes a Th/U decrease. While the upper mantle Th/U will tend to be restored to its original value when the basalt is returned to the mantle during subduction, low temperature alteration of the basalt during its residence on the sea floor decreases Th/U (Aumento 1971; Bacon 1978). The cycle of eruption, alteration, and subduction will thus result in a net decrease in Th/U of the upper mantle with time. This decrease implies that Th/U of the upper mantle did not decrease in one step early in the Earth's history, but is rather an ongoing process. In addition, Th/U of continental crustal sediments appears to have been steadily increasing since the early archaean (Taylor and McClennan 1985), consistent with a gradual decrease in Th/U of the upper mantle. Thus, Tatsumoto's model may be the most realistic. One possible scenario in which the necessary changes in Th/U could come about is as follows: During cooling of

an initially molten Earth, fractional crystallization of garnet preferentially removed U from the magma, leaving a residual liquid with high Th/U (4.2 - 4.5) that became the early upper mantle. Upon solidification, the water oceans were present or were outgassed by 3.96 Ga (Muehlenbachs and Bowring 1992). The onset of plate tectonics in the presence of water would then initiate fluid-based U-Th fractionations, presumably the mechanism that operates at present, that would generate the Th/U enriched melts necessitated by ^{238}U-^{230}Th disequilibrium. This process will preferentially extract Th from the upper mantle, and continual operation of this process throughout the remainder of Earth history would then decrease Th/U of the residual upper mantle to its present-day value of $\approx 2 - 2.5$.

This model is only speculative, and the required large decrease in Th/U may not be possible from MORB extraction as it occurs today. Nonetheless, it is consistent with the decrease in <Th/U> for ophiolites and komatiites throughout geologic time observed by Allègre et al. (1986). However, as the nature of the present U-Th fractionation mechanism that generates (^{230}Th)-enrichments in oceanic basalts is still not constrained, any detailed discussion of the long term evolution of Th/U of the Earth would be of little value.

4.4.3 Th/U in The Solar System

The CI chondrites are thought to represent the most primitive sample of the solar system known. The primary reason for believing this is that the chemical abundance patterns in these meteorites approximately matches the abundance pattern of the solar photosphere (e.g., Dodd 1981). The mean Th/U for CI chondrites is 3.63 (Anders and Grevesse 1989), and it is generally accepted that Th/U in the solar system is between about 3.5 and 4.0.

Given the initial Th/U of the solar system, variations in Th/U between and within different solar system bodies could be useful for understanding the geochemistry of Th and U during planetary formation and evolution. Th/U in most chondrites is between about 3.5 and 4.0 (Hagee et al. 1990; Chen et al. 1992a,b; Anders and Grevesse 1989), although

there are some significant exceptions. The Harleton and Glatten L6 chondrites are the most extreme exceptions, with Th/U > 6 (Unruh 1982; Chen et al. 1992a). Aside from included chondrules, chondrites have not been melted, ruling out crystal-melt partitioning as a source of U-Th fractionation. It is possible that U and Th are fractionated during the intense recrystallization that type 6 meteorites have undergone: phosphate minerals that form during chondrite metamorphism, (predominantly merrilite with minor apatite) preferentially incorporate Th over U (Hagee et al. 1990; Benjamin et al. 1980; Crozaz 1979). Over representation of phosphates in sampling could give the observed high Th/U in Harleton and Glatten. However, the high Th/U in these meteorites appears to result from U-depletion rather than Th-enrichment (D.S. Burnett, pers. comm.), which is inconsistent with addition of Th-rich phosphates. Other type 6 meteorites have normal Th/U, indicating that recrystallization does not necessarily result in large scale Th/U heterogeneities.

The whole Earth Th/U has been estimated from Pb isotope measurements of conformable Pb ore deposits (Stacy and Kramers 1975; Cumming and Richards 1975). These estimates are based on models and give Th/U = 3.8, suggesting that U and Th were not severely fractionated during formation of the Earth. As discussed in sections *4.4.1-2*, above, however, Th/U within the Earth has not remained homogeneous, demonstrating that large U-Th fractionations occur during Earth evolution.

Th/U for the Moon can be estimated very approximately from analyses of mare basalts, glasses, KREEP, and granitic rocks. The large majority of samples from Apollo 11 through 16 have Th/U between three and four, with the mare basalts displaying a relatively constant value of Th/U = 3.8 ± 0.2 (Taylor et al. 1991; Laul and Fruchter 1976). The Apollo 17 mare basalts are anomalous, however, having a significantly lower Th/U of 2 - 3.5 (Laul and Fruchter 1976). The low Th/U in these samples has been attributed to U-Th fractionation by clinopyroxene-melt partitioning during partial melting. This is the opposite sense of U-Th fractionation required by ^{238}U-^{230}Th disequilibrium oceanic basalt

genesis, and the results of this study show that very small Th-depletions can be generated by clinopyroxene-melt partitioning under terrestrial fO_2s (see Fig 4.4). On the moon, however, the presence of metallic iron indicates that melting occurred at an fO_2 below Fe-FeO. The trend in Fig. 3.9 indicates that $D_U^{cpx/liq} \approx D_{Th}^{cpx/liq}$ at IW+1, further reducing, possibly even reversing, the U-Th fractionation possible by clinopyroxene-melt partitioning during mare basalt genesis. Thus, the low Th/U of the Apollo 17 samples is very difficult to explain by partial melting. In addition, the absence of water on the moon eliminates any fluid partitioning mechanisms.

Smith et al. (1984), among others, have raised the possibility that the Shergottites, Nakhlites, and Chassignites (SNCs) are pieces of Mars. Chen and Wasserburg (1986) measured Th/U in Shergotty, Zagami, and Elephant Moraine EETA 79001 and Laul et al. (1986) report multiple Th/U measurements each of two chips of Shergotty. With the exception of one of the latter chips, Shergotty and Zagami give Th/U = 3.75 - 4.12. The anomalous Shergotty chip has Th/U = 2.6 - 3.1 (measured in two laboratories) and is from the same piece as the other chip, which has normal Th/U (3.89). EETA 79001 has a somewhat high Th/U = 4.40. In an analogy to the Earth, where low Th/U in the mantle and high Th/U in the crust is well documented, the two SNC samples with anomalously low and high Th/U could conceivably represent the Martian mantle and crust, respectively. It is also possible that the Th/U heterogeneities in the SNCs could reflect sampling bias.

In summary, Th/U in the chondrites, Moon, possibly Mars, and bulk Earth are generally within the solar system range, but there are a small number of notable exceptions. Much more extensive sampling of the Earth has revealed that internal U-Th fractionations are common in planetary evolution, and in this light the Th/U anomalies in the other bodies are not surprising. Still, the source of these fractionations is unknown. On Earth it is possible that fluids fractionate U from Th, and this remains a possibility for Mars and possibly the chondrite parent bodies. This is not a likely mechanism on the Moon, as there is no evidence for water ever existing there. Crystal-melt partitioning may contribute to

fractionations on the Earth, Moon, and Mars, but not for the chondrites. Evidence for U-Th fractionations under virtually all petrogenetic conditions known in the solar system suggests that there are multiple mechanisms.

References

Anders E. and Grevesse N. (1989) Abundances of the elements: Meteorites and solar. *Geochim. Cosmochim. Acta* **53**, 197-214.

Anderson D. L. (1989) *Theory of the Earth.* Blackwell, Boston.

Allègre C. J. and Condomines M. (1982) Basalt genesis and mantle structure studied through Th-isotopic geochemistry. *Nature* **299**, 21-24.

Allègre C. J., Dupré B. and Lewin E. (1986) Thorium/uranium ratio of the Earth. *Chem. Geol.* **56**, 219-227.

Armstrong J. T. (1988) Quantitative analysis of silicate and oxide materials: Comparison of Monte Carlo, ZAF, and $\phi(\rho z)$ procedures. In *Microbeam Analysis - 1988* (ed. D. E. Newberry), San Francisco Press, 239-246.

Armstrong R. L. (1968) A model for the evolution of strontium and lead isotopes in a dynamic Earth. *Rev. Geophys.* **6**, 175-199.

Aumento F. (1971) Uranium content of mid-ocean ridge basalts. *Earth Planet. Sci. Lett.* **11**, 90-94.

Bacon C. R. (1992) Partially melted granitoid blocks from Crater Lake caldera, Oregon. *Trans. R. Soc. Edinburgh, Earth Sci.* Hutton Symposium Volume (in press).

Bacon M. P. (1978) Radiocative disequilibrium in altered mid-oceanic basalts. *Earth Planet. Sci. Lett.* **39**, 250-254.

Beckett J. R., Spivack A. J., Hutcheon I. D., Wasserburg G. J. and Stolper E. M. (1990) Crystal chemical effects on the partitioning of trace elements between mineral and melt: An experimental study of melilite with applications to refractory inclusions from carbonaceous chondrites. *Geochim. Cosmochim. Acta* **54**, 1755-1774.

Ben Othman D. and Allègre C. J. (1990) U-Th isotopic systematics at 13°N East Pacific Ridge segment. *Earth Planet. Sci. Lett.* **98**, 129-137.

Bender J. F., Langmuir C. H. and Hansen G. N. (1984) Petrogenesis of basalt glasses from the Tamoyo region, East Pacific Rise. *Jour. Petrol.* **25**, 213-254.

Benjamin T. M. (1980) Experimental actinide element partitioning between whitlockite, apatite, diopsidic clinopyroxene, and anhydrous melt at one bar and 20 kilobars pressure. Ph.D. dissertation, California Institute of Technology.

Benjamin T. M., Heuser W. R. and Burnett D. S. (1980) Actinide crystal-liquid partitioning for clinopyroxene and $Ca_3(PO_4)_2$. *Geochim. Cosmochim. Acta* **44**, 1251-1264.

Bottinga Y. and Weill D. F. (1970) The viscosity of magmatic silicate liquids: A model for calculation. *Amer. Jour. Sci.* **272**, 438-475.

Burnett D. S. and Woolum D. S. (1983) In situ trace element microanalysis. *Ann. Rev. Earth Planet. Sci.* **11**, 329-358.

Calas G. (1979) Etude expérimentale du comportement de l'uranium dans les magmas: États d'oxydation et coordinance. *Geochim. Cosmochim. Acta* **43**, 1521-1531.

Carmichael I. S. E. (1991) The redox states of basic and silicic magmas: A reflection of their source regions? *Contrib. Mineral. Petrol.* **106**, 129-141.

Chen J. H., Wasserburg G. J. and Papanastissiou D. A. (1992a) Th and U in some chondrites. 23rd Lunar and Planetary Science Conference (oral presentation).

Chen J. H., Wasserburg G. J. and Papanastissiou D. A. (1992b) Th and U in some chondrites (abstr.). *Lunar Planet. Sci.* **XXIII**, 223-224.

Christie D. M., Carmichael I. S. E. and Langmuir C. H. (1986) Oxidation states of mid-ocean ridge basalt glasses. *Earth Planet. Sci. Lett.* **79**, 397-411.

Clague D. A. (1987) Hawaiian alkaline volcanism. In *Alkaline Igneous Rocks* (eds. J. G. Fitton and B. J. G. Upton). *Geol.Soc. Lond. Spec. Publ.* **30**, Blackwell, Palo Alto, 227-252.

Cohen R. E. (1986) Themodynamic solution properties of aluminous pyroxenes: Nonlinear least squares refinements. *Geochim. Cosmochim. Acta* **50**, 563-575.

Colson R. O., McKay G. A. and Taylor L. A. (1988) Temperature and composition dependencies of trace element partitioning: Olivine/melt and low-Ca pyroxene/melt. *Geochim. Cosmochim. Acta* **52**, 539-553.

Condomines M., Bernat M. and Allègre C. J. (1976) Evidence for contamination of recent lavas from ^{230}Th-^{238}U data. *Earth Planet. Sci. Lett.* **33**, 122-125.

Condomines M., Morand P. and Allègre C. J. (1981a) ^{230}Th-^{238}U radioactive disequilibria in tholeiites from the FAMOUS zone (Mid-Atlantic ridge, 36°50'N): Th and Sr isotopic geochemistry. *Earth Planet. Sci. Lett.* **55**, 247-256.

Condomines M., Morand P., Allègre C. J. and Sigvaldason G. (1981b) ^{230}Th-^{238}U disequilibria in historical lavas from Iceland. *Earth Planet. Sci. Lett.* **55**, 393-406.

Condomines M., Tanguy J. C., Kieffer G. and Allègre C. J. (1982) Magmatic evolution of a volcano studied by ^{230}Th-^{238}U disequilibrium and trace elements systematics: The Etna case. *Geochim. Cosmochim. Acta* **46**, 1397-1416.

Condomines M., Hemond Ch. and Allègre C. J. (1988) U-Th-Ra radioactive disequilibria and magmatic processes. *Earth Planet. Sci. Lett.* **90**, 243-262.

Crank J. (1975) *The Mathematics of Diffusion, second edition.* Oxford University Press, New York.

Crozaz G. (1979) Uranium and thorium microdistributions in stony meteorites. *Geochim. Cosmochim. Acta* **43**, 127-136.

Cumming G. L. and Richards J. R. (1975) Ore lead isotope ratios in a continuously changing Earth. *Earth Planet. Sci. Lett.* **28**, 155-171

DeLong S. E. and Chatelain C. (1990) Trace-element constraints on accessory-phase saturation in evolved MORB magma. *Earth Planet. Sci. Lett.* **101**, 206-215.

Dick H. J. B., Fisher R. L. and Bryan W. L. (1984) Mineralogic variability of the uppermost mantle along mid-ocean ridges. *Earth Planet. Sci. Lett.* **69**, 88-106.

Dodd R. T. (1981) *Meteorites.* Cambridge University Press, New York.

Dostal J. and Capedri S. (1975) Partition coefficients of uranium for some rock-forming minerals. *Chem. Geol.* **15**, 285-294.

Dostal J., Capedri S. and Dupuy C. (1976) Uranium and potassium in calc-alkaline volcanic rocks from Sardinia. *Lithos* **9**, 179-183.

Dostal J., Dupuy C., Carron J. P., Le Guen De Kerneizon M. and Maury R. C. (1983) Partition coefficients of trace elements: Application to volcanic rocks of St. Vincent, West Indies. *Geochim. Cosmochim. Acta* **47**, 525-533.

Drake M. J. and Weill D. F. (1972) New rare earth element standards for electron microprobe analysis. *Chem. Geol.* **10**, 179-181.

Dunn T. (1987) Uranium (VI) diffusion in a supercooled borosilicate melt. *Jour. Non-Cryst. Solids* **92**, 1-10.

Dupuy C., Barsczus H. G., Liotard J-M. and Dostal J. (1988) Trace element evidence for the origin of ocean island basalts: An example from the Austral Islands. *Contrib. Mineral. Petrol.* **98**, 293-302.

Eaby J., Clague D. A. and Delaney J. R. (1984) Sr isotopic variations along the Juan de Fuca ridge. *Jour. Geophys. Res.* **89**, 7883-7890.

Elthon D. and Scarfe C. M. (1984) High-pressure phase equilibria of a high-magnesia basalt and the genesis of primary oceanic basalts. *Amer. Mineral.* **69**, 1-15.

Fleischer R. L., Price P. B. and Walker R. M. (1975) *Nuclear Tracks in Solids: Principles and Applications.* Univ. Calif. Press, Berkeley.

Francalanci L. Peccerillo A. and Poli G. (1987) Partition coefficients for minerals in potassium-alkaline rocks: Data from Roman province (Central Italy). *Geochem. Jour.* **21**, 1-10.

Frey F. A., Garcia M. O., Wise W.S., Kennedy A. K., Gurriet P. and Albarede F. (1991) The evolution of Mauna Kea Volcano, Hawaii: Petrogenesis of tholeiitic and alkalic basalts. *Jour. Geophys. Res.* **96**, 14347-14375.

Friedlander G., Kennedy J. W. and Miller J. M. (1964) *Nuclear and Radiochemistry.* Wiley, New York.

Fujimaki H., Tatsumoto M. and Aoki K-I. (1984) Partition coefficients of Hf, Zr, and REE between phenocrysts and groundmasses. *Proc. Lunar Planet. Sci. Conf.* **14**, B662-B672.

Galer S. J. G. and Goldstein S. L. (1991) Early mantle differentiation and its thermal consequences. *Geochim. Cosmochim. Acta* **55**, 227-239.

Galer S. J. G. and O'Nions R. K. (1985) Residence time of thorium, uranium, and lead in the mantle with implications for mantle convection. *Nature* **316**, 778-782.

Gill J. B. and Williams R. W. (1990) Th isotope and U-series studies of subduction-related rocks. *Geochim. Cosmochim. Acta* **54**, 1427-1442.

Gill J. B., Pyle D. M. and Williams R. W. (1992) Igneous rocks. In *Uranium Series Disequilibrium: Applications to Environmental Problems, second edition* (eds. M. Ivanovitch and R. S. Harmon). Oxford University Press, New York.

Goldstein S. J., Murrell M. T. and Janecky D. R. (1989) Th and U isotopic systematics of basalts from the Juan de Fuca and Gorda Ridges by mass spectrometry. *Earth Planet. Sci. Lett.* **96**, 134-146.

Goldstein S. J., Murrell M. T. and Janecky D. R., Delaney J. R. and Clague D. A. (1992) Geochronology and petrogenesis of MORB from the Juan de Fuca and Gorda ridges by ^{238}U-^{230}Th disequilibrium. *Earth Planet. Sci. Lett.* **109**, 255-272.

Gregory R. T. and Taylor H. P. Jr., (1981) An oxygen isotope profile in a section of cretaceous oceanic crust, Samail Ophiolite, Oman: evidence for $d^{18}O$ buffering of the oceans by deep (>5 Km) seawater-hydrothermal circulation at mid-ocean ridges. *Jour. Geophys. Res.* **86**, 2737-2755.

Green T. H. and Pearson N. J. (1983) Effect of pressure on rare earth element partition coefficients in common magmas. *Nature* **305**, 414-416.

Green T. H. and Pearson N. J. (1985) Experimental determination of REE partition coefficients between amphibole and basaltic to andesitic liquids at high pressure. *Geochim. Cosmochim. Acta* **49**, 1465-1468.

Green T. H. and Ringwood A. E. (1968) Genesis of the calc-alkaline igneous rock suite. *Contrib. Mineral. Petrol.* **18**, 105-162.

Gromet L. P. and Silver L. T. (1983) Rare earth element distributions among minerals in a granodiorite and thier petrogenetic implications. *Geochim. Cosmochim. Acta* **47**, 925-939.

Grutzeck M., Kridelbaugh S. and Weill D. (1974) The distribution of Sr an REE between diopside and silicate liquid. *Geophys. Res. Lett.* **1**, 273-275.

Hagee, B. Bernatowicz T. J., Podosk F. A., Johnson M. L., Burnett D. S. and Tatsumoto M. (1990) Actinide abundances in ordinary chondrites. *Geochim. Cosmochim. Acta* **54**, 2847-2858.

Harrison W. J. (1981) Partitioning of REE between minerals and coexisting melts during partial melting of a garnet lherzolite. *Amer. Mineral.* **66**, 242-259.

Hart S. R. and Zindler A. (1986) In search of a bulk-Earth composition. *Chem. Geol.* **57**, 247-267.

Hemond Ch., Condomines M., Fourcade S., Allègre C. J., Oskarsson N. and Javoy M. (1988) Thorium, strontium and oxygen isotopic geochemistry in recent tholeiites from Iceland: Crustal influence on mantle-derived magmas. *Earth Planet. Sci. Lett.* **87**, 273-285.

Holloway J. R., Pan V. and Gudmundsson G. (1992) High-pressure fluid-absent melting experiments in the presence of graphite – oxygen fugacity, ferric ferrous ratio and dissolved CO_2. *Eur. J. Min.* **4**, 105-114.

Huebner J. S. (1987) Use of gas mixtures at low pressure to specify oxygen fugacities of furnace atmoshperes. In *Hydrothermal Experimental Techniques* (eds. G. C. Ulmer and H. L. Barnes). Wiley, New York, 20-60.

Humphris S. E. and Thompson G. (1983) Geochemistry of rare earth elements in basalts from the Walvis Ridge: Implications for its origin and evolution. *Earth Planet. Sci. Lett.* **66**, 223-242.

Ito E., White W. M. and Göpel C. (1987) The O,Sr, Nd, and Pb isotope geochemistry of MORB. *Chem. Geol.* **62**, 157-176.

Jagoutz E., Palme H., Baddenhausen H., Blum K., Cendales M., Dreibus G., Spettel B., Lorenz V. and Wänke H. (1979) The abundances of major, minor, and trace elements in the Earth's mantle as derived from primitive ultramafic nodules, *Proc. Lunar Planet. Sci. Conf.* **10**, 2031-2050.

Jochum K. P., Hofmann A. W. Ito, E., Seufert H. M. and White W. M. (1983) K, U and Th in mid-ocean ridge basalt glasses and heat production, K/U and K/Rb in the mantle. *Nature* **306**, 431-436.

Johnson K. T. M., Dick H. J. B. and Shimizu N. (1990) Melting in the oceanic upper mantle: an ion microprobe study of diopsides in abyssal peridotites. *Jour. Geophys. Res.* **95**, 2661-2678.

Jones J. H. and Burnett D. S. (1987) Experimental geochemistry of Pu and Sm and the thermodynamics of trace element partitioning. *Geochim. Cosmochim. Acta* **51**, 769-782.

Kashkarov L. L., Pavlenko A. S., Baryshnikova G. V., Serenko V. P. and Ukhanov A. V. (1988) Uranium in mantle xenoliths from the Udachnaya and Obnazhennaya North Yakutia kimberlite pipes: new f-radiography determinations *Geochem. Int.* **25**, no. 8, 84-96.

Kato T., Ringwood A. E. and Irifune T. (1988) Experimental determination of element partitioning between silicate perovskites, garnets and liquids: Constraints on early differentiation of the mantle. *Earth Planet. Sci. Lett.* **89**, 123-145.

Kay R. W. and Gast P. W. (1973) The rare earth content and origin of alkali-rich basalts. *Jour. Geol.* **81**, 653-682.

Kennedy A. K., Lofgren G. and Wasserburg G. J. (1992) A study of trace element partitioning between olivine, orthopyroxene and melt in chondrules: Equilibrium values and kinetic effects (abstr.). *Lunar Planet. Sci.* **XXIII**, 679-680.

Keppler H. and Wyllie P. J. (1990) Role of fluids in transport and fractionation of uranium and thorium in magmatic processes. *Nature* **348**, 531-533.

Kinzler R. J. and Grove T. L. (1992a) Primary magmas of mid-ocean ridge basalts 1. Experiments and methods. *Jour. Geophys. Res.* **97**, 6885-6906.

Kinzler R. J. and Grove T. L. (1992b) Primary magmas of mid-ocean ridge basalts 2. applications. *Jour. Geophys. Res.* **97**, 6907-6926.

Klein E. M. and Langmuir C. H. (1987) Global correlations of ocean ridge basalt chemistry with axial depth and crustal thickness. *Jour. Geophys. Res.* **92**, 8089-8115.

Kostopoulos D. K. (1991) Melting of the shallow upper mantle: A new perspective. *Jour. Petrol.* **32**, 671-699.

Krishnaswami S., Turekian K. K. and Bennett J. T. (1984) The behavior of ^{232}Th and the ^{238}U decay chain nuclides during magma formation and volcanism. *Geochim. Cosmochim. Acta* **48**, 505-511.

Kuehner S. M., Laughlin J. R., Grossman L., Johnson M. L. and Burnett D. S. (1989) Determination of trace element mineral/liquid partition coefficients in mellilite and diopside by ion and electron microprobe techniques. *Geochim. Cosmochim. Acta* **53**, 3115-3130.

Kuno H. (1965) Aluminian augite and bronzite in alkali olivine basalt from Taka-sima, North Kyushu, Japan. *Advancing Front. Geol. Geophys.* **1964**, 205-220.

Langmuir C. H., Bender J. F., Bence A. E., Hansen G. N. and Taylor S. R. (1977) Petrogenesis of basalts from the FAMOUS area: Mid-Atlantic Ridge. *Earth Planet. Sci. Lett.* **36**, 133-156.

Larson L. M. (1979) Distribution of REE and other trace elements between phenocrysts and peralkaline undersaturated magmas, exemplified by rocks from the Gardar igneous province, South Greenland. *Lithos* **12**, 303-315.

LaTourrette T. Z., Burnett D. S. and Bacon C. R. (1991) Uranium and minor element partitioning in Fe-Ti oxides and zircon from partially melted granodiorite, Crater Lake, Oregon. *Geochim. Cosmochim. Acta* **55**, 457-469.

Laul J. C. and Fruchter J. S. (1976) Thorium and uranium variations in Apollo 17 basalts and systematics. *Proc. Lunar Planet. Sci. Conf.* **1**, 1545-1559.

Laul J. C., Smith M. R., Wänke H., Jagoutz E., Dreibus G., Palme H., Spettel B., Burghele A., Lipschutz M. E. and Verkouteren R. M. (1986) Chemical systematics of

the Shergotty meteorite and the composition of its parent body (Mars). *Geochim. Cosmochim. Acta* **50**, 909-926.

Lemarchand F., Villemant B. and Calas G. (1987) Trace element distribution coefficients in alkaline series. *Geochim. Cosmochim. Acta* **51**, 1071-1081.

Lesher C. E. (1986) Effects of silicate liquid composition on mineral-liquid element partitioning from soret diffusion studies. *J. Geophys. Res.* **91**, 6123-6141.

Liias R. A. (1986) Geochemistry and petrogenesis of basalts erupted along the Juan de Fuca ridge. Ph.D. Thesis, University of Massachusetts.

Lindsley D. M. and Andersen D. J. (1983) A two pyroxene thermometer. *Proc. Lunar Planet. Sci. Conf.* **13**, A887-A906.

Lindstrom D. J. (1983) Kinetic effects on trace element partitioning. *Geochim. Cosmochim. Acta* **47**, 617-622.

London D., Hervig R. L. and Morgan G. B., VI (1988) Melt-vapor solubilities and elemental partitioning in peraluminous granite-pegmatite systems: Experimental results with Macusani glass at 200 MPa. *Contrib. Mineral. Petrol.* **99**, 360-373

MacRae N. D. and Russell M. R. (1987) Quantitative REE SIMS analyses of komatiite pyroxenes, Munro Township, Ontario, Canada. *Chem. Geol.* **64**, 307-317.

Mahood G. and Hildreth W. (1983) Large partition coefficients for trace elements in high-silica rhyolites. *Geochim. Cosmochim. Acta* **47**, 11-30.

Mahood G. A. and Stimac J. A. (1990) Trace-element partitioning in pantellerites and trachytes. *Geochim. Cosmochim. Acta* **54**, 2257-2276.

McDonough W. F. (1990) Constraints on the composition of the continental lithospheric mantle. *Earth Planet. Sci. Lett.* **101**, 1-18.

McKay G. A. (1986) Crystal/liquid partitioning of REE in basaltic systems: Extreme fractionation of REE in olivine. *Geochim. Cosmochim. Acta* **50**, 69-79.

McKay G. A. (1989) Partitioning of rare earth elements between major silicate minerals and basaltic melts. In *Geochemistry and Mineralogy of Rare Earth Elements* (eds. B. R. Lipin and G. A. McKay). *MSA Reviews in Mineralogy* **21**, 45-77.

McKay G. A. and Weill D. F. (1977) KREEP petrogenesis revisited. *Proc. Lunar Planet. Sci. Conf.* **8**, 2339-2355.

McKay G., Wagstaff J. and Yang S-R. (1986) Clinopyroxene REE distribution coefficients for shergottites: The REE content of the Shergotty melt. *Geochim. Cosmochim. Acta* **50**, 927-937.

McKenzie D. (1985) ^{230}Th-^{238}U disequilibrium and the melting processes beneath ridge axes. *Earth Planet. Sci. Lett.* **72**, 149-157.

McKenzie D. and Bickle M. J. (1988) The volume and composition of melt generated by extension of the lithosphere. *Jour. Petrol.* **29**, 625-679.

McKenzie D. and O'Nions R. K. (1991) Partial melt distributions from inversion of rare earth element concentrations. *Jour. Petrol.* **32**, 1021-1091.

Morris R. V. (1975) Electron paramagnetic resonance study of the site preferences of Gd^{3+} and Eu^{2+} in polycrystalline silicate and aluminate minerals. *Geochim. Cosmochim. Acta* **39**, 621-634.

Mory J., DeGuillebon D. and Delsarte G. (1970) Measurement of the mean range of fission fragments using mica as a detector– Influence of the crystalline structure. *Rad. Effects* **5**, 37-40.

Muehlenbachs K. (1986) Alteration of the oceanic crust and the ^{18}O history of seawater. In *Stable Isotopes* (ed. J. W. Valley, H. P. Taylor, Jr. and J. R. O'Neil), *MSA Reviews in Mineralogy* **16**, 425-444.

Muehlenbachs K. and Bowring S. A. (1992) Is the imprint of the primordial ocean evident in the 3.96 Ga Acasta Gneiss? (abstr.) *Eos* **73**, 324.

Murrell M. T. and Burnett D. S. (1987) Actinide chemistry in Allende Ca-Al-rich inclusions. *Geochim. Cosmochim. Acta* **51**, 985-999.

Mysen B. O. and Virgo D. (1980) Trace element partitioning and melt structure: An experimental study at 1 atm pressure. *Geochim. Cosmochim. Acta* **44**, 1917-1930.

Nagawasa H. and Wakita H. (1968) Partition of uranium and thorium between augite and host lavas. *Geochim. Cosmochim. Acta* **32**, 917-922.

Nash W. P. and Crecraft H. R. (1985) Partition coefficients for trace elements in silicic magmas. *Geochim. Cosmochim. Acta* **49**, 2309-2322.

Newman S., Finkel R. C. and Macdougall J. D. (1983) ^{230}Th-^{238}U disequilibrium systematics in oceanic tholeiites from 21 °N on the East Pacific Rise. *Earth Planet. Sci. Lett.* **65**, 17-33.

Newman S., Finkel R. C. and Macdougall J. D. (1984) Comparison of ^{230}Th-^{238}U disequilibrium systematics in lavas from three hot spot regions: Hawaii, Prince Edward and Samoa. *Geochim. Cosmochim. Acta* **48**, 315-324.

Nicholls I. A. and Harris K. L. (1980) Experimental rare earth partition coefficients for garnet, clinopyroxene and amphibole coexisting with andesitic and basaltic liquids. *Geochim. Cosmochim. Acta* **44**, 287-308.

Nickel K. G. (1986) Phase equilibria in the system SiO_2-MgO-Al_2O_3-CaO-Cr_2O_3 (SMACCR) and their bearing on spinel/garnet lherzolite relationships. *Nues Jahrbuch Mineral. Abh.* **155**, 259-287.

Nielsen R. L. (1985) A method for the elimination of the compositional dependence of trace element distribution coefficients. *Geochim. Cosmochim. Acta* **49**, 1775-1779.

Nielsen R. L., Gallahan W. E. and Newberger F. (1992) Experimentally determined mineral-melt partition coefficients for Sc, Y, and REE for olivine, orthopyroxene, pigionite, magnetite, and ilmenite. *Contrib. Mineral. Petrol.* **110**, 488-499.

Nordstrom D. K. and Munoz J. L. (1986) *Geochemical Thermodynamics*. Blackwell, Palo Alto.

Oberti R. and Caporuscio F. A. Crystal chemistry of clinopyroxenes from mantle eclogites: A study of the key role of the M2 site population by means of crystal-structure refinement. *Amer. Mineral.* **76**, 1141-1152.

Ohtani E., Kawabe I., Moriyama J. and Nagata Y. (1989) Partitioning of elements between majorite garnet and melt and implications for petrogenesis of komatiite. *Contrib. Mineral. Petrol.* **103**, 263-269.

Onuma N., Higuchi H., Wakita H. and Nagasawa H. (1968) Trace element partitioning between two pyroxenes and the host lava. *Earth Planet. Sci. Lett.* **5**, 47-51.

Onuma N., Ninomiya S. and Nagasawa H. (1981) Mineral/groundmass partition coefficients for nepheline, melilite, clinopyroxene and perovskite in melilite-nepheline basalt, Niyiragongo, Zaire. *Geochem. Jour.* **15**, 221-228.

Oversby V. M. and Gast P. W. (1968) Lead isotope compositions and uranium decay series disequilibrium in recent volcanic rocks. *Earth Planet. Sci. Lett.* **5**, 199-206.

Polve M. and Kurz M. D. (1984) Helium isotopic and fission track studies of ultramafic xenoliths (abstr.). *EOS* **65**, 1154.

Ray G. L., Shimizu N. and Hart S. R. (1983) An ion microprobe study of the partitioning of trace elements between clinopyroxene and liquid in the system diopside-albite-anorthite. *Geochim. Cosmochim. Acta* **47**, 2131-2140.

Reinitz I. and Turekian K. K. (1989) $^{230}Th/^{238}U$ and $^{226}Ra/^{230}Th$ fractionation in young basaltic glasses from the East Pacific Rise. *Earth Planet. Sci. Lett.* **94**, 199-207.

Ringwood A. E. (1977) Basaltic magmatism and the bulk composition of the Moon I. Major and heat producing elements. *The Moon* **16**, 389-423.

Rubin K. H. and Macdougall J. D. (1988) ^{226}Ra excesses in mid ocean ridge basalts and mantle melting. *Nature* **355**, 158-161.

Ryerson F.J. and Hess P. C. (1980) The role of P_2O_5 in silicate melts. *Geochim. Cosmochim. Acta* **44**, 611-625.

Salters V. J. M. and Hart S. R. (1989) The hafnium paradox and the role of garnet in the source of mid-ocean ridge basalts. *Nature* **342**, 420-422.

Schreiber H. D. (1980) Properties of redox ions in glasses: An interdisciplinary perspective. *Jour. Non-Cryst. Solids* **42**, 175-184.

Schreiber H. D. (1983) The chemistry of uranium in glass-forming aluminosilicate melts. *Jour. Less Common Metals* **91**, 129-147.

Schreiber H. D., Merckel R. C. Jr., Lea Schreiber V. and Balazs G. B. (1987) Mutual interactions of redox couples via electron exchange in silicate melts: Models for geochemical melt systems. *Jour. Geophys. Res.* **92**, 9233-9245.

Seitz M. G. (1973a) Uranium and thorium diffusion in diopside and fluorapatite. *Carnegie Inst. Wash. Yearb.* **72**, 586-588.

Seitz M. G. (1973b) Uranium and thorium partitioning in diopside-melt and whitlockite-melt systems. *Carnagie Inst. Wash. Yearb.* **72**, 581-586.

Shannon R. D. (1976) Revised effective ionic radii and systematic studies of interatomic distances in halides and chalcogenides. *Acta Cryst.* **A32**, 751-767.

Shaw D. M. (1970) Trace element fractionation during anatexis. *Geochim. Cosmochim. Acta* **34**, 237-243.

Shimizu N. (1974) An experimental study of the partitioning of K, Rb, Cs, Sr and Ba between clinopyroxene and liquid at high pressures. *Geochim. Cosmochim. Acta* **38**, 1789-1798.

Shimizu N. and Kushiro I. (1975) The partitioning of rare earth elements between garnet and liquid at high pressures: Preliminary experiments. *Geophys. Res. Lett.* **2**, 413-416.

Sigmarsson O., Condomines M. and Fourcade S. (1992) Mantle and crustal contribution in the genesis of recent basalts from off-rift zones in Iceland: Constraints from Th, Sr, and O isotopes. *Earth Planet. Sci. Lett.* **110**, 149-162.

Sisson T. W. (1991) Pyroxene-high silica rhyolite trace element partition coefficients measured by ion microprobe. *Geochim. Cosmochim. Acta* **55**, 1575-1585.

Sisson T. W. and Bacon C. R. (1992) Garnet/high-silica rhyolite trace element partition coefficients measured by ion microprobe. *Geochim. Cosmochim. Acta* **56**, 2133-2136.

Smith M. R., Laul J. C., Ma M-S., Huston T., Verkouteren R. M., Lipschutz M. E. and Schmitt R. A. (1984) Petrogenesis of the SNC (shergottites, nakhlites, chassignites) meteorites; implications for their origin from a large dynamic planet, possibly Mars. *Proc. Lunar Planet. Sci. Conf.* **14**, B612-B630.

Smyth D.M. (1989) Defect equilibria in perovskite oxides. In *Perovskite: A Structure of Great Interest to Geophysics and Materials Science* (eds. A. Navrotsky and D.J. Weidner). Amer. Geophys. Union, Washington, D. C., 99-103.

Sneeringer M., Hart S. R. and Shimizu N. (1984) Strontium and samarium diffusion in diopside. *Geochim. Cosmochim. Acta* **48**, 1589-1608.

Somayajulu B. L. K., Tatsumoto M., Rosholt J. N. and Knight R. J. (1966) Disequilibrium of the ^{238}U series in basalt. *Earth Planet. Sci. Lett.* **1**, 387-391.

Stacy J. S. and Kramers J. D. (1975) Approximation of terrestrial lead isotope evolution by a two-stage model. *Earth Planet. Sci. Lett.* **26**, 207-221.

Stolper E. and Newman S. (1992) The role of water in the petrogenesis of Mariana Trough magmas: Implications for the heterogeneity of the mantle, *Earth Planet. Sci. Lett.* (in revision).

Sun S. S. (1980) Lead isotopic study of young volcanic rocks from mid-ocean ridges, ocean islands and island arcs. *Phil. Trans. R. Soc. Lond.* **A297**, 409-445.

Sun S. S. and Hansen G. N. (1975) Origin of Ross Island basanitoids and limitations upon the heterogeneity of mantle sources for alkali basalts and nephelenites. *Contrib. Mineral. Petrol.* **52**, 77-106.

Tatsumoto M. (1978) Isotopic composition of lead in oceanic basalt and its implication to mantle evolution. *Earth Planet. Sci. Lett.* **38**, 63-87.

Tatsumoto M., Hedge C. E. and Engel A. E. G. (1965) Potassium, rubidium, strontium thorium, uranium and the ratio of strontium-87 to strontium-86 in oceanic basalt. *Science* **150**, 886-888.

Taylor G. J., Warren P., Ryder G., Delano J., Pieters C. and Lofgren G. (1991) *Lunar Rocks.* In *Lunar sourcebook: A user's guide to the Moon* (ed. G. Heiken, D. Vaniman and B. M. French). Cambridge University Press, New York, 183-284.

Taylor S. R. (1979) Relative refractory and volatile element contents of the Earth and the Moon (abstr.). *Lunar Planet. Sci.* **10**, 1217-1218.

Taylor S. R. (1982) *Planetary science– a lunar perspective.* Lunar Planetary Inst., Houston.

Taylor S. R. and McClennan S. M. (1985) *The Continental Crust: Its composition and evolution.* Blackwell, Palo Alto.

Taylor W.R. and Green D. H. (1986) The role of reduced C-O-H fluids in mantle partial melting. In *Kimberlites and Related Rocks, v. 1* (ed. J. Ross et al.). *Proceedings of the 4th Kimberlite Conference*, Blackwell, Cambridge, 592-602.

Thompson R. N. (1987) Phase equilibria constraints on the genesis and magmatic evolution of oceanic basalts. *Earth Sci. Rev.* **24**, 161-210.

Turekian K. K., Krishnaswami, S., Reinitz I. M. and Ribe N. M. (1991) Radioactive diseauilibrium of ^{238}U, ^{230}Th and ^{226}Ra in contemporary volcanics and inferred time constants of magma formation (abstr.). *Geol. Soc. Am. Abstr.With Prog.* **23**, A113.

Unruh D. M. (1982) The U-Th-Pb age of equilibrated L-chondrites and a solution to the excess radiogenic Pb problem in chondrites. *Earth Planet. Sci. Lett.* **58**, 75-94.

Villemant B., Jaffrezic H., Joron J-L. and Treuil M. (1981) Distribution coefficients of major and trace elements; fractional crystallization in the alkali basalt series of Chaîne des Puys (Massif Central, France). *Geochim. Cosmochim. Acta* **45**, 1997-2016.

Wänke H., Dreibus G. and Jagoutz E. (1984) Mantle chemistry and accretion history of the Earth. In *Archaean Geochemistry* (ed. A. Kröner, G. N. Hanson and A. M. Goodwin), Springer-Verlag, Berlin, 1-24.

Watson E. B. (1977) Partitioning of manganese between forsterite and silicate liquid. *Geochim. Cosmochim. Acta* **41**, 1363-1374.

Watson E. B. (1980) Apatite and phosphorus in mantle source regions: An experimental study of apatite/melt equilibria at pressures to 25 Kbar. *Earth Planet. Sci. Lett.* **51**, 322-335.

Watson E. B., Ben Othman D., Luck J-M. and Hofmann A. W. (1987) Partitioning of U, Pb, Cs, Yb, Hf, Re and Os between chromian diopsidic pyroxene and haplobasaltic liquid. *Chem. Geol.* **62**, 191-208.

White W. M. (1985) Sources of oceanic basalts: Radiogenic isotope evidence. *Geology* **13**, 115-118.

White W. M., Tapia M. D. M. and J-G Schilling (1979) The petrology and geochemistry of the Azores Islands. *Contrib. Mineral. Petrol.* **69**, 201-213.

Williams R. W. and Gill J. B. (1989) Effects of partial melting on the uranium decay series. *Geochim. Cosmochim. Acta* **53**, 1607-1619.

Wörner G., Beusen J-M., Duchateau N., Gijbels R. and Schmincke H. U. (1983) Trace element abundances and mineral/melt distribution coefficients in phonolites from the Laacher See Volcano (Germany). *Contrib. Mineral. Petrol.* **84**, 152-173.

Yurimoto H. and Ohtani E. (1992) Element partitioning between majorite and liquid: A secondary ion mass spectrometry study. *Geophys. Res. Lett.* **19**, 17-20.

Yudintsev S. V., Omel'yanenko B. I. and Lyubomilova G. L. (1990) Uranium valency state in granitic melts. *Geochem. Int.* **28(4)**, 65-71.

Zinner E. and Crozaz G. (1986) A method for the quantitative measurement of the rare earth elements in the ion microprobe. *Int. Jour. Mass Spec. Ion Proc.* **69**, 17-38.

Geochimica et Cosmochimica Acta Vol. 55, pp. 457–469

0016-7037/91/$3.00 + .00

Uranium and minor-element partitioning in Fe-Ti oxides and zircon from partially melted granodiorite, Crater Lake, Oregon

T. Z. LA TOURRETTE,[1] D. S. BURNETT,[1] and CHARLES R. BACON[2]

[1]Division of Geological and Planetary Sciences, California Institute of Technology, Pasadena, CA 91125, USA
[2]US Geological Survey, 345 Middlefield Road, Menlo Park, CA 94025, USA

(*Received February* 26, 1990; *accepted in revised form November* 21, 1990)

Abstract—Crystal-liquid partitioning in Fe-Ti oxides and zircon was studied in partially melted granodiorite blocks ejected during the climactic eruption of Mt. Mazama (Crater Lake), Oregon. The blocks, which contain up to 33% rhyolite glass (75 wt% SiO_2), are interpreted to be portions of the magma chamber walls that were torn off during eruption. The glass is clear and well homogenized for all measured elements except Zr. Results for Fe-Ti oxides give $D_U^{oxide/liq} \approx 0.1$. Partitioning of Mg, Mn, Al, Si, V, and Cr in Fe-Ti oxides indicates that grains surrounded by glass are moderately well equilibrated with the melt for many of the minor elements, while those that are inclusions in relict plagioclase are not. Uranium and ytterbium inhomogeneities in zircons indicate that the zircons have only partially equilibrated with the melt and that uranium appears to have been diffusing out of the zircons faster than the zircons were dissolving. Minimum U, Y, and P concentrations in zircons give maximum $D_U^{zrc/liq} = 13$, $D_Y^{zrc/liq} = 23$, and $D_P^{zrc/liq} = 1$, but these are considerably lower than reported by other workers for U and Y. Based on our measurements and given their low abundances in most rocks, Fe-Ti oxides probably do not play a major role in U-Th fractionation during partial melting. The partial melts were undersaturated with zircon and apatite, but both phases are present in our samples. This demonstrates an actual case of non-equilibrium source retention of accessory phases, which in general could be an important trace-element fractionation mechanism. Our results do not support the hypothesis that liquid structure is the dominant factor controlling trace-element partitioning in high-silica rhyolites. Rough calculations based on Zr gradients in the glass indicate that the samples could have been partially molten for 800 to 8000 years.

INTRODUCTION

THE PRIMARY PURPOSE of this study is to evaluate the degree to which Fe-Ti oxides and zircon can fractionate U and Th during crustal melting and crystallization. Although actinide elements were generally assumed to be almost totally incompatible in typical rock forming minerals, the fractionation of U relative to Th can be surprisingly large as indicated by measurements of ^{238}U-^{230}Th disequilibrium in rocks less than 350,000 years old. Such measurements can provide information about the age of the rock (CONDOMINES et al., 1982a,b; OMURA et al., 1988), the time-scale for melting and transport of magma (CONDOMINES et al., 1988; WILLIAMS et al., 1986), and the nature of the source region (NEWMAN et al., 1983, 1984; ALLÈGRE and CONDOMINES, 1982). In principle, this disequilibrium also can be used to determine the degree of partial melting and constrain melt generation models, but such conclusions are subject to large uncertainties because of limited knowledge of U and Th partitioning. To the extent that ^{238}U-^{230}Th disequilibrium is produced by igneous fractionations of U and Th, knowledge of the phases responsible and their partitioning behavior is required to interpret the data correctly. We have examined the partitioning of U, Mg, Mn, Al, Si, V, and Cr in Fe-Ti oxides and U, Y, and P in zircons coexisting with rhyolite glass in quenched partially melted granodiorites from Crater Lake, Oregon.

There are three reasons for studying Fe-Ti oxides. First, since U-Th fractionations are found in a variety of geologic environments and in rock types ranging from ocean ridge basalts to arc andesites to carbonatites (CONDOMINES et al., 1988), either the fractionation mechanism is ubiquitous or a variety of fractionation mechanisms are at work. Examples of fractionation involving enrichment of U over Th can (qualitatively) be readily understood given the extreme incompatibility of penta- and hexavalent U relative to tetravalent Th or U. However, fractionations involving enrichment of Th over U, apparently requiring a phase with a relatively high D_U, are less readily understood. Thus, the present measurements have focused on U and phases, such as Fe-Ti oxides, that incorporate U in preference to Th. Titanomagnetite and ilmenite are common accessory phases in many igneous rocks and are thus possible candidates for a fractionating phase. Second, many studies that use ^{238}U-^{230}Th disequilibrium to date young volcanic rocks find that magnetite separates often have high U contents and high U/Th (ALLÈGRE and CONDOMINES, 1976; CONDOMINES and ALLÈGRE, 1980; CONDOMINES et al., 1982a,b; OMURA et al., 1988; DENIEL, 1988). This clearly indicates that in many cases Fe-Ti oxides have preferentially incorporated U relative to Th, although there has been no prior attempt to determine the cause of this fractionation. Third, Fe-Ti oxides in alteration zones can have high U contents (STURCHIO et al., 1986; VILLEMANT and FLÉHOC, 1989; GUTHRIE, 1989). In these cases U may be concentrated by surface adsorption in an aqueous system (LANGMUIR, 1978; HSI and LANGMUIR, 1985), but there may be analogous surface partitioning effects in igneous environments as well. If hydrothermal alteration with accompanying U-enrichment of Fe-Ti oxides were to occur soon after the eruption of a volcanic rock, the Fe-Ti oxides could lie on the internal isochron defined by the whole-rock and other mineral separates even though the U-Th fractionation was, strictly speaking, secondary.

Zircon was studied because it is a well-known host for U in most intermediate to silicic rocks. While the abundance of zircon generally is low, its high U content and high U/Th may give it significant control over U/Th during partial melting of continental crustal rocks.

A secondary objective of our study was to measure partition coefficients for high-silica systems. Some studies suggest that melt structure can play a role as great or greater than crystal chemistry in controlling trace-element partitioning behavior in silica-rich compositions (MAHOOD and HILDRETH, 1983; NASH and CRECRAFT, 1985). However, studies of phenocryst-matrix partitioning for rhyolitic compositions based on mineral separates have been controversial because of the effects of contamination by trace element–rich minor phases (MICHAEL, 1988; CAMERON and CAMERON, 1986). In this study we base all partition coefficient measurements on *in situ* data from individual grains, which allows us to reduce greatly the effects of minor phase contamination.

SAMPLES

The samples for this study are partially melted granitic blocks that were ejected in the caldera-forming eruption of Mt. Mazama (Crater Lake), Oregon. For a description of the geology and petrology of Mt. Mazama see BACON and DRUITT (1988) and DRUITT and BACON (1989). These blocks are interpreted by BACON (1987) to be pieces of the magma chamber walls that were partially melted in place before the climactic eruption. The blocks are found only in the 6845 ± 50 year B.P. climactic eruption deposit, and none have any juvenile magma adhering to them. The maximum melt fraction observed is about 0.35–0.40, suggesting that more completely fused rock was assimilated by the climactic magma and the ejected blocks represent material outboard of the juvenile magma/wallrock interface (BACON et al., 1989).

The samples have textures typical of subvolcanic intrusions and are granodioritic in composition ($SiO_2 \approx 68\%$; BACON and DRUITT, 1988). Based on the mineralogy of unmelted and very low melt fraction samples they originally consisted of plagioclase, quartz, alkali feldspar, orthopyroxene, hornblende, biotite, titanomagnetite, ilmenite, zircon, and apatite. The original alkali feldspar and most of the mafic minerals in the most melted samples have been consumed leaving plagioclase, quartz, titanomagnetite, ilmenite, zircon, and apatite coexisting with a rhyolitic glass and newly crystallized alkali feldspar and possibly pyroxene, magnetite, and ilmenite. The relatively anhydrous glass is clear and shows no sign of quench crystals or secondary alteration. Figure 1 is a photomicrograph taken under transmitted light of a sample (1038) with a high melt fraction.

Fe-Ti oxide temperatures and oxygen fugacities for our samples are high, ranging from about 955–980°C and 1.8 log units more oxidizing than FMQ (C. R. BACON, unpubl. data, 1987; ANDERSEN and LINDSLEY, 1988). This is supported by oxygen isotope measurements consistent with $T \geq 900$°C (BACON et al., 1989). The glass fractions of the blocks show a positive correlation with temperature which may be related to the distance from the chamber wall. There is evidence for glass extrusion into fractures in a few similar samples (BACON and DRUITT, 1988), so there may be significant uncertainties in equating the glass fraction with the degree of melting. Infrared spectroscopic measurement of the glass from sample 1038 gives a water content of 0.41 ± .02 wt% (S. NEWMAN, pers. comm.), and Cl and F contents are 0.23 and 0.11 wt%, respectively (C. R. BACON, unpubl. microprobe data, 1989). While some samples are vesiculated, the high temperatures and absence of hydrous phases indicate that the water content of the partial melts decreased rapidly soon after the onset of melting, leaving a relatively dry melt.

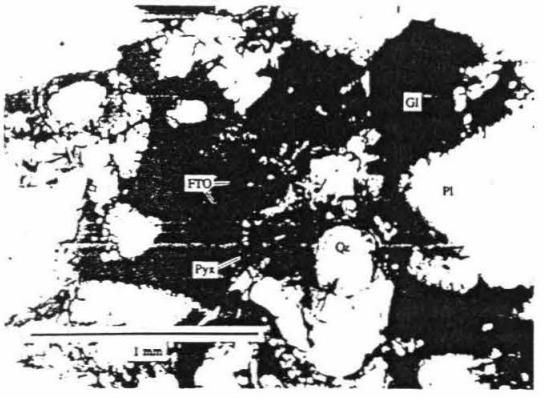

FIG. 1. Transmitted light photomicrograph of sample 1038. Glass fraction = 0.33. Pl = plagioclase, Qz = quartz, FTO = Fe-Ti oxide (magnetite + ilmenite), Pyx = pyroxene, Gl = glass.

These samples are of interest for trace-element geochemistry because the long time that they existed in a molten state may have permitted a close approach to equilibrium. Based on the magmatic time scale for Mt. Mazama (BACON and DRUITT, 1988), the crystals and liquid may have coexisted under approximately isothermal conditions for up to several thousand years and were then rapidly quenched during the climactic eruption of Mt. Mazama. High temperature re-equilibration of O isotopes in quartz, plagioclase, and glass indicates the sampled rocks had been partially molten in a near steady-state condition for a time sufficient for O isotopic equilibration before ejection (BACON et al., 1989). These samples thus offer an opportunity to study trace-element partitioning under conditions totally impossible experimentally.

ANALYTICAL METHODS

Uranium concentrations were determined by fission track radiography on polished thin sections on silica glass. Other trace- and major-element concentrations were measured on the same sections with an electron microprobe. X-ray fluorescence and instrumental neutron activation analyses of bulk rocks and of a glass separate for sample 1038 are given in BACON and DRUITT (1988).

Fission Track Radiography

Quantitative U microdistributions were obtained using fission track radiography (BURNETT and WOOLUM, 1983). The choice of neutron fluence used in this technique depends on the range of U concentrations expected in the various phases in the sample, and it is often difficult to accommodate the entire range with one fluence. In this case the problem was handled by setting a lower limit of interest for $D_U^{oxide/liq}$. Given their typical low abundance in terrestrial rocks, Fe-Ti oxides require a relatively high U partition coefficient to affect U/

Th of a liquid significantly. In our samples, even if the partition coefficient for Th is zero, U is required to be a highly compatible element in Fe-Ti oxides ($D_U^{oxide/liq}$ = 2–9) to produce U-Th fractionations of 10–30%. Considering systems with lower degrees of partial melting permits larger fractionations, but even in the case of 5% melting the U partition coefficient would have to be at least 0.2 for Fe-Ti oxides to be a significant host phase and play a role in U-Th fractionations. We used a relatively low fluence so that good data would be obtained if $D_U^{oxide/liq} \geq 0.2$ but also so that track densities would not be saturated for U-rich phases such as zircon. A loss of precision for $D_U^{oxide/liq} < 0.2$ would result, but this was acceptable because a partition coefficient below about 0.2 does not appear to be important in terms of U-Th fractionation.

Freshly cleaved muscovite detectors were tightly clamped on the sections, and the samples were irradiated with a thermal fluence of about 2×10^{16} neutrons/cm^2. Three pieces of a U standard glass (NBS 963) were included in the irradiation to measure U concentrations and monitor neutron flux gradients. After the irradiation, the muscovite detectors were etched in 49% HF at 26°C for 7 min (zircon) or 35 min (Fe-Ti oxides).

Track densities in the fission track images corresponding to the Fe-Ti oxides were low ($\approx 2 \times 10^5$ tracks/cm^2), but they were measurable with careful mapping using transmitted light. The high track densities corresponding to the zircons were counted in backscattered electron photographs of the micas. The area of the crystals counted always excluded the outer 10 μm in order to avoid fission tracks from the surrounding glass. The track densities in glass near each crystal were measured by the same technique (SEM photographs or optically) as for the crystal.

Electron Microprobe Analyses

Microprobe analyses were obtained with a JEOL Superprobe 733, and raw data were reduced with the CITZAF correction procedure (ARMSTRONG, 1988). The major elements in the glasses were measured with a 35 nA beam current and a 30 μm spot size to minimize alkali loss. Sodium was always measured first. Tests show that crystal spectrometer efficiency remains close to 100% with a 30 μm beam spot, and standards were measured with a 20 μm spot. Trace elements in the glasses (Zr, Mn, V, Cr, P) were measured on the same spots in a separate run with a 200 nA current and a 30 μm spot size. Fe-Ti oxides and zircons were analyzed with 50 and 100 nA currents and 15 and 1–2 μm spot sizes, respectively. Vanadium measurements were corrected for interference from Ti Kβ. Special attention was given to setting background positions and checking that linear background interpolations were accurate.

Special problems arise in the measurement of Si in the Fe-Ti oxides. Measured Si concentrations in magnetite for sample 1038 are uniform at around 530 ppm, and Si concentrations in 1038 ilmenite are lower and variable (90–400 ppm). An experiment was performed to check for four possible sources of error: background X-rays from scattered electrons, secondary Si fluorescence from silicates surrounding the Fe-Ti oxides, fourth-order Fe Kβ interference, and polishing contamination. Synthetic magnetite crystals ($\approx$60–80 μm) or 0.5–1 mm size pieces of high-purity Fe wire were mixed with powdered synthetic Di_2AbAn glass and melted in less than 5 min at 1300°C. Using the same microprobe operating conditions as for the natural samples, Si counting rates were compared with epoxy mounted control samples of these materials. All samples showed significant Si counting rates. Wavelength scans showed that Si was really being counted; both crystal spectrometer and pulse height discrimination completely resolved Fe Kβ counts. Large increases (equivalent to about 600 ppm Si for the synthetic magnetite) were observed for both silicate-encapsulated samples. Center-to-edge comparisons showed the combined effects of beam scatter and secondary fluorescence to be worth only around 60 ppm, so that the bulk of the increases must be ascribed to polishing contamination, assuming that Si diffusion into the magnetites was negligible during the 5 min heating time. The observed excess Si counting rates in our test experiments are comparable to the largest measured rates in the natural samples. Although quantitative comparisons cannot be made, polishing contamination clearly cannot be ignored in the natural samples. Thus, for 1038 we can set an upper limit of about 0.0006 for $D_{Si}^{ilm/liq}$. For magnetite one approach is to use the measured ilmenite Si counting rates as a polishing blank correction. Thus we infer a relatively homogeneous magnetite Si content corresponding to $D_{Si}^{mt/liq} = 0.0013 \pm .0003$. The upper end of the quoted range assumes negligible polishing contamination; the lower bound uses the ilmenite as a blank correction.

RESULTS

In a perfectly equilibrated crystal-liquid system, crystals and liquid are expected to be homogeneous. Few natural samples are likely to meet this criterion, so partitioning studies based on individual grain analyses must set standards for an acceptable degree of heterogeneity. Consequently, assessments of intra- and intergrain homogeneity play a major role in our data analysis. In our samples some Fe-Ti oxide and zircon crystals that would normally have melted or re-equilibrated during partial fusion were prevented from doing so because they are included in relict plagioclase crystals. Because individual grain analyses are used, this is a minor complication, and attention was focused on Fe-Ti oxides and zircons that are surrounded by glass. These crystals are chemically and texturally distinct from the included ones, as discussed below. Many minor elements in the Fe-Ti oxides are relatively well equilibrated with the liquid, while none in the zircons are.

Glass

Three samples with glass fractions ranging from 15 to 33% were studied in detail. A fourth sample with less than 5% glass (1423) was briefly examined, but good microprobe analyses were not obtained. The glasses are metaluminous (atomic (Na + K)/Al $\approx$ 1) and are high-silica rhyolites. An overall degree of chemical homogeneity in the glass is required for these samples to be a useful source of phenocryst-matrix partition coefficients. This criterion is well satisfied for major elements, Mn, P, and U (Table 1). Zirconium is not homogeneous and is discussed separately. In addition to the average composition, Table 1 lists the observed standard deviation of the distribution of microprobe analyses and the ratio of this standard deviation to that calculated from counting statistics. One criterion for compositional homogeneity is that this ratio be less than two. A second criterion for homogeneity is based on microprobe analyses of the same sample on different days, giving a measure of precision based on reproducibility, about 2%. Based on these two criteria only the TiO_2 content of sample 1327 has analytically significant variability, but this is only about 9%. With the exception of CaO, which is about a factor of two lower in our analysis, there is good agreement between our glass analysis for sample 1038 (including U) and that of BACON and DRUITT (1988). The glass homogeneity supports the assumption that any residual effects from slow dissolution of the major phases in the original granodiorite are not important.

The special minor-element microprobe operating conditions produced relatively high-precision Mn (±5–10% for individual analyses) results despite low concentrations. Phosphorous contents are low and the analyses have large counting statistics errors which prohibit firm conclusions about homogeneity, but the data for a given sample are quite consistent and intersample differences are probably real.

While the glass in individual samples is well homogenized, there are noticeable intersample variations for many elements.

Table 1
CHEMICAL COMPOSITIONS OF GLASS[a]

Sample	1326	σ[b]	σ/σ$_{cs}$	1038	σ	σ/σ$_{cs}$	1327	σ	σ/σ$_{cs}$
% Melt[c]	15			30			33		
weight %									
SiO_2	74.8	.49	3.3	74.9	1.18	7.9	75.9	.56	3.7
Al_2O_3	11.45	.10	4.3	11.43	.18	7.7	11.74	.16	6.9
FeO[d]	1.69	.03	1.3	2.08	.05	2.0	1.59	.04	1.
MgO	.167	.004	1.9	.213	.004	1.9	.176	.004	1.7
CaO	.138	.013	1.4	.259	.009	.9	.215	.015	1.6
Na_2O	3.68	.08	1.8	4.04	.10	2.4	3.76	.07	1.6
K_2O	5.17	.04	1.9	4.65	.04	1.9	4.76	.15	8.
TiO_2	.428	.017	2.0	.524	.007	.8	.411	.036	4.
MnO[d]	.0271	.0030	1.3	.0306	.0016	.7	.0214	.0026	1.1
ppm									
P	76	17	.4	118	25	1.0	87	21	.9
U	5.64	.48	1.4	6.15	.47	1.7	3.41	.38	1.6
Total	97.61			98.15			98.58		

(a) For samples 1326, 1038, and 1327, major elements were measured on 11, 14, and 21 points; MnO, P, and other minor elements were measured on 9, 10, and 17 points; U was measured on 4, 8, and 12 areas, respectively.
(b) σ is the observed standard deviation of the distribution of concentrations; σ$_{cs}$ is the standard deviation calculated from counting statistics.
(c) Melt fraction was determined from digitized photomosaics of transmitted light sections.
(d) Fe and Mn are calculated as FeO and MnO, but multiple valence states are undoubtedly present.

These variations are small for the major elements, but considerably higher for minor and trace elements. The variation in U content in Table 1 (65%) is not inversely correlated with melt fraction, as would be expected, but when sample 1423 is considered (<5% glass, 12 ppm U) the U content varies by more than a factor of three, indicative of a general inverse correlation of U concentration with glass fraction. Lack of a perfect correlation reflects uncertainties in the melt fractions, U inhomogeneity in the parent granodiorites, and intersample variations in the degree of dissolution of U host phases (at least zircon) for a given degree of melting.

Fe-Ti Oxides

Uranium partitioning

A grain-by-grain summary of apparent Fe-Ti oxide-liquid partition coefficients for uranium ($D_i^{crystal/liq} = [i]_{crystal}/[i]_{glass}$) is shown in Fig. 2. Partition coefficients were calculated from the track densities of the oxide grains and the nearby glass with a correction added for fission fragment range differences (BENJAMIN, 1980). The errors are large because of the relatively low partition coefficient and small grain sizes. It should be emphasized that much more precise results can be obtained with higher neutron fluences, but the additional work does not seem justified following the previous discussion on the magnitude of $D_U^{oxide/liq}$ in the fission track radiography section. Grains surrounded by glass are the most likely to be in equilibrium with the liquid. Unfortunately, such grains > 100 μm in size are rare. The other grains in Fig. 2 occur as inclusions in plagioclase, making equilibration with the liquid unlikely; nevertheless, some have partition coefficients consistent with those for grains surrounded by glass. Because the oxides often occur as touching (not exsolved) sections of titanomagnetite and ilmenite it was difficult to make separate U concentration measurements for each phase. However, the grain in sample 1327 (solid square) is ilmenite and may have a higher partition coefficient. Six of the nine grains are compatible with $D_U^{oxide/liq} = 0.10$–0.13; partition coefficients for the other three included grains are lower by as much as a factor of three. Although more data would be required for conclusive proof, it appears that equilibration with the relatively U-rich liquid results in Fe-Ti oxides with a higher U concentration than those characteristic of the host granodiorite.

Most of the Fe-Ti oxides in these samples contain small inclusions of apatite and rare zircon. The presence of such inclusions, especially apatite, in Fe-rich phases is quite common (BACON, 1989), and they probably systematically affect the results of mineral separate partitioning studies. A great advantage of fission track radiography is that analyses are made on individual grains and unsuitable grains can be avoided. Apatite or zircon crystals larger than 1–2 μm were not present in the grains used for Fig. 2. Fission fragments in Fe-Ti oxides can be observed from depths as great as 8 μm, and buried inclusions could produce an occasional high value, but, statistically, it is not reasonable for most of the grains to give high U contents for this reason. We cannot rule out a high abundance of sub-micron inclusions, and a

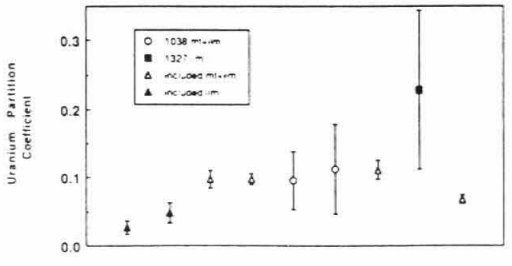

FIG. 2. Crystal-liquid partition coefficients for U in individual Fe-Ti oxide grains. Open symbols are touching magnetite + ilmenite grains; filled symbols are ilmenite only. Circles: grains from sample 1038 surrounded by glass; square: grain from sample 1327 surrounded by glass; triangles: grains from 1038, 1326, and 1423 included in plagioclase. All of these values are too low to significantly fractionate U and Th.

conservative interpretation of our data is that $D_U^{oxide/liq}$ for our sample is less than 0.2. To the extent that a large population of U-rich micro-inclusions is unreasonable, our data indicate that $D_U^{oxide/liq}$ is about 0.1.

The high U-Th fractionations found in Fe-Ti oxide mineral separates for ^{238}U-^{230}Th disequilibrium studies are most likely due to impurities, inclusions, or disequilibrium. The range of apparent $D_U^{oxide/liq}$ values determined from mineral separate studies is large, ranging up to >2 (CONDOMINES et al., 1982b), but the lowest values for magnetite (0.09 in trachytes: LEMARCHAND et al., 1987; 0.08–0.09 in andesites: ALLÈGRE and CONDOMINES, 1976; 0.08–0.13 in rhyolitic pumice: OMURA et al., 1988; TRUMBLE et al., 1984) and ilmenite (0.06 in rhyolite: MAHOOD and HILDRETH, 1983) are similar to our values.

Minor-element partitioning

A number of minor element substitutions occur in Fe-Ti oxides. We determined crystal-liquid partition coefficients for both titanomagnetite and ilmenite and coexisting magnetite-ilmenite crystal-crystal partition coefficients using electron microprobe analyses. The consistency of single grain partition coefficients can be used to assess how nearly equilibrium between the oxides and the liquid was approached.

High microprobe beam currents (50 nA) and long counting times yielded meaningful analyses for concentrations as low as 100 ppm. Two or three analyses were made on most grains of titanomagnetite and ilmenite, and the replicate analyses usually agree within counting statistics, justifying the use of average values for a given grain. Exceptions are Cr and V in magnetite and ilmenite, respectively, and Si in both phases. Although real, these intragrain variations in Si, Cr, and V are commonly much less than the intergrain variations. Representative analyses of grains surrounded by glass are listed in Table 2.

Using our previously defined standards for homogeneity, the Fe-Ti oxides do not form a homogeneous population, but, if attention is focused on only those grains surrounded by glass, the compositions converge significantly. The results are summarized in terms of individual grain crystal-liquid partition coefficients for Mg, Mn, and Al (Fig. 3a and b) and in terms of a simple correlation plot for V_2O_3 and Cr_2O_3 (Fig. 3c), as there are no data for these elements in the glass.

Considering only grains surrounded by glass, the data for Mn, Mg, and Al for both magnetite and ilmenite form a relatively tight cluster for a given rock (Fig. 3a and b), indicating well-defined (approaching equilibrium) partition coefficients for these elements. For sample 1327 ilmenite, there are small correlated variations for Mn and Mg outside the analytical errors, but all values for both phases in 1327 are systematically higher than those in 1038. In contrast, there is no systematic difference in Al partition coefficients for ilmenite between the two samples, and the single 1327 magnetite grain has only about 10% more Al than 1038. As 1038 and 1327 are very similar samples, the differences in Mg and Mn in ilmenite are surprising, indicating that the ilmenites are somewhat further from equilibrium or there is a high degree of sensitivity of ilmenite partition coefficients to petrologic conditions. (It is worth noting that if oxide concentrations rather than partition coefficients for Mg and Mn are compared, the intersample difference disappears; nevertheless, the proper comparison is in terms of partition coefficients.)

Table 2
REPRESENTATIVE Fe-Ti OXIDE COMPOSITIONS[a]

	Magnetite				Ilmenite			
	1038		1327		1038		1327	
FeO	81.2	±.2[b]	81.5	±.2	59.9	±.1	60.2	±.1
MgO	2.22	±.01	2.16	±.01	2.01	±.01	2.04	±.01
MnO	.46	±.01	.44	±.01	.255	±.008	.253	±.007
TiO_2	10.97	±.05	10.01	±.05	33.7	±.1	34.0	±.1
SiO_2	.095	±.019	.067	±.016	≤.037		≤.031	
Al_2O_3	1.35	±.01	1.52	±.01	.288	±.004	.311	±.004
V_2O_3	.55	±.01	.62	±.01	.358	±.008	.291	±.004
Cr_2O_3	.25	±.01	.122	±.007	.088	±.007	.046	±.001

(a) Analyses are from grains surrounded by glass.
(b) Errors calculated from counting statistics except for Si, where errors are analytical (see text).

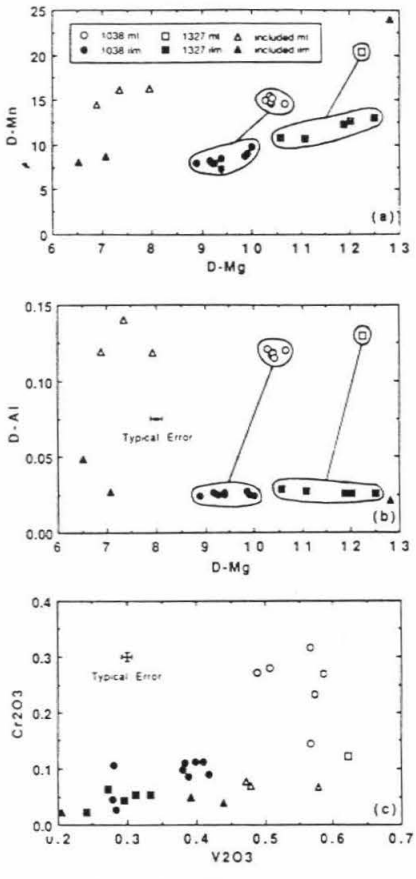

FIG. 3. Fe-Ti oxide-liquid partition coefficients for Mg, Mn, Al, and Fe-Ti oxide concentrations for V_2O_3 and Cr_2O_3. Note that the scales vary. Symbols are the same as Fig. 2 except open symbols are magnetite only and included grains are all from 1038. In (a) and (b) magnetite and ilmenite grains from the same sample are circled and connected for clarity. Typical errors are representative of the center of the diagram. (a) D_{Mn} vs. D_{Mg}. For D_{Mn} in ilmenite spread is ±10% for 1327, ±14% for 1038. (b) D_{Al} vs. D_{Mg}. The range in D_{Al} for each sample is about ±3% for magnetite and ±6% for ilmenite. (c) Cr_2O_3 vs. V_2O_3. Spread in Cr_2O_3 is up to a factor of two for magnetite and a factor of four for ilmenite. Different elements appear to have equilibrated to different degrees.

The V data (Fig. 3c) show larger variations than those for Mn, Mg, and Al. The range of ilmenite concentrations overlap, but those for 1327 tend to be lower. The 1327 magnetite has a higher V concentration than any measured in 1038.

As discussed in the analytical methods section, for sample 1038, $D_{Si}^{ilm/liq}$ and $D_{Si}^{mt/liq}$ are ≤0.0006 and 0.0013 ± .0003, respectively, where the uncertainty for magnetite is analytical. Silicon in magnetite appears homogeneous to better than ±20%.

On the basis of trace-element data given by BACON and DRUITT (1988) for a glass separate from a sample (1023G) similar to these, the Cr content of the glass in these samples is estimated to be approximately 2 ppm. This corresponds to a Cr partition coefficient of 500–1000 in magnetite and 100–500 in ilmenite. These values are extremely high; consequently, the Fe-Ti oxide Cr concentration would be very sensitive to fluctuations in the Cr content in liquid boundary layers around growing crystals. Such effects would be a reasonable explanation for the large variations in Fe-Ti oxide Cr concentrations if the Fe-Ti oxides grew from the melt. This raises an interesting question: are the Fe-Ti oxides in the glass phenocrysts or relicts that have approached equilibrium with the melt? Although equivocal, petrographic evidence suggests that they are relicts in that they lack euhedral faces and have a tendency to be on glass-plagioclase boundaries, sometimes filling glass embayments in plagioclase crystals. This suggests that the Fe-Ti oxide grains were part of the original granodiorite assemblage and were undergoing partial dissolution. Many elements (Al, Si, Mg, Mn) in the Fe-Ti oxides are relatively close to equilibrium with the coexisting liquid; however, the spread in the Cr concentrations may reflect relatively sluggish diffusion (DIECKMANN et al., 1978), making this element the furthest from equilibrium. Vanadium is intermediate.

There are sufficient systematic compositional differences between the included grains and grains surrounded by glass (Fig. 3a–c) to indicate that the included grains are not in equilibrium with the glass. This indicates that the crystals in the glass are distinctly different and their compositions are predominantly the result of equilibration with the melt. Our Mg and Mn data for touching magnetite-ilmenite grains in glass satisfy the Mg/Mn equilibrium test of BACON and HIRSCHMANN (1988), but included oxide pairs plot slightly below their Fig. 1 "2σ" band. Finally, in essentially all included oxide grains the titanomagnetite phase has ilmenite lamellae characteristic of oxidation during sub-solidus cooling (BUDDINGTON and LINDSLEY, 1964; HAGGERTY, 1976a).

Table 3
MINOR ELEMENT PARTITION COEFFICIENTS FOR MAGNETITE AND ILMENITE[a]

	Crystal-Liquid Partition Coefficient		Magnetite-Ilmenite Crystal-Crystal
	Magnetite	Ilmenite	Partition Coefficient
Mg	10.3	9.5	1.04
Mn	15	8	1.67
Al	.117	.025	4.73
V	>130	>80	1.3
Cr	850	225	2.6
Si	.0013	≤.0006	≥2

(a) Except for V, Cr, and Si, uncertainties are ±1 of the last significant figure. See text for explanation of Si analyses. Crystal-liquid partition coefficients for V and Cr based on assuming <30 ppm V and 2 ppm Cr in the glass from Bacon and Druitt (1988).

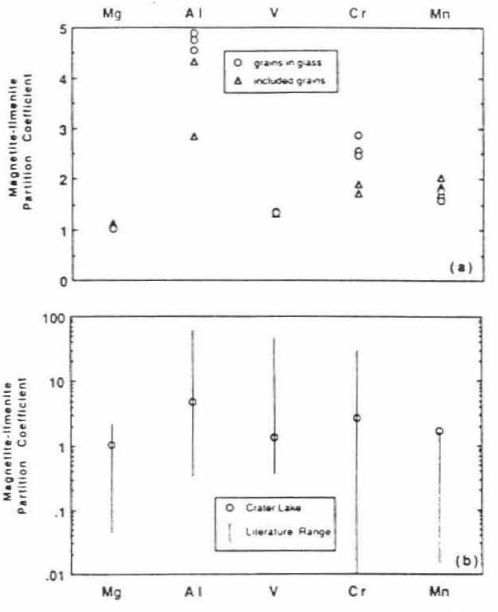

FIG. 4. (a) Magnetite-ilmenite crystal-crystal partition coefficients for touching grains from sample 1038. Circles: grains surrounded by glass; triangles: grains included in plagioclase. (b) Data from (a) for grains surrounded by glass superimposed upon the literature range of magnetite-ilmenite partition coefficients determined from Haggerty (1976b). The range in our data is much smaller.

Since these lamellae are present in the included grains but very rare in the exposed ones, they are interpreted to be a remnant of the original cooling of the parent granodiorite. When the rock was subsequently melted by the Mt. Mazama magmatic system, the grains exposed to the liquid were able to approach equilibrium under the new conditions and the rapid quench on eruption prevented them from oxidizing again.

The possibility that some minor elements (Cr, V) are not completely equilibrated, even for Fe-Ti oxide grains in glass, raises the possibility that U is also not equilibrated. The clustering on Fig. 2 argues against the possibility that the true partition coefficient is greatly higher than 0.1, although the errors on individual grains in the glass are relatively large.

Table 3 summarizes the minor-element Fe-Ti oxide partition coefficients based on the 1038 grains surrounded by glass. Estimates for V and Cr are uncertain, but they are definitely extremely high. As discussed later, our magnetite partition coefficients are much higher for Cr and V and lower for Mn than most in the literature. The available data for transition metal partition coefficients vary over a range of 10–100, but the relative order appears to be Cr > V > Mn. Our data are consistent with this order. Compared to the overall literature range the intergrain variations described above are relatively small, reinforcing the conclusion that our crystals are at least moderately well equilibrated with respect to these elements.

Among the Fe-Ti oxides analyzed from sample 1038, five consist of touching titanomagnetite and ilmenite. Titanomagnetite-ilmenite crystal-crystal partition coefficients for

these grains are shown in Fig. 4a, and average values for grains in contact with the glass are given in Table 3. In the case of crystal-crystal partitioning there seems to be less difference between the included and exposed grains than for crystal-liquid partitioning. This is a reasonable result because crystal-crystal equilibration is approached by exchange between the touching oxides and does not require interaction with the melt. However, the included grains do have systematic differences in crystal-crystal partition coefficients for some elements and a much larger spread in Fe/Ti (not shown). For the grains exposed to the glass, all the crystal-crystal partition coefficients are quite consistent.

Figure 4b shows our results superimposed on the range of literature values for magnetite-ilmenite partition coefficients determined from a tabulation by HAGGERTY (1976b). The typical spread of the literature range is about two orders of magnitude. The causes of this spread are unknown, but its existence suggests that solid-solid partitioning is very sensitive to the ambient conditions of equilibration. Thus, the overall close coherence of our data is a good argument for equilibration between the Fe-Ti oxide phases.

Zircon

Unlike the Fe-Ti oxides, zircons are not equilibrated with the liquid, even when only grains in contact with the glass are considered. In addition to the U fission track distributions, electron microprobe data with good ($\leq$10%) precision were obtained for Y, Hf, and in many cases P. All of these elements show relatively large intragrain and intergrain variations.

It appears that the zircons in the partially melted granodiorites were still in the process of dissolving at the time of the Mt. Mazama climactic eruption. This is best illustrated by the glass Zr concentrations which, in contrast to other elements, are not homogeneous. Measurements of three profiles from sample 1327 show no apparent Zr gradients in the

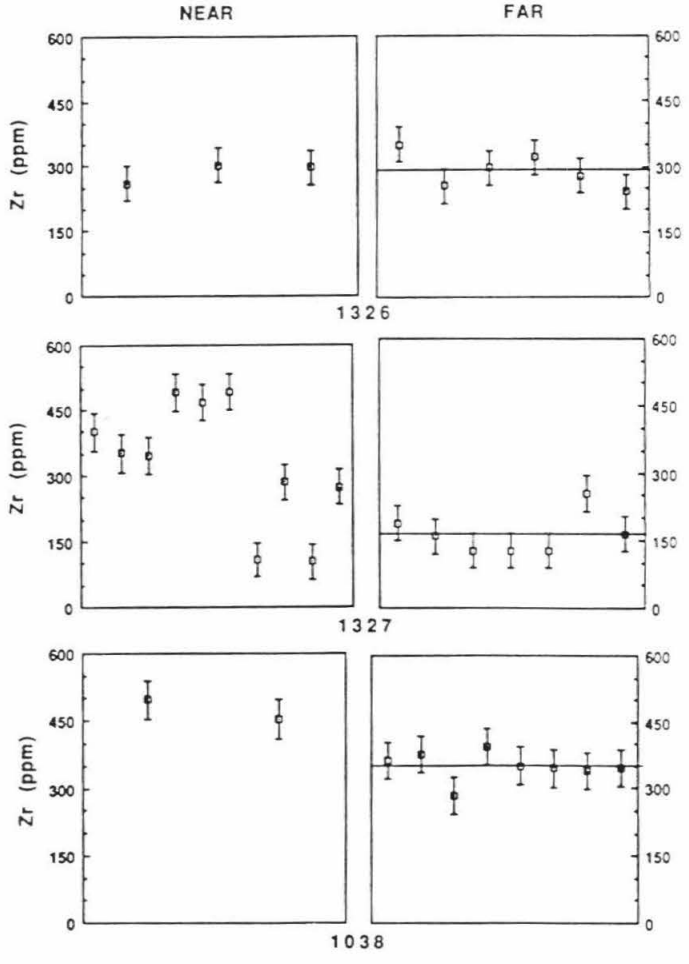

FIG. 5. Zirconium concentration in the glass. Data are divided into points near to (<100 μm) and far from (>500 μm) zircon grains. Horizontal line represents average value for far grains; for sample 1327 near value is up to three times greater than far value. Horizontal scale has no significance. Unlike all other elements, Zr is inhomogeneous, showing gradients away from dissolving zircons.

glass within 200 μm of the zircons. However, as shown in Fig. 5, when analyses near to (<100 μm) and far from (>500 μm) zircons are compared, the near concentrations tend to be systematically higher by as much as a factor of 3 for two of the three samples studied. This variation is not due to electron beam scatter, based on the experiments described in the electron microprobe analyses section, or polishing contamination, as the Zr concentrations in 1038 were quantitatively reproduced after the sample was repolished using a different technique. The characteristic length scale of the Zr gradients appears to be on the order of 200–500 microns. Studies with higher sensitivity and larger numbers of analyses would be required to document these gradients in detail. The Zr concentration far from zircons in sample 1038 is in good agreement with the 375 ppm given by BACON and DRUITT (1988).

The Zr concentration required for zircon saturation is poorly constrained for nearly anhydrous liquids, but HARRISON and WATSON (1983) suggest that it is about a factor of two less than that required for hydrous (>2% H_2O) melts (about 1000 ppm Zr for this composition and temperature; WATSON and HARRISON, 1983). Thus, the saturation concentration for these samples (about 500 ppm Zr) is greater than the measured Zr concentrations in these samples, supporting the interpretation that the zircons were dissolving. Zirconium diffusion data (HARRISON and WATSON, 1983) indicate that zircon dissolution is very dependent on water concentration and is extremely slow in relatively dry systems so that unstable grains may exist for several thousand years. Extrapolation of their Fig. 5 to 980°C shows that for 0.4 wt% water a 100 μm zircon in a Zr-undersaturated liquid would require about 10^4 years to dissolve.

There is a general intersample correlation of glass Zr and U contents, suggesting that zircon is the primary source of U during melting. However, eleven specific comparisons of U concentrations in the glass near and far from zircons show only one example of an enhancement near a zircon significant at the 2σ level (30%; compare Fig. 5). Even though zircon was the major Zr and U host phase in the parent granodiorite, U is better homogenized in the liquid, apparently diffusing more rapidly than Zr, although the systematics of HOFMANN (1980) predict similar diffusion coefficients.

The intra- and intergrain variations in zircon U contents are quite large. While most individual zircons have a fairly homogeneous U concentration, many zircons near glass-plagioclase boundaries have "polarized" U distributions with higher concentrations in regions closest to plagioclase crystals. Figure 6 is an example of such a U distribution. Electron microprobe analyses (1–2 μm spot, 7 points) show that trends for Y and P are qualitatively consistent with that seen for U. The simplest interpretation of this observation is that (a) these elements were diffusing out of the zircon more rapidly than the zircon was dissolving. The area of the zircon crystal in Fig. 6 with high U adjacent to glass must then be a younger contact. Alternatively, (b) variations in U concentrations could reflect increasing exposure of concentrically zoned zircons to the liquid as dissolution progressed from one side, or (c) the samples contain two populations of zircons: one with a high, homogeneously distributed U concentration and a second with a lower, more inhomogeneous U distribution.

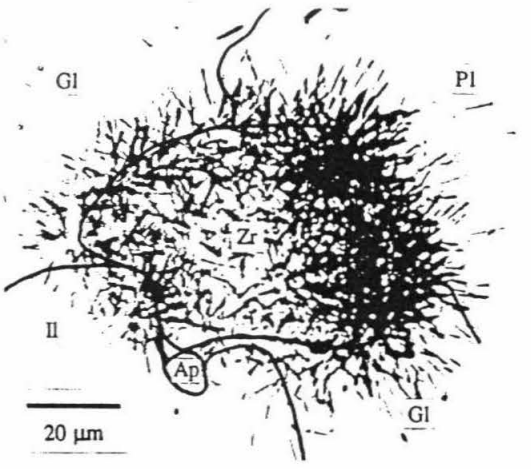

FIG. 6. Transmitted light photomicrograph of fission tracks in mica detector from a zircon on a plagioclase-glass boundary. Grain boundaries are included for reference. Zr = zircon, Pl = plagioclase, Il = ilmenite, Gl = glass, Ap = apatite. Note much higher track density in region near plagioclase crystal. Uranium appears to be diffusing out faster than the zircon is dissolving.

Explanations (b) and (c) are less likely for the following reasons: 17 zircons totally enclosed in plagioclase are not zoned and, moreover, all have 3–5 times higher U concentrations (and at least 1 with comparable enhancements in Y and P) than even the highest-U regions of the grains in contact with the glass. In addition, a visual survey of fission track images from ≈30 zircons from an unmelted sample revealed no inhomogeneous zircons. The existence of two populations of zircons is also unlikely because early crystallized zircons in the original granodiorite would tend to preferentially occur as inclusions in plagioclase, but these would be expected to be U-poor relative to the later ones, contrary to observation.

The Y and P contents of the zircons are fairly well correlated (Fig. 7). Because of the coupled substitution $Y + P \Leftrightarrow Zr + Si$, a 1:1 correlation is expected but, surprisingly, is not found. Most of the data are compatible with an atomic Y/P = 2.5, but this has no obvious interpretation. (Y + REEs)/P > 1 is common (SPEER, 1982), and the apparent positive charge deficit could be the consequence of oxygen vacancies, halogen substitution for oxygen, or, most likely, hydroxyl substitution, as hydrated zircons are common (G. ROSSMAN, pers. comm.).

The Hf content of these zircons varies from 1.14 to 1.43 wt% (0.5% counting statistics). Hafnium concentrations tend to be higher near crystal rims and generally do not correlate with any other trace element. Variations within some crystals are as large as the total intergrain range. These Hf contents are slightly lower than the average (1.7 wt%) of a large suite of zircons compiled by AHRENS and ERLANK (1969).

The approach to equilibrium of the zircons with liquid is accompanied by decreasing concentrations of U, Y, and P in the zircons. The intergrain range in minimum concentrations may reflect different times of exposure of zircon to melt. The minimum observed concentrations for these elements are found in homogeneous zircons in the glass (not the po-

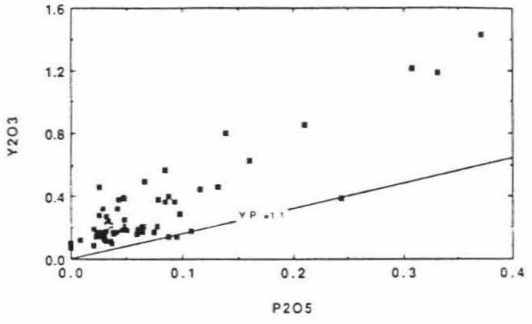

FIG. 7. Plot of Y_2O_3 vs. P_2O_5 for zircons with line representing atomic one-to-one correlation shown for reference. They are well correlated, but Y/P > 1, possibly due to hydroxyl substitution for oxygen.

larized ones); these give upper limits for partition coefficients. For U, partition coefficient upper limits are 16, 28, and 15 for samples 1326, 1327, and 1038, respectively, based on analyses of 4, 6, and 2 zircons. Within errors the upper limits for the P partition coefficients are about 1 for all samples. Using the BACON and DRUITT (1988) glass Y content of 43 ppm for sample 1038 permits an upper limit of 23 for the Y partition coefficient.

Other Phases

The P content of the glass (around 100 ppm) is well below the apatite saturation level of 530 ppm from HARRISON and WATSON (1984). Nevertheless, occasional apatite is found as small grains surrounded by glass or at margins between glass and relict phases. It is not obvious petrographically whether or not the apatites were dissolving, but, as with zircon, P diffusion data (HARRISON and WATSON, 1984) indicate that apatite dissolution in dry melts is very slow. Inspection of the fission track images shows that apatite is not highly enriched in U. With detailed mapping, two larger grains from sample 1327 give the same U partition coefficient of 2.3 ± 0.1. This compares well with an experimental partition coefficient for chlorapatite of 1.8 (BENJAMIN et al., 1980), although we have no constraint on equilibrium in the present case.

Pyroxene is common but occurs as fine (5–10 μm) skeletal crystals tightly interspersed with glass, making fission track analyses impossible.

Plagioclase and quartz are essentially U-free. Measurement of one large plagioclase crystal in 1327 gives an upper limit for the U concentration of 0.07 ppm.

DISCUSSION

U-Th Fractionation and ^{238}U-^{230}Th Disequilibrium

A major goal of this study was to evaluate the role of the Fe-Ti oxides in U-Th fractionation. Disequilibrium between ^{238}U and its short-lived daughter ^{230}Th ($t_{1/2}$ = 75,400 a) is produced when U/Th is changed. A decrease in U/Th results in a transient excess in ^{230}Th, and the amount of ^{230}Th will eventually decrease to the amount in radioactive equilibrium with ^{238}U. If the ^{238}U and ^{230}Th in a source region were in equilibrium before melting and if the Th isotopes are homogeneous after melting, then the degree of disequilibrium in a zero age (<10,000 years old relative to the melting event) rock is equal to the degree of U-Th fractionation produced during melting and crystallization (i.e. $(^{238}U/^{230}Th)_{rock} = [U/Th]_{rock}/[U/Th]_{source}$, where parentheses indicate activity ratios and brackets indicate elemental ratios). Summarizing the discussion in the introduction, there are three striking features of the ^{238}U-^{230}Th systematics for young volcanic rocks: (1) The magnitude of the observed fractionations is quite large: fractionations are commonly 5–20% but can be as high as 60% (NEWMAN et al., 1983). This is surprising for two nominally similar and very incompatible elements. (2) The fractionations occur in all volcanic compositions. (3) Fractionations resulting in U depletion are common and more difficult to explain than the converse. Ocean ridge and ocean island basalts are U depleted, while arcs tend to be U enriched. In continental arcs both directions are observed (CONDOMINES et al., 1988; NEWMAN et al., 1986; GILL and WILLIAMS, 1990). Producing the observed fractionations using major phases, such as clinopyroxene, requires low degrees of partial melting (WILLIAMS and GILL, 1989), but a wider range of melt fractions would be possible if accessory phases with high U partition coefficients are present.

The simplest mechanism to fractionate U and Th with a depletion of U in volcanic rocks is by leaving a residual solid phase with a high U/Th in the source region during partial melting. If Fe-Ti oxides were such a phase they would help explain feature (2) and, accepting the results of ^{238}U-^{230}Th disequilibrium mineral separate studies at face value, feature (3) as well (however, MAHOOD and HILDRETH, 1983, report $D_{Th} > D_U$). The most difficult observation to account for is feature (1). This requires a relatively high U partition coefficient and is the reason we have focused on U in this study. If our data can be generalized, $D_U^{oxide/liq}$ is about 0.1. Even if Fe-Ti oxides have highly enriched U/Th, given their typical abundances this partition coefficient is too small to be an important source of U-Th fractionation, even if the partition coefficient for Th is assumed to be 0. Consequently, even in a case where Fe-Ti oxide fractionation in young dacites is indicated by a marked decrease in TiO_2 with increasing SiO_2, there is no evidence for U-Th fractionation (RUBIN et al., 1989).

An understanding of U crystal-liquid partitioning must take into account the multivalent character of this element. The samples from this study last equilibrated under relatively high oxygen fugacity ($\log f O_2$ = FMQ + 1.8). Although compositional dependence of the valence state distribution of U for a given $f O_2$ may be important, an extrapolation of the data of SCHREIBER (1980) suggests that up to 80% of the U may be pentavalent or hexavalent for our samples. Thus, it is possible that significant amounts of penta- and hexavalent U may be present, which would tend to lower all U partition coefficients relative to the situation when much of the U is tetravalent (e.g., BENJAMIN et al., 1980). On the other hand, the oxygen fugacity of our samples is not uncommonly high for terrestrial rocks, and it is likely that our conclusions about the unimportance of Fe-Ti oxides probably stand despite the lack of understanding of the U valence state distribution.

In addition to affecting silicate melt partitioning, the va-

lence state of U plays an important role in its mobility during post-magmatic alteration. Under oxidizing conditions, U is very soluble in hydrothermal fluids and seawater as U^{+6}, and it is also subject to adsorption onto surfaces of Fe-Ti oxides (LANGMUIR, 1978; HSI and LANGMUIR, 1985). This may be accompanied by local reduction and precipitation of tetravalent U at Fe-Ti oxide-fluid interfaces. Fe-Ti oxides are observed to contain appreciable amounts of U in alteration zones (STURCHIO et al., 1986; VILLEMANT and FLÉHOC, 1989; GUTHRIE, 1989). Such surface concentration of U is also conceivable in an igneous environment, but it appears not to have occurred in our samples (there are no U-rich crystal rims). It is possible that the highly fractionated U/Th measured in Fe-Ti oxides in some mineral separate studies is due to U adsorption processes accompanying alteration.

Although generally absent from mafic and ultramafic rocks, zircon is a minor phase in most intermediate to silicic rocks and U-Th fractionation by zircon is another possible mechanism to explain ^{238}U-^{230}Th disequilibrium in such samples. Because $D_U^{zrc/liq}$ is large and greater than $D_{Th}^{zrc/liq}$, a small amount of zircon can have a significant effect on U-Th fractionation during crustal fusion, satisfying features (1) and (3). For example, using $D_U^{zrc/liq} = 20$ (this study) and $D_{Th}^{zrc/liq} = 4.4$ (assuming $D_U/D_{Th} = 4.5$ from MAHOOD and HILDRETH, 1983), 0.2% modal zircon retained in the source during 20% equilibrium partial melting will result in a U depletion of about 10% in the liquid. Zircon solubility is often quite high and would tend to cause all of the zircon in the source to be consumed during melting, given sufficient time. However, sluggish dissolution rates and isolation from melt contact as inclusions can allow chemically unstable zircon to remain in the magma source region (HARRISON and WATSON, 1983). This is clearly demonstrated by the abundance of zircon, both included and surrounded by glass, in our samples, which have undergone 15–33% melting with the possibility of extended time scales for melt-residue contact.

Although in some instances zircon could cause significant U-Th fractionations, mass balance calculations indicate that this is not true for sample 1038. Comparison of our compositional and modal data with the whole-rock analysis of BACON and DRUITT (1988) shows that essentially all of the U is in the glass, whereas almost half of the total Zr remains in the solid (presumably in zircon). As proposed in the results section, this is best explained as the result of a higher rate of U diffusion relative to zircon dissolution. As with U, the whole-rock and glass analyses of BACON and DRUITT show that all of the Th is in the glass; thus, liquid separation in 1038 probably would not result in substantial U-Th fractionation even with a large amount of zircon left behind. Nevertheless, the fact that zircon remains in the source indicates that in the general case of crustal melting zircon retention could be a common source of U-Th fractionation.

Lack of ^{238}U-^{230}Th disequilibrium, even with the retention of zircon or other accessory phases in the source region, may also be possible in an "all or nothing" situation where some zircons completely dissolve and others remain unchanged from their original state in the source. In the extreme case where all of the U in the source is in zircon, the separated liquid would have ^{238}U-^{232}Th fractionation but no ^{238}U-^{230}Th disequilibrium.

Apatite is a minor phase in essentially all igneous rocks, so it could satisfy feature (2) of ^{238}U-^{230}Th systematics. Limited experimental data from BENJAMIN et al. (1980) indicate that $D_U > D_{Th}$, which would satisfy feature (3). As with zircon, the solubilities of P_2O_5 are often too high for apatite stability, but, again like zircon, dissolution rates are extremely slow. The presence of apatite in our samples confirms the analysis of HARRISON and WATSON (1984) indicating that retention of apatite during melting can occur. Assuming that $D_U^{ap/liq} = 1.8$ and $D_{Th}^{ap/liq} = 1.3$ (BENJAMIN et al., 1980), unreasonably large apatite abundances of 4–5 wt% are required to produce significant (8–12%) U-Th fractionations even if no apatite melts at all. Using the whole-rock P_2O_5 content of sample 1038 (BACON and DRUITT, 1988), we find that 93% of the P is in the solid, corresponding to an apatite concentration (assuming all P_2O_5 is in apatite) of only 0.3 wt%.

Apatite inclusions are common in Fe-Ti oxides and are a possible explanation for the high apparent U partition coefficients and U/Th in Fe-Ti oxide mineral separates. There are quantitative difficulties, however. For example, assuming $D_U^{ap/liq} = 1.8$ and $D_U^{oxide/liq} = 0.1$, an apatite abundance of 24 wt% in the oxides would be required to produce an apparent $D_U^{oxide/liq}$ of 0.5 in an Fe-Ti oxide separate. This high apatite abundance is not reasonable and other U-rich impurities such as zircon may be present. Also, U incorporation by secondary alteration, as discussed above, may be a reasonable explanation.

The preceding discussion has focused on examples of partial melting to explain U-Th fractionation. A detailed treatment of partial melting models which produce U-Th fractionation is given by WILLIAMS and GILL (1989). U-Th fractionation by minor phases probably cannot be the dominant cause of ^{238}U-^{230}Th disequilibrium observed in ocean ridge basalts. The high frequency of such fractionations and the observation of both U enhancements and depletions indicate that other mechanisms may be at work also. Relatively complex models of melting and magma transport that can effectively separate elements with very low partition coefficients have been proposed (MCKENZIE, 1985; O'HARA, 1985; NAVON and STOLPER, 1987; WILLIAMS and GILL, 1989). A complication with such models (as well as simple equilibrium and fractional melting models) is that uncomfortably large fractionations are often produced for other incompatible elements whose partition coefficients are not extremely small. Uranium depletions and enrichments in magmas resulting from contamination by hydrothermal fluids near source regions and in shallow magma chambers have been proposed to explain the existence of both positive and negative U-Th fractionations (VILLEMANT and FLÉHOC, 1989), but the physical difficulties of mixing hydrothermal fluids with silicate melts argues that the latter process occurs only under rare circumstances. Lastly, preferential U volatilization may be a significant fractionation mechanism in subaerial environments (DIXON and BURNETT, 1987).

Anomalous Partition Coefficients for High-Silica Rhyolites

Based on phenocryst-matrix mineral separate data, MAHOOD and HILDRETH (1983) proposed that trace-element partition coefficients were anomalously high for high-silica

liquids because of melt polymerization effects. They attempted to correct for inclusions in their mineral separates and in some cases based their conclusions on electron microprobe data, but a subsequent study by MICHAEL (1988) showed that the high apparent partition coefficients for REES in pyroxenes reported by Mahood and Hildreth were dominated by accessory mineral impurities in the pyroxene separates. CAMERON and CAMERON (1986) attribute similar REE partitioning patterns in high-silica rhyolites to the same effect. The glass compositions of our samples and those studied by Mahood and Hildreth are quite similar, and, while there are major differences in water content and temperature between the two systems, we can qualitatively re-examine the fundamental issues raised by Mahood and Hildreth.

Our lower limit of 130 for $D_V^{mt/liq}$ (Table 3) is in the range quoted by Mahood and Hildreth (50–250), and our values for $D_{Cr}^{mt/liq}$ and $D_{Cr}^{ilm/liq}$ are much higher than values from mineral separates for a rhyolite of lower silica content obtained by NASH and CRECRAFT (1985; $D_{Cr}^{mt/liq} = 164$, $D_{Cr}^{ilm/liq} = 3$). Given the extreme compatibility of V and Cr in Fe-Ti oxides, partition coefficients based on mineral separates will tend to be low because of impurities in the glass separates. For example, 0.1 wt% of magnetite contamination in glass will reduce a measured Cr partition coefficient by approximately a factor of two. However, this still would not explain the difference between ours and those of NASH and CRECRAFT (1985), as our Cr partition coefficients are 5 to 75 times greater than theirs. It therefore appears that our data for V and Cr are at least compatible with Mahood and Hildreth's proposition, although there is no clear way to identify melt composition as opposed to other factors as the source of the differences.

Magnesium also has a relatively high partition coefficient (around 10) for both magnetite and ilmenite (Table 3), but there is little literature data for comparison. From data given by NASH and CRECRAFT (1985) much lower partition coefficients are obtained (0.5 and 1.8 for magnetite and 0.4 for ilmenite in three different rocks). However, their partition coefficients were calculated by material balance and are sensitive to errors in pyroxene modes, which are given to only one significant figure.

Our partition coefficients for Mn in Fe-Ti oxides and U and Y in zircon, on the other hand, are considerably lower than values reported for other high-silica systems. Our Mn partition coefficients are a factor of two lower than the relatively narrow range of 22–28 found by MAHOOD and HILDRETH (1983) for Fe-Ti oxides from Sierra La Primavera or magnetite from the Bishop Tuff. Bishop Tuff ilmenite ($D_{Mn}^{ilm/liq} = 50$) and data from NASH and CRECRAFT (1985; $D_{Mn}^{mt/liq} = 30$–40, $D_{Mn}^{ilm/liq} = 115$) show still higher values. Mineral separate purity should not be an issue in this case. Also, our magnetite-ilmenite crystal-crystal partition coefficient for Mn is higher than most literature values (Fig. 4b). The Crater Lake samples have a higher fO_2 than the Bishop Tuff, and a plausible explanation is to ascribe these differences to the higher oxygen fugacities of our samples. This may result in a higher proportion of trivalent and possibly tetravalent Mn, and may point to the valence-state distribution dominating melt structure effects as the main variable controlling Mn partitioning in high-silica systems.

Our U partition coefficients for zircon are at least 15 to 20 times lower than the values of 380 and 300 given for two Bishop Tuff samples (MAHOOD and HILDRETH, 1983). Purity of either zircon or glass separates is not important in this case, and the apparent homogeneity of U in the Bishop Tuff zircons, emphasized by Mahood and Hildreth, is probably a good argument that the zircons are not relict phases. Since the Crater Lake samples have a higher fO_2 it is tempting to appeal to a greater proportion of penta- and hexavalent U for our samples, but the interpolated $D_{Ho}^{zrc/liq}$ for the Bishop Tuff of 150 is also much higher than our upper limit of 23 for Y. By conventional wisdom these partition coefficients should be the same, and redox conditions do not affect this comparison. In addition, the range in interpolated Ho partition coefficients for zircons from dacites and granites measured by NAGASAWA (1970) is 40–250, and WATSON (1980) determined experimentally that $D_{Ho}^{zrc/liq} > 340$ in a synthetic felsic system, indicating that our Y partition coefficient is lower than published results for silica-rich compositions.

In summary, our data do not support the hypothesis that trace-element partition coefficients are anomalously large in high-silica systems. While our data for V and Cr may be consistent with this, our data for Mn, U, and possibly Y give no support to such an hypothesis. In addition, our partition coefficients are usually much lower than Mahood and Hildreth's, yet our samples have around 0.5 wt% water (S. NEWMAN, pers. comm.) compared to 4–6% for the Bishop Tuff (ANDERSON et al., 1989). Water is known to depolymerize silicate melts (STOLPER, 1982), and thus consistently higher partition coefficients for all elements in all phases would be expected for our samples, which is not the case. If liquid polymerization were the dominant factor in partitioning in high-silica systems, we might have expected more similarities between our results and those of MAHOOD and HILDRETH (1983), regardless of the differences between the two systems (temperature, water content, fO_2). It is almost certainly true that silica content is important in trace-element partitioning, but it appears that melt polymerization does not override all other factors in high-silica liquids.

Equilibration Time Scale for Crater Lake Partial Melts

The only time constraint from our data comes from the Zr concentrations in the glass. Zirconium variations were determined in the glass in two of the three samples (Fig. 5). Zirconium released by zircon dissolution does not produce measurable gradients in the region within 200 μm of the grain, so the characteristic length for Zr diffusion is at least 200 μm, but Zr has not been homogenized over 500 μm, setting this as an upper limit for a characteristic Zr diffusion length.

The diffusion data from HARRISON and WATSON (1983) indicate values for the diffusion coefficient for Zr of about 10^{-13}–10^{-14} cm^2/sec, corresponding to Zr diffusion time scales ($t \approx l^2/D$) of 800 to 8000 years (this calculation assumes that the Zr concentration profiles in these samples are the result of diffusion and are not complicated by relative movement of melt and solid). These time-scale estimates are consistent with the magmatic time scale for Mt. Mazama estimated by BACON and DRUITT (1988). Either time estimate is long compared to any practical laboratory experiment duration.

One might have expected that the Fe-Ti oxides would be better equilibrated, given the estimated time scales. The Fe-Ti oxides are phenocrysts in the sense of being stable crystals in the glass in which they are found. However, assuming that the Fe-Ti oxide grains are relicts, minor- and trace-element equilibration is dependent on diffusion in the crystals. For diffusion not to be complete in 100–1000 years in 20–100 μm Fe-Ti oxides, cation diffusion coefficients on the order of 10^{-14}–10^{-17} cm^2/sec at 1000°C are required, which seem somewhat low compared to the tracer diffusion study by DIECKMANN et al. (1978).

It should be emphasized that, compared to the present study, partition coefficients measured by the conventional phenocryst-matrix approach require the assumption that the crystals be in equilibrium with the coexisting liquid. The traditional phenocryst-matrix studies are based on mineral separates and cannot address the issue of equilibration at the level we have done in this study. It remains to be seen if phenocryst-matrix partitioning studies with the new generation of instruments for *in situ* trace-element microanalysis will show better defined partition coefficients than the present study.

CONCLUSION

These samples provide a good illustration of the complex effects of accessory phases on trace-element partitioning discussed by WATSON and HARRISON (1984). The effectiveness of accessory phases in contributing to U-Th and other incompatible element fractionations during igneous processes is governed by their three "fundamental accessory phase parameters": solubilities of the accessory phases, partition coefficients for the trace elements of interest, and diffusivities that govern the equilibration rates. The data from these samples provide no support for the hypothesis that trace-element partition coefficients are anomalously large in high-silica systems. Our U partition coefficient for Fe-Ti oxides is not large enough for this phase to cause significant U depletion relative to Th, even if $D_{Th} = 0$. The samples are undersaturated with zircon and apatite, yet both are present, presumably due to slow dissolution rates. In turn, this reflects the silica-rich and H_2O-poor compositions and the consequent extremely slow diffusion rates of Zr and P in the liquid. While apparently not true for U in zircon in our samples, incompletely dissolved and included phases could result in larger fractions of incompatible elements being retained in the source than is predicted by equilibrium partitioning. Conversely, entrainment of Fe-Ti oxides from the source in a separated liquid would result in much higher concentrations of the highly compatible light transition metals (Ti, V, Cr, Mn) in the magma than predicted by simple equilibrium partitioning considerations. It is quite likely that source retention of unstable accessory phases during partial melting is not a unique feature of our samples and is probably an important trace-element fractionation mechanism.

Given that ^{238}U-^{230}Th disequilibrium is quite common and that it results from processes occurring a relatively short time prior to emplacement (equilibrium is restored in $\approx$0.3 Ma), it is likely that a variety of mechanisms, probably including complicated non-equilibrium and non-magmatic processes, are responsible.

Acknowledgments—P. Carpenter and J. Armstrong assisted with the electron microprobe analyses. Neutron irradiations were carried out by T. Crofoot at the TRIGA reactor facility at U. C. Irvine. Reviews by M. Harrison, P. Henderson, M. Clynne, T. Sisson, and an anonymous reviewer and helpful discussions with S. Newman, G. Rossman, and L. Silver are greatly appreciated. This study was initiated while CRB was a visiting professor at Caltech.

Editorial handling: J. D. Macdougall

REFERENCES

AHRENS L. H. and ERLANK A. J. (1969) Hafnium. In *Handbook of Geochemistry II/5*. Secs. B–O. Springer-Verlag, New York.

ALLÈGRE C. J. and CONDOMINES M. (1976) Fine chronology of volcanic processes using ^{238}U-^{230}Th systematics. *Earth Planet. Sci. Lett.* **28**, 395–406.

ALLÈGRE C. J. and CONDOMINES M. (1982) Basalt genesis and mantle structure studied through Th-isotopic geochemistry. *Nature* **299**, 21–24.

ANDERSEN D. J. and LINDSLEY D. H. (1988) Internally consistent solution models for Fe-Mg-Mn-Ti oxides: Fe-Ti oxides. *Amer. Mineral.* **73**, 714–726.

ANDERSON A. T., JR., NEWMAN S., WILLIAMS S. T., DRUITT T. H., SKIRIUS C., and STOLPER E. (1989) H_2O, CO_2, Cl, and gas in plinian and ash-flow Bishop rhyolite. *Geology* **17**, 221–225.

ARMSTRONG J. T. (1988) Quantitative analysis of silicate and oxide materials: comparison of Monte Carlo, ZAF, and $\phi(\rho z)$ procedures. In *Microbeam Analysis—1988* (ed. D. E. NEWBERRY), pp. 239–246. San Francisco Press.

BACON C. R. (1987) Granitoid blocks in climactic ejecta of Mount Mazama, Oregon: quenched samples of a magma chamber's fused walls (abstr.). *Geol. Soc. Amer. Abstr. Prog.* **19**, 577.

BACON C. R. (1989) Crystallization of accessory phases in magmas by local saturation adjacent to phenocrysts. *Geochim. Cosmochim. Acta* **53**, 1055–1066.

BACON C. R. and DRUITT T. H. (1988) Compositional evolution of the zoned calcalkaline magma chamber of Mount Mazama, Crater Lake, Oregon. *Contrib. Mineral. Petrol.* **98**, 224–256.

BACON C. R. and HIRSCHMANN M. M. (1988) Mg/Mn partitioning as a test for equilibrium between coexisting Fe-Ti oxides. *Amer. Mineral.* **73**, 57–61.

BACON C. R., ADAMI L. H., and LANPHERE M. A. (1989) Direct evidence for the origin of low-^{18}O silicic magmas: quenched samples of a magma chamber's partially-fused granitoid walls. *Earth Planet. Sci. Lett.* **96**, 199–208.

BENJAMIN T. M. (1980) Experimental actinide element partitioning between whitlockite, apatite, diopsidic clinopyroxene, and anhydrous melt at one bar and 20 kilobars pressure. Ph.D dissertation, California Institute of Technology.

BENJAMIN T. M., HEUSER W. R., and BURNETT D. S. (1980) Actinide crystal-liquid partitioning for clinopyroxene and $Ca_3(PO_4)_2$. *Geochim. Cosmochim. Acta* **44**, 1251–1264.

BUDDINGTON A. F. and LINDSLEY D. H. (1964) Iron-Titanium oxide minerals and synthetic equivalents. *J. Petrol.* **5**, 310–357.

BURNETT D. S. and WOOLUM D. S. (1983) *In situ* trace element microanalysis. *Ann. Rev. Earth Planet. Sci.* **11**, 329–358.

CAMERON K. L. and CAMERON M. (1986) Whole rock/groundmass differentiation trends for rare earth elements in high-silica rhyolites. *Geochim. Cosmochim. Acta* **50**, 759–769.

CONDOMINES M. and ALLÈGRE C. J. (1980) Age and magmatic evolution of Stromboli volcano from ^{230}Th-^{238}U disequilibrium data. *Nature* **288**, 354–357.

CONDOMINES M., MORAND P., CAMUS G., and DUTHOU L. (1982a) Chronological and geochemical study of lavas from the Chaîne des Puys, Massif Central, France: evidence for crustal contamination. *Contrib. Mineral. Petrol.* **81**, 296–303.

CONDOMINES M., TANGUY J. C., KIEFFER G., and ALLÈGRE C. J. (1982b) Magmatic evolution of a volcano studied by ^{230}Th-^{238}U disequilibrium and trace elements systematics: the Etna case. *Geochim. Cosmochim. Acta* **46**, 1397–1416.

CONDOMINES M., HEMOND CH., and ALLÈGRE C. J. (1988) U-Th-

Ra radioactive disequilibria and magmatic processes. *Earth Planet. Sci. Lett.* **90**, 243–262.

DENIEL C. (1988) ^{230}Th-^{238}U radioactive disequilibrium in some differentiated lavas from Piton Des Neiges (Reunion Island) (abstr.). *Chem. Geol.* **70**, 126.

DIECKMANN R., MASON, T. O., HODGE, J. D., and SCHMALZRIED, H. (1978) Defects and cation diffusion in magnetite (III). Tracer-diffusion of foreign tracer cations as a function of temperature and oxygen potential. *Ber. Bunsenges Phys. Chem.* **82**, 778–783.

DIXON J. E. and BURNETT D. S. (1987) U volatilization as a mechanism for ^{238}U-^{230}Th disequilibrium in young volcanic rocks (abstr.). *IUGG General Assembly XIX* (Vancouver), 406.

DRUITT T. H. and BACON C. R. (1989) Petrology of the zoned calc-alkaline magma chamber of Mt. Mazama, Crater Lake, Oregon. *Contrib. Mineral. Petrol.* **101**, 245–259.

GILL J. B. and WILLIAMS R. W. (1990) Th isotope and U-series studies of subduction-related volcanic rocks. *Geochim. Cosmochim. Acta* **54**, 1427–1442.

GUTHRIE V. A. (1989) Fission-track analysis of uranium distribution in granitic rocks. *Chem. Geol.* **77**, 87–103.

HAGGERTY S. E. (1976a) Oxidation of opaque mineral oxides in basalts. In *Oxide Minerals* (ed. D. RUMBLE III); *MSA Reviews in Mineralogy 3*, pp. Hg1–Hg98.

HAGGERTY S. E. (1976b) Opaque mineral oxides in terrestrial igneous rocks. In *Oxide Minerals* (ed. D. RUMBLE III); *MSA Reviews in Mineralogy 3*, pp. Hg101–Hg277.

HARRISON T. M. and WATSON E. B. (1983) Kinetics of zircon dissolution and zirconium diffusion in granitic melts of variable water content. *Contrib. Mineral. Petrol.* **84**, 66–72.

HARRISON T. M. and WATSON E. B. (1984) The behavior of apatite during crustal anatexis: equilibrium and kinetic considerations. *Geochim. Cosmochim. Acta* **48**, 1467–1477.

HOFMANN A. W. (1980) Diffusion in natural silicate melts: a critical review. In *Physics of Magmatic Processes* (ed. R. B. HARGRAVES), pp. 385–417. Princeton Univ. Press.

HSI C. D. and LANGMUIR D. (1985) Adsorption of uranyl onto ferric oxyhydroxides: application of the surface complexation site-binding model. *Geochim. Cosmochim. Acta* **49**, 1931–1941.

LANGMUIR D. (1978) Uranium solution-mineral equilibria at low temperatures with applications to sedimentary ore deposits. *Geochim. Cosmochim. Acta* **42**, 547–569.

LEMARCHAND F., VILLEMANT B., and CALAS G. (1987) Trace element distribution coefficients in alkaline series. *Geochim. Cosmochim. Acta* **51**, 1071–1081.

MAHOOD G. and HILDRETH W. (1983) Large partition coefficients for trace elements in high-silica rhyolites. *Geochim. Cosmochim. Acta* **47**, 11–30.

MCKENZIE D. (1985) ^{230}Th-^{238}U disequilibrium and the melting processes beneath ridge axes. *Earth Planet. Sci. Lett.* **72**, 149–157.

MICHAEL P. J. (1988) Partition coefficients for rare earth elements in mafic minerals of high silica rhyolites: the importance of accessory mineral inclusions. *Geochim. Cosmochim. Acta* **52**, 275–282.

NAGASAWA H. (1970) Rare earth concentrations in zircons and apatites and their host dacites and granites. *Earth Planet. Sci. Lett.* **9**, 359–364.

NASH W. P. and CRECRAFT H. R. (1985) Partition coefficients for trace elements in silicic magmas. *Geochim. Cosmochim. Acta* **49**, 2309–2322.

NAVON O. and STOLPER E. (1987) Geochemical consequences of melt percolation: the upper mantle as a chromatographic column. *J. Geol.* **95**, 285–307.

NEWMAN S., FINKEL R. C., and MACDOUGALL J. D. (1983) ^{230}Th-^{238}U disequilibrium systematics in oceanic tholeiites from 21°N on the East Pacific Rise. *Earth Planet. Sci. Lett.* **65**, 17–33.

NEWMAN S., FINKEL R. C., and MACDOUGALL J. D. (1984) Comparison of ^{230}Th-^{238}U disequilibrium systematics in lavas from three hot spot regions: Hawaii, Prince Edward and Samoa. *Geochim. Cosmochim. Acta* **48**, 315–324.

NEWMAN S., MACDOUGALL J. D., and FINKEL R. C. (1986) Petrogenesis and ^{230}Th-^{238}U disequilibrium at Mt. Shasta, California, and in the Cascades. *Contrib. Mineral. Petrol.* **93**, 195–206.

O'HARA M. J. (1985) Importance of the 'shape' of the melting regime during partial melting of the mantle. *Nature* **314**, 58–62.

OMURA A., KAWAI S., and TAMANYU S. (1988) Dating of volcanic products by the radioactive disequilibrium system between ^{238}U and ^{230}Th. *Bull. Geol. Surv. Japan* **39**, 559–572.

SCHREIBER H. D. (1980) Properties of redox ions in glasses: an interdisciplinary perspective. *J. Non-Cryst. Solids* **42**, 175–184.

SPEER J. A. (1982) Zircon. In *Orthosilicates* (ed. P. H. RIBBE); *MSA Reviews in Mineralogy 5*, 2nd ed., pp. 67–113.

STOLPER E. M. (1982) The speciation of water in silicate melts. *Geochim. Cosmochim. Acta* **46**, 2609–2620.

STURCHIO N. C., MUEHLENBACHS K., and SEITZ M. G. (1986) Element redistribution during hydrothermal alteration of rhyolite in an active geothermal system: Yellowstone drill cores Y-7 and Y-8. *Geochim. Cosmochim. Acta* **50**, 1619–1631.

RUBIN K. H., WHELLER G. E., TANZER M. O., MACDOUGALL J. D., VARNE R., and FINKEL R. (1989) ^{238}U decay series systematics of young lavas from Batur volcano, Sunda Arc. *J. Volcanol. Geotherm. Res.* **38**, 215–226.

TRUMBLE D. A., CLYNNE M. A., and ROBINSON S. W. (1984) The application of uranium-thorium systematics to rocks from the Lassen Dome Field, California. *USGS Open-File Rep. OFR 84-371*.

VILLEMANT B. and FLÉHOC C. (1989) U-Th fractionation by fluids in K-rich magma genesis: the Vico volcano, Central Italy. *Earth Planet. Sci. Lett.* **91**, 312–326.

WATSON E. B. (1980) Some experimentally determined zircon/liquid partition coefficients for the rare earth elements. *Geochim. Cosmochim. Acta* **44**, 895–897.

WATSON E. B. and HARRISON T. M. (1983) Zircon saturation revisited: temperature and composition effects in a variety of crustal magma types. *Earth Planet. Sci. Lett.* **64**, 295–304.

WATSON E. B. and HARRISON T. M. (1984) Accessory minerals and the geochemical evolution of crustal magmatic systems: a summary and prospectus of experimental approaches. *Phys. Earth Planet. Int.* **35**, 19–30.

WILLIAMS R. W. and GILL J. B. (1989) Effects of partial melting on the uranium decay series. *Geochim. Cosmochim. Acta* **53**, 1607–1620.

WILLIAMS R. W., GILL J. B., and BRULAND K. W. (1986) Ra-Th disequilibria systematics: timescale of carbonatite magma formation at Oldoinyo Lengai volcano, Tanzania. *Geochim. Cosmochim. Acta* **50**, 1249–1259.

Earth and Planetary Science Letters, 110 (1992) 227–244
Elsevier Science Publishers B.V., Amsterdam

[CL]

Experimental determination of U and Th partitioning between clinopyroxene and natural and synthetic basaltic liquid

T.Z. LaTourrette and D.S. Burnett

Division of Geological and Planetary Sciences, California Institute of Technology, Pasadena, CA 91125, USA

Received October 8, 1991; revision accepted February 28, 1992

ABSTRACT

Clinopyroxene–silicate liquid partition coefficients for U and Th have been determined by particle track radiography from 1 atm crystallization experiments at controlled fO_2. Two natural basaltic and one synthetic composition were studied at fO_2 values from the Ni–NiO oxygen buffer to 1 log unit more oxidizing than Fe–FeO (IW + 1). Over the range of fO_2 values and compositions studied, $D_U^{cpx/liq} = 0.0034–0.015$, $D_{Th}^{cpx/liq} = 0.008–0.036$, and $D_{Th}/D_U = 3.4–1.1$. With decreasing fO_2, D_{Th}/D_U can decrease by up to a factor of 3 for a given composition, primarily from an increase in $D_U^{cpx/liq}$, which we interpret as resulting from an increase in the proportion of tetravalent U in the system with decreasing fO_2. This demonstrates that crystal–liquid U–Th fractionation is fO_2 dependent and that U in terrestrial magmas is not entirely tetravalent. $D_{Th}^{cpx/liq}$ appears to decrease in the two basalts at the lowest fO_2, possibly as a result of changes in composition with fO_2.

Our data show the sense of U–Th fractionation by clinopyroxene–liquid partitioning is consistent with previous experimental determinations, in that $D_{Th}^{cpx}/D_U^{cpx} > 1$ in all cases. This indicates that, during partial melting, the liquid will have a Th/U ratio less than the clinopyroxene in the source. The observed $^{238}U–^{230}Th$ disequilibrium in MORB requires that the partial melt should have a Th/U ratio greater than the bulk source, and, therefore, cannot result from clinopyroxene–liquid partitioning. Further, the magnitudes of the measured partition coefficients are too small to generate significant U–Th fractionation in either direction. Assuming that clinopyroxene contains the bulk of the U and Th in MORB source, our results indicate that $^{238}U–^{230}Th$ disequilibrium in MORB may not be caused by partial melting at all.

1. Introduction

The actinide elements exhibit similar igneous geochemical behavior and are strongly partitioned into silicate melts relative to the major rock forming minerals. Thus, relatively little U–Th fractionation is expected in planetary igneous processes and, during planetary differentiation, actinide elements become highly concentrated in the crust. There is a strong coherence of U and Th in most lunar rocks and meteorites [1]. However, significant fractionation of U and Th can also occur. There are well documented fractionations in ordinary chondrites [2,3], meteoritic CAIs (e.g., [4]), Apollo 17 mare basalts [5], and virtually all types of terrestrial volcanic rock [6,7]. An understanding of these fractionations is important because U–Th fractionations may provide important clues to planetary igneous processes, and whole-planet U and Th abundances, necessary for cosmochemical and heat flow modelling, must be obtained from crustal values.

The magnitude of terrestrial U–Th fractionation is clearly revealed by radioactive disequilibrium between ^{238}U and ^{230}Th in young volcanic rocks. ($^{238}U/^{230}Th$) (parentheses signify activities) enrichments of up to 79% in island arc lavas and depletions as large as 38% in MORB have been observed [8,9]. Measurements of U-series disequilibria help us to understand the geochronology of young volcanic rocks, the timing of magmatic systems, and spatial variations of mantle Th/U [6,7,10]. In addition, the time scale at which ^{238}U and ^{230}Th return to equilibrium is short enough that the initial condition of secular

Correspondence to: T.Z. LaTourrette, California Institute of Technology, Division of Geological and Planetary Sciences, Mail Stop 170-25, Pasadena, CA 91125, USA

equilibrium in most magmatic source regions is well constrained. This presents a unique method for determining the magnitude of U–Th fractionations and, in principle, the degree of partial melting in the source. This latter application depends on the assumption that the disequilibrium arises from partial melting and requires detailed knowledge of the crystal–liquid partitioning behavior of U and Th, which is presently unavailable. In fact, ^{238}U–^{230}Th disequilibrium data have sometimes been used to try to constrain U and Th partition coefficients [9,11]. The motivation for this work was to constrain the modelling by elevating U and Th partition coefficients from free parameters to known values.

In this paper we present experimental measurements of U and Th partition coefficients between clinopyroxene and synthetic and natural basaltic liquid. These data help constrain the magnitude of U–Th fractionation that will result from crystal–liquid partitioning, thereby providing some insights into the origin of ^{238}U–^{230}Th disequilibrium.

2. Experimental and analytical methods

2.1 Choice of conditions

We used three starting compositions in this study (Table 1). The first is an aphyric MORB from the southern Juan de Fuca ridge (TT152-37 [12,13]). MORB is the most voluminous volcanic rock type on Earth and consistently shows significant U–Th fractionation relative to its source. The second is an alkali basalt from Takashima, Japan [14]. We chose this sample for compositional variation and because U and Th partition coefficients between augite and groundmass have been measured in the original rock by Nagasawa and Wakita [15]. The analytical work of Nagasawa and Wakita appeared to be carefully done, thus this sample offered an interesting opportunity for comparing experimental and phenocryst–matrix partition coefficients. The third is a synthetic diopside + anorthite glass ($Di_{71}An_{29}$ by mole), which was included to increase the compositional variation among the samples and to compare to the results of Benjamin et al. [16]. The major compositional differences among the three are the FeO and alkali contents.

TABLE 1

Starting compositions [a] and run temperatures

	Takashima [b] basalt	Juan de Fuca [b] basalt	$Di_{71}An_{29}$
SiO_2 (wt%)	49.9	51.2	50.2
TiO_2	1.64	1.71	–
Al_2O_3	14.09	12.43	12.25
Cr_2O_3	0.005	–	–
FeO_{tot}	8.30	10.49	–
MnO	0.151	0.197	–
MgO	7.21	6.19	11.83
CaO	12.58	14.68	24.2
Na_2O	2.41	1.88	–
K_2O	1.41	0.087	–
U (ppm)	1020	730	1000
Th	790	700	780
Total	98.6	99.7	99.3
T_i (°C) [c]	1210	1210	1312
T_l	1193	1200	1306
T_f	1160	1179	1273
$F_{crystal}$ [d]	0.12	0.07	0.24

[a] Analyses of super-liquidus quench glasses (average of 3 points).

[b] With 10 wt% wollastonite added.

[c] Initial, liquidus, and final temperatures for crystallization runs (see text).

[d] Typical crystal fraction.

Crystallization experiments were run at atmospheric pressure; consequently, 10 wt% $CaSiO_3$ was added to the two basalts in order to make clinopyroxene the liquidus phase. Adding wollastonite raises the CaO content, but the SiO_2 content is virtually unchanged, as wollastonite has about the same amount of SiO_2 as the basalts.

Th is solely tetravalent, while U has been shown to be multivalent in systems of similar composition and fO_2 values [17,18]. It is therefore likely that the degree of U–Th fractionation is a function of fO_2. To investigate this, we crystallized each composition at oxygen fugacities corresponding to three different oxygen buffers: Ni–NiO (NNO), Fa–Mt–Qz (FMQ) and 1 log unit more oxidizing than Fe–FeO (IW + 1).

2.2 Starting materials

Preparation of the starting materials generally followed the technique of Benjamin et al. [16]. The $Di_{71}An_{29}$ composition and wollastonite component were made by mixing thoroughly and de-

carbonating Puratronic oxides and $CaCO_3$. The $Di_{71}An_{29}$ mixture was then fused in Pt in air for 2 h and then crushed in an agate mortar and pestle. Five grams of each basalt + wollastonite mixture was ground in agate and fused at FMQ for 2 h in a Fe-saturated Pt crucible. The result-

TABLE 2

Microprobe analyses of runs [a]

	Run (fO_2)									
	B (FMQ)		C (NNO)		D (IW+1)		H (IW+1)			
	glass	cpx	glass	cpx	glass	cpx	glass	cpx		
Takashima Basalt										
SiO_2	50.2	50.2	51.7	51.6	50.9	50.8	54.0	52.1		
TiO_2	1.68	1.24	1.71	1.00	1.68	1.38	1.80	1.17		
Al_2O_3	15.03	4.59	15.63	4.41	15.39	4.75	16.34	4.43		
Cr_2O_3	–	0.071	–	0.044	–	0.054	–	0.050		
FeO	8.08	4.35	7.63	4.42	7.06	3.89	5.87	3.42		
MnO	0.151	0.111	0.153	0.118	0.149	0.123	0.152	0.134		
MgO	6.08	15.54	5.77	15.76	6.29	16.12	6.18	16.85		
CaO	11.25	22.0	10.95	22.0	11.78	21.7	12.00	21.8		
Na_2O	2.61	0.203	2.58	0.238	1.86	0.157	1.36	0.141		
K_2O	1.58	–	1.57	0.030	1.41	–	1.06	–		
Total	97.5	98.5	98.7	99.8	97.4	99.2	99.7	100.3		
Na_2O/Na_2O_i [b]	0.97		0.90		0.68		0.46			
FeO/FeO_i [b]	0.92		0.84		0.80		0.62			
	Run (fO_2)									
	E (FMQ)		F (FMQ)		G (NNO)		H (IW+1)		L (IW+1)	
	glass	cpx	glass	cpx	glass	cpx	glass	cpx	glass	cpx
Juan de Fuca Basalt										
SiO_2	52.4	52.3	51.7	52.4	51.0	51.9	50.4	51.6	53.0	52.2
TiO_2	1.81	0.933	1.79	0.929	1.81	1.011	1.78	0.998	1.76	0.869
Al_2O_3	13.41	3.57	13.38	3.54	13.39	3.86	13.30	3.31	13.35	3.03
Cr_2O_3	–	0.015	–	0.018	–	0.020	–	0.015	–	0.015
FeO	9.53	5.44	9.91	5.65	9.96	5.80	9.12	5.15	7.43	4.49
MnO	0.202	0.148	0.216	0.145	0.205	0.131	0.200	0.148	0.203	0.163
MgO	5.52	15.33	5.46	15.36	5.45	15.01	5.91	15.71	6.03	16.12
CaO	14.19	22.8	14.13	22.6	14.00	22.7	14.68	22.5	14.93	22.7
Na_2O	1.67	0.151	1.71	0.160	1.87	0.181	1.23	0.119	0.716	0.075
K_2O	0.091	–	0.086	–	0.103	–	0.068	–	0.025	–
Total	99.7	100.9	99.2	101.0	98.6	100.7	97.6	99.6	98.5	99.8
Na_2O/Na_2O_i	0.81		0.84		0.92		0.63		0.36	
FeO/FeO_i	0.86		0.90		0.92		0.86		0.67	
	Run (fO_2)									
	E (FMQ)		F (FMQ)		G (NNO)		H (IW+1)		L (IW+1)	
	glass	cpx	glass	cpx	glass	cpx	glass	cpx	glass	cpx
$Di_{71}An_{29}$										
SiO_2	49.6	52.6	50.4	54.0	48.0	54.5	49.2	54.4	50.9	53.9
Al_2O_3	14.82	3.00	15.01	3.37	15.07	3.46	15.13	3.38	12.96	3.55
MgO	10.03	18.16	9.83	17.95	9.88	17.89	9.67	18.09	11.43	18.13
CaO	24.1	25.3	24.0	25.3	24.0	25.4	23.9	25.2	23.4	24.8
Total	99.6	99.2	100.2	100.7	98.0	101.3	98.9	101.2	100.5	98.8

[a] Averages of 3–4 points for glass, 1–2 points for crystals.

[b] Na and Fe loss during run: sum of concentration in crystals and glass divided by concentration in starting material.

ing glass was then re-ground in agate for 2 h and dried at 110°C.

U and Th were added as acid solutions to the starting glass powders in the amounts to result in concentrations of about 1000 ppm ^{238}U and ^{232}Th and 50 ppm ^{235}U and ^{230}Th. The spiked powder was fused in sealed Pt (Fe-saturated for the basalts) for 3–5 h at 70–100°C above its liquidus and ball-milled in agate for 10 min to insure homogenization. Experimental charges were made two to four at a time by mixing the spiked glass with polyvinyl alcohol and drying on Fe-unsaturated Pt wire loops. We used 0.004″ Pt wire to minimize Fe loss during the runs, however Fe-loss was significant in some runs (Table 2).

2.3 Crystallization runs

All experiments were run at 1 atm pressure in a vertical quench furnace (Deltech). The fO_2 was controlled with $CO-CO_2$ gas mixtures and monitored with a doped zirconia oxygen sensor calibrated to the Fe–FeO transition [19]. The precision and accuracy of the fO_2 are believed to be ± 0.07 and ± 0.12 log units, respectively. Temperature was measured with a Pt/90Pt–10Rh thermocouple periodically calibrated to the melting points of gold and palladium. The precision and accuracy of the temperature are believed to be ± 2 and ± 5 °C, respectively.

Crystals were grown by slowly cooling the sample in order to produce the large crystals necessary for particle track analysis. Diffusion in the crystals is too slow to allow continual re-equilibration with the liquid [20], but the cooling rates were slow enough to allow homogenization by diffusion within the liquid; thus the crystallization should approach Rayleigh fractionation. We crystallized the samples using the following recipe: melt for 1.5 h at 6–16°C above the liquidus (T_i), drop to 0–2°C below the liquidus (T_l) and hold for 24 h, cool at 1.7°C/h to 20–35°C below the liquidus (T_f), and hold for 1–24 hours at this temperature. The period at T_l is needed to nucleate crystals and to allow the U valence-state distribution in the liquid to equilibrate with the fO_2 [21]. T_i, T_f, T_l, and the degree of crystallization for each composition are listed in Table 1. This technique resulted in 7–25% crystallization in the different compositions and generated euhedral crystals 30–300 μm in size. The lowest degree of crystallization is in the Juan de Fuca basalt and is limited by the onset of plagioclase crystallization. Runs were initiated by putting the charge directly into the hot spot of the furnace at T_i and ended by drop quenching in distilled water.

2.4 Actinide track measurements

U and Th microdistributions were determined from ^{235}U fission track and ^{230}Th α track maps [16,22]. For U, samples were mounted in epoxy, ground until one or more suitable (> 100 μm) crystals were exposed, and irradiated with muscovite detectors with 1.8×10^{15} n/cm^2. We etched the detectors in 50% HF in two steps. An initial 3 min etch was performed, and the high track density in the glass ($\approx 10^8$ trx/cm^2) was measured at three or four points at 18,000 power magnification with a scanning electron microscope. The detectors were then re-etched for 3 min, and the low track densities in the crystals ($\approx 10^6$ trx/cm^2) were measured at 1000 power magnification with an optical microscope using transmitted light. A single fission fragment has an average range of around 10 μm in these samples, so the outer 20 μm of the crystals adjacent to the glass was not counted to avoid any tracks contributed by the glass. The additional etching made the tracks easier to see at the lower magnification. Tests indicated that SEM counts are 10% higher than optical, and we therefore include a 10% increase in all crystal track densities to compare with SEM data on the glass.

A map of ^{230}Th α particle tracks was made by exposing the sample to a cellulose nitrate plastic detector. However, because the plastic detectors have a much wider range in track widths and lengths than the micas, large errors can arise in comparing counts in plastics with highly differing track densities [16]. Thus, we made two exposures: one for the glass (1–2 days) and one for the crystals (30 days). The exposure times were such that the densities in the glass and crystals were similar, and both detectors were etched simultaneously. This way, all the α tracks were counted at about the same density, so any errors in the glass and crystal counts tended to cancel in the ratio $\rho_{crystal}/\rho_{glass}$. Detectors are etched in 6 N NaOH for 50–60 min at 40°C, and tracks are counted at 1000 power magnification with an

optical microscope using transmitted light. As with the fission tracks, the outer 20 μm of the crystal is not counted, as ^{230}Th α particles have a fixed range of 15 μm in these samples.

We counted 1000–2000 tracks for the glass, and individual crystal counts ranged from 14 to 654, averaging about 100. All counting was carried out by the same person under the same conditions. Counts on randomly selected samples were closely reproduced by another person, indicating little counting bias occurred. Occasional checks of older samples indicated no change in counting efficiency with time.

To convert track density ratios to partition coefficients, we made three adjustments. The first was the previously mentioned 10% fission track correction because of the two different instruments used. The second was an atomic number correction, which corrected for the difference in particle range in the crystal and glass; this correction was in the order of 1–3% [16]. Thirdly, since the crystals were grown by fractional crystallization and were thus zoned, a crystallization correction was required. Ideally, the track density we measure in a crystal would reflect the actinide concentration in the liquid integrated over the entire range of crystallization. However, in practice, our measurements are biased towards the core of the crystal because we cannot count the outer 20 μm of the crystal. Although this typically only excludes about 20% of the crystal dimension in cross section, such a rim contains 49% of the crystal volume for a 100 μm crystal. Thus, we assumed that the measured track density in the crystal was the average density integrated up to 50% of the total crystallization. The correction then takes the form:

$$D_z = D_m \frac{F/2}{(F-1)\ln(1-F/2)}$$

(see appendix), where D_z is the zoning corrected partition coefficient; D_m is the measured partition coefficient; and F is the crystal fraction. F was determined from a least squares mass balancing routine [M.B. Baker, pers. commun.] using the SiO_2, Al_2O_3, CaO, MgO, and TiO_2 concentrations of the starting material and the crystals and glass from the runs. This was probably a slight over-correction because the sectioned face of the crystal did not necessarily contain the crystal nucleus and some crystals may have nucleated later than others; in any case, this correction is always less than the amount of crystallization, which is relatively small (Table 1).

2.5 Microprobe measurements

All of the experiments and quench glasses were analyzed with a JEOL 733 electron microprobe, and raw data were reduced with the CITZAF correction procedure [23]. Analyses were made at 50 nA with a 10 μm diameter beam. Na was always measured first, but alkalis were probably lost during glass analysis, as evidenced by the low totals for glasses relative to crystals and the lower totals for the more alkali rich Takashima basalt (Table 2). Glass compositions were measured at 3 or 4 points in the sample, and each crystal was measured at a point approximately half-way between the center and the edge. In addition, core to rim profiles in crystals showed little major element zoning and normal zoning (rim/core $\sim 1 + F$) of incompatible minor elements.

3. Results

3.1 Approach to equilibrium

The crystals in these experiments were grown by fractional crystallization, and hence the bulk crystal is not in equilibrium with the final liquid composition. The time–temperature path, however, was chosen to maintain equilibrium at the crystal–liquid interface during crystal growth. Using this assumption we can calculate actinide partition coefficients with the simple zoning correction described above. One argument for interface equilibrium is that Benjamin et al. [16] found no dependence of actinide partition coefficients on cooling rate for rates up to 10°C/h. However, since a reversal of this type of experiment is not possible, we cannot prove that interfacial equilibrium is maintained, and for some crystals it may not have been. If interfacial equilibrium is not maintained during growth, incompatible elements will be incorporated into crystals in excess of their equilibrium amounts and the partition coefficients we report will be too high. However, based on their geochemical similarity and general coupled behavior in many geologic processes (see

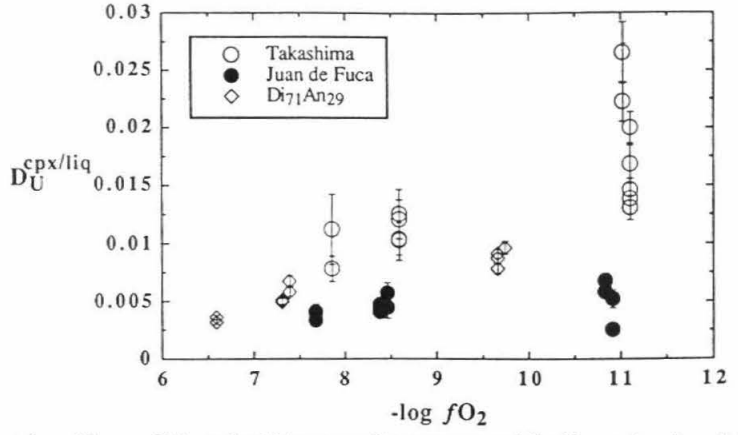

Fig. 1. Individual crystal partition coefficients for U between clinopyroxene and liquid as a function of the negative log of the oxygen fugacity. Experiments were run at the Ni–NiO, Fa–Mt–Qz, and 1 log unit more oxidizing than the Fe–FeO oxygen buffers. Offsets in $-\log fO_2$ between compositions for a given buffer are the result of temperature differences. Separate experiments at a single composition and buffer are distinguished by small offsets in $-\log fO_2$ for clarity. Increase in $D_U^{cpx/liq}$ with decreasing fO_2 is interpreted as resulting from an increase in the proportion of U^{4+} in the melt.

Fig. 4), it is likely that U and Th will be similarly enhanced, making D_{Th}^{cpx}/D_U^{cpx} less sensitive to deviations from interfacial equilibrium than $D_U^{cpx/liq}$ or $D_{Th}^{cpx/liq}$ alone.

3.2 Homogeneity

Microprobe and particle track analyses of the glasses were made on the same points in most cases, and data were taken both near and far from crystals. Line profiles in the glass moving away from crystals were also measured in some samples. Aside from small (10% over 825 μm) MgO and Al_2O_3 gradients in the $Di_{71}An_{29}$ samples, microprobe analyses and track densities near the crystals are indistinguishable from those far from crystals in all samples, indicating that diffu-

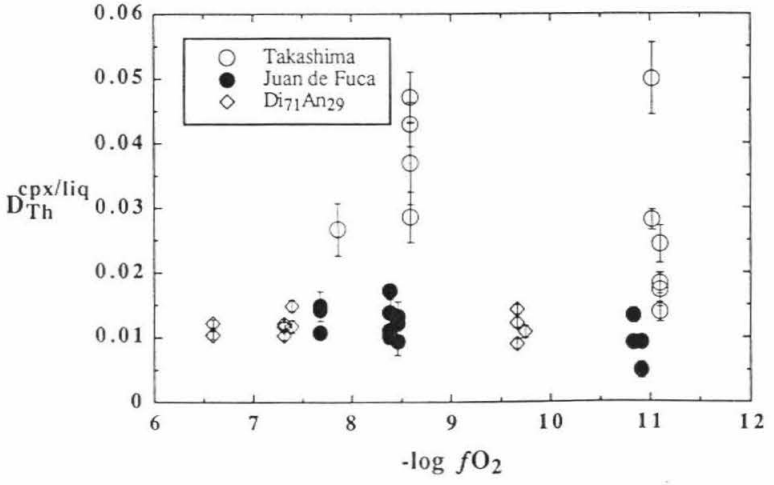

Fig. 2. Individual crystal partition coefficients for Th between clinopyroxene and liquid plotted against the negative log of the oxygen fugacity. In most cases the same crystals were analyzed for U and Th. Offsets in fO_2 are as in Fig. 1. Apparent decrease in $D_{Th}^{cpx/liq}$ for the natural basalts at IW + 1 may be due to compositional changes with fO_2.

TABLE 3

Summary of U and Th partition coefficients

	$D_U^{cpx/liq}$	$D_{Th}^{cpx/liq}$	$D_{Th}^{cpx/liq}/D_U^{cpx/liq}$
$Di_{71}An_{29}$			
NNO	0.0034± 3 [a]	0.0113±13	3.3± 5
FMQ	0.0055± 8	0.0115± 8	2.1± 3
IW+1	0.0089± 8	0.0099±13	1.1± 2
Juan de Fuca			
NNO	0.0038± 4	0.013 ± 2	3.4± 6
FMQ	0.0047± 6	0.0116±18	2.5± 5
IW+1	0.004 ± 2 [b]	0.008 ± 2	2.0±11
Takashima			
NNO	0.0095±17	0.027 ± 8	2.8±10
FMQ	0.0113±12	0.036 ± 7	3.2± 7
IW+1	0.0146±16	0.016 ± 2	1.1± 2

[a] Error applies to last digit and is the sample standard deviation.

[b] Average of crystals within 3σ of lowest point (see text).

sive homogeneity in the liquid was well maintained during the crystallization. This observation supports the assumption of interfacial equilibrium. The standard deviation among the U and Th track densities at the various points in the glass divided by the average counting statistics error was less than 1.7 for all samples; thus the actinides are homogeneous, and the glass track density adopted is calculated using the sum of all tracks counted in the sample.

3.3 U and Th partitioning

A great advantage of in situ analysis is that partition coefficients for both U and Th can be determined on individual crystals, allowing important checks for internal consistency. U and Th partition coefficients for individual crystals are shown in Fig. 1 and 2, and our adopted values are listed in Table 3. These results show that $D_U^{cpx/liq}$ and $D_{Th}^{cpx/liq}$ are both quite small, illustrating the extremely incompatible nature of the actinides.

The $Di_{71}An_{29}$ composition displays the most consistent partitioning for both U and Th. Intra-run variations are small, $D_{Th}^{cpx/liq}$ is consistent in nine out of eleven crystals analyzed, and $D_U^{cpx/liq}$ clearly increases with decreasing fO_2. Similarly, the Juan de Fuca basalt has a relatively well-behaved $D_{Th}^{cpx/liq}$ and $D_U^{cpx/liq}$, but there is some variability beyond counting statistics, increasing at IW + 1. In contrast to the other compositions, there is no clear change in $D_U^{cpx/liq}$ with fO_2 for the Juan de Fuca basalt. There is, however, an apparent decrease in $D_{Th}^{cpx/liq}$ at IW + 1. In the Takashima basalt, both $D_{Th}^{cpx/liq}$ and $D_U^{cpx/liq}$ are consistently larger, but also more variable than in the other two compositions. $D_U^{cpx/liq}$ increases with decreasing fO_2 and $D_{Th}^{cpx/liq}$ appears to decrease at IW + 1. Due to the fact that an increase in $D_U^{cpx/liq}$ with decreasing fO_2 is apparent in two of the compositions and is readily interpretable in terms of the presence of multiple valence states of U, we are confident that it is real. A clear conclusion about the apparent decrease in Th partition coefficients at IW + 1 is more difficult. As Th is solely tetravalent, the cause for such a decrease is not obvious. One possible clue is the observation that the simplified $Di_{71}An_{29}$ composition shows no change in $D_{Th}^{cpx/liq}$ with fO_2. This suggests that Th partitioning in the basaltic compositions may be sensitive to changes in composition that arise from changes in fO_2 (see below).

There is some variability in the partition coefficients that is beyond counting statistics errors. Some of the inter-crystal and inter-run variation may arise from inherent errors in the zoning correction—different crystals may nucleate at different times during the slow cooling, and the cores of some crystals are not analyzed. However, as it is limited by the degree of crystallization, this effect cannot explain all of the variation.

Several studies have shown that trace element partition coefficients depend on crystal and melt composition [e.g., 24,25]. Thus, variations in composition may result in variations in actinide partition coefficients. While all experimental charges for a given composition were made from the same batch of starting material, the composition of the phases and the bulk charge can vary with fO_2 (Table 2). One such compositional change results from Na and Fe loss, which increases with decreasing fO_2. There is some suggestion that variations in $D_{Th}^{cpx/liq}$ and $D_U^{cpx/liq}$ in the lowest fO_2 runs are correlated with the amounts of Na and Fe loss, with greater loss resulting in lower partition coefficients (Tables 2 and 3). This is supported by the fact that the Na- and Fe-free $Di_{71}An_{29}$ compositions show less variability than the basalts and may indicate that actinide activities depend on Na and/or Fe concentrations.

Such a compositional dependence is also consistent with both the apparent decrease in $D_{Th}^{cpx/liq}$ for the basaltic compositions at IW + 1 and the absence of an increase in $D_{U}^{cpx/liq}$ with decreasing fO_2 for the Juan de Fuca basalt (Figs. 1 and 2). In both cases, the relatively lower partition coefficients at low fO_2 could result from decreasing concentrations of Na or Fe. For the Juan de Fuca basalt, this effect could approximately cancel the increase in $D_{U}^{cpx/liq}$ that would result from reducing the U valence state in the system. The absence of a drop in $D_{Th}^{cpx/liq}$ for $Di_{71}An_{29}$ at IW + 1 lends further support to this theory. In the case of Na, this dependence would occur if there is a coupled substitution in the pyroxene, such as $(U,Th)^{4+} + 2Na^{+} \Leftrightarrow 3Ca^{2+}$. That such a mechanism may exist is supported by a positive correlation between D and $[Na_2O]_{crystal}$ and from the fact that the more alkali-rich Takashima basalt has higher partition coefficients than the other compositions.

In addition to compositional variation, it is possible that some of the observed partition coefficient variability is due to changes in the partition coefficients with temperature during crystallization. In principle, all crystals nucleate at T_l and grow over the same temperature range, so such an effect would affect all crystals equally. In reality, although the majority of crystals are of similar size, crystal size does vary, and it is possible that crystals nucleate over a range in temperature. However, the temperature range over which crystals were grown is quite small (Table 1), and in addition, our particle track measurements are only made on the central regions of the larger crystals, further filtering any temperature effects. Another effect of temperature is to change the U valence state distribution in the melt at a given fO_2 [17]. This may affect the U data, but there is no equivalent mechanism for the Th variations. Thus, temperature variations can only play a minor role in accounting for the partition coefficient variations.

While none of the crystals synthesized in this study are morphologically anomalous, a final possibility is that some of the variation is the result of crystal growth too fast for interfacial equilibrium to be maintained. As previously noted, deviations from interfacial equilibrium will tend to make the measured U and Th partition coefficients high. In such a case the lower values would best approximate the equilibrium values. Thus it is possible that the lower values of $D_{Th}^{cpx/liq}$ in the basalts at IW + 1 reflect the true equilibrium values, with the higher values at the higher fO_2 values being caused by non-equilibrium effects.

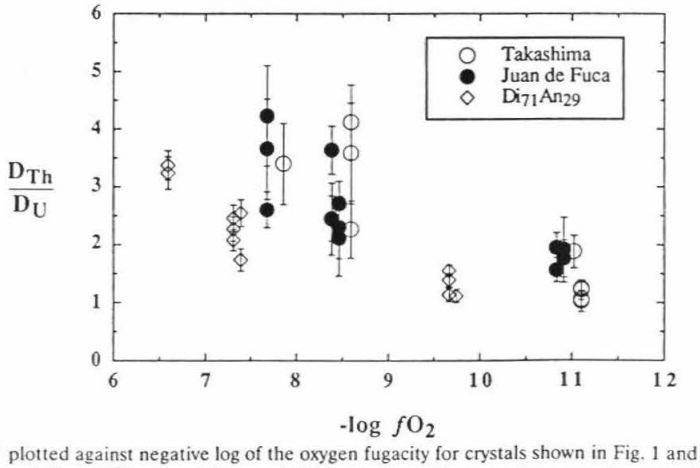

Fig. 3. $D_{Th}^{cpx/liq}/D_{U}^{cpx/liq}$ plotted against negative log of the oxygen fugacity for crystals shown in Fig. 1 and 2. Offsets in fO_2 are as in Fig. 1. Much of the variation in Fig. 1 and 2, especially in the low fO_2 runs, has gone because $D_{Th}^{cpx/liq}$ and $D_{U}^{cpx/liq}$ are correlated. The decrease with increasing fO_2 is due primarily to the increase in $D_{U}^{cpx/liq}$. Note that $D_{Th}^{cpx}/D_{U}^{cpx} > 1$ in all cases, showing that U–Th fractionation by clinopyroxene–liquid partitioning during partial melting will result in a liquid that has a Th/U ratio less than the clinopyroxene in its source.

This implies that the low fO_2 somehow induces a closer approach to equilibrium; but the absence of a change in $D_{Th}^{cpx/liq}$ with fO_2 for the $Di_{71}An_{29}$ composition argues against this interpretation. We, therefore, favor the interpretation that the change in $D_{Th}^{cpx/liq}$ at low fO_2 is compositionally controlled, as discussed above. Nonetheless, the partition coefficient variations at a single fO_2 cannot be completely explained by errors in the zoning correction and compositional and temperature variations, and it is likely that some of the spread is due to non-equilibrium effects. Therefore, a straight average will not reflect the equilibrium value. In order to weight the lower end of the distributions, the adopted values, listed in Table 3, are the averages of all crystals that plot within two counting statistics standard deviations of the crystal with the lowest value. In most cases this value is the average of all crystals for U, while some of the highest Th values are excluded using this criteria. One exception was made for U at IW + 1 for the Juan de Fuca basalt: to prevent the single low point from dominating, the crystals within three standard deviations of the lowest crystal were averaged. The values in Table 3 are our best estimates of equilibrium partition coefficients for the compositions and conditions studied.

Most importantly, both the inter-crystal and inter-run variations in $D_{Th}^{cpx/liq}$ and $D_U^{cpx/liq}$ tend to be correlated (i.e., the crystals with lower $D_{Th}^{cpx/liq}$ also have lower $D_U^{cpx/liq}$). Such a correlation would be expected for any of the variability mechanisms discussed above, and the result is that much of the variation in the partition coefficients cancels in their ratio (Fig. 3). This is evidence of the fact that D_{Th}^{cpx}/D_U^{cpx}, which gives a measure of the degree of U–Th fractionation possible by clinopyroxene–liquid partitioning, is more reliable and robust than either partition coefficient separately.

4. Discussion

The results of this study are actinide partition coefficients between clinopyroxene and basaltic liquid as a function of fO_2 for three different compositions. Over the range of fO_2 values studied, $D_{Th}^{cpx/liq}$ was greater than $D_U^{cpx/liq}$ in all cases. As fO_2 decreases, D_{Th}/D_U can decrease by up to a factor of 3 for a given composition, demonstrating that crystal–liquid U–Th fractionation is fO_2 dependent (Table 3, Fig. 3). This dependence arises predominantly from an increase in $D_U^{cpx/liq}$ with decreasing fO_2, as seen for the Takashima and $Di_{71}An_{29}$ compositions (Fig. 1), which we interpret as resulting from an increase in the proportion of U^{4+} relative to higher valence states in the melt with decreasing fO_2. While the valence state of U in clinopyroxene has never been measured, we assume that it is predominantly tetravalent and that an increase in U^{4+} in the melt therefore causes an increase in $D_U^{cpx/liq}$. This assumption is securely based on partition coefficient–ionic radius systematics [e.g., 26] which show that trace cations prefer to substitute into crystallographic sites of similar ionic radius and charge as the major cation (e.g., Sr in plagioclase), with U^{4+} being closest to Ca^{2+} in this respect. There is a strong decrease in crystal–liquid partition coefficients as the charge difference between the trace element and the major cation increases. Thus, in clinopyroxene, where $D_{REE^{3+}}^{cpx/liq} \gg D_{Th^{4+}}^{cpx/liq}$, it is inevitable that $D_{U^{4+}}^{cpx/liq} \gg D_{U^{5-6+}}^{cpx/liq}$.

It is perhaps surprising that no clear increase in $D_U^{cpx/liq}$ is observed for the Juan de Fuca basalt. As previously mentioned, one possible reason for this is that actinide activities in Fe- and Na-bearing systems appear to be sensitive to compositional changes that stem from changes in fO_2, with partition coefficients decreasing under more reducing conditions. A second possibility is that the valence state distribution of U in this composition does not change with fO_2 in our experiments. Calas [18] has demonstrated that, in addition to oxygen fugacity, the U valence state distribution in silicate melts depends strongly on composition. Subsequent studies have shown specific dependence on the concentrations of other multivalent elements [27] and alkalis [28]. Thus, in the Juan de Fuca basalt, it is quite possible that the concurrent changes in fO_2 and composition, particularly Na and Fe, compete to pull the U valence state distribution in opposite directions, resulting in no net change in $D_U^{cpx/liq}$ in the various experiments.

There are few experimental data with which we can compare our results. Benjamin et al. [16] measured $D_{Th}^{cpx/liq} = 0.029$ and $D_U^{cpx/liq} = 0.018$ for

$Di_{50}Ab_{25}An_{25}$ at 20 kbar, which are somewhat higher than our values for $Di_{71}An_{29}$ (Table 3). The higher values in the Di–Ab–An system may be due to the presence of Na or the higher pressure and temperature of those experiments. From experiments with a natural Kilauea tholeiite at 14 kbar, Tatsumoto [29] measured $D_{Th}^{cpx/liq} = 0.021$ and $D_U^{cpx/liq} = 0.014$, which are comparable to the values for the Takashima composition. Watson et al. [30] measured $D_U^{cpx/liq} = 0.0003$ for Cr-diopside in an Fe free haplobasalt sealed in air. However, as they point out, the high valence states of U likely to be present in these runs casts doubt on the significance of their value to natural conditions. Significantly, both studies that report U and Th partition coefficients are consistent with our results in finding $D_{Th}/D_U > 1$.

Nagasawa and Wakita [15] measured U and Th partition coefficients between large augite crystals and groundmass in the Takashima basalt. In contrast to our results, they measured a lower $D_{Th}^{aug/matrix} = 0.0121$ and a higher $D_U^{aug/matrix} = 0.0167$, giving a significantly lower $D_{Th}/D_U = 0.73$. By analogy with the general consistency of the shape of the REE partition coefficient pattern for clinopyroxene [e.g., 31], we consider it unlikely that D_{Th}^{cpx}/D_U^{cpx} can be > 1 in some cases and < 1 in others. As Nagasawa and Wakita [15] state, there is no definite evidence that the augites are in equilibrium with the groundmass, and we suggest that the composition of the groundmass they analyzed may not represent the liquid that the augites equilibrated with. Based on the high Al_2O_3 content of the augites and bronzites, Kuno [14] concluded that these phases crystallized near the base of the crust. Subsequent lower pressure differentiation, partial resorption of high pressure phases, assimilation of the various mafic inclusions present, or any other fractionation mechanism during the (possibly long) time between augite crystallization and eruption may have changed the U/Th ratio of the liquid. One such process is the crystallization of U- and Th-rich accessory phases after the augite. A fission track map of a section of the Takashima basalt reveals pervasive, small, U-rich stars throughout the groundmass. SEM study of the section revealed micron size apatite and zircon crystals, which are undoubtedly the source of these stars. These minerals have high solubilities in basalts [32,33] and probably crystallized from the glass during quenching. If these apatite and zircon crystals, which preferentially incorporate U over Th, were then separated from the groundmass in

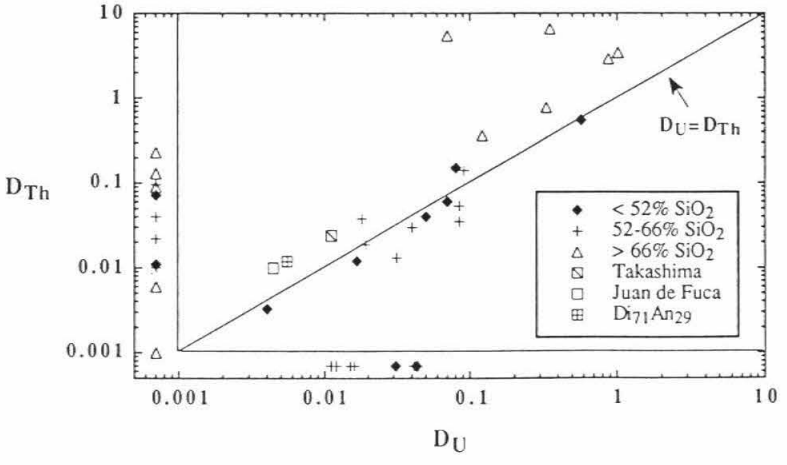

Fig. 4. Clinopyroxene–matrix partition coefficients for U and Th taken from the literature. Points along the axes are from studies that report only U or Th data. Data are subdivided by SiO_2 content, and our experimentally determined values for the three compositions at FMQ are shown for reference. Note the tremendous amount of scatter even within a single SiO_2 range. Data from [15,31,34–44].

the mineral separation process, the reported $D_U^{aug/matrix}$ will be too high and D_{Th}^{aug}/D_U^{aug} too low.

Clinopyroxene–matrix partition coefficients from natural rocks for U and Th give D_{Th}^{cpx}/D_U^{cpx} ratios both greater than and less than 1. Partition coefficients collected from the literature (determined from mineral separates) and our experimentally determined values for the three compositions at FMQ are shown in Fig. 4. The data are distinguished by the whole rock SiO_2 content. Although it is not obvious that this is the best discriminant, very often it is the only data available. Phenocryst–matrix partition coefficients for incompatible elements are typically larger than those determined experimentally, and in many cases this discrepancy can be attributed to impure mineral separates. This is especially likely for highly incompatible elements such as U and Th, and this problem is almost certainly responsible for much of scatter in Fig. 4. Even within a single range in SiO_2 the partition coefficients vary by up to 4 orders of magnitude, making the existing phenocryst–matrix data set for the actinides basically unreliable. This large scatter has confused U–Th fractionation modelling, permitting U and Th partition coefficients to be treated as essentially free parameters. Our experiments constrain actinide partition coefficients for basaltic systems and show that $D_{Th}^{cpx/liq}$ is larger than $D_U^{cpx/liq}$.

5. Application to ^{238}U–^{230}Th disequilibrium

A unique aspect of U and Th series disequilibrium is that a system will always return to secular equilibrium in ≈ 5 daughter half-lives, providing well-constrained initial conditions. In the case of the ^{238}U–^{230}Th disequilibrium, this means that, if a system has been undisturbed by any fractionating processes for approximately 375 000 yrs or more, the $^{238}U/^{230}Th$ activity ratio will have a value of 1. Immediately following a fractionation event, the degree of radioactive disequilibrium is equal to the degree of parent–daughter fractionation produced during the event (i.e., $(^{238}U/^{230}Th)_{rock} = [U/Th]_{rock}/[U/Th]_{source}$). Therefore, we know that a young volcanic rock with $(^{238}U/^{230}Th) < 1$ has U/Th less than that of its source.

^{238}U–^{230}Th disequilibrium measurements have been made on volcanic rocks from a variety of geologic settings. Good reviews are presented by Condomines et al. [6] and Gill et al. [7]. Based on such measurements, MORBs and OIBs are clearly distinguished from other rock types by consistently having $k \leqslant 1$, where $k \equiv (^{238}U/^{230}Th)$ after Allègre and Condomines [10]. As shown in Fig. 5,

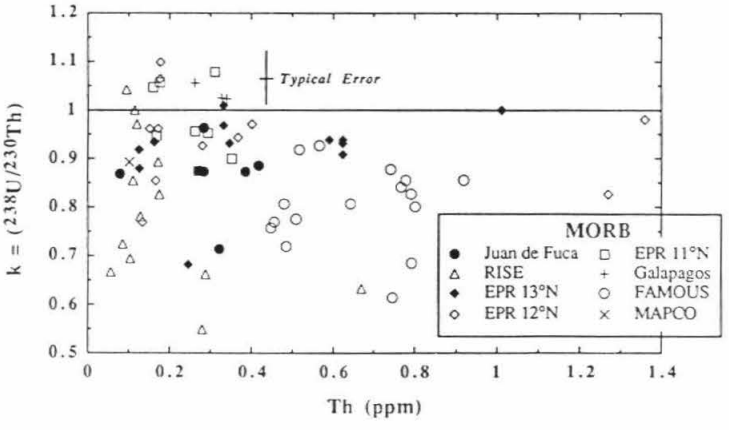

Fig. 5. ^{238}U–^{230}Th disequilibrium plotted against Th content for young MORB from the literature. Samples that authors claim have had activities changed by seawater alteration have been excluded. For young rocks (< 10,000 yrs old) the degree of disequilibrium, k, equals U–Th fractionation. Within the indicated typical error, almost all samples have $k \leqslant 1$. There is no correlation between k and Th content, suggesting that the degree of disequilibrium is not related to degree of melting. Data from [45] (FAMOUS and MAPCO), [46] (Juan de Fuca), [9] (RISE), [47] (EPR 13°N), [48] (EPR 12°N), [49] (EPR 11°N), [50] (Galapagos).

the maximum degree of disequilibrium observed in MORBs is about $k = 0.6$, with an average of about $k = 0.84$ [51]. This disequilibrium results from a process that fractionates U from Th, the nature of which has been speculated upon, but never determined. It is important to point out, however, that among the different mechanisms thought to exist, fractionation in MORBs and OIBs is usually ascribed to partial melting (e.g. [6,47]). In the following paragraphs we use our results to evaluate this hypothesis.

The most important consequence of our experimental results is that the measured ^{238}U–^{230}Th disequilibrium in MORB cannot be produced by clinopyroxene–liquid fractionation during partial melting. This is because the sense of fractionation produced by clinopyroxene–liquid partitioning is the opposite of what is required for the observed disequilibrium.

Clinopyroxene is almost certainly an essential source constituent in generating MORB melts [e.g. 52] and, while it is typically considered to be the primary host phase for incompatible trace elements as well, it is important to evaluate the extent to which phases other than clinopyroxene contribute to actinide element signature of the MORB source. Clinopyroxenes from ultramafic xenoliths and ophiolites virtually always concentrate U relative to orthopyroxene, olivine, and spinel, usually to a great extent [29,53–57], and the few available measurements indicate that this is also true for Th [29,57]. In addition, it has been shown repeatedly that most other large ion lithophile elements (K, Rb, Cs, Sr, Ba, Y, REE) in ultramafic xenoliths are concentrated in clinopyroxene [e.g. 58–62]. Finally, our preliminary results for olivine–liquid partitioning experiments give $D_{U,Th}^{ol/liq} < 0.0001$. Thus, clinopyroxene appears to contain the bulk of the U and Th in the MORB source. Contribution of actinides by accessory phases cannot be ruled out; however, the ubiquitous nature of U–Th fractionations in MORB suggests that the behavior of U and Th is dictated by primary phases. Thus, our partition coefficients, appropriately scaled for the modal abundance of clinopyroxene, should be applicable to the complete MORB source, indicating that ^{238}U–^{230}Th disequilibrium in MORB may not result from partial melting at all.

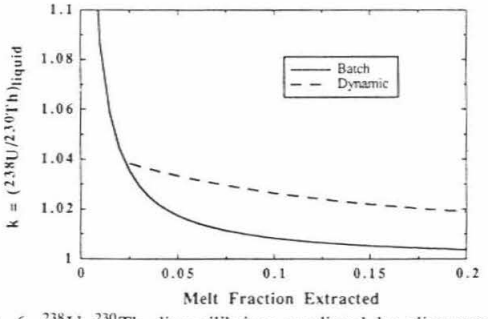

Fig. 6. ^{238}U–^{230}Th disequilibrium predicted by clinopyroxene–liquid partitioning as a function of melt fraction extracted for batch (equilibrium and dynamic [11] melting. Both models use $D_U^{cpx/liq} = 0.0045$, $D_{Th}^{cpx/liq} = 0.01$, assume 17% clinopyroxene in the source [65], all U and Th in clinopyroxene (bulk $D_U = 0.00077$, $D_{Th} = 0.0017$), and modal melting. Parameters were chosen so that the magnitude of the calculated disequilibrium is an upper limit (see text). For dynamic melting, upwelling rate (roughly half spreading rate at ridge) = 5 cm/yr, thickness of melting region = 40 km [67], $\rho_{solid} = \rho_{liquid} = 2.7$, and initial batch melt = porosity throughout melting = 2%. Note that k is always > 1, and disequilibrium is $< 5\%$ for all melt fractions above 2%.

As an illustration of this we have calculated the degree of ^{238}U–^{230}Th disequilibrium produced during partial melting using our results. Analyses of Fe^{3+}/Fe^{2+} in MORB glasses indicate that melting in the MORB source region occurs at an fO_2 of about 2 log units more reducing than NNO [63,64]. Interpolation of our data for the Juan de Fuca basalt gives $D_{Th}^{cpx/liq} = 0.01$, $D_U^{cpx/liq} = 0.0045$, and $D_{Th}/D_U = 2.2$ under these conditions. The modal abundance of clinopyroxene in spinel lherzolites is variable, and a single value for the MORB source cannot be safely assigned. For our example we chose 17%, the highest value found in the primitive group of spinel lherzolites analyzed by Jagoutz et al. [65]. Assuming that this represents the upper limit, an upper limit on U–Th fractionation is defined: values below 17% will result in less fractionation. Using these parameters, we have plotted the locus of k values generated by various degrees of partial melting of a source in secular equilibrium for two simple melting models (Fig. 6). The solid curve is for a batch melting case, assuming $k = [U/Th]/[U/Th]_{source}$, as explained above. The dashed curve is calculated using a dynamic melting model [66] adapted to ^{238}U–^{230}Th disequilibrium by Williams and Gill [11]. A significant

aspect of this model, pertinent to radioactive disequilibrium, is that it allows for changes in k during a finite melting time. Modal melting, while obviously unrealistic, was used because dynamic melting models have not been worked out for non-modal melting. However, allowing clinopyroxene to melt in a more realistic proportion of 50–70% [52] will decrease fractionation, so our model again represents a maximum degree of ^{238}U–^{230}Th disequilibrium.

From Fig. 6 we see that during partial melting it is exceedingly difficult for either model to generate large U–Th fractionations. Moreover, it is impossible for the liquid to have $k < 1$, as this would require $D_U > D_{Th}$, the opposite of what we find in our experiments. This sense of fractionation follows from the measured partition coefficients and is independent of any specific model parameters. At 5% melt extraction, dynamic melting produces less than 4% disequilibrium, far less than the average observed value of 16% [51]. Much larger degrees of melting are indicated for MORB (e.g. [67]), resulting in even less fractionation. Again, the predicted disequilibrium is in the opposite sense from that observed for MORB, clearly ruling out clinopyroxene–liquid fractionation during partial melting as the source of ^{238}U–^{230}Th disequilibrium in MORB. By similar arguments, no significant U–Th fractionation in a liquid will result from fractional crystallization of less than about 95%.

This result has important significance for our understanding of melting at mid-ocean ridges. Based on ^{238}U–^{230}Th disequilibrium, certain constraints on MORB genesis have been proposed. Assuming that the bulk partition coefficients for U and Th are 0.005 and 0, respectively, McKenzie [66] argued that the melting region beneath a ridge is over 100 km wide, the porosity must be less than 2%, and that the melting time must be long compared to the half-life of ^{230}Th. Williams and Gill [11] propose that MORBs are mixtures of varying proportions of a 1% melt and a 15% melt. While we are not necessarily opposed to these models, our results fail to confirm that ^{238}U–^{230}Th disequilibrium can be used to support such interpretations. On the other hand, to the extent that Th isotope ratios reflect the source region and not U–Th fractionation processes, conclusions regarding mantle heterogeneity or contamination based on variations in ($^{230}Th/^{232}Th$) are unaffected by our results [e.g. 47,68].

The conclusion that ^{238}U–^{230}Th disequilibrium in MORB may not result from crystal–liquid fractionation during partial melting is supported by additional observations. Dynamic melting predicts that lavas from slow spreading ridges should have greater disequilibrium than those from faster spreading ridges, but no correlation is observed [7]. Disequilibrium produced by crystal–liquid fractionation should also result in a correlation between k and some indicator of degree of melting, such as the Th content, but it does not (Fig. 5, [7]). Finally, it has been shown that ^{238}U–^{230}Th disequilibrium in arc rocks and the extreme ^{230}Th-^{226}Ra disequilibrium in some MORB require models more complex than partial melting [48,69].

Beyond ^{238}U–^{230}Th disequilibrium there are other geochemical data which have been interpreted as indicating that Th is more incompatible than U. There is a positive correlation between Th/U and Th for MORB [70], and a negative correlation between ($^{230}Th/^{232}Th$) and $^{87}Sr/^{86}Sr$ in MORB and OIB [45]. The former was interpreted as evidence that Th is preferentially extracted over U with progressive melting in the mantle, and the latter correlation implies that Th/U and Rb/Sr are correlated in the mantle, and has been similarly interpreted [6]. Our results show that these interpretations cannot be the case for a source where most of the U and Th is in clinopyroxene, and suggests that neither U–Th nor Rb–Sr fractionations are crystal–liquid controlled.

In order to explain the observed ^{238}U–^{230}Th disequilibrium in MORB, any U–Th fractionation mechanism must be large, ubiquitous, and result in a value of $k < 1$. Possible alternatives to clinopyroxene–liquid fractionation during partial melting include: (a) fractionation of the mantle source prior to MORB genesis, either by extraction of a minute melt fraction or infiltration by a mobile fluid phase; (b) melt–vapor fractionation during degassing; (c) recent contamination of the magma by hydrothermally altered oceanic crust; (d) reversal of the sense of U–Th fractionation by clinopyroxene at the pressure of MORB melting (i.e., $D_{Th}^{cpx}/D_U^{cpx} < 1$ at high pressure); and (e) fractionation of U and Th by some other crys-

talline phase, most plausibly garnet, during partial melting.

Mechanism (a) is tempting because U and Th are extremely magmaphile and will concentrate in the liquid phase after a very small amount of melting. A recent event will leave behind a highly fractionated (in the correct sense for MORB; i.e., $k < 1$) residual solid that may be still fertile enough to produce MORB. A difficulty with this type of fractionation is separating and hiding the highly fractionated initial melt. Recently, Stolper and Newman [71] have successfully modelled variations of 20 trace elements, including U and Th, in a suite of Marianas trough basalts as resulting from the addition of a trace element laden, H_2O-rich, component to the source. This component is enriched in Th relative to U, and if this enrichment is recent, addition of this component will decrease k. They assumed that the ultimate origin of this fluid is the subducting slab. Designating the origin of a similar component in the MORB source is somewhat more problematic, but this type of mechanism appears to be viable.

Because of the low volatile content of MORBs, vapor–melt fractionation (b) requires large U and Th enrichments in the vapor phase to be significant. Fission track data from fluid inclusions in ultramafic xenoliths [72] and rhyolite melt–vapor partitioning experiments [73,74] indicate that very little U or Th partitions into the vapor phase.

Most MORB has undergone extensive hydrothermal alteration (c), as is evident from ^{18}O exchange [75]. Based on detailed sampling of the Oman ophiolite, Gregory and Taylor [76] concluded that hydrothermal systems completely surround the magma chamber, and it is likely that stoping of such hydrothermally altered wall and roof rocks contaminates the magma prior to eruption [H.P. Taylor, pers. commun.]. The effect of seawater alteration on U-series disequilibrium in MORB has been addressed in several previous studies [9,45,46,49], and it appears that, despite the high U/Th in seawater, the net effect of alteration is to decrease k. In addition, $k < 1$ in some Hawaiian lavas have been attributed to recent assimilation of ^{230}Th-rich altered crust at depth by the primary magma [77], indicating that alteration by deep hydrothermal circulation may affect mid-ocean ridge magma chambers as well. Further, this process may be difficult to detect as the assimilant will typically have the same composition as the magma. It, therefore, appears that assimilation of hydrothermally altered crust is a possible explanation for the low k of MORB.

The effect of pressure on actinide fractionation by clinopyroxene (d) is poorly constrained. There is no appreciable difference between the results of Tatsumoto [29] for a Kilauean basalt at 14 kbar and our results for the Takashima basalt at 1 bar. Compositional differences may compensate for any pressure effect, however. In the $Di_{50}Ab_{25}An_{25}$ system, Seitz [78] also saw no change in actinide partition coefficients between 10 and 25 kbar. On the other hand, Benjamin et al. [16] report $D_U^{cpx/liq} = 0.018$ at 20 kbar, which is significantly greater than the value measured by LaTourrette et al. [79, and unpublished data] for the same composition at 1 bar and comparable fO_2. It is likely that this increase is a consequence of the large temperature difference (200°C) and changes in phase compositions with pressure, but it is also possible that the U valence state distribution is sensitive to pressure, in which case pressure might be an important variable in considering U–Th fractionation. However, as previously noted, Benjamin et al. [16] report a comparably high value of $D_{Th}^{cpx/liq}$, resulting in $D_{Th}^{cpx}/D_U^{cpx} > 1$, consistent with our 1 bar results. The concurrent increase in both U and Th partition coefficients suggests that the changes are structurally controlled and that any effect of pressure on the U valence state distribution is not important. This is further supported by similar small increases in clinopyroxene–liquid partition coefficients with pressure for REE [80]. Thus, while it is possible that the absolute values of clinopyroxene–liquid actinide partition coefficients change with pressure, the ratio of the partition coefficients will not be significantly different at high pressure.

Evidence for garnet remaining in the MORB source comes from Lu–Hf isotopes [81] and REE abundances in East Pacific Rise basalts [82] and abyssal peridotites [83]. To our knowledge, there are no published garnet-matrix partition coefficients for the actinides in natural rocks. Fission track studies of the U-distribution in garnet-bearing xenoliths from kimberlites and basalts show that the ratio of U in garnet to that in

clinopyroxene is highly variable, both greater than and less than 1 ([54] and references therein). Kato et al. [84] have published the only experimental garnet–liquid partitioning data for the actinides, and they report only that $D_U^{gt/liq}$ and $D_{Th}^{gt/liq}$ are probably smaller than 0.1. If these values can be used as upper limits for melting in the MORB source, U–Th fractionation by garnet cannot be ruled out on this basis.

Of the possibilities listed, we feel the most plausible U–Th fractionation mechanisms for MORB appear to be fractionation of the source region by a fluid phase shortly before melting (a) or fractionation of the magma prior to eruption by stoping of altered crust (c). Although there is no direct evidence for these processes affecting ^{238}U–^{230}Th disequilibrium in MORB, they are preferred because they have been shown to fractionate U and Th in the correct sense for MORB in other environments and have the potential to produce variable amounts of disequilibrium under fairly uniform petrogenetic conditions.

Acknowledgements

We thank H. Nagasawa and D. Stakes for providing the basalt samples. Neutron irradiations were carried out by P. Rogers at the TRIGA reactor facility. C. Irvine and P. Carpenter assisted with the electron microprobe analyses. Discussions with M. Baker, J. Beckett, D. Bell, I. Carmichael, M. Johnson, G. Mattioli, G. Rossman and E. Stolper were very helpful. Critical reviews by C. Lesher and B. Mysen resulted in considerable improvements in the manuscript. This research was supported by a NASA Graduate Student Researchers Program Fellowship.

Appendix: Derivation of zoning correction

Due to the fact that we cannot count tracks right up to the crystal–glass boundary, the measured track density in a crystal corresponds to the average concentration of a trace element, i, in the crystal integrated up to 50% of the total crystallization (see above). This can be expressed as:

$$\langle C_i^{xtl}\rangle = \frac{\int_0^{F/2} C_i^{xtl}\,dF'}{\int_0^{F/2} dF'} \tag{1}$$

where C is concentration and F is the crystal fraction. If the true partition coefficient, D, is defined as C_i^{xtl}/C_i^{liq}, then, at any point during fractional crystallization, the concentrations in the crystal and liquid are:

$$C_i^{xtl} = C_{i_o}^{liq} D(1-F)^{D-1} \tag{2}$$

and

$$C_i^{liq} = C_{i_o}^{liq}(1-F)^{D-1} \tag{3}$$

where $C_{i_o}^{liq}$ is the initial concentration of i in the liquid. Substituting (2) into (1) and performing the integration yields:

$$\langle C_i^{xtl}\rangle = (2/F)C_{i_o}^{liq}\left[1-(1-F/2)^D\right] \tag{4}$$

The measured partition coefficient, D_m, is given by $\langle C_{xtl}\rangle/C_{liq}$. Substituting (3) and (4) into this expression gives:

$$D_m = \frac{(2/F)\left[1-(1-F/2)^D\right]}{(1-F)^{D-1}} \tag{5}$$

This can be linearized by setting $g(D) = (1-F/2)^D$ and taking a first order Taylor Series expansion about $D = 0$:

$$g(D) = 1 + D\,\ln(1-F/2) \tag{6}$$

and

$$1-(1-F/2)^D = 1-g(D) = -D\,\ln(1-F/2) \tag{7}$$

Similarly, setting $y = D-1$, $h(y) = (1-F)^y$, and taking a first order Taylor Series expansion about $y = -1$ we get:

$$h(y) = \left[1 + D\,\ln(1-F)\right]/(1-F) \tag{8}$$

Substituting (7) and (8) into (5) and solving for D results in:

$$D = D_m \frac{1}{(2/F)(F-1)\ln(1-F/2) - D_m \ln(1-F)} \tag{9}$$

Noting that the right hand term in the denominator is much smaller than the left hand term for the very small partition coefficients we measure, this can be simplified to:

$$D = D_m \frac{F/2}{(F-1)\ln(1-F/2)} \tag{10}$$

where D is the zoning corrected partition coefficient.

References

1 S.R. Taylor, Planetary Science: A Lunar Perspective, 481 pp., Lunar Planet. Inst., Houston, 1982.

2 G. Crozaz, Uranium and thorium microdistributions in stony meteorites, Geochim. Cosmochim. Acta 43, 127–136, 1979.

3 B. Hagee, T.J. Bernatowicz, F.A. Podosek, M.L. Johnson, D.S. Burnett and M. Tatsumoto, Actinide abundances in ordinary chondrites, Geochim. Cosmochim. Acta 54, 2847–2858, 1990.

4 M.T. Murrell and D.S. Burnett, Actinide chemistry in Allende Ca–Al-rich inclusions, Geochim. Cosmochim. Acta 51, 985–999, 1987.

5 J.C. Laul and J.S. Fruchter, Thorium and uranium variations in Apollo 17 basalts and systematics, Proc. Lunar Planet. Sci. Conf. 1, 1545–1559, 1976.

6 M. Condomines, Ch. Hemond and C.J. Allègre, U-Th-Ra radioactive disequilibria and magmatic processes, Earth Planet. Sci. Lett. 90, 243–262, 1988.

7 J.B. Gill, D.M. Pyle and R.W. Williams, Igneous rocks, in: Uranium Series Disequilibrium: Applications to Environmental Problems, M. Ivanovitch and R.S. Harmon, eds., 2nd ed., Oxford University Press, 1992.

8 S. Newman, J.D. Macdougall and R.C. Finkel, ^{230}Th-^{238}U disequilibrium in island arcs: Evidence from the Aleutians and the Marianas, Nature 308, 268–270, 1984.

9 S. Newman, R.C. Finkel and J.D. Macdougall, ^{230}Th–^{238}U disequilibrium systematics in oceanic tholeiites from 21°N on the East Pacific Rise, Earth Planet. Sci. Lett. 65, 17–33, 1983.

10 C.J. Allègre and M. Condomines, Basalt genesis and mantle structure studied through Th-isotopic geochemistry, Nature 299, 21–24, 1982.

11 R.W. Williams and J.B. Gill, Effects of partial melting on the uranium decay series, Geochim. Cosmochim. Acta 53, 1607–1619, 1989.

12 J. Eaby, D.A. Clague and J.R. Delaney, Sr isotopic variations along the Juan de Fuca ridge, J. Geophys. Res. 89, 7883–7890, 1984.

13 R.A. Liias, Geochemistry and petrogenesis of basalts erupted along the Juan de Fuca ridge, Ph.D. Thesis, Univ. Massachusetts, 1986.

14 H. Kuno, Aluminian augite and bronzite in alkali olivine basalt from Taka-sima, North Kyushu, Japan, Advancing Front, Geol. Geophys. 1964, 205–220, 1965.

15 H. Nagasawa and H. Wakita, Partition of uranium and thorium between augite and host lavas, Geochim. Cosmochim. Acta 32, 917–922, 1968.

16 T.M. Benjamin, W.R. Heuser and D.S. Burnett, Actinide crystal–liquid partitioning for clinopyroxene and $Ca_3(PO_4)_2$, Geochim. Cosmochim. Acta 44, 1251–1264, 1980.

17 H.D. Schreiber, The chemistry of uranium in glass-forming aluminosilicate melts, J. Less Common Metals 91, 129–147, 1983.

18 G. Calas, Etude expérimentale du comportement de l'uranium dans les magmas: États d'oxydation et coordinance, Geochim. Cosmochim. Acta 43, 1521–1531, 1979.

19 J. Myers and H.P. Eugster, The system Fe–Si–O: Oxygen buffer calibrations to 1500K, Contrib. Mineral. Petrol. 82, 75–90, 1983.

20 M. Seitz, Uranium and thorium diffusion in diopside and fluorapatite, Carnegie Inst. Wash. Yearb. 72, 586–588, 1973.

21 H.D. Schreiber, Properties of redox ions in glasses: An interdisciplinary perspective, J. Non-Cryst. Solids 42, 175–184, 1980.

22 D.S. Burnett and D.S. Woolum, In situ trace element microanalysis, Annu. Rev. Earth Planet. Sci. 11, 329–358, 1983.

23 J.T. Armstrong, Quantitative analysis of silicate and oxide materials: Comparison of Monte Carlo, ZAF, and $\phi(\rho z)$ procedures, in: Microbeam Analysis—1988, D.E. Newberry, ed., pp. 239–246, San Francisco Press, 1988.

24 B.O. Mysen and D. Virgo, Trace element partitioning and melt structure: An experimental study at 1 atm pressure, Geochim. Cosmochim. Acta 44, 1917–1930, 1980.

25 J.R. Beckett, A.J. Spivack, I.D. Hutcheon, G.J. Wasserburg and E.M. Stolper, Crystal chemical effects on the partitioning of trace elements between mineral and melt: An experimental study of melilite with applications to refractory inclusions from carbonaceous chondrites, Geochim. Cosmochim. Acta 54, 1755–1774, 1990.

26 N. Onuma, H. Higuchi, H. Wakita and H. Nagasawa, Trace element partition between two pyroxenes and the host lava, Earth Planet. Sci. Lett. 5, 47–51, 1968.

27 H.D. Schreiber, R.C. Merckel Jr., V. Lea Schreiber and G.B. Balazs, Mutual interactions of redox couples via electron exchange in silicate melts: Models for geochemical melt systems, J. Geophys. Res. 92, 9233–9245, 1987.

28 S.V. Yudintsev, B.I. Omel'yanenko and G.L. Lyubomilova, Uranium valency state in granitic melts, Geochem. Int. 28 (4), 65–71, 1991.

29 M. Tatsumoto, Isotopic composition of lead in oceanic basalt and its implication to mantle evolution, Earth Planet. Sci. Lett. 38, 63–87, 1978.

30 E.B. Watson, D. Ben Othman, J-M. Luck and A.W. Hofmann, Partitioning of U, Pb, Cs, Yb, Hf, Re and Os between chromian diopsidic pyroxene and haplobasaltic liquid, Chem. Geol. 62, 191–208, 1987.

31 F. Lemarchand, B. Villemant and G. Calas, Trace element distribution coefficients in alkaline series, Geochim. Cosmochim. Acta 51, 1071–1081, 1987.

32 E.B. Watson, Apatite and phosphorus in mantle source regions: An experimental study of apatite melt equilibria at pressures to 25 kbar, Earth Planet. Sci. Lett. 51, 322–335, 1980.

33 S.E. DeLong and C. Chatelain, Trace-element constraints on accessory-phase saturation in evolved MORB magma, Earth Planet. Sci. Lett. 101, 206–215, 1990.

34 J. Dostal, C. Dupuy, J.P. Carron, M. Le Guen de Kerneizon and R.C. Maury, Partition coefficients of trace elements: Application to volcanic rocks of St. Vincent, West Indies, Geochim. Cosmochim. Acta 47, 525–533, 1983.

35 L.M. Larson, Distribution of REE and other trace elements between phenocrysts and peralkaline undersaturated magmas, exemplified by rocks from the Gardar igneous province, South Greenland, Lithos 12, 303–315, 1979.

36 G. Mahood and W. Hildreth, Large partition coefficients for trace elements in high-silica rhyolites, Geochim. Cosmochim. Acta 47, 11–30, 1983.

37 N. Onuma, S. Ninomiya and H. Nagasawa, Mineral/groundmass partition coefficients for nepheline, melilite, clinopyroxene and perovskite in melilite–nepheline basalt, Niyiragongo, Zaire, Geochem. J. 15, 221–228, 1981.

38 B. Villemant, H. Jaffrezic, J.-L. Joron and M. Treuil, Distribution coefficients of major and trace elements; fractional crystallization in the alkali basalt series of Chaîne des Puys (Massif Central, France), Geochim. Cosmochim. Acta 45, 1997–2016, 1981.

39 J. Dostal and S. Capedri, Partition coefficients of uranium for some rock-forming minerals, Chem. Geol. 15, 285–294, 1975.

40 J. Dostal, S. Capedri and C. Dupuy, Uranium and potassium in calc-alkaline volcanic rocks from Sardinia, Lithos 9, 179–183, 1976.

41 L. Francalanci, A. Peccerillo and G. Poli, Partition coefficients for minerals in potassium–alkaline rocks: Data from Roman province (Central Italy), Geochem. J. 21, 1–10, 1987.

42 G.A. Mahood and J.A. Stimac, Trace-element partitioning in pantellerites and trachytes, Geochim. Cosmochim. Acta 54, 2257–2276, 1990.

43 W.P. Nash and H.R. Crecraft, Partition coefficients for trace elements in silicic magmas, Geochim. Cosmochim. Acta 49, 2309–2322, 1985.

44 G. Wörner, J.-M. Beusen, N. Duchateau, R. Gijbels and H.U. Schmincke, Trace element abundances and mineral/melt distribution coefficients in phonolites from the Laacher See Volcano (Germany), Contrib. Mineral. Petrol. 84, 152–173, 1983.

45 M. Condomines, P. Morand and C.J. Allègre, ^{230}Th-^{238}U radioactive disequilibria in tholeiites from the FAMOUS zone (Mid-Atlantic ridge, 36°50'N): Th and Sr isotopic geochemistry, Earth Planet. Sci. Lett. 55, 247–256, 1981.

46 S.J. Goldstein, M.T. Murrell and D.R. Janecky, Th and U isotopic systematics of basalts from the Juan de Fuca and Gorda Ridges by mass spectrometry, Earth Planet. Sci. Lett. 96, 134–146, 1990.

47 D. Ben Othman and C.J. Allègre, U–Th isotopic systematics at 13°N east Pacific Ridge segment, Earth Planet. Sci. Lett. 98, 129–137, 1990.

48 K.H. Rubin and J.D. Macdougall, ^{226}Ra excesses in mid ocean ridge basalts and mantle melting, Nature 355, 158–161, 1988.

49 I. Reinitz and K.K. Turekian, ^{230}Th/^{238}U and ^{226}Ra/^{230}Th fractionation in young basaltic glasses from the East Pacific Rise, Earth Planet. Sci. Lett. 94, 199–207, 1989.

50 S. Krishnaswami, K.K. Turekian and J.T. Bennett, The behavior of ^{232}Th and the ^{238}U decay chain nuclides during magma formation and volcanism, Geochim. Cosmochim. Acta 48, 505–511, 1984.

51 B. Bourdon, A bidimensional model for U series disequilibria in MORB, EOS, Trans. Am. Geophys. Union 72, 295, 1991 (Abstr.).

52 D.K. Kostopoulos, Melting of the shallow upper mantle: A new perspective, J. Petrol. 32, 671–699, 1991.

53 J. Dostal, S. Capedri and F. Aumento, Uranium as an indicator of the origin of the Tethyan ophiolites, Earth Planet. Sci. Lett. 26, 345–352, 1975.

54 L.L. Kashkarov, A.S. Pavlenko, G.V. Baryshnikova, V.P. Serenko and A.V. Ukhanov, Uranium in mantle xenoliths from the Udachnaya and Obnazhennaya North Yakutia kimberlite pipes: New f-radiography determinations, Geochem. Int. 25(8), 84–96, 1988.

55 S. Nishimura, Partition of uranium between peridotite nodule and host basalt, Chem. Geol. 10, 211–221, 1972.

56 J.D. Kleeman, D.H. Green and J.F. Lovering, Uranium distribution in ultramafic inclusions from Victorian basalts, Earth Planet. Sci. Lett. 5, 449–458, 1969.

57 A. Meijer, T.-T. Kwon and G.R. Tilton, U–Th–Pb partitioning behavior during partial melting in the upper mantle: Implications for the origin of high mu components and the "Pb paradox", J. Geophys. Res. 95, 433–448, 1990.

58 F.A. Frey and D.H. Green, The mineralogy, geochemistry, and origin of lherzolite inclusions in Victorian basanites, Geochim. Cosmochim. Acta 38, 1023–1059, 1974.

59 H.-G. Stosch, Rare earth element partitioning between minerals from anhydrous spinel peridotite xenoliths, Geochim. Cosmochim. Acta, 46, 793–811, 1982.

60 A. Zindler and E. Jagoutz, Mantle cryptology, Geochim. Cosmochim. Acta, 52, 319–333, 1988.

61 S.Y. O'Reilly, W.L. Griffin and C.J. Ryan, Residence of trace elements in metasomatized spinel lherzolite xenoliths: A proton microprobe study, Contrib. Mineral. Petrol. 109, 98–113, 1991.

62 J.A. Philpotts, C.C. Schnetzler and H.H. Thomas, Petrogenetic implications of some new geochemical data on eclogitic and ultrabasic inclusions, Geochim. Cosmochim. Acta 36, 1131–1166, 1972.

63 D.M. Christie, I.S.E. Carmichael and C.H. Langmuir, Oxidation states of mid-ocean ridge basalt glasses, Earth Planet. Sci. Lett. 79, 397–411, 1986.

64 I.S.E. Carmichael, The redox states of basic and silicic magmas: A reflection of their source regions?, Contrib. Mineral. Petrol. 106, 129–141, 1991.

65 E. Jagoutz, H. Palme, H. Baddenhausen, K. Blum, M. Cendales, G. Dreibus, B. Spettel, V. Lorenz and H. Wänke, The abundances of major, minor, and trace elements in the Earth's mantle as derived from primitive ultramafic nodules, Proc. Lunar Sci. Conf. 10, 2031–2050, 1979.

66 D. McKenzie, ^{230}Th-^{238}U disequilibrium and the melting processes beneath ridge axes, Earth Planet. Sci. Lett. 72, 149–157, 1985.

67 D. McKenzie and J.M. Bickle, The volume and composition of melt generated by extension of the lithosphere, J. Petrol. 29, 625–679, 1988.

68 Ch. Hemond, M. Condomines, S. Fourcade, C.J. Allègre, N. Oskarsson and M. Javoy, Thorium, strontium and oxygen isotopic geochemistry in recent tholeiites from Iceland: Crustal influence on mantle-derived magmas, Earth Planet. Sci. Lett. 87, 273–285, 1988.

69 J.B. Gill and R.W. Williams, Th isotope and U-series studies of subduction-related rocks, Geochim. Cosmochim. Acta 54, 1427–1442, 1990.
70 K.P. Jochum, A.W. Hofmann, E. Ito, H.M. Seufert and W.M. White, K, U and Th in mid-ocean ridge basalt glasses and heat production, K/U and K/Rb in the mantle, Nature 306, 431–436, 1983.
71 E. Stolper and S. Newman, The role of water in the petrogenesis of Mariana Trough magmas: Implications for the heterogeneity of the mantle, Earth Planet. Sci. Lett., submitted.
72 M. Polve and M.D. Kurz, Helium isotopic and fission track studies of ultramafic xenoliths, EOS, Trans. Am. Geophys. Union 65, 1154, 1984 (Abstr.).
73 D. London, R.L. Hervig and G.B. Morgan, VI, Melt-vapor solubilities and elemental partitioning in peraluminous granite-pegmatite systems: Experimental results with Macusani glass at 200 MPa, Contrib. Mineral. Petrol. 99, 360–373, 1988.
74 H. Keppler and P.J. Wyllie, Role of fluids in transport and fractionation of uranium and thorium in magmatic processes, Nature 348, 531–533, 1990.
75 K. Muelenbachs, Alteration of the oceanic crust and the ^{18}O history of seawater, in: Stable Isotopes, J.W. Valley, H.P. Taylor, Jr. and J.R. O'Neil, eds., Mineral. Soc. Am. Rev. Mineral. 16, 425–444, 1986.
76 R.T. Gregory and H.P. Taylor, Jr., An oxygen isotope profile in a section of cretaceous oceanic crust, Samail Ophiolite, Oman: Evidence for $\delta^{18}O$ buffering of the oceans by deep (> 5 km) seawater-hydrothermal circulation at mid-ocean ridges, J. Geophys. Res. 86, 2737–2755, 1983.
77 M. Condomines, M. Bernat and C.J. Allègre, Evidence for contamination of recent lavas from ^{230}Th-^{238}U data, Earth Planet. Sci. Lett. 33, 122–125, 1976.
78 M.G. Seitz, Uranium and thorium partitioning in diopside–melt and whitlockite–melt systems, Carnegie Inst. Wash. Yearb. 72, 581–586, 1973.
79 T.Z. LaTourrette, M.L. Johnson and D.S. Burnett, Actinide element fractionation in solar system processes: The role of oxygen fugacity, Lunar Planet. Sci. XXI, 684–685, 1990 (Abstr.).
80 T.H. Green and N.J. Pearson, Effect of pressure on rare earth element partition coefficients in common magmas, Nature 305, 414–416, 1983.
81 V.J.M. Salters and S.R. Hart, The hafnium paradox and the role of garnet in the source of mid-ocean ridge basalts, Nature 342, 420–422, 1989.
82 J.F. Bender, C.H. Langmuir and G.N. Hansen, Petrogenesis of basalt glasses from the Tamoyo region, East Pacific Rise, J. Petrol. 25, 213–254, 1984.
83 K.T. Johnson, H.J.B. Dick and N. Shimizu, Melting in the oceanic upper mantle: An ion microprobe study of diopsides in abyssal peridotites, J. Geophys. Res. 95, 2661–2678, 1990.
84 T. Kato, A.E. Ringwood and T. Irifune, Experimental determination of element partitioning between silicate perovskites, garnets and liquids: Constraints on early differentiation of the mantle, Earth Planet. Sci. Lett. 89, 123–145, 1988.